Characterization of geochemical interactions and migration of hydrogen in sandstone sedimentary formations : application to geological storage

Alireza Ebrahimiyekta

Centre Val de Loire UNIVERSITÉ

UNIVERSITÉ D'ORLÉANS

UNIVERSITE D'ORLEANS

ÉCOLE DOCTORALE
ENERGIE, MATERIAUX, SCIENCES DE LA TERRE ET DE L'UNIVERS

INSTITUT DES SCIENCES DE LA TERRE D'ORLÉANS

THÈSE présentée par :

Alireza EBRAHIMIYEKTA

soutenue le : **5 Juillet 2017**
Discipline : *Sciences de l'environnement*

pour obtenir le grade de : **Docteur de l'université d'Orléans**

Characterization of geochemical interactions and migration of hydrogen in sandstone sedimentary formations: Application to geological storage

THÈSE dirigée par :

Pascal AUDIGANE	Docteur HDR**,** BRGM
Michel PICHAVANT	Directeur de Recherche, Université d'Orléans

RAPPORTEURS :

Laurent TRUCHE	Professeur, Université Grenoble Alpes - ISTerre
Marc FLEURY	Professeur, IFP Energies nouvelles
Michael KÜHN	Professeur, GFZ, POTSDAM

JURY :

Bruno SCAILLET	Directeur de Recherche, CNRS, Président du jury
Patrick EGERMANN	Ingénieur de Recherche, Storengy
Vincent LAGNEAU	Professeur, MINES ParisTech

To my dearest Mojdeh,

For your love, understanding and encouragement which made me, work harder every day, without it and your patience and sacrifice, I would not be where I am now

To my Lovely daughter, Elia,

You made me stronger whenever I needed it

I love you both dearly

Résumé

Dans les années récentes, les énergies renouvelables (comme le vent et l'énergie solaire) ont été en forte demande pour réduire la pollution de l'environnement. Selon la feuille de route de l'UE, 20% de l'énergie totale sera fournie par les énergies renouvelables en 2020. Toutefois, les énergies renouvelables sont variables, largement incontrôlables et difficiles à prédire. En outre, en raison de la fluctuation de ce type d'énergies, le stockage de l'énergie devient un paramètre clé pour, à court et à long terme, ajuster la puissance générée à la consommation. L'hydrogène a longtemps été discuté comme un candidat pour le stockage d'énergie à grande échelle. Lorsque la production d'énergie d'éolienne ou solaire est excédentaire, le surplus d'électricité peut être utilisé pour produire de l'hydrogène par électrolyse (« power to gas »). Ensuite, l'utilisation de ce gaz à des fins énergétiques peut être déclinée en différentes applications parmi lesquelles le transport, la réinjection dans le réseau ou bien le stockage (géologique ou autre) pour des utilisations futures. Le stockage géologique est la technologie la plus prometteuse pour stocker de grandes quantités d'hydrogène à moindre coût. L'hydrogène peut être stocké dans des formations souterraines, par exemple dans des cavités salines ou en milieu poreux (champs d'hydrocarbures déplétés ou aquifères). Lorsque la demande d'électricité dépasse la production d'électricité, l'hydrogène stocké peut être converti en énergie. Actuellement, le stockage en milieu poreux semble présenter plusieurs avantages par rapport au stockage en cavité saline, notamment en termes de volume de gaz stocké et de coût. La recherche sur les procédés de stockage de l'hydrogène est donc en développement. Parmi les options en cours d'investigation, le stockage souterrain de l'hydrogène dans les formations sédimentaires comme les grès pourrait offrir un potentiel unique pour stocker de grandes quantités d'énergie.

En raison de la petite taille et de la grande mobilité de la molécule, l'hydrogène a une forte capacité à migrer dans les milieux poreux. Il peut également être très réactif avec les minéraux des roches. Donc, il est important d'étudier les risques de fuites de gaz ou de réaction entre le gaz et les minéraux des roches réservoirs. Dans le cas d'un stockage dans des roches sédimentaires comme les grès, les transformations minéralogiques dues à la présence d'hydrogène pourraient modifier la structure poreuse de la roche et affecter les propriétés de stockage. En outre, et de façon analogue à d'autres types de stockage souterrain à grande échelle (dioxyde de carbone et gaz naturel par exemple), un défi important pour le développement d'un projet de stockage est la bonne compréhension de la migration du fluide pendant et après l'injection. Caractériser les paramètres de la migration est donc de première importance. Les propriétés intrinsèques de la roche (porosité, perméabilité) et les propriétés d'écoulement multiphasiques (relations constitutives entre perméabilité relative / pression capillaire et saturation en eau) sont d'une importance essentielle. Les propriétés intrinsèques de la roche réservoir peuvent être déterminées une fois le projet de stockage défini. Les propriétés d'écoulement multiphasiques dépendent du fluide à injecter et sont aujourd'hui pratiquement inconnues dans le cas de l'hydrogène. Le

développement du stockage souterrain de l'hydrogène souligne la nécessité de déterminer ces propriétés. L'évaluation des modalités de stockage souterrain de l'hydrogène nécessite donc à la fois une connaissance précise des transformations minéralogiques dues à la présence de l'hydrogène et l'acquisition de données sur le comportement hydrodynamique des fluides.

En outre, il est important d'intégrer les interactions géochimiques et les propriétés d'écoulement des fluides in situ dans les conditions d'un site de stockage. Bien que certains auteurs aient étudié numériquement le comportement hydrodynamique de l'hydrogène en conditions de stockage souterrain, ou aient testé la viabilité de l'hydrogène comme méthode de stockage à grande échelle de l'énergie, peu d'études ont pris en compte de façon couplée processus de migration in situ de l'hydrogène et transformations minéralogiques des roches. Le fonctionnement dynamique du réservoir sous de longues échelles de temps, son intégrité et sa durabilité doivent être déterminés pour évaluer le potentiel et la viabilité du stockage souterrain de l'hydrogène. Cela comprend la mise en œuvre d'approches numériques de simulation du fonctionnement des réservoirs souterrains.

Par conséquent, cette thèse se composera de trois parties :

1. *Etude des interactions géochimiques de l'hydrogène dans des formations sédimentaires gréseuses : approche expérimentale et modélisation numérique ;*

Dans cette partie, l'interaction géochimique de l'hydrogène et de roches gréseuses a été évaluée expérimentalement et numériquement. Des expériences ont été réalisées pour tester la possibilité de transformations minérales dues à l'hydrogène, soit pur soit en présence d'eau. Les expériences ont été réalisées principalement à 100 °C et plus rarement à 200 °C. Des pressions d'hydrogène maximales de 100 bars ont été imposées et les durées expérimentales ont varié de 1,5 à 6 mois. Les produits expérimentaux portent la marque d'une réaction très limitée entre les minéraux du grès et l'hydrogène. Si les résultats expérimentaux sont combinés aux résultats numériques, l'étude démontre que l'hydrogène, une fois injecté, peut être considéré comme relativement inerte. De façon globale, nos résultats renforcent la faisabilité du confinement de l'hydrogène dans des réservoirs géologiques comme les grès.

2. *Etude de la migration de l'hydrogène dans les grès : détermination expérimentale de la perméabilité relative (Kr) et de la pression capillaire (Pc) du système hydrogène-eau ;*

Afin de fournir des données quantitatives pour le développement du stockage souterrain de l'hydrogène dans les roches sédimentaires poreuses, la pression capillaire et la perméabilité relative ont été mesurées pour le système hydrogène-eau. Les tests ont été effectués sur un grès triasique. Deux conditions potentielles de stockage souterrain de l'hydrogène («moins profond» : 55 bars, 20 ° C et «plus profond» : 100 bars, 45 ° C) ont été étudiées. La courbe de pression capillaire a été mesurée suivant une technique semi-dynamique modifiée. Les données ont été combinées avec des mesures de type « Mercury injection capillary pressure » (MICP) pour obtenir un modèle de pression capillaire valide sur presque toute la

plage de saturation en eau. Les tensions inter-faciales et les angles de contact pour le système hydrogène-eau ont également été dérivés.

Les courbes de perméabilité relative mesurées donnent des valeurs faibles pour des saturations d'eau minimales de ~ 40%. En les combinant avec les données de pression capillaire, la perméabilité relative de l'hydrogène dans le grès peut être évaluée pour pratiquement la plage totale de saturation en eau. Les pressions capillaires et les perméabilités relatives varient peu entre les deux ensembles de conditions expérimentales. Ceci indique que les données obtenues sont applicables à l'ensemble des conditions de stockage de l'hydrogène. Les nombres capillaires calculés pour nos expériences de perméabilité relative sont < 0,5, ce qui suggère un régime d'écoulement limité par capillarité pour le système hydrogène-eau. Malgré les deux différents ensembles de conditions étudiées, les perméabilités relatives restent très proches l'une de l'autre, un effet attribué à la viscosité presque constante de l'hydrogène dans nos conditions de pression et de température. Ce comportement contraste avec d'autres types de fluides (par exemple, le système CO_2-eau) pour lequel les nombres capillaires peuvent fortement varier avec la pression et la température.

3. Modélisation numérique d'un site de stockage géologique d'hydrogène ;

La simulation numérique présentée dans cette partie a été effectuée pour caractériser l'évolution dynamique d'un site de stockage d'hydrogène pur. Une fluctuation saisonnière du fonctionnement du réservoir et l'effet des fuites d'hydrogène dues aux réactions microbiennes et minérales ont été pris en compte. Le stockage est réalisé dans l'aquifère d'un grès, analogue aux grès triasiques du Buntsandstein du bassin de Paris. Le transport réactif du gaz hydrogène à travers le réservoir a été modélisé. Les résultats des études expérimentales présentées dans les deux parties précédentes ont été utilisés dans l'étude numérique. Pendant la période de développement, le réservoir a été pressurisé en injectant 280 millions d'hydrogène Sm^3. Ce volume permet une production annuelle maximum de 140 millions de Sm^3 de gaz, et il correspond à une consommation annuelle d'électricité d'environ 83 185 ménages en France. Les résultats indiquent que les réactions (principalement biotiques) peuvent affecter la production d'hydrogène. Environ 10% de l'hydrogène produit (~ 15 millions de Sm^3) pourrait être perdu lors des réactions souterraines.

Abstract

In recent years, renewable energy (like wind and solar) has been in high demand to reduce environmental pollution. According to the EU Roadmap, 20% of total energy will be supplied by renewable energy in 2020. However, the renewable energies are variable, largely uncontrollable and hard to predict, while the most favorable locations for generating variable renewables are often far from consumptions centers. In addition, due to the fluctuation of renewable energy, the storage of energy is the key parameter to equalize the generated power and consumption in short and long term. Hydrogen has long been discussed as one candidate for large-scale energy storage. At the time of excess wind or solar power generation, the surplus electricity can be used to produce hydrogen by electrolisis. Hydrogen can be stored in subsurface formations: for instance, salt caverns, depleted gas/oil and saline aquifers. When electricity demand is surpassing electricity generation, hydrogen can be converted into energy. In France, salt formations are already used for fluid underground storage sites but the majority of the natural gas storage is performed in porous sedimentary rocks. In this thesis research on hydrogen storage in porous rocks is evaluated as a storage solution for renewable energy systems as it offers a unique potential to store large amounts of energy compared to salt or crystalline rocks.

However, being composed of small molecules, hydrogen has a strong ability to migrate in porous media and can also be highly reactive with rock-forming minerals. In the case of storage in sedimentary rocks such as sandstones, mineralogical transformations due to the presence of hydrogen may modify the porous structure of the rock and affect the storage properties. In addition, as for other types of large-scale underground fluid storage (carbon dioxide, natural gas for instance), an important challenge for the development of a storage project is the good understanding of the fluid migration during and after the injection. Characterizing the parameters governing the migration is therefore of first importance. Rock intrinsic properties (porosity, absolute permeability) and the multi-phase flow properties (constitutive relationships between relative permeability/capillary pressure and the fluid saturation) are, in this view, essential. These flow characteristics appear as usual inputs in classical large-scale flow simulations. Rock intrinsic properties might be known prior to a storage project, but multiphase flow properties are usually unknown as they are dependent on the fluid to be injected. The development of underground hydrogen storage emphasizes the need of determining those properties. Evaluating the underground hydrogen storage requires a precise knowledge of the hydrodynamic behavior of the fluids and of mineralogical transformations due to the presence of hydrogen that may modify the porous structure of the rock and affect the storage properties.

Furthermore, since the geochemical changes upon hydrogen injection are susceptible to vary with reservoir conditions, it is important to investigate potential chemical reactions and changes in flow properties under the in-situ conditions anticipated at the storage site. Although some authors studied numerically the hydrodynamic behavior of underground hydrogen storage or the viability of hydrogen

storage as a large-scale energy storage, in-situ migration of hydrogen coupled to geochemical alterations of the rocks or the brine components interaction to study the influence of the hydrogen reactions on the reservoir operations are scarce.

Hence, the objectives of this thesis are to evaluate the potential of underground hydrogen storage and to estimate the integrity and sustainability of the natural underground reservoir. This includes determining the chemical rock reactivity and the hydrodynamic behavior of hydrogen-bearing fluid mixtures experimentally and by using numerical modeling. Therefore, this thesis will consist in three parts:

1. *Study of geochemical reactivity of hydrogen in sandstone sedimentary formations: experimental approach and numerical modeling;*

   In this study, the geochemical reactivity of hydrogen with sandstone was assessed both experimentally and numerically. Experiments were performed to test the possibility of mineral transformations due to hydrogen, either pure or in presence of water. The experiments were carried out mostly at 100 and more rarely at 200 °C. Maximum hydrogen pressures of 100 bar were imposed and experimental durations ranged from 1.5 to 6 months. The experimental products bear the mark of only very limited reaction between sandstone minerals and hydrogen. Taken together with the numerical results, this study demonstrates that hydrogen, once injected, can be considered as relatively inert. Overall, our results support the feasibility of hydrogen confinement in geological reservoirs such as sandstones.

2. *Study of the migration of hydrogen in sandstone: experimental determination of relative permeability (kr) and capillary pressure (Pcap) of hydrogen-water system;*

   To provide quantitative data for the development of underground hydrogen storage in porous sedimentary rocks, capillary pressures and relative permeabilities have been measured for the hydrogen-water system. The tests have been performed on a Triassic sandstone. Two potential underground hydrogen storage conditions (‘shallower’: 55 bar, 20 °C and ‘deeper’: 100 bar, 45 °C) have been investigated. Capillary pressure curves have been measured following a modified semi-dynamic technique. The data have been combined with Mercury injection capillary pressure measurements to derive a model for capillary pressure valid over almost the entire water saturation range. Interfacial tensions and contact angles for the hydrogen-water system have been also derived. Relative permeability curves measured with the steady-state technique yield low values for minimum water saturations of ~40%. When combined with the capillary pressure data, the relative permeability of hydrogen in sandstone can be evaluated for almost the total range of water saturation. Capillary pressures and relative permeabilities values vary slightly between the two different sets of experimental conditions indicating that the obtained data are applicable for the entire range of hydrogen storage conditions. Capillary numbers calculated for our relative permeability experiments are < 0.5, indicating a capillary-limited flow regime for the hydrogen-water system. Despite the two

differing sets of conditions investigated, the relative permeability curves stay very close from each other, an effect attributed to the almost constant viscosity of hydrogen under our pressure and temperature conditions. This is in contrast with other fluid pairs (e.g., CO2-water system) where capillary numbers can strongly vary with pressure and temperature.

3. *Numerical simulation of a geological hydrogen storage site on a commercial scale;*

   The numerical simulation presented in this study was performed to characterize the evolution of pure hydrogen storage, by considering the seasonal fluctuation of renewable energy and the effect of hydrogen leakage due to the microbial and mineral reactions. The aquifer storage from typical eastern France sedimentary Triassic sandstone in Buntsandstein layer of the Paris Basin was consider to model reactive transport of hydrogen gas through the reservoir. Results of the two previously presented experimental studies were used in the numerical study. During the development period, the reservoir pressure was pressurized by injecting 280 million Sm^3 hydrogen. The numerical simulation calculates a peak hydrogen extraction amount of 140 million Sm^3 in one annual gas withdrawal. This volume is equal to an annual electricity consumption of roughly 83,185 France average households. The results indicated that the reactions in the storage due to the contact of hydrogen gas and water components and biotic reactions affected the hydrogen produced during one year and that approximately 10% of produced hydrogen (~15 million Sm^3) could be consumed because of underground reactions.

Acknowledgements

I would like to express my deepest gratitude and sincere appreciation to Professor Michel Pichavant and Dr. Pascal Audigane for all their support, guidance and encouragement throughout of this study. Without you, especially during some difficult times that I have had during this journey, accomplishment of this work would not be possible.

I would also like to give special thanks to Dr. Jean-Charles Manceau for all their advice, support and help during the development of my study.

I would also like to thank Dr. Catherine Lerouge and Dr. Joachim Tremosa for their precious advices and thoughtful discussions.

I am deeply grateful to Remy Champallier, Colin Fauguerolles and Johan Villeneuve for their guidance and helps.

I would also like to thank the École des Mines, Vincent Lagneau and Irina Sin that help me to complete my work.

I am debited to many others at ISTO for providing me with all the support I needed.

I am grateful to ISTO and BRGM for the financial support that made this work possible.

Finally, I thank my parents, my **Mother** and my **Father** to their continuous support and encouragement and also my sister and brothers.

Table of contents

Chapter 1

General introduction

According to the Paris climate change agreement (*COP21* 2016), increasing renewable energies (i.e. wind and solar power) to 36% of the global energy mix by 2030 would provide about half of the emissions reduction needed to hold warming to 2°C (*International Renewable Energy Agency -IRENA* 2016). Indeed, due to greenhouse gas warming stemming from fossil energy uses, the transition of energy supply from fossil sources to renewable energy sources is essential for mitigating climate change effects and preparing for a future of sustainable energy supply (*IEA* 2013). Furthermore, due to the earthquake accident at the Fukushima nuclear power plant in Japan, countries like Germany, have also decided to phase out nuclear energy generation within one decade (until 2022) which would further accelerate the switch to renewable energy sources (*Bruninx et al.,* 2013). Wind and solar power are seen to play an important role in this energy transition. However, both of them are variable renewable energy sources, and as such, their integration in the power sector is challenging (geographical dispersion, fluctuation over different time horizons see e.g. *Schaber et al.,* 2012; *Després et al.,* 2016). In addition, renewable energies are variable, largely uncontrollable and hard to predict. Therefore, due to the fluctuation of renewable energy, the storage of energy and its capacity are key parameters to equalize the generated power and consumption in both the short and long terms (*Denholm et al.,* 2010). Hence, energy storage technologies, which consist in storing energy to make it available to meet demand when needed, are listed as a solution to facilitate the integration of intermittent energy sources (*Reitenbach et al.,* 2015).

1.1 Energy storage technologies

Several criteria allows for a classification and a selection of the storage technologies efficiency and applications. The most common criteria are the lifetime, life cycle, power and energy, self-discharge rates, environmental impact, cycle efficiency, capital cost, storage duration, and technical maturity. On

this basis, the appropriateness of the various applications has been evaluated for a panel of energy storage technologies (batteries, superconducting, flywheels, capacitors, fuel cells, hydrogen, thermal, compressed air and pumped hydro systems). When comparing these techniques with the discharge rate versus the power capacity, a large spectrum of possible applications is revealed (Figure 1-1). Among the panel of massive storage technologies, one can find (i) the Underground Pumped Hydro-Storage (UPHS) which are an adaptation of classical Pumped Hydro Storage system often connected with dam constructions, (ii) the compressed air storage (CAES) and (iii) the hydrogen storage from conversion of electricity into H_2 and O_2 by electrolysis. Aquifer Thermal Energy Storage (ATES) is also mentioned but applies for local network (buildings) implantation. Hydrogen underground storage is part of the "Power to gas" concept which allows for converting electricity into a gas available for reuse in refineries, mobility or injection in natural gas grid (up to a threshold ranging from few to 10 % (*HyUnder project* 2013) depending on the studies).

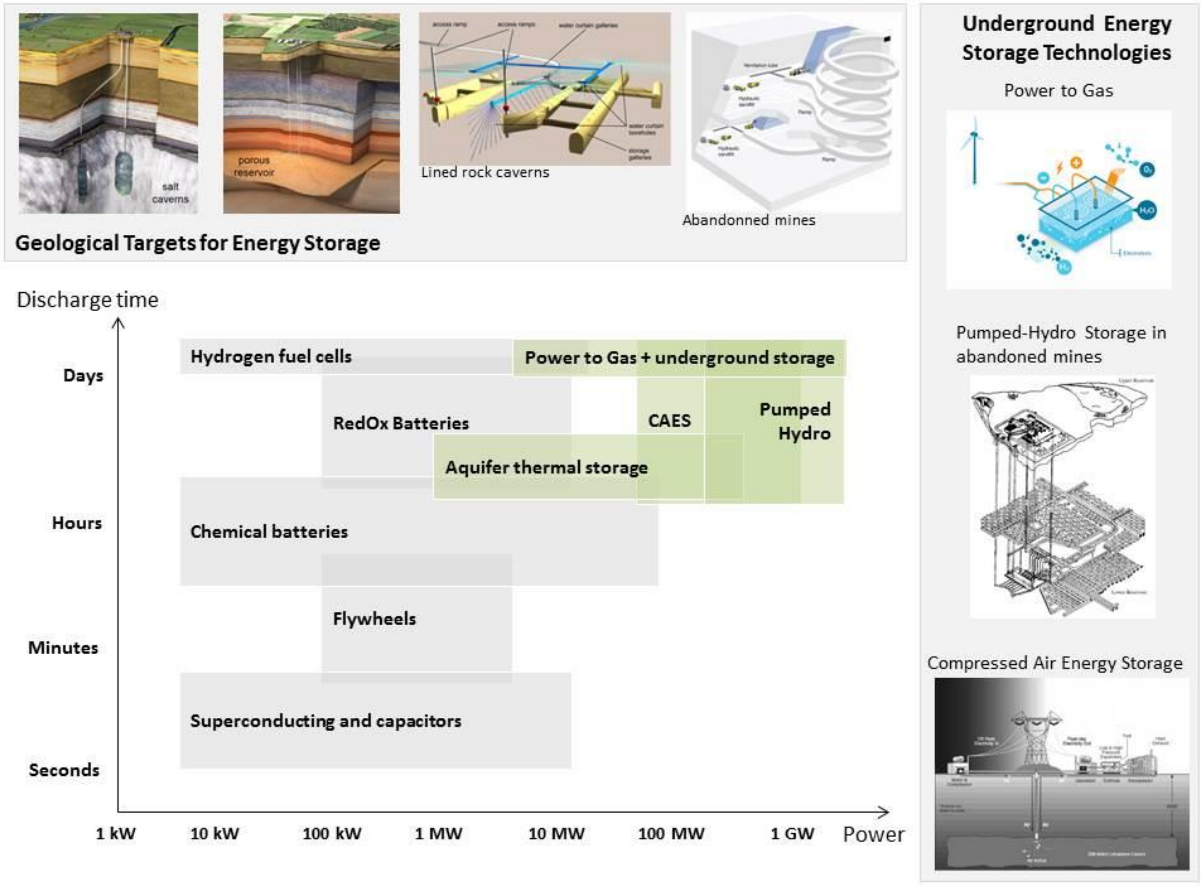

Figure 1-1 Ranking of electrical storage technologies according to discharge time and power capacity (Audigane et al., 2015). In green are represented those related to the use of underground: Power to gas (Hychico, Argentina), Underground Pumped-Hydro (Uddin and Asce, 2003), CAES (Windpower Engineering & Development) and aquifer thermal storage. Four typical geological targets are envisaged: salt cavern, porous reservoir (KBB, Germany), lined rock caverns (Geostock, France), and abandoned mines (Atlas Copco, Sweden).

Power-to-Gas (P2G) is the process of converting surplus renewable energy into hydrogen gas by electrolysis (*Winkler-Goldstein et al.*, 2013) and its subsequent, injection into the reservoir to store it or inject to the gas distribution network via blending or further conversion to methane (Figure 1-2).

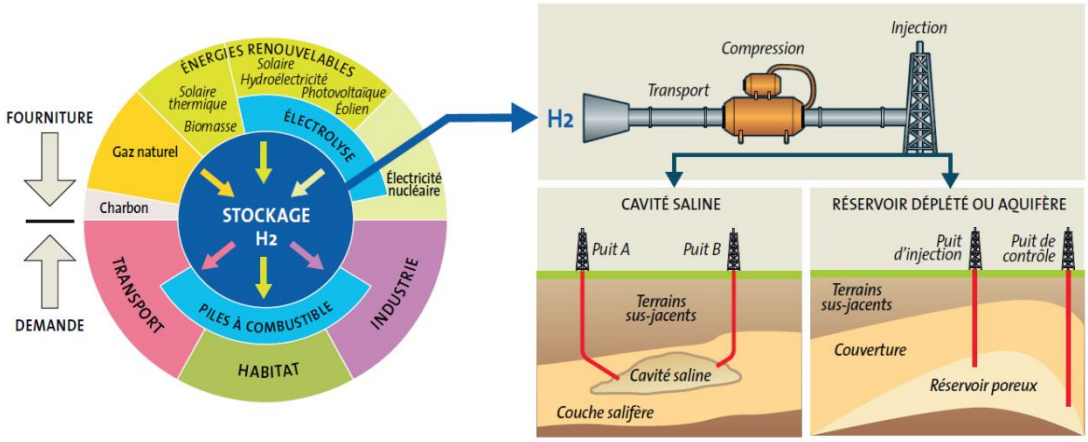

Figure 1-2 The role of storage in the hydrogen economy (*Bader et al.*, 2014)

In times of high energy demand, hydrogen can be transformed back directly into the electrical energy through electrochemical processes with well-developed fuel cells or into thermal energy through thermochemical reaction processes with combustion engines and turbines (*Pudukudy et al.*, 2014). However, hydrogen storage and its energy applications can include a wide power range; from small-scale use in fuel cells to hydrogen powered vehicles and to large-scale applications i.e., thermal combustion turbines and in the main engines of the space shuttle and in rocket engines.

Fuel cells convert chemical energy directly in to electrical energy by the reverse process to that of electrolysis. Fuel cells do not need combustion to produce energy, therefore, they are more efficient and cleaner than combustion engines (*Pudukudy et al.*, 2014). However, hydrogen gas reacts with oxygen to produce water and an electrical current:

$$2H_2 + O_2 = 2H_2O + energy \qquad (1\text{-}1)$$

where the energy released is electrical. This process, produce electricity directly and do not require any mechanical parts (unlike combustion in gas turbines), thus, makes fuel cells more reliable. It has to be noted that any impurities of hydrogen can reduce the energy production. Therefore, the pure hydrogen should be used in this process. However, practically, the process of converting hydrogen into electricity has a poor level of energy efficiency, ranging from around 30% to 48% (*Decourt et al.*, 2014). Although, by recovering heat losses from re-electrification (recycling heat), the energy efficiency of the hydrogen-to-electricity conversion system can increase up to 60% (*Decourt et al.*, 2014).

Hydrogen, as a fuel gas, can also be used in combustion turbines. Combusting hydrogen with oxygen generates water and heat (Equation (1-1) that energy released in that process is heat). Heated vapor is transferred into a turbine to produce mechanical energy, which, in turn, is converted into electricity by

a generator. In addition, hydrogen can be mixed with natural gas to use in conventional gas turbine or use as a fuel that could be injected into the gas pipeline. This technology is also known as power-to-gas. However, just only use 1% to 5% volume of hydrogen blended with natural gas could be caused prevent the risks of materials damaging (*Decourt et al.,* 2014). Otherwise, hydrogen could harm the turbine and cause accidents due to steel susceptibility.

Moreover, pure hydrogen produced from electrolysis can be converted to methane (CH_4) by reacting with CO_2 and CO (Methanogenesis). The subject of this process that is called methanation is to enrich the energy potential of the gas by reaction of hydrogen and CO_2 and converting to methane (*Panfilov* 2016). Methane can be used then in a turbine to produce electricity. Methane from such processes has usually a high purity, it is easy to store and to transport and its combustion emits few pollutants compared to oil and coal combustion (*Burkhardt et al.,* 2013).

$$4H_2 + CO_2 = CH_4 + 2H_2O - 167\ KJ/mol \quad (1\text{-}2)$$

$$3H_2 + CO = CH_4 + H_2O - 206\ KJ/mol \quad (1\text{-}3)$$

These reactions can occur at high temperature and higher pressure conditions in presence of expensive catalysts with a resulting lower overall efficiency or in presence of microorganism at low temperature around 37°C and pH range from 6.8 to 7.2 with high priority of methane (up to 98%) that was proven experimentally by *Goldman et al.* (2009). This process in underground storage could happen due to the bacteria activity at low temperature (Sabatier's methanation reaction Equation (1-2) that was suggested in research by *Panfilov* (2010) and *Panfilov and Reitenbach* (2016).

1.2 Underground geological storage

Geological hydrogen storage has long been discussed as a candidate for large-scale energy storage. *Walters* (1976) is one of the earliest to compare hydrogen underground storage with existing natural gas storage facilities while the main conclusion of the comparison was that there are no insurmountable or environmental problems in using underground hydrogen storage. In addition, *Carden and Paterson* (1979) investigated the possibility of hydrogen leakage in storage reservoirs.

Brookhaven National Laboratories from the Gas Technology Institute in the United States (*Foh et al*., 1979) have presented extensive descriptions of geological storage. They documented various storage types and discussed the advantages and disadvantages of the different types in relation with hydrogen storage. They confirmed that geological storage of hydrogen is technically feasible. *Taylor et al.,* (1986) investigated the economics of developing and operating the main underground storage types and demonstrated that storing large quantities of gaseous hydrogen is the lowest-cost option.

Paterson (1983) studied miscible viscous fingering in aquifers by injecting hydrogen, theoretically and experimentally. They also studied the probability of hydrogen loss due to viscous instability during underground hydrogen storage and the methods to prevent these disadvantages.

Some reports and articles have been published on hydrogen behavior in underground storage (*Bulatov* 1979), especially on salt caverns (*Lindblom* 1985). They concluded that hydrogen storage can be considered as similar to the storage of natural gas and that it involves no major problem.

In 1990, *Smigai et al.* reported significant variation in the composition of stored town gas (significant reduction of H_2 and CO_2, and a simultaneous increase in CH_4) due to the microbial activity in Lobodice town gas storage in Czech Republic. The phenomenon of gas leakage was explained by *Buzek et al.* (1994). He found that methanogenic bacteria present in the reservoir converted hydrogen into methane. However, he could not explain how this reaction took place at such low temperature conditions (35°C). In addition, bacterial activity has already been observed in a town gas storage aquifer site at Beynes, France (*Albes* 2014).

These observations show that the behavior of underground hydrogen storage can be influenced by biotic reactions and that this is an area that deserves more study. *Panfilov et al.* (2006) developed a mathematical model of microbial behavior during underground hydrogen storage. He found a direct connection between bacterial growth and the amount of injected town gas that is consistent with the study of *Buzek et al.*, (1994). Leakage problems and hydrogen consumption due to the microbial activity were further investigated by *Panfilov* (2010), *Toleukhanov et al.* (2012), the more advanced model being presented by *Hagemann et al.*, (2015) and *Panfilov et al.*, (2016). All these evaluations show that underground hydrogen storage is faced with uncontrolled gas leakages and safety problems that need to be seriously considered (*Reitenbach et al.*, 2015).

Moreover, abiotic reactions between hydrogen and rock minerals, which are mainly restricted to redox reactions given the low expected reservoir temperatures, have also been recently taken into consideration. *Truche et al*, (2013) studied experimentally abiotic redox reaction induced by hydrogen at low temperatures. He documented the reduction of pyrite into pyrrhotite under hydrogen partial pressures up to > 30 bar and temperatures as high as 150°C. In addition, he demonstrated that the alkalinity of geological storage impacts the abiotic redox reaction and that the pH of the media is a critical parameter to control the extent of the reaction at low temperature. Hence, hydrogen storage under acidic conditions may prevent pyrite reduction. However, this experimental study shows that abiotic redox reactions induced by hydrogen at timescales commensurate for geological storage should be considered as a significant issue. These interactions include dissolution of minerals and precipitation of others (*Ganzer et al.*, 2013; *Truche et al.*, 2013) or mobilization of initial components not only may change the chemical, but rather the physical properties of the reservoir system such as permeability, porosity or injectivity and also storage capacity, as well as long-term safety and stability of the reservoir.

Hence, precise knowledge of the hydrogen-induced interactions both mechanisms and kinetics of redox reactions between injected hydrogen and reservoir rocks and the resulting changes in chemical and physical properties of the reservoir system is therefore a prerequisite for any secure operation of a storage site that should be studied.

Chemical effects of hydrogen on reservoir fluids were investigated by *Lassin et al.* (2011). He presented an investigation of the hydrogen solubility in pore waters of an unsaturated clay (argillite) under different temperatures and capillary pressures. An increase in the hydrogen solubility in the pore water–rock–gas system was reported along with a decrease in relative humidity or capillary water pressure.

In general, injection of hydrogen into a largescale geological storage site (i.e., a depleted gas or saline aquifer) could impact the geological subsurface. Potential effects include a pressure increase, migration of reservoir fluids, geochemical reactions and so on. However, due to the low density and low viscosity of hydrogen, a hydrogen storage site is expected to behave differently than natural gas reservoirs. Therefore, studying the development of underground hydrogen storage at the reservoir scale is essential to assess the applicability of this method as large-scale energy storage.

Feldmann et al. (2016) have studied numerically the hydrodynamic behavior of hydrogen during injection. He numerically demonstrated the difference between aquifer and depleted gas reservoirs upon hydrogen injection. He also showed the importance of alternative cushion gases (nitrogen for instance) during the development period of the aquifer storage site. An equivalent numerical model studied the planning of underground storage including injection and withdrawal of hydrogen to assess the feasibility of long-term hydrogen storage (*Feldmann et al*., 2016). Furthermore, *Pfeiffer et al.* (2016) numerically simulated the actual geological structure in north Germany and concluded that hydrogen storage in porous media is a viable option in the long-term and at a large-scale.

However, none of these numerical simulations considered the possibility that geochemical reactions, either abiotic (*Truche et al.,* 2013) or biotic (*Panfilov et al.*, 2006), would negatively affect the applicability of hydrogen storage operations and in-situ migration of hydrogen coupled to geochemical alterations of the rocks or the brine rock interaction are scarce.

In addition, as shown in other types of large-scale underground fluid storage (carbon dioxide, natural gas for instance), an important challenge for the development of a storage project is to control the migration of the injected fluid during and after the injection. Characterizing the parameters governing the migration is therefore of first importance. Rock intrinsic properties (porosity, absolute permeability) and multi-phase flow properties (constitutive relationships between relative permeability/capillary pressure and fluid saturation) must be determined since these are critical input variables in classical large-scale flow simulations. Rock intrinsic properties can be determined a priori for a given lithology, but multiphase flow properties are strongly dependent on the fluid to be injected and, so, they must be measured for the fluid system of interest. For the hydrogen-water system, there is to date no published

data on relative permeabilities and capillary pressures. For the development of underground hydrogen storage, there is an obvious need for the determination of such properties.

1.3 Objectives of the thesis

The objectives of this thesis are to evaluate the potential of underground hydrogen storage and estimate the integrity and sustainability of underground geological reservoirs. This included investigating the chemical reactivity of reservoir rocks and the hydrodynamic behavior of the hydrogen-bearing fluid system. Two main approaches, experimental and numerical modeling, have been followed. Thus, this thesis consists of three main parts:

1. A study of chemical interactions of hydrogen with natural sandstone sedimentary formations using both experimental and numerical modeling approaches;
2. A study of the migration of hydrogen in sandstone involving an experimental determination of the relative permeability (k_r) and capillary pressure (P_c) for the hydrogen-water system;
3. A numerical simulation of the operation of a large-scale geological hydrogen storage site;

The thesis manuscript is divided in eight chapters organized as follows. After a general introduction in the present ***Chapter 1***, ***Chapter 2*** introduces underground hydrogen storage, presents the hydrogen storage methods and details the scientific basis for these technologies. In addition, the chemical reactivity (both biotic and abiotic) of hydrogen in the context of underground storage is reviewed. ***Chapters 3 and 4*** present laboratory experimental methods used for investigating the geochemical reactivity of hydrogen with sandstone and for the hydrodynamic measurements on the hydrogen-bearing fluid system, respectively. ***Chapter 5*** provides a review on the underground storage context in France and details a geochemical reactive transport modeling of hydrogen storage in the French Triassic sandstone. General conclusion and applications of this study are presented in ***Chapter 6*** and in ***Chapter 8*** the perspective of this work is presented. In ***Chapter 8*** two manuscripts that have been prepared for publication in peer-reviewed journals from this work are given.

Chapter 2

Underground hydrogen storage

2.1 Types of underground hydrogen storage

Like natural gas, hydrogen could be compressed and injected into the subsurface to be stored underground in several types of geological formation: deep aquifers, depleted oil and gas and salt caverns (Roads2HyCom 2008) as shown in Figure 2-1.

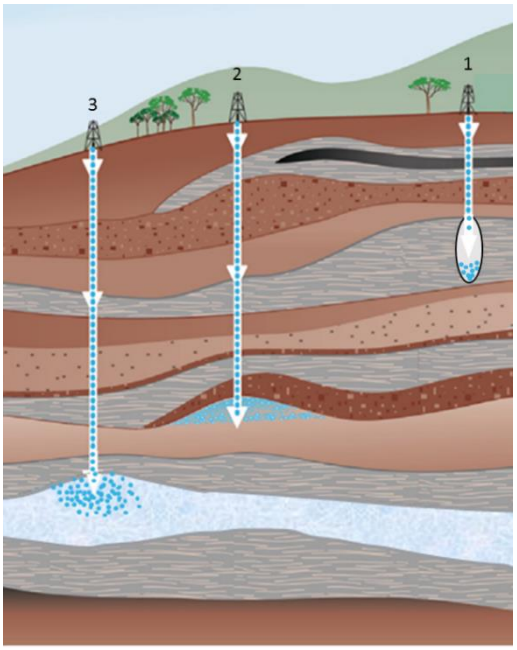

Figure 2-1 Geological profile of different ways of hydrogen underground storage
(1) Salt caverns, (2) depleted oil and gas, (3) Saline aquifer (modified after *Bai et al.,* 2014)

However, so far, only salt caverns are known and proved as a safe storage solution. Unfortunately, salt formations are not always in areas where electricity-storage facilities are needed, in addition, the volume

capacity of salt caverns may not be sufficient for hydrogen as the energy storage. Therefore, research in to alternatives to salt storage (i.e. natural reservoirs in deep aquifers and depleted oil and gas fields) is underway. In the following a review of existing hydrogen geological storage options is presented.

Salt caverns

Salt caverns are often used to store natural gas and they could be a good option for underground hydrogen storage that has been tried and tested in the United States, Britain and Germany (see Table 2-1). The salt keeps the cavern extremely gas-tight and does not react with hydrogen and hydrogen has been successfully stored in rock-salt deposits by theoretical leakage rate of 0.01% a year (*Crotogino et al.,* 2010). For underground hydrogen storage in salt caverns, usually a thickness of 9–90 m of salt layer is needed (*Decourt et al.,* 2012). Fresh water is injected, circulated and salt is dissolved in order to create a cave with certain volume. Hydrogen is injected after draining out saline water (*Tu, 2005*).

Compared with depleted oil and gas reservoirs and deep aquifers, salt deposits allow higher injection and withdrawal rates (*Crotogino et al.,* 2010). As a result, cycling are higher. However, *Foh et al.,* (1979) and *Evans* (2008) mention the lack of volume and the sensibility to pressure changes of the salt caverns.

However, in highly concentrated brine, the activity of bacteria is assumed low, considering that they could not survive in such highly concentrated salty environment (*Kireeva and Berestovskaya,* 2012). Therefore, hydrogen should not be transformed to other gases, while in contrast in porous depleted gas or saline aquifer the bacteria activity can be considered by consuming hydrogen (*Panfilov,* 2010).

Typical parameters of salt caverns are 700,000 m^3 geometrical volume (Table 2-1) and, depending on the cavern depth, the corresponding working gas volume may range from a few million to 100 million Sm^3. The maximum operating pressure in salt caverns is 20 MPa (*Bai et al.,* 2014), and the maximum power of single salt cavern is 700 MW that can generate up to 140 GWh (*HyUnder project* 2013).

In Germany, at Kiel, town gas with up to 60% hydrogen has been stored in a salt cavern with the volume of 32 000 m^3 (*Schiebahn* et al., 2015) Storage pressure ranged between 8.0 to 10.0 MPa (see Table 2-1).

In UK, Yorkshire, hydrogen storage at Teesside consists of three elliptic salt caverns, located at depth of between 350-400 m. The stored gas consists of about 95% hydrogen and 3%-4% CO_2 (*Stone* et al., 2009). Each caverns has a volume about 700 000 m^3. The caverns at Teesside are operated at the constant pressure of about 45 MPa by alteration injection and withdrawal of hydrogen and brine. The energy storage capacity is about 30 GWh for the working gas (*Lord* 2009).

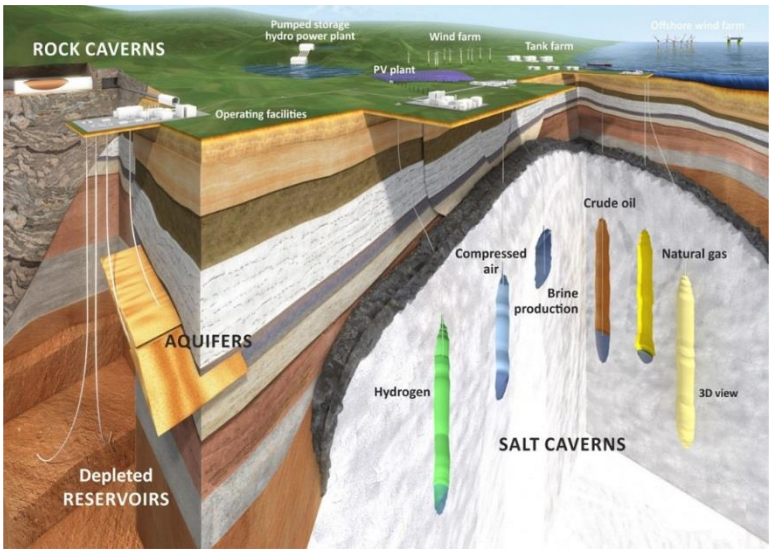

Figure 2-2 Potential storage sites of hydrogen in the geological underground storage: salt caverns, saline aquifers and depleted gas reservoirs (© KBB Underground Technologies)

Saline Aquifer

Aquifers storages are rock formations that are porous, permeable and saturated with saline water (Figure 2-3). The storage of hydrogen in aquifers remains an immature concept. These structures require additional exploration, which is usually costly (*Decourt et al.*, 2014). Aquifers present the highest potential in volume to store hydrogen (see, Table 2-1). However, the risks related to the high potential of hydrogen's interaction with the various components of reservoir i.e. rocks, fluids and microorganism and also the risk of pressure losses when hydrogen is injected at a high rate and its limitations on difficulty of gas-water contact control and operating cost may prevent the development.

In France, near Paris (Beynes), from 1956 to 1974, Gaz de France (GDF) stored manufactured gas containing up to 50% of hydrogen in a saline aquifer with 385 million sm^3 capacity (*Carden* et al., 1979) for which no losses of hydrogen were reported during the 18 years operation (Foh et al., 1979). Recently, bacterial activity and consecutive transformation of the gas composition has been observed (*Panfilov* 2016).

In addition, at Lobodice, Czech Republic (see Table 2-1), town gas (54% hydrogen) has been stored in a saline aquifer at the depth of about 400-500m. After about seven months of injection gas the composition of the gas town showed notable losses of hydrogen (from 54% to 37%) and CO (from 9.0% to 3.3%) and gains of CH_4 (from 22% to 40%) and N_2 (from 2.5% to 8.6%) (*Buzek* et al., 1994). In addition, the pressure of reservoir decreased below the value calculated and predicted (*Stolten* et al., 2016). Experimental study on the formation fluid samples from the reservoir, proved the presence of methanogenic microorganism in the reservoir, suggesting that microbial activities are responsible for the observed compositional changes (*Panfilov* 2016).

Moreover, at Ketzin Germany (see Table 2-1), gas losses of the order of $2x10^8$ m^3 were detected between 1964 and 1985 at the working gas volume of about $1.30x10^8$ m^3 (*Stolten* et al., 2016). Detailed

investigations proved tightness and integrity of the cap rock and wells. Chemical and the microbiological process in the reservoir have been determined as the main reason for the observed gas losses (*Gniese* et al., 2013). In addition, to the observed gas losses, corrosion of the technical underground installations, changes in reservoir permeability, and changes in gas composition. The available data indicate a general loss of CO and gain of CO_2. The observed change in composition differ from those observed at Lobodice, Czech Republic and cannot be explained by simple microbial degradation of the stored hydrogen with related reduction of carbon dioxide and carbon monoxide and formation of methane (*Stolten* et al., 2016). The exact reasons for the observed changes in the gas composition at Ketzin are not fully resolved. They maybe due to the contribution of physical (diffusion), chemical processes (formation of new minerals and dissolution of rock-forming minerals) and microbial activity (*Liebscher et al.*, 2016).

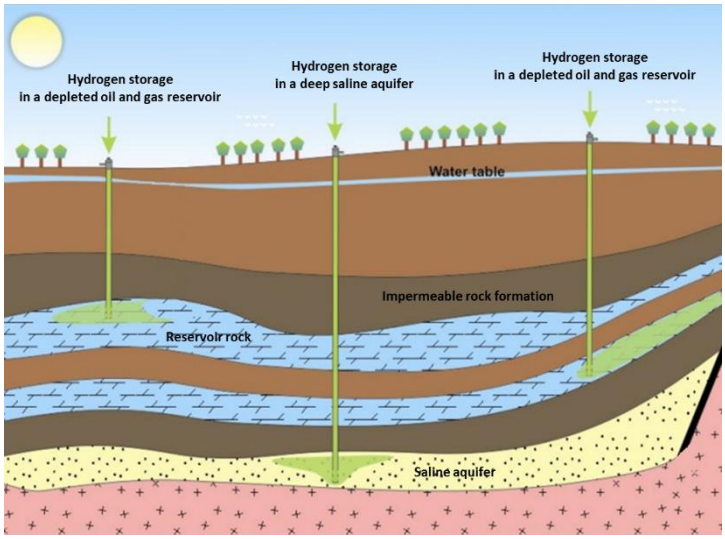

Figure 2-3 Hydrogen storage in depleted gas reservoir and deep saline aquifer (modified after *Bai et al.,* 2014)

Depleted oil and gas reservoirs

The pore space of permeable rock formations sealed by a closed surface layer in depleted oil and gas fields makes them ideal candidates for high-volume underground storage (*Decourt et al.*, 2014). Over millions of years, their tightness has been proved and the geological risk is minimum (*Metz* et al., 2005). The advantages of these reservoirs are the situations of the geological settings that already well known, wells and surface facilities used in oil and gas development can be reused, the need for cushion gas is less, and investment and operating costs are lower (*Bai et al.*, 2014).

So far, few experiences of hydrogen storage in depleted oil and/or gas can be found. In Argentina, from 2015, Hychico C.A. starts injection of hydrogen into a sandstone geological structure associated with the storage of natural gas, in Diadema, Patagonia, under a pressure of 10 bar, temperature of 50 °C at a depth of 600–800 m. A Hydrogen Plant producing 120 Nm^3/h (99,998 % purity), with an average annual capacity factor of 50% constitute. Geological study to start underground hydrogen storage in a depleted gas has begun from 2010. Diadema has two reservoirs, one serves for the storage of methane, while the

second is devoted to the storage of hydrogen produced by a wind plant and electrolyzes. In addition, Hychico and BRGM cooperation has developed the pilot project that focus on the potential of depleted gas reservoir to accomplish methane production by biological processes. The goal is to find out the key factors involved in the processes, including the characterization of microorganisms, and optimization of processes (*Perez et al.,* 2016).

Experiences with subsurface porous media hydrogen storage are relatively scarce, but the research projects related to investigate the feasibility of storing hydrogen in porous geological formations that are under development, illustrate the explosion of industrial and research interest in this field. So far, two projects have been identified: the H2STORE and the SUN.STORAGE projects.

The objective of the H2STORE ("hydrogen to store") project is to investigate the feasibility of storing hydrogen produced from excessive wind and solar power in porous geological formations as well as the investigation of potential geohydraulic, petrophysical, mineralogical, microbiological and geochemical interactions induced by the injection of hydrogen into depleted gas reservoirs and CO_2- and town gas storage sites. H2STORE is a joint research project of the universities Jena and Clausthal and the national research centers GFZ, Potsdam in Germany and CNRS, Nancy in France started in 2012. The project is supported by international industrial partners and funded by the German national research program on "energy storage" (*Ganzer et al.,* 2013). The published results of this project are limited on the numerical simulation of the hydrodynamic behavior of hydrogen in underground storage coupled with bacteria (self-organization phenomena). This model was suggested at the first in *Panfilov* (2010), and completed by *Hagemann et al.,* (2015) and *Panfilov and Reitenbach* (2015) by developing the advanced model of the process that includes a two-phase fluid, several bioreactions, and several types of bacteria. In addition, the hydrodynamic behavior of underground hydrogen storage during development and operation was studied with *Feldmann et al.,* (2016).

Austrian underground SUN.STORAGE project (2013-2017) coordinated by RAG (Rohöl-Aufsuchungs Aktiengesellschaft) was a project to verify the possibility of storing energy from renewables in underground geological structures in the form of a natural gas and hydrogen mixture. The vison of the project is to test the technologies and to study the possibilities of storing the large surpluses of energy from renewable sources. The project consisted of various phases which different partners were involved in, to study the influence of the hydrogen admixture on the reservoir rock, the corrosion of steel components typically used in the storage facility and the behavior of the mixture under static and dynamic reservoir conditions. The studies included laboratory tests, simulations and in-situ experiments. The expected culmination of the project was the initial pilot injection and the withdrawal of the natural gas and hydrogen mixture under actual reservoir conditions (*Bauer et al.,* 2013). Regarding to the website of the project (http://www.underground-sun-conversion.at) the project is successful and new development will be proposed in a next stage (the Underground Sun Conversion project) aiming at carrying out the research into the principles for producing large quantities of

renewable natural gas using a carbon-neutral process, and storing it in environmentally friendly, naturally formed reservoirs, which will in turn provide urgently needed flexibility for renewable energy. The project has been designated a flagship project by the Austrian Climate and Energy Fund and granted EUR 4.9 million as part of the fund's energy research programme. The Austrian consortium is managed by RAG. The total cost of the project amount to EUR 8 million. The project partners are the University of Leoben; the BOKU - University of Natural Resources and Life Sciences, Vienna (Department of Agrobiotechnology, IFA-Tulln); acib - Austrian Centre of Industrial Biotechnology; the Energy Institute at Johannes Kepler University Linz; and Axiom Angewandte Prozesstechnik. The project is scheduled to be completed by the end of 2020.

Several examples of underground storage of hydrogen in the world are given in Table 2-1. According to this table, capacity of salt caverns reservoirs are less important than other storage formations. In addition, further works are needed to determine the possible risks of using aquifers and/or depleted oil and gas field in conditions deemed safe for hydrogen storage. While the main geologic requirements and characteristics are the same for porous rock storage in the saline aquifer and depleted oil and gas reservoir, the pressure conditions are notably different. In saline aquifer the pore space is filled with saline formation brine, thus well be assumed to represent hydrostatic pressure conditions. Injection of hydrogen therefore has to first displace the formation brine to create available pore space. This brine/water displacement of aquifer could increase the pressure of the reservoir above hydrostatic (*Feldmann et al.*, 2016). However, in depleted oil and gas reservoir, the pore space already partly available of other gas like hydrocarbon and the reservoir is typically below hydrostatic pressure. Therefore, injection of hydrogen first has to re-rise the pressure of reservoir to a level at which injection and withdrawal is possible. In addition, injection gas (hydrogen or cushion gas) in aquifer storage, a certain amount of the injected gas is trapped in the pore space by capillary forces (residual gas saturation) and cannot be back produced. This is contrast to depleted oil and gas reservoir storage where this pore space is already filled by the residual gas (*Stolten et al.*, 2016).

Table 2-1 Underground storage of hydrogen worldwide

	Type of storage	Depth	From when	Electricity generation	Hydrogen percentage	Pressure	Capacity
Teesside (ICI) UK	Salt caverns	370 m	Since 30 years	30 GWh	95%	45 bar	3x70,000 m^3
Moss Bluff, (Praxair) US	Salt caverns	850-1,400 m	Since 2007	80 GWh		70-135 bar	566,000 m^3
Spindletop, (Air Liquide) US	Salt caverns	850-1,400 m			95%	up to 150 bar	600,000 m^3
Clemens Dome, (ConocoPhillips) US	Salt caverns	850 m	Since 1986	92 GWh	95%	150 bar	580,000 m^3
Kiel Germany	Salt caverns	1335 m	Since 1971		62%	80-100 bar	32,000 m^3

Ketzin Germany	Aquifer	200-250	Since 1964		62%		
Beynes (GDF) France	Aquifer	430 m	nearly 20 years		50-60%		1,185 million sm^3
Lobodice, Czech	Aquifer	400-500 m	Since 1960		45-50%	45-59 bar	400 million sm^3
Kasimovskoie, Russian	Aquifer						1,8000 million sm^3
Hychico Argentina	Depleted gas	600–800 m	2015	24.6 GWh	Pure hydrogen	25 bar	

2.2 Hydrodynamic behavior of underground hydrogen storage

Hydrogen was discovered by *Henry Cavendish* in 1766, is the highly abundant and the main element (about 75%) in the universe and has the second lowest melting (13.99K) and boiling points (20.271K) at atmospheric pressure (Figure 2-4) with only Helium being below. This is one of the reasons why hydrogen is not used as a primary fuel. Indeed, hydrogen is more difficult to store under standard conditions compared to other gases which can be liquefied at standard temperature. The boiling point of hydrogen can only be increased to 20K peaking at a pressure of 13 bar.

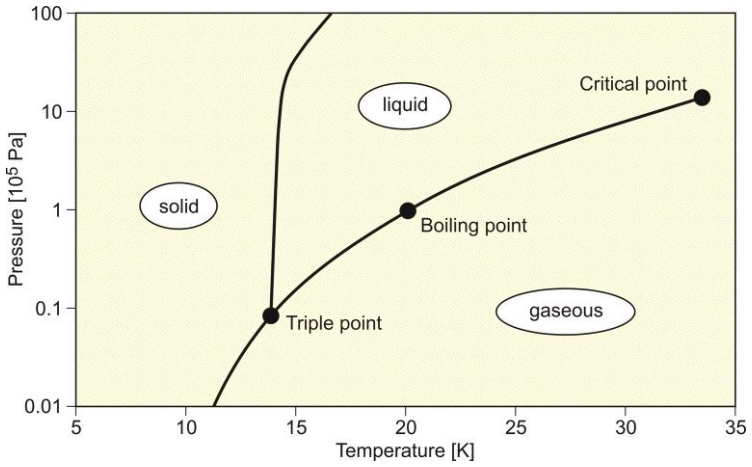

Figure 2-4 Hydrogen phase diagram (*McCarty et al.*, 1981)

However, at standard temperature and pressure conditions, hydrogen is a colorless, odorless, tasteless, nontoxic, noncorrosive, nonmetallic which is in principle physiologically not dangerous. One of its most important characteristics is its low density (0.084 Kg/m^3 at surface conditions – *Mallard et al.,* 1998) making it less dense than air, which makes it necessary for any practical applications to either compress the hydrogen or liquefy it. However, hydrogen gas has one of the widest flammability ranges of concentrations between 4 percent and 75 percent by volume (*Lanz et al.,* 2001). Due to its high molecular velocity, hydrogen also has the highest diffusivity of any gas. For instance, hydrogen molecules disperse in air four times faster than molecules of natural gas. Thus, if hydrogen does leak, it will disperse rapidly. This has very important implications for managing hydrogen safety. Hydrogen is only dangerous if it is

released in rooms where it can accumulate to explosive mixtures. In open areas, outdoors or in a large area, even big leaks do not pose a threat, because of the high buoyancy and diffusivity of hydrogen allows to rise rapidly, moving away from potential ignition sources, personnel, or other equipment. Although hydrogen is highly reactive and can be ignited very easily, the risk of spontaneous ignition is low because of its auto ignition temperature is 585°C (*NIST* 2012).

Hydrogen has a specific energy density of 33.3 kWh/kg or ~124 MJ/kg (*Carden and Paterson* 1979) which offers a unique potential to store large amounts of energy (*Zittel et al.,* 1996). Compared to methane (representing natural gas), hydrogen has roughly 1/3 smaller energy content per m^3. Each m^3 of hydrogen produces 12.7 MJ of energy by combustion (*Züttel* 2004) instead of 40 MJ for methane. Thus, energy potential of hydrogen is not enough to be considered as a primary source of energy such as petroleum (*Marbán et al.,* 2007).

2.2.1 Hydrogen Water fluid flow equations

The classical mass conservation in terms of mass fraction $X_{\alpha,k}$ of species k in fluid phase α is (*Bear* 1972):

$$\frac{\partial\left(\emptyset \sum_\alpha S_\alpha \rho_\alpha X_{\alpha,k}\right)}{\partial t} + \nabla . \sum_\alpha \left(\rho_\alpha X_{\alpha,k} v_\alpha + J_{\alpha,k}\right) = R_{\alpha,k} + Q_{\alpha,k} \quad (2\text{-}1)$$

where $\emptyset$ is the porosity, $R_{\alpha,k}$ is the reaction term, $Q_{\alpha,k}$ is the source term, ρ_α is the molar density, S_α is the phase saturation, v_α is the Darcy velocity of fluid phase, $J_{\alpha,k}$ is the total diffusive and dispersive flux. Moreover, below equations are considered for the phase saturations and concentrations sum to 1:

$$\sum_\alpha S_\alpha = 1 \quad (2\text{-}2)$$

$$\sum_k X_{\alpha,k} = 1 \quad (2\text{-}3)$$

The momentum balance for each phase at macroscale is formulated with the multi-phase Darcy law:

$$v_\alpha = -\frac{K k_{r\alpha}}{\mu_\alpha}(\nabla P_\alpha - \rho_\alpha g) \quad (2\text{-}4)$$

where K is the absolute permeability, $k_{r\alpha}$ is the relative permeability, P_α is the phase pressure, μ_α is the phase viscosity and g is the gravity. Phase pressures are correlated by capillary pressure, for instance for water and the gas:

$$P_c(S_w) = P_g - P_w \quad (2\text{-}5)$$

Hydraulic properties of porous media (capillary pressure and relative permeabilities of water and hydrogen) are dependent to water saturation, which they could be measured experimentally (see section 5).

Total diffusive and dispersive flux is the sum of the molecular diffusion and mechanical dispersion:

$$J_{\alpha,k} = -\rho_\alpha \left(D^k_{diff,\alpha} + D^k_{disp,\alpha}\right)\nabla X_{\alpha,k} \tag{2-6}$$

where D_{diff} and D_{disp} are the effective molecular diffusion coefficient and effective mechanical dispersion coefficient. Molecular diffusion is driven by the existence of a concentration gradient, i.e., fluid particles move from high-concentration areas to low-concentration areas and it happens when there is no hydraulic gradient driving flow and the pore water is static. Generally, diffusion in groundwater systems is a very slow process and the rate at which particles diffuse depends on the physical and chemical properties of the fluid, porosity, saturation state and tortuosity of the porous medium. Fick's law determines the molecular diffusion coefficient in water phase:

$$D^k_{diff,\alpha} = \emptyset S_w \tau \bar{D}^k_{diff,\alpha} \qquad \alpha = water \tag{2-7}$$

where τ is the tortuosity of porous medium and $\bar{D}^k_{diff,\alpha}$ is diffusion coefficient of components k in water. In the gas phase, the molecular diffusion coefficient can be described by the Stefan-Maxwell equation which was simplified to Blanc's law for homogeneous mixture (*Poling et al.*, 2001):

$$D^k_{diff,\alpha} = \emptyset S_w \tau \sum_{\substack{j=1 \\ j\neq k}}^{n} \frac{c^j_\alpha}{\bar{D}^{kj}_{diff,\alpha}} \qquad \alpha = gas \tag{2-8}$$

where $\bar{D}^{kj}_{diff,\alpha}$ is the binary diffusion coefficient between component k and component j in the gas phase. Diffusion coefficient of hydrogen has been measured by *Boulin* (2008) and *Didier* (2012) in the argillite of the Callovo-Oxfordian ($5x10^{-11}$ m^2/s) at standard pressure and temperature but no studies can be found at the reservoir conditions in the literature. Diffusion coefficient of hydrogen is estimated at $6.1x10^{-5}$ m^2/s (*Foh et al.*, 1979), and $4.5x10^{-9}$ m^2/s (*Cussler* 2009) in air and in water, respectively. And in clay rocks saturated with water at 25 °C values of $3x10^{-11}$ m^2/s have been measured (*Krooss* 2008) while for comparison, it is around $0.2x10^{-11}$ m^2/s for methane at 90°C.

In contrast to molecular diffusion, mechanical dispersion is dependent on the structure of the porous medium (Figure 2-5). Mechanical dispersion is a mixing process caused by the velocity variations of fluids due to the heterogeneities in the porous medium.

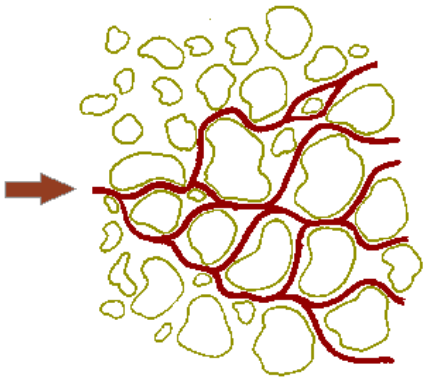

Figure 2-5 Mechanical dispersion in porous media

Scheidegger (1961) suggested the relationship between the dispersion coefficients and the velocity as follows:

$$D_{disp,\alpha}^{k} = \emptyset S_{\alpha}\left(a_T\|v_i\| + \frac{a_L - a_T}{\|v_i\|} v_i v_i^T\right) \quad (2\text{-}9)$$

where a_L is the longitudinal dispersivity and a_T is the transverse dispersivity.

Bear & *Bachmat* (1967), in contrast of previous study, considered the linear expressions depends on the velocity and the direction of flow:

$$\overline{D}_{disp,L} = a_L\|v_i\| \qquad \overline{D}_{disp,T} = a_T\|v_i\| \quad (2\text{-}10)$$

The values of longitudinal and transverse dispersivities are measured experimentally. For instance, *De Josselin de Jong* (1958) proposed from his experiments, a_T to be equal to 3/16 of the average grain size or Tracer experiments have demonstrated that a_L is between 1 and 100m (*Tek* 1989; *Carriere et al.*, 1985). In hydrogen storage the longitudinal mechanical dispersion coefficient is estimated at approximately 10^{-4} m^2/s (*Feldmann et al.*, 2016) which is considerable compared to the molecular diffusion.

2.2.2 Thermodynamics and geochemical fluid-rock modeling

In general, geochemical reactive modeling is based on the primary species formulation, therefore, the equilibrium chemical reactions between the primary and secondary species take the following form (see *Steefel et al.*, 2015 and references in this paper review):

$$A_j \rightleftharpoons \sum_{i=1}^{N_c} \beta_{ij} A_i \quad (2\text{-}11)$$

where A_i and A_j are the chemical formulas of the primary and secondary species, respectively, $\beta_{ij}$is the number of moles of primary species i in one mole of secondary species j and N_c is the number of independent chemical components in the system. The primary and secondary species are linked by the equilibrium reaction via the law of mass action for each reaction:

$$A_j = K_j \gamma_j^{-1} \prod_{i=1}^{N_c} (\gamma_i A_i)^{\upsilon_{ij}} \qquad i = 1, \dots, N_x \quad (2\text{-}12)$$

where γ_i^{-1} and γ_j are the activity coefficients for the primary and secondary species, respectively, K_j is the reaction equilibrium constant and N_x is the total number of species. Therefore, the total concentrations is:

$$\psi_j = A_j + \sum_{j=1}^{N_x} \beta_{ij} A_j \quad (2\text{-}13)$$

Density and viscosity of the hydrogen and water are correlated with respect to the pressure, temperature and phase composition. However, the compositional flow system (Equation (2-1)) has to be closed by the phase equilibria conditions. The equilibrium criterion (equilibrium between hydrogen and water), dictates a minimum of the Gibbs free energy at constant temperature T, pressure P and composition:

$$G = \mathrm{H} - \mathrm{TS} \tag{2-14}$$

where H is the enthalpy, T the temperature and S the entropy. The partial molar quantity related to G is the chemical potential:

$$\mu_i = \left(\frac{\partial G}{\partial n_k}\right)_{p,T,n_{j,j\neq k}} \tag{2-15}$$

where n_k the molar quantities of the species present in the system considered, μ_k is the chemical potential of the species k. However, from Equation (2-14):

$$dG = Vdp - SdT + \sum_k \mu_k dn_k \tag{2-16}$$

V is the volume of the system. However, assuming standard expression for G by using Euler integrals from Equation (2-14):

$$G(p,T) = \sum_k n_k \mu_k \tag{2-17}$$

and combination with Equation (2-16), gives the Gibbs-Duhem equation:

$$\sum_k \mu_k dn_k = Vdp - SdT \tag{2-18}$$

Therefore for two phases (water and hydrogen gaseous) at equilibrium condition (*T* and *P* are constant):

$$\mu_{k,w} dn_{k,w} = -\mu_{k,g} dn_{k,g} \tag{2-19}$$

Considering a close system ($dn_k = 0 = dn_{k,w} + dn_{k,g}$), then:

$$\mu_{k,w} = \mu_{k,g} \tag{2-20}$$

It means, the evolution of the chemical system is controlled by the evolution of the chemical potential and chemical potential of the two phases should be equal at the equilibrium conditions. Chemical potential can be written as the reference chemical potential and a term of mixing:

$$\mu_k = \mu_k^0 + RT \ln a_k \tag{2-21}$$

where a_k is the activity of the component k in the mixture. Activity of a compound for a liquid mixture (like water) is described by an activity coefficient γ_k and the function of the mixture composition, mole fraction ($x_k = n_k/n_{tot}$):

$$a_k = \gamma_k x_k \tag{2-22}$$

For hydrogen gaseous, activity is described by the fugacity that is expressed as the product of the pressure and a fugacity coefficient:

$$a_k = \frac{f_k}{f_k^0} \tag{2-23}$$

f_k is the fugacity of component k and $f_k^0 = p^0 = 1\ bar$ is the reference fugacity of the gas in its standard state, that is when it is pure and perfect, whatever the temperature of the system.
Equation (2-20) requires the equality of the chemical potentials of species k in all phases, therefore the equality of the fugacity $f_{\alpha,k}$ (for instance for two phases of gas and water):

$$f_{g,k}\left(T, P, X_{g,k}\right) = f_{w,k}\left(T, P, X_{w,k}\right) \tag{2-24}$$

The phase equilibrium (Equation (2-24)) can be presented by fugacity-activity $(\varphi - \gamma)$ approach (*Sin et al.*, 2016):

$$P y_k \varphi_{k,g} = K_{H\,k} \gamma_k x_k \tag{2-25}$$

where y_k is the mole fraction of species k in the gas phase, x_k is the mole fraction of species k in the liquid phase, $K_{H\,k}$ Henry's constant of species k, γ_k is the activity coefficient of species i, $\varphi_{k,g}$is the fugacity coefficient of the species k in the gas phase that can be obtained by a virial development of the compressibility factor $Z = PV/RT$. If the gases are considered as ideal, the compressibility factor reduces to the mole quantity of gas considered. Finally, fugacity coefficient can be calculated by equation of state (EOS):

$$\ln \varphi_{k,g} = \int_0^P \left(\bar{Z}^k - 1\right) \frac{dp}{p} \tag{2-26}$$

$$\bar{Z}^k = \left(\frac{\partial (nZ)}{\partial n^k}\right)_{T,P,n_{j \neq k}} \tag{2-27}$$

An EOS establishes a relation between pressure, molar volume and temperature and allows to evaluate fugacity, solubility, enthalpy and density (for instance, the Peng–Robinson EOS (*Robinson and Peng*, 1978)). However, *De Lucia et al.*, (2015) proposed the third order virial EOS of *Sakoda et al.*, (2012) that was approved experimentally for pure hydrogen at underground storage conditions:

$$\frac{PV}{nRT} = 1 + \left(\frac{a}{T^2} + \frac{b}{T} + c\right) P + \left(\frac{d}{T^2} + \frac{e}{T} + f\right) P^2 \tag{2-28}$$

where the values of coefficient are:

A	b	c	d	e	f
-12.5908	0.25978	-7.24730×10^{-5}	0.47194×10^{-2}	-2.69962×10^{-5}	2.15622×10^{-8}

This equation allows a derivation of fugacity coefficients, which is convenient for geochemical modeling.

2.3 Hydrogen issues on porous storage

The most important difference between storage of natural gas and storage of hydrogen (regardless to hydrogen biotic and abiotic reactions) is related to the properties of hydrogen. Hydrogen has a lower density and lower viscosity than other gases that influence the subsurface behavior and the reservoir performance. Moreover, hydrogen has the lower volumetric heating value than natural gas that impact the energy storage capacity, injection and withdrawal rates and also within the reservoir process.

2.3.1 Solubility

The dissolution of hydrogen in water needs to be understood because it could increases the pH and reduces the redox potential of the system (*Lassin et al.* 2011). Hydrogen is a gas with very little solubility in water. At the surface conditions (1 atm and 25°C) the solubility of hydrogen in pure water is about 0.784 mol/m^3 and it increase to 37 mol/m^3 at 50 bar and 30°C (*Ortiz et al.*, 2002) or at 100 bar and 25°C it is 80 mol/m^3 (*Crozier et al.*, 1974).

In general, solubility of the gas in the water is calculated with Henry's law (*Jauregui-Haza et al.*, 2004; *Purwanto et al.*, 1996):

$$c_{g,w} = P/K_H \tag{2-29}$$

where $c_{g,w}$ is the gas concentration in the aqueous phase (water), K_H is the Henry's constant and P is the partial pressure of the gas phase under equilibrium conditions. The logarithmic variation of the Henry's constant associated with hydrogen is shown in Figure 2-6 (Stefánsson and Seward, 2003).

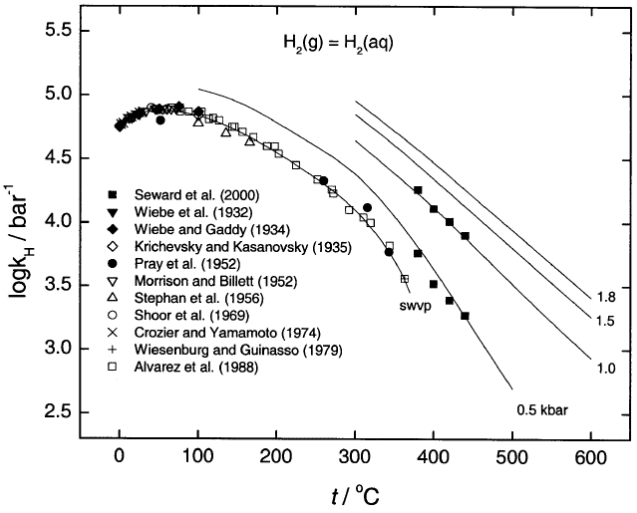

Figure 2-6 Logarithmic variation of the Henry constant of hydrogen in the water depending on the temperature and pressure. Symbols derived from experimental data and the curves are from calculations based on the equations of state for gases (Stefánsson and Seward, 2003)

The Henry's constant increases slightly in the range below 100° C, which implies that the solubility of the hydrogen in the water will decrease to a limited extent within this temperature range (Figure 2-6). *Lassin et al.* (2011) illustrated that increasing the temperature of the system will induced a decreasing of the solubility of hydrogen in water up to a certain point, where it starts to increase again. This point for pure water is located at about 60°C (Figure 2-7a). It should be noticed that any dissolved species in water reduces hydrogen solubility (Figure 2-7b).

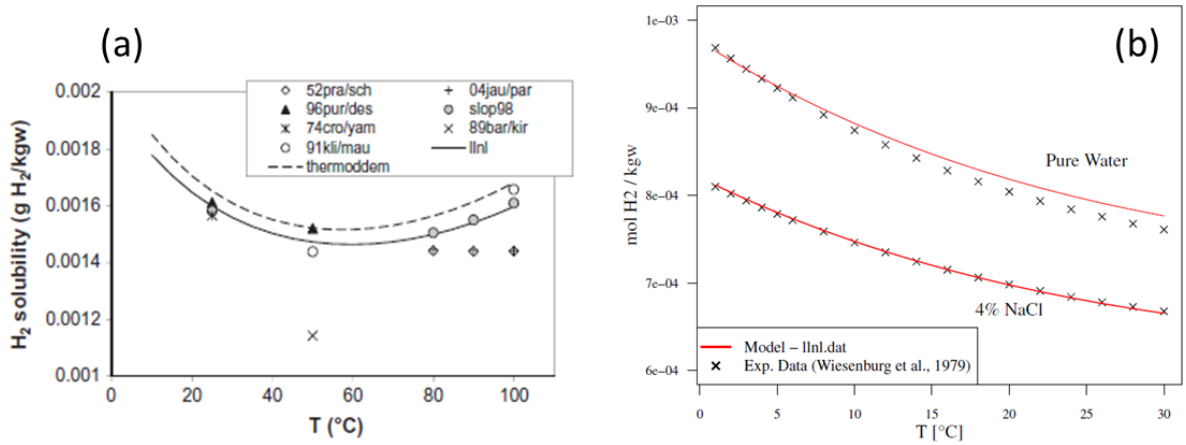

Figure 2-7 Hydrogen solubility in water at 1 bar experimental data (dot) vs. numerical models (a) solubility in pure water, (Lassin et al., 2011), (b) solubility in pure water and saline water with 4% NaCl (De Lucia et al., 2015)

The solubility of hydrogen gaseous (as a real gas) in an aqueous solution can be calculated with Henry's law that is extended to real gas, as in following equations (*De Lucia et al.*, 2015):

$$a_{H_2(aq)} = \frac{\varphi_{H_2} P}{K_H} exp\left(-\frac{\bar{v}_{H_2}}{RT}(P-1)\right) \qquad (2\text{-}30)$$

where $a_{H_2(aq)}$ is the activity of dissolved hydrogen, φ and P are the fugacity coefficients and the partial pressure of hydrogen, respectively, K_H is the Henry's constant and $\bar{v}_{H_2}$ is the average molar volume of hydrogen. Fugacity coefficients can be calculated from Equation (2-26) by the considered EOS of Equation (2-28). However, the experimental results and numerical simulation illustrate that the dissolution of hydrogen in water at the underground storage conditions is low, however, it is unclear whether it can be ignored.

2.3.2 Viscous instability

In the fluids displacement in porous media, an unstable fluid front can be observed when the displacing phase has a larger mobility than the displaced phase (less viscous fluid -like gas- displace a more viscous fluid-like water), which can result in fingering of the displacing phase. In concept of the gas reservoir, instability of water displacement by gas is the major hydrodynamic problem. In fact, the non-viscous

highly mobile gas prefers to find preferential paths to penetrate through the viscous displaced liquid. Consequently, any small perturbation of the initial plane interface between gas and liquid leads to gas penetration into water in the form of fingers, with the consecutive fast development of fingers (*Panfilov* 2016). Viscous instabilities are correlated to the mobility ratio that is the ratio of displacing mobility to displaced mobility:

$$M = \frac{k_{rg}/\mu_g}{k_{rw}/\mu_w} \tag{2-31}$$

In general, if the mobility ratio M<1, then the displacement process is very simple and efficient (*Sahimi et al.*, 2005). Since typically if M>1, the fluids are unstable and viscous instability or viscous fingering phenomena will be happened. In fact, this unfavorable physical phenomenon is commonly liked to the gas injection process and well known from natural gas storages in saline aquifers, but with hydrogen, they will be more prominent.

Mobility ratio of hydrogen-water system, due to low viscosity of hydrogen in contrast to water is high (about 100 at the reservoir conditions). Therefore, viscous instability or viscous fingering are expected to occur during H_2 storage operation period and could reduce strongly the efficiency of the gas displacements. *Feldmann et al.*, (2016) illustrated numerically that the displacement of the methane by hydrogen (gas-gas, without viscous instability) is around 10 times faster than the hydrogen-water migration (due to the viscous fingering).

One consequence of fingering is that the hydrogen extends much further out from the well than it would be expected from a displacement with a circular perimeter (*Paterson* 1983). It could spread laterally and blow the cap rock and get lost further the spill point of the reservoir structure. It will present restrictions to economical operation because it increases losses (Figure 2-8).

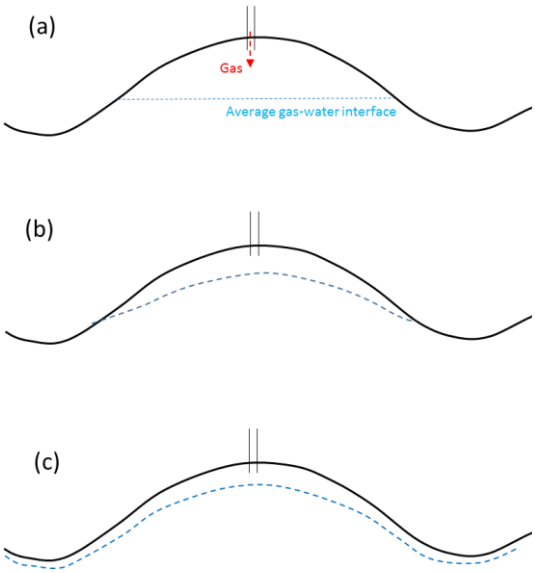

Figure 2-8 The injection of hydrogen into an anticlinal trap and lateral spread.

(a) Slow injection, gravitational forces dominate;

(b) Fast injection, viscous forces dominate, fingering;

(c) Gas spilling due to fingering

A control parameter for this behavior is the injection rate. For low injection rates, gravitational and capillary forces are higher than viscous forces (low capillary number) and displacement become more

stable and the displacement of water is uniform, while the higher hydrogen rates leads to the domination of viscous forces (high capillary number) and consequently an unstable displacement or viscous fingering could happen. Hence, a limitation on the injection rate could reduce and control hydrogen losses (*Paterson* 1983).

2.3.3 Gravity Overriding

Another phenomenon of the natural gas storage in saline aquifer is the gravity overriding in which a less dense fluid (gas) flows preferentially on the top of a storage. This buoyancy phenomena is more noticeable for hydrogen storage due to the low density of hydrogen in comparison with water. Gravity overriding is promoted by small injection rates and large vertical permeabilities.

Gravity overriding could be desirable when cushion gas is applied to displace water during the development period of saline aquifer storage. In fact, using another gas with higher viscosity and density like nitrogen (as the cushion gas) would cause the displacement of water to be more efficient. Hence, hydrogen will be in contact with gas instead of water and the efficiency of operation could be improved. Due to gravity overriding, hydrogen and cushion gas rise up to the top of the storage and the density difference could separate the mixture of gases. In depleted gas reservoir, different gases like methane and nitrogen have been suggested for cushion gas. Nitrogen is more efficient because it is more dense than methane but it limits to 50-80% the hydrogen production the first years (*Pfeiffer et al.,* 2015). Carbon dioxide is also recommend for cushion gas (*Oldenburg et al.,* 2003), because at reservoir conditions, carbon dioxide is very dense in comparison to hydrogen and the density segregation would be relatively strong. But attention should be paid for the hydrogen reactivity with CO_2 (methanation).

2.3.4 Diffusion

Hydrogen gaseous is composed of small and light molecule; therefore, it has a strong ability to migrate in porous media. Hence, hydrogen could penetrate through any holes or fracture in cap rocks that could be leaking. However, due to its low solubility in water (which is 40 times lower than CO_2 at the same conditions), the water saturated cap rock present a practically impermeable barrier to hydrogen (*Panfilov* 2016). For this reason, the losses of hydrogen due to diffusion through cap rocks at the lifetime of storage is estimated low and about 2% (*Carden and Paterson,* 1979).

Typically, a diffusion coefficient is 10^4 greater in air than in water. For instance carbon dioxide in air has a diffusion coefficient of 16 mm^2/s, while in water its diffusion coefficient is 0.0016 mm^2/s. Diffusion coefficient of hydrogen in air is $6.1x10^{-5}$ m^2/s (Foh et al., 1979) while in water it is $4.5x10^{-9}$ m^2/s (Cussler 2009) at 25°C.

Hydrogen migration through porous rocks has not been experimentally studied so far. It has been modelled (*Montel et al.,* 1993; *Bourgeat et al.,* 2009), or experimentally studied using helium as a proxy (*Horseman et al.,* 1999; *Boulin et al.,* 2008; *Didie* 2012). However, hydrogen flux in porous medium

saturated with water is reduced by a factor of 10 with respect to migration in pure water (*Vacquand et al.*, 2011) while it decreases with pressure and increase with temperature (*Didie* 2012).

2.3.5 Oxidation-Reduction (RedOx) potential

The geochemical reactivity of hydrogen, with respect to oxidized species, depends on its oxidation-reduction potential at a given temperature and pressure. The redox potential is measured in volts, and it describes the tendency of a chemical system, to either accept (reduction) or donate electrons (oxidation). By assuming a reduction half reaction of an oxidant Ox to the corresponding reduced species R_{ed}:

$$O_x + ne^- = R_{ed} \tag{2-32}$$

A thermodynamic constant for this reaction is:

$$K = \frac{\{R_{ed}\}}{\{O_x\}\{e^-\}^n} \tag{2-33}$$

To obtain a complete redox reaction, the half reaction (Equation (2-32)) is combined with the oxidation of $H_2(g)$ to H^+, the hydrogen half reaction:

$$1/2\, H_{2(g)} = H^+ + e^- \tag{2-34}$$

The overall redox reactions is thus:

$$O_x + \frac{n}{2} H_2 = R_{ed} + nH^+ \tag{2-35}$$

The redox potential (E_H) associated with this reaction (Equation (2-35)) is defined by the Nernst equation (For a de-tailed discussion see e.g. *BARD & FAULKNER*, 1980) that gives the relationship between the redox potential and the activities of the oxidised and reduced species:

$$E_H = E_H^\circ + \frac{RT}{nF} \log \frac{\{O_x\}}{\{R_{ed}\}} \tag{2-36}$$

where E_H° is redox potential under normal conditions, R is gas constant (8.314 J/mol/K), T is temperature in K, F is 1 faraday (= 96,490 C/mol) and n is number of exchanged electrons.

In addition, from Equation (2-33), it could be derived:

$$\log \frac{\{O_x\}}{\{R_{ed}\}} - n \log\{e^-\} = \log K \tag{2-37}$$

and

$$p\varepsilon = \frac{1}{n} \log K + \frac{1}{n} \log \frac{\{O_x\}}{\{R_{ed}\}} \tag{2-38}$$

where $p\varepsilon$ is the redox intensity that is $-\log\{e^-\}$ and consequently:

$$E_H = \frac{RT}{F} \text{p}\varepsilon \qquad (2\text{-}39)$$

This equation indicates that the redox potential E_H and pε are two equivalent scales to classify the redox reactions at equilibrium (Figure 2-9).

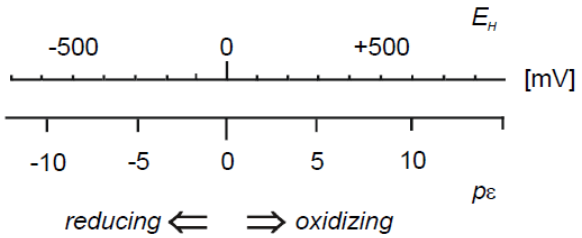

Figure 2-9 Redox potential and pε range encountered in natural systems at near-neutral pH. Redox potentials in the positive range (up to about +800 mV) indicate the presence of strong oxidants; negative values indicate the presence of strong reductants.

It is essential to recognize that the redox potential is based on the concepts of equilibrium thermodynamics and that it can only be adequately measured at equilibrium. However, knowledge of the redox potential of the couple H^+/H_2 is essential to determine its reactivity on the conditions of reservoir. If the pH of water is near neutrality, as is the case of the water in this study, the major potential redox couples are shown in Figure 2-10.

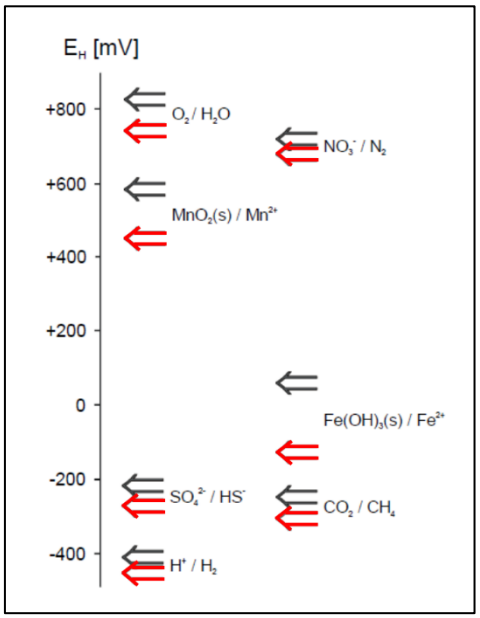

Figure 2-10 Redox potential of some important redox reactions in natural waters at pH 7 (black) and pH 8 (red) (*Sigg*, 1999)

E_H potential for the couple H^+/H_2 is -400 mV and if the pressure in H_2 (g) increases to 5 atm, the potential will be equal to -440 mV. More hydrogen pressure will increase and the potential E_H couple H^+/H_2 will decrease.

2.4 Hydrogen geochemical interactions

As mentioned before, porous rock storages like deep saline aquifer or depleted oil and gas reservoir are the most promising hydrogen geological storage options on the regional to global scale based on their estimated storage capacities and their widespread distribution. However, the injection of hydrogen into these porous rock storages disturb the initial equilibrium and could be caused chemical interactions between injected hydrogen, saline formation fluid and reservoir rock. These interactions include dissolution of minerals and precipitation of others (*Ganzer et al.*, 2013; *Truche et al.*, 2013) and not only change the chemical, but rather the physical properties of the reservoir system such as permeability, porosity or injectivity. The chemical interactions may lead to mobilization of initial components while the changes in physical properties influence operation, storage capacity, as well as long-term safety and stability of the reservoir. Hence, precise knowledge of the hydrogen-induced interactions between injected hydrogen and reservoir rocks and the resulting changes in chemical and physical properties of the reservoir system is therefore a prerequisite for any secure operation of a storage site.

Various supplementary methods can be undertaken to evaluate the behavior of the gas stored (like CO_2 or Hydrogen storage) in sedimentary formation and its interactions with water and the minerals of the host formation in a storage site.

Field study is the fundamental method to characterize of natural gas storage sites, which makes it possible to consider geological timescales at the reservoir scales. This method maybe not possible for hydrogen storage due to the absence of natural hydrogen storage and the investigation of hydrogen storage on sedimentary formation returns to recent years. Other methods are laboratory experiments and numerical simulations. Laboratory experiments provide direct observations of gas-fluid-rock interactions, however, at the experiment duration and spatial scales. This method is applicable for hydrogen gaseous that interaction of hydrogen with components of rock mineral compositions at the experiment time scales can be investigated. The last method is numerical simulations to interpret the geochemical reactivity behavior of a hydrogen storage site. This method include overlarge time and spatial scales that for gas storage modeling requires a good description of the process taking place and a precise characterization of the parameters involved in the calculations.

Laboratory experiments support numerical method with rate data for a large number of minerals at various temperatures, solute concentrations and at various distances from equilibrium. Thus, numerical modeling requires information from laboratory experiments and without any laboratory experiments and valid data, the results from numerical simulation not reliable.

However, laboratory experiments at simulated reservoir pressure and temperature conditions are an elegant way to study the hydrogen-water-rock interactions. Despite the importance of this study for underground hydrogen storage, unfortunately, experimental analysis at the reservoir conditions are scarce. Therefore, further experimental studies (either focus on individual minerals or on whole rock

samples) that cover additional physico-chemical conditions (e.g., pressure, temperature, lithology, brine composition), refer to the problem of potential slow reaction kinetics by needed prolonged run.
Hydrogen through the water dissolution reaction has a strong reduction power in a chemical system (*Lassin et al.,* 2011). Molecule of hydrogen has a polar nature and the strong H-H binding energy (436 kJ/mol) requires the overstepping of a high energetic barrier (*Truche et al.,* 2013). Thus, most of the possible redox reactions induced by hydrogen remain insignificant at low temperature, even on a geological time scale, provided no bacteria is present.
In general, two types of reactions induced by hydrogen in the underground storage could be considered: abiotic and biotic reactions.

2.4.1 Abiotic reactions

The mechanisms and kinetics of redox reactions induced by hydrogen on confining rocks are yet poorly documented. However, recently abiotic hydrogen reactivity with rock minerals, which are restricted to redox reactions at reservoir temperature, has been taken into consideration. *Truche et al,.* (2013) studied experimentally abiotic redox reaction induced by hydrogen at low temperature. However, he has illustrated Pyrite mineral reduction into Pyrrhotite and releasing sulfide anions in the solution (Equation (2-40)), under hydrogen partial pressure above 30 bar and temperature as high as 150°C, which is higher for the underground hydrogen storage. In addition, he has demonstrated that the alkalinity of the geological storage impact the abiotic redox reaction and the pH of the media is a critical parameter to control the extension of the reaction at low temperature. Hence, pH changes can also lead to mineralogical transformations.

$$FeS_2 + (1-x)H_2 = FeS_{1+x} + (1-x)H_2S\,, \qquad 0 \le x < 0.125 \qquad \text{(2-40)}$$

However, injecting hydrogen in the porous formation storage can promote abiotic reaction of hydrogen with minerals of host reservoir and caprocks that could be caused dissolution of carbonate, sulfate, feldspars and clay minerals and also precipitation of illite, iron sulfide and pyrrhotite (*Reitenbach et al.,* 2015) which should be approved experimentally.

2.4.2 Biotic reactions

Besides the abiotic reactions, at underground hydrogen storage the microbial activities that could cause hydrogen consumption is the most likely phenomenon, which can affect the geochemical environment of a gas storage and lead to a loss of hydrogen (*Reitenbach et al.,* 2015). In fact, bacteria consume the energy produced from redox reaction that initiated from hydrogen and the other components in reservoir, while they do not consume hydrogen directly (*Panfilov* 2016). However, the evidences from town gas storages in Lobodice (Czech Republic) and also in Beynes (France) reveal the biotic reactions and bacteria activity in hydrogen storage.

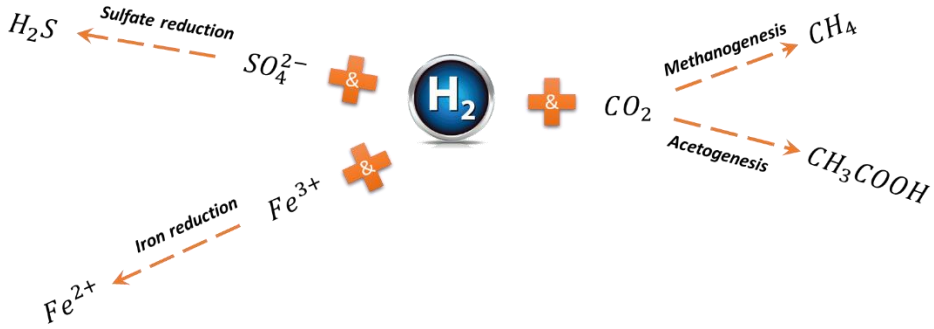

Figure 2-11 Four type of biotic reaction in underground hydrogen storage

In general, four hydrogen trophic microbial process could be considered in geological hydrogen storage where there is a residual water (Figure 2-11). In fact, residual water is favorable for bacteria to live and use hydrogen as the electron donor and other substances as the electron acceptors:

- Methanogenesis:

$$CO_2 + 4H_2 = CH_4 + 2H_2O \quad (2\text{-}41)$$

  CO_2 is present in the injected gas (town gas) or in the carbonate reservoir rock minerals;

- Acetogenesis:

$$2CO_2 + 4H_2 = CH_3COOH + 2H_2O \quad (2\text{-}42)$$

- Sulfate-reduction (SRB):

$$SO_4^{2-} + 5H_2 = H_2S + 4H_2O \quad (2\text{-}43)$$

  sulfate is present as a dissolution in aquifer of the reservoir;

- Ferric-reduction:

$$3Fe_2^{+3}O_3 + H_2 = 2Fe_3^{+2}O_4 + H_2O \quad (2\text{-}44)$$

  that Iron Oxide is present in reservoir rock minerals;

These hydrogen perturbation effects are not initially observed in the reservoir. In fact, these reactions are progressive and kinetically controlled with the activity of bacteria that consume hydrogen to lead reduction reactions.

The growth of microorganisms in an aqueous environment was modeled mathematically in empirically observation with *Monod et al.,* (1949) and *Moser* (1988). Moreover, the kinetics of reactions and bacterial population growth were studied with *Jin et al.,* (2005) and recently developed with *Panfilov* (2010 and 2015). In addition, *Ebigbo et al.*, (2013) were developed a numerical model to evaluate the methanogenic microbial activity in hydrogen storage. Furthermore, *Hagemann et al.*, (2015) presented the mathematical model which describes the hydrodynamic behavior of underground hydrogen storage coupled with biochemical reactions and microbial population dynamics. *Panfilov et al.*, (2016) developed the advanced mathematical model of hydrogen storage that converts hydrogen and CO_2 to the methane due to the activity of bacteria.

Overall, considering the injection of hydrogen in porous formations needs to investigate a large range of processes which include the role of abiotic (fluid rock geochemical) interactions that would change the properties of the rock formation and reservoir, the biotic (microbial) reactions, which can alter the composition of the stored gas (in a positive or negative way according to the final use), the properties of the hydrogen fluid migrating into a brines (or other fluids) porous media, which controls the level of risk of leakage of the storage reservoir. In this study, we will limit our approach to abiotic reactions between hydrogen gas and confining sandstone to evaluate the impact of hydrogen on the mineralogical components, and we will also assess the evaluation of parameters which control the migration of the gas in a water saturated porous rock, i.e. the relative permeability and the capillary pressure. Therefore, many further works would still need to be investigated upon the progress proposed by this study.

Chapter 3

Experimental study of geochemical reactivity of hydrogen in sandstone

As previously mentioned, laboratory experiments to study abiotic reactions between hydrogen gas and confining sandstone under typical reservoir conditions are scarce. Hence, in this Chapter, we have performed laboratory experiments to evaluate the impact of hydrogen on the mineralogical components of sandstone under conditions of natural hydrogen storage. The methods and the results of this study are detailed below. Data from this Chapter will be complemented and integrated with results from Chapter 6. Overall, the experimental study emphasizes the very limited reactivity of sandstone to hydrogen gas.

3.1 Rock core samples and analytical methods

The purpose of this study was the testing of sandstone lithologies for underground hydrogen storage. Therefore, lower Triassic sandstones from the Buntsandstein (Lower Triassic) formation east of the Paris Basin were chosen. The Paris Basin is the largest on-shore French sedimentary basin (Bader et al., 2014). It has been identified as a major site for geothermal storage (Aquilina et al., 1997; Blaise et al., 2016). The Buntsandstein was deposited under calm tectonic conditions and represents the main subsidence period of the eastern layer of the Paris Basin. Therefore, deposits exhibit uniform lithologies and thicknesses over large distances. The Buntsandstein represents the lower group of the Trias (Figure 3-1). It is subdivided by lithological criteria into three levels: (a) Voltzia sandstone, (b) Couches intermediate sandstone, and (c) the Vosges sandstone.

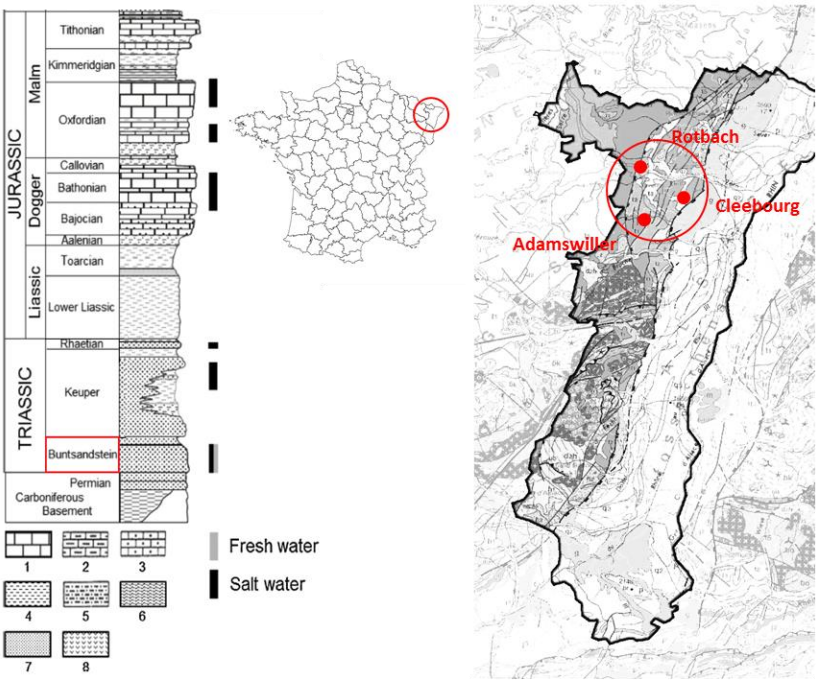

Figure 3-1 Right: the position of Vosges sandstone samples considered in this study, Left: Synthetic lithostratigraphic column.
The geological levels considered in this study are outlined in red, respectively. (1) Limestone, (2) clayey limestone, (3) sandy limestone, (4) clay, (5) sandy clay, (6) marl, (7) sandstone and (8) gypsum.

Three Vosges sandstones from the quarries of Rotbach, Adamswiller and Cleebourg (Figure 3-2) were sampled for this study. They are of different colors from red, yellow to greyish. Cores of two sizes (40 mm length and 5 mm diameter for the geochemical experiments and 60 mm length and 15 mm diameter for the core-flooding experiments) were drilled from the rock samples (Figure 3-2).

Figure 3-2 Adamswiller, Cleebourg and Rotbach sandstone rock samples

- **Physical properties**

The physical properties of the sandstones (porosity, density and absolute permeability) were measured experimentally.

Porosity: The porosity was measured from the total volume (determined from the size of the core samples), knowing the pore volume determined by mercury intrusion porosimetry using a Micromeritics Autopore IV 9500 instrument working from vacuum to 200 MPa. The intrusion and extrusion curves were obtained with an equilibration time of 60 s from low to high pressure.

Absolute permeability: The absolute permeability of the core was measured by the water and gas (hydrogen/argon) core-flooding method using Darcy's law, as described in section 5.2.1.

Density: The density of the cores was measured by weighing the samples in air and knowing the total and pore volume of samples.

The physical data for the three sandstones are reported in Table 3-1. Although some dispersion is apparent, permeabilities do not vary by more than a factor of 2 between samples. Porosities are in the 15-20 % range and tightly grouped. The Rotbach sandstone has a high density compared to the two other samples.

Table 3-1 Physical parameters of the studied sandstones

Parameters	Adamswiller	Cleebourg	Rotbach
Permeability (mD)	46	85	98
Porosity (%)	19.8	16.4	18.8
Density ($g.cm^{-3}$)	1.96	1.85	2.31

- **Mineralogical study**

In order to study the mineral components of the core samples, several analytical techniques were employed. The workflow scheme from the macro- to the micro-scale is illustrated in Figure 3-3. In most cases, the different characterization steps were accomplished before and after the experiments so as to unambiguously reveal modifications associated with the experimental treatment.

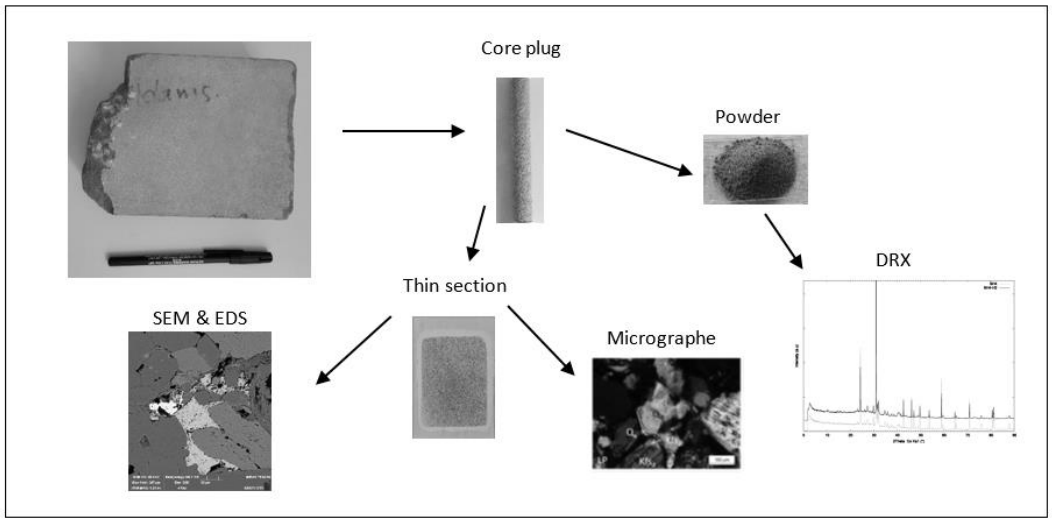

Figure 3-3 Schematic illustration of the different analytical techniques used for the characterization of the sandstone samples. SEM: scanning electron microscopy; EDS: energy dispersive spectroscopy; DRX: X-ray diffraction.

Parts or blocks of each sample were crushed, then sieved to grain sizes between 30 and 50 µm and the resulting powders used for X-ray diffraction (XRD) analysis. In addition, thin sections of samples were prepared (Figure 3-4) for point counting and optical microscopy.

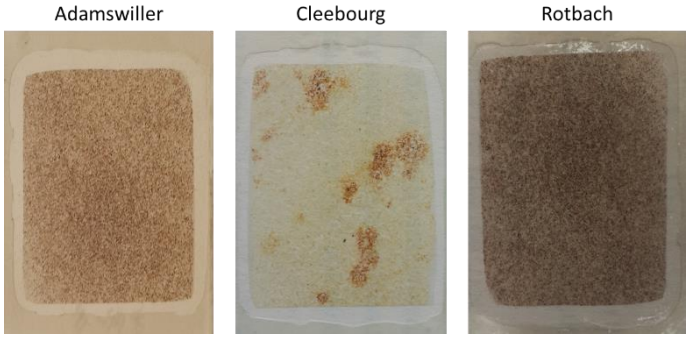

Figure 3-4 Adamswiller, Cleebourg and Rotbach sandstone thin sections

Optical microscopy: The thin sections were examined with a Zeiss petrographic microscope. Modal proportions of mineral phases in samples were determined with an automated Peltron point counter coupled with a petrographic microscope.

Optical microscopy showed that all sandstones contain dominant detrital quartz and feldspar, and minor accessories Muscovite occurs as a medium to large sub-euhedral birefringent phase. Clay minerals and iron oxides are present in small amounts, appearing as very fine-grained phases, very often coating detrital grains. The three studied samples have the same mineralogy. However, they have different grain sizes and the proportion of accessory minerals, muscovite, clay minerals and iron oxides can also be variable (Figure 3-5).

(a)

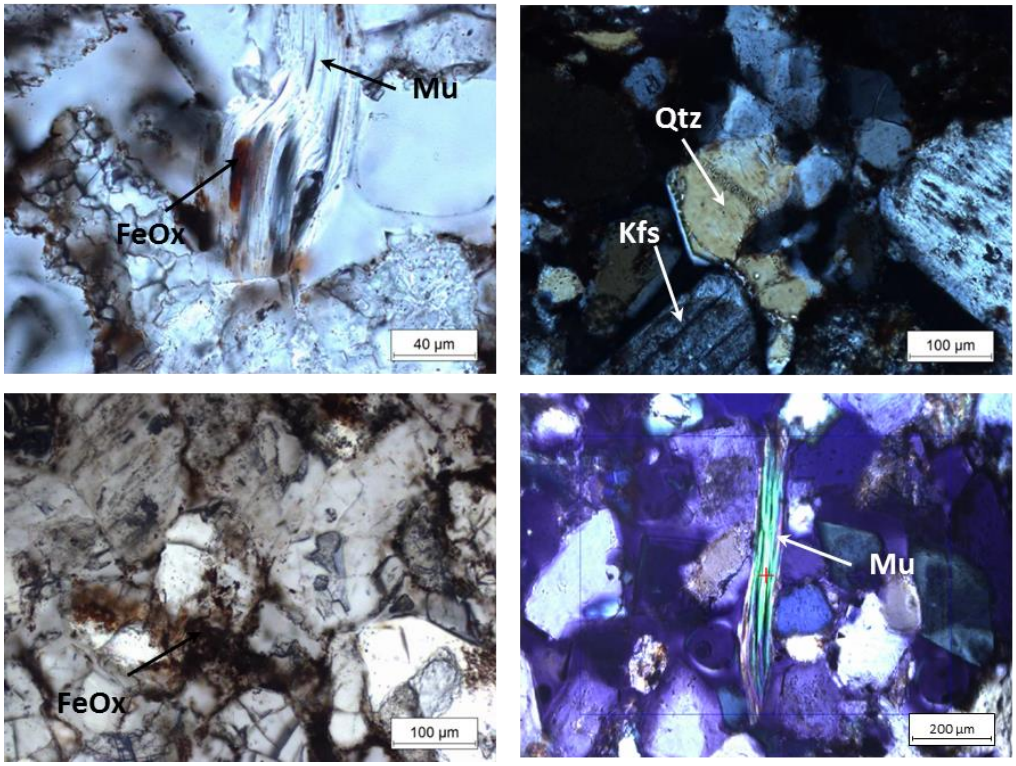
Mu
FeOx
40 µm
Qtz
Kfs
100 µm
FeOx
100 µm
Mu
200 µm

(b)

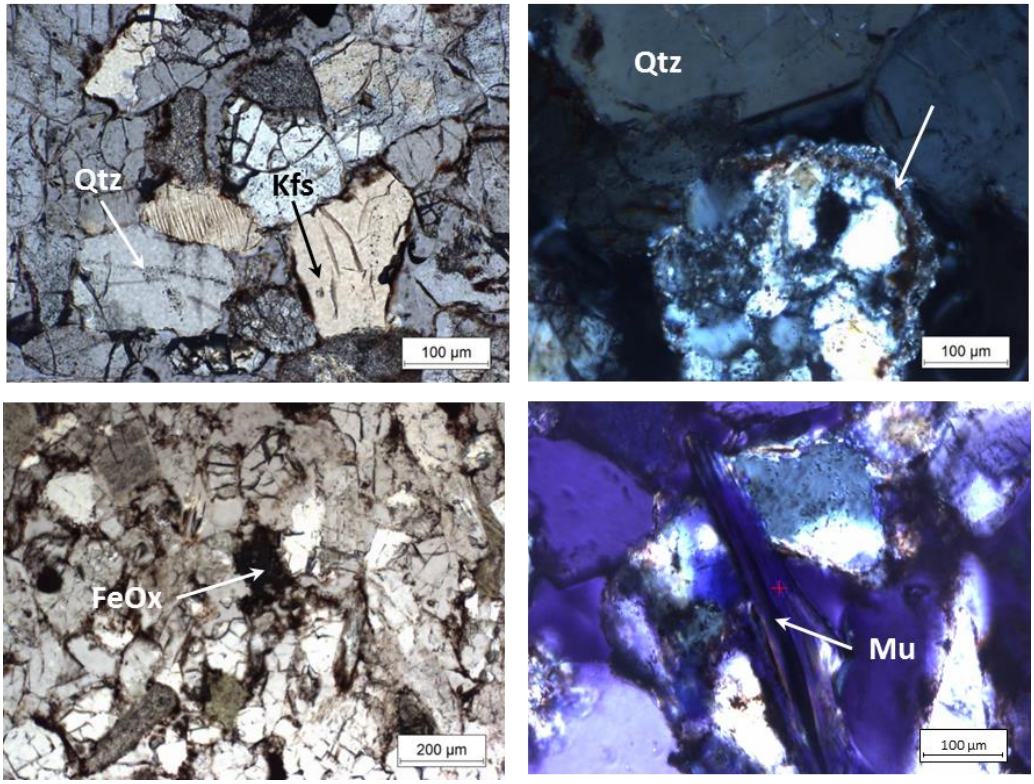
Qtz
Kfs
100 µm
Qtz
100 µm
FeOx
200 µm
Mu
100 µm

(c)

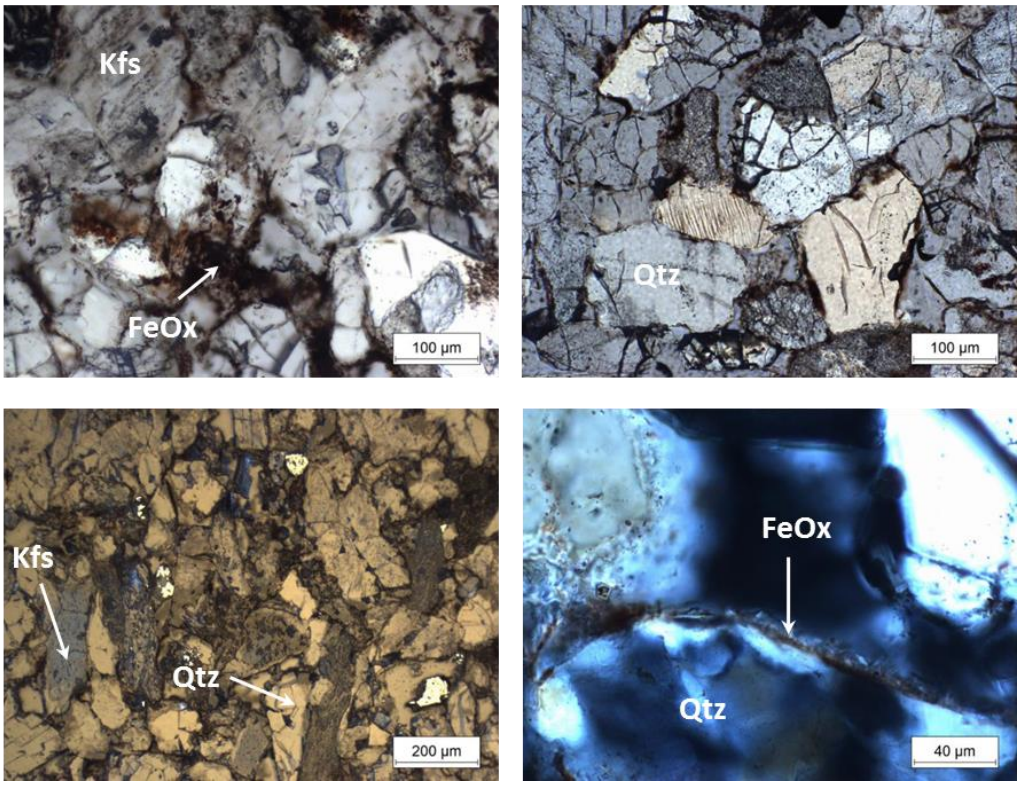

Figure 3-5 Photomicrographs of studied sandstones: (a) Adamswiller, (b) Rothbach, (c) Cleebourg (Qtz: Quartz, FeOx: iron oxides, Kfs: K-feldspar, Mu: Muscovite)

Point counting: The point-counting method was used to determine accurate mineral modes in the three rock samples. The basic process is to set up a grid of points on a thin section and identify the mineral at each grid point. The number of grid points necessary for a given rock or thin section is determined by the precision needed for the modes. The percentage of each mineral in the sample is given by points counted on mineral divided by the total points counted for each thin section. In this study, 500 points were counted per thin section using an electromechanical point counting stage.

X-ray diffraction (XRD): The X-ray diffraction (XRD) data were obtained with an INEL diffractometer equipped with a curved position-sensitive detector. Sample powders were loaded in a glass capillary (Hilgenberg GmbH n°50). A Cu anode was used and the Co Kα1 X-ray line was selected using a bent quartz crystal monochromator. The scan parameters used were 0–90° 2θ, with a step size of 0.02° 2θ. XRD results for the initial core (pre-experimental) samples are shown in Figure 3-6. Quartz is the dominant component in all samples. K-feldspar is the second abundant mineral phase and there are small amounts of muscovite and hematite (iron oxide).

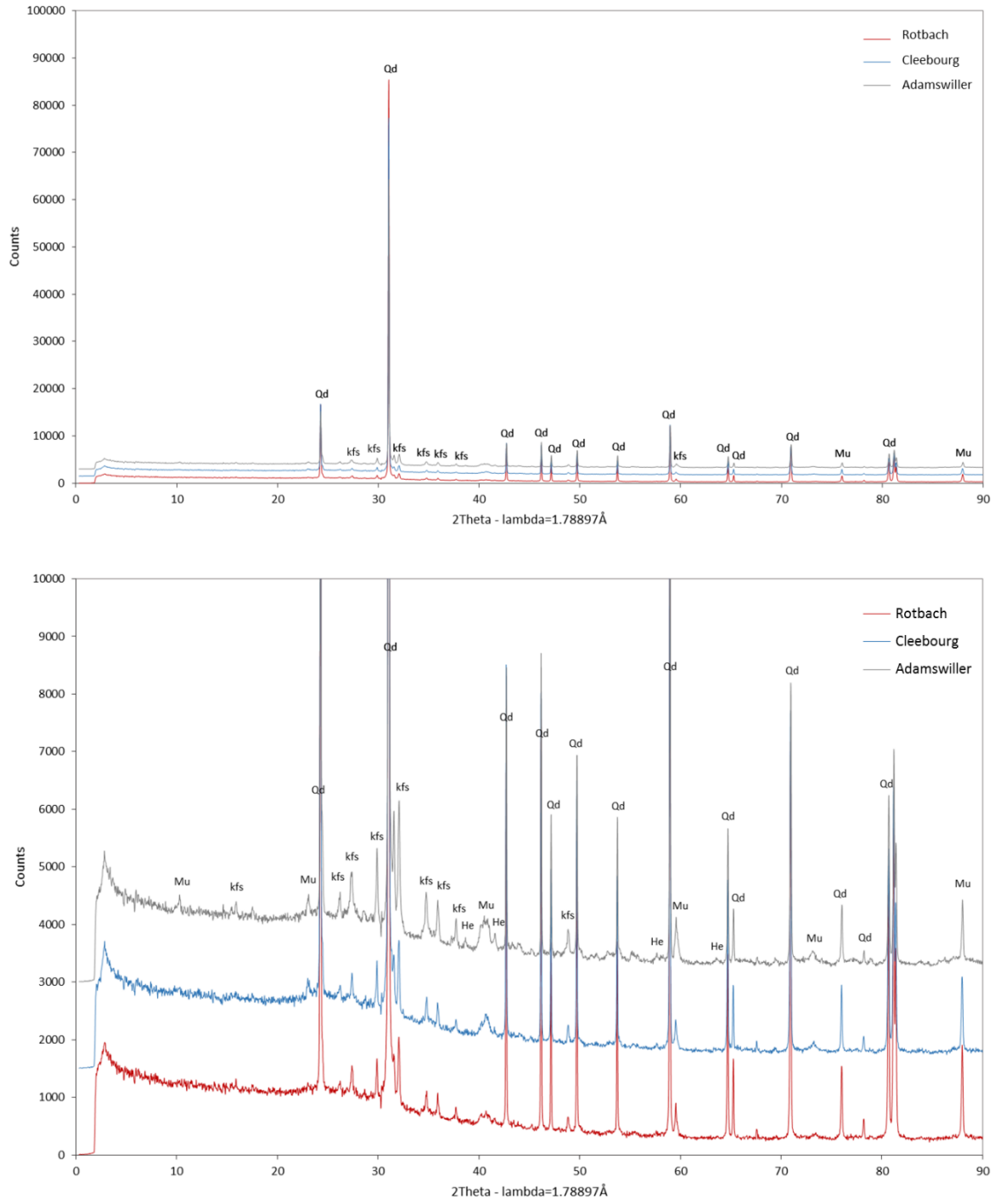

Figure 3-6 X-ray powder diffraction analysis for Adamswiller, Cleebourg and Rotbach sandstones before the experiments (Qd: Quartz, He: Hematite, kfs: K-feldspar, Mu: Muscovite).

The mineral modes of the three studied sandstones are detailed in Table 3-2. The point counting results, plus the XRD data, enable the mineralogical composition of the samples to be determined. Quartz and feldspar are the dominant minerals in the three rocks and, together, they account for 95-97 % of the total mineral proportion. With a modal amount of 74-80 %, quartz is the most abundant phase, followed by K-feldspar (17-26 %). Mica (muscovite according to the XRD results) is the main accessory mineral (0.6-2.3 %). An oxide phase (hematite according to the XRD results) and clay minerals (only

distinguished from muscovite by microscopic examination) occur as minor phases (modal proportions 0.3-0.9 and 0.6-1.0 %, respectively). Although phase proportions can vary (Table 3-2), there is no change in mineral assemblage between the three studied samples. Because mica and oxide proportions are the highest in sample 1# (Adamswiller quarry), this sandstone was selected for the experimental study.

Table 3-2 Mineral modes of the studied sandstones

Sandstone sample #	Mineral types and content (Vol %)[a]				
	Quartz	K-feldspar	Mica	Oxide	Clay minerals
(1) Adamswiller	73.8	22.4	2.3	0.9	0.6
(2) Cleebourg	71.6	25.7	1.4	0.3	1.0
(3) Rotbach	80.9	17.2	0.6	0.5	0.8

[a]Point counting of 500 points per thin section.

Scanning electron microscopy (SEM): The thin sections (sandstones and experimental cores) were carbon-coated and mineral textures examined with a TESCAN MIRA 3 XMU instrument from the ISTO-BRGM analytical platform at Orléans. Energy-dispersive spectroscopy (EDS) analyses of specific grains were also performed for mineral identification and element distribution maps acquired to assist mineral identification.

Electron microprobe (EMPA): Mineral phases in thin sections (sandstones and experimental cores) were analyzed with the Cameca SX Five instrument of the ISTO-BRGM analytical platform at Orléans (Figure 3-7). The microprobe was operated at 15 kV acceleration voltage and 6 nA sample current. Natural mineral standards were used. Counting times were 10 s on peak and 5 s on background, and a focused beam was used.

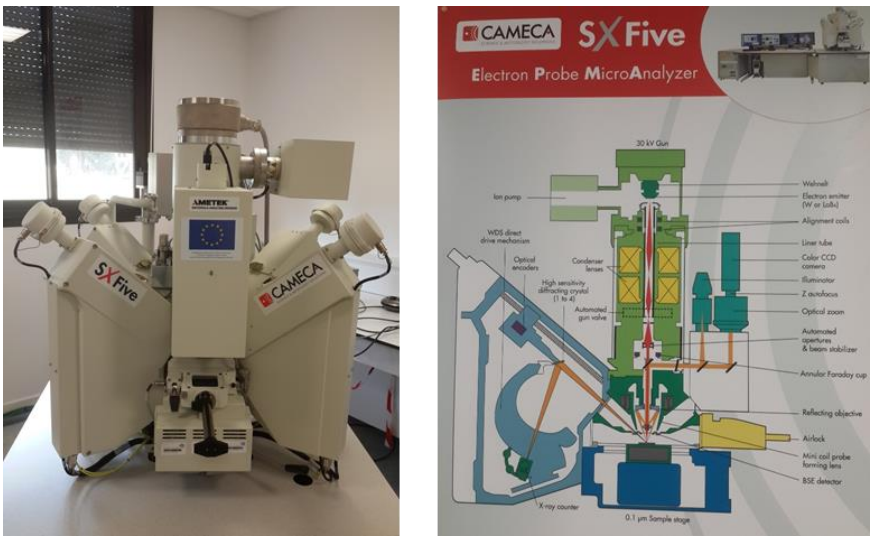

Figure 3-7 Electron probe micro analyzer

3.2 Experimental methods and procedure

Static batch reactor experiments were conducted to evaluate the effect of gaseous hydrogen on sandstone at pressures and temperatures representative of reservoir conditions (Figure 3-8). In these experiments, duration was taken as the main experimental parameter.

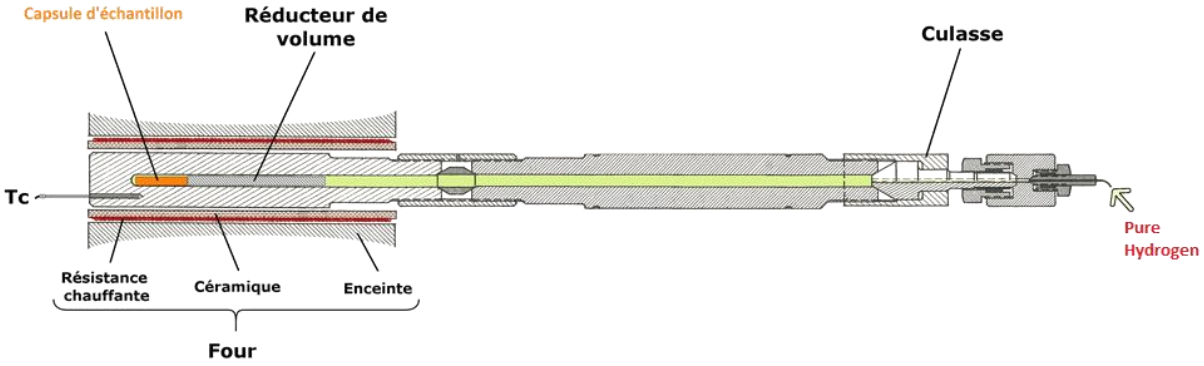

Figure 3-8 Apparatus used for the sandstone-hydrogen gas interaction experiments

- **Experimental charges**

Both cores and powders were experimentally tested and results with these two rock types are combined below. The starting materials (1.5 g for each charge) were dried in an oven at 120°C for 20 min and then loaded in Au capsules of 50 mm length (Figure 3-9).

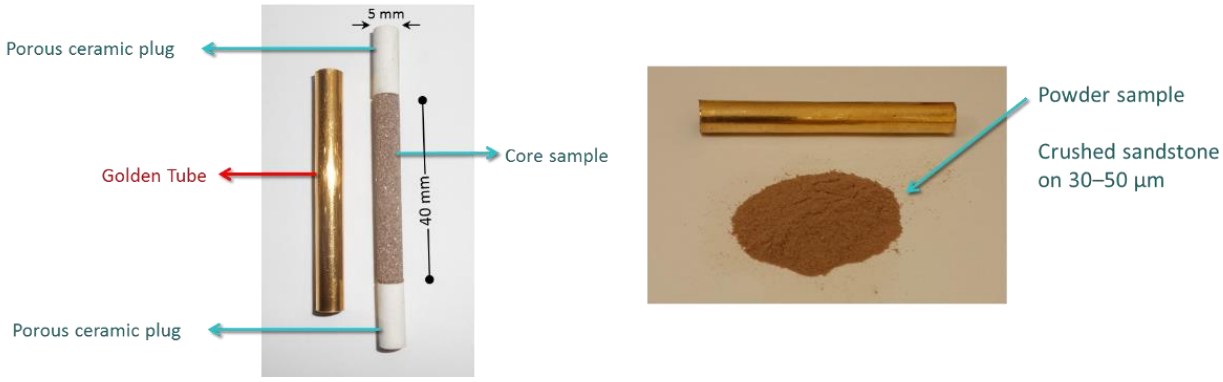

Figure 3-9 Experimental charge components: Au capsule, porous ceramic end plugs and sandstone (either core or powder)

In one experiment, the core was saturated with water before being loaded in the capsule. In most cases, capsules were fitted with a porous ceramic plug at both ends (Figure 3-10). This procedure enabled gas from the pressure medium (either H_2 or Ar) to access freely to the sandstone during the experiment while preserving the charge from being in contact with the autoclave walls. It also ensured the confinement of the charge for experiments performed with powders.

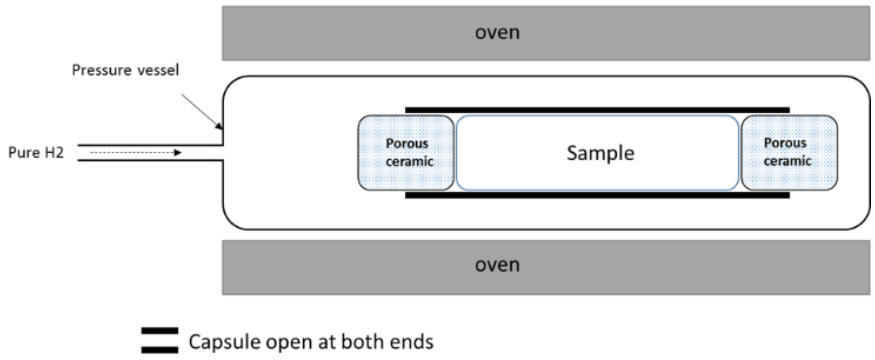

Figure 3-10 Configuration of experimental charges performed under pure H_2 gas. The sandstone sample (either core or powder) is loaded in an Au capsule fitted with porous ceramic plugs at both ends, allowing H_2 to freely access to the sample.

In one experiment designed to test the effect of hydrogen on sandstone in presence of water, a different charge assembly was used (Figure 3-11). The charge (1.4 g of sandstone plus 140 mg of H_2O, water/rock ratio of ~0.1) was loaded in the Au capsule together with pure Fe powder, and the capsule was hermetically closed at both ends by welding. Hydrogen was generated from inside the capsule by allowing the water present to react with the Fe powder. The sandstone inside the capsule was thus allowed to react with a H_2O-H_2 fluid mixture. To prevent contamination with Fe, the sandstone was physically separated from the Fe powder by a porous ceramic plug. Experimental charges such as in Figure 3-10 or Figure 3-11 are then placed in a horizontal pressure vessel.

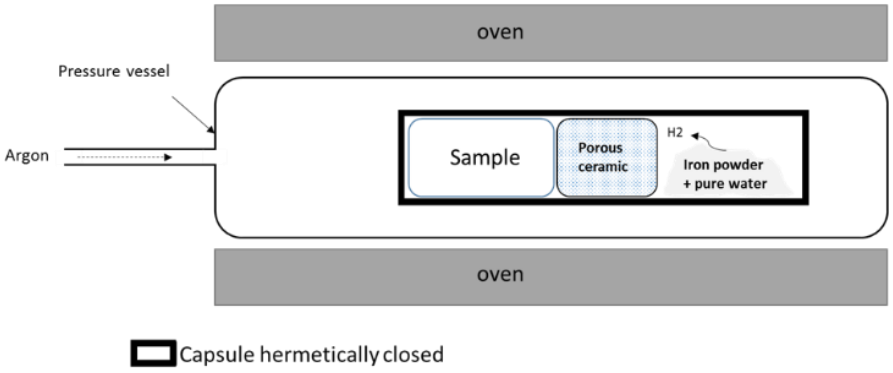

Figure 3-11 Configuration of experimental charges performed with a H_2O-H_2 gas mixture. The sample is loaded together with Fe powder and H_2O in a Au capsule that is hermetically closed by welding

- **Experimental equipment and procedures**

Capsules with experimental charges were placed inside a rapid-quench hydrothermal pressure vessel made of a Ni-rich alloy (Figure 3-12) and working horizontally (Pichavant, 1987). After being closed, the vessel was pressurized to a total pressure of 100 bar and then inserted into the furnace. In most cases, the pressurizing gas was pure hydrogen. In two cases (synthesis of the XRD reference and H_2O-H_2 fluid mixture experiment), Ar was used instead of hydrogen. During the experiment, temperature was

monitored with an Eurotherm regulator and permanently recorded with a thermocouple inserted in the autoclave wall. Pressure was measured with a manometer (pressure range: 0–500 bar; measurement error < 1 % of full scale value) and adjusted during the course of the experiment, if necessary. Uncertainties on temperature and pressure are +/-10°C and +/-20 bar respectively. Once the experiment was completed, the pressure vessel was removed from the furnace, allowed to cool at room temperature (< 1 hour) and opened. The capsules were recovered and the samples prepared for analysis.

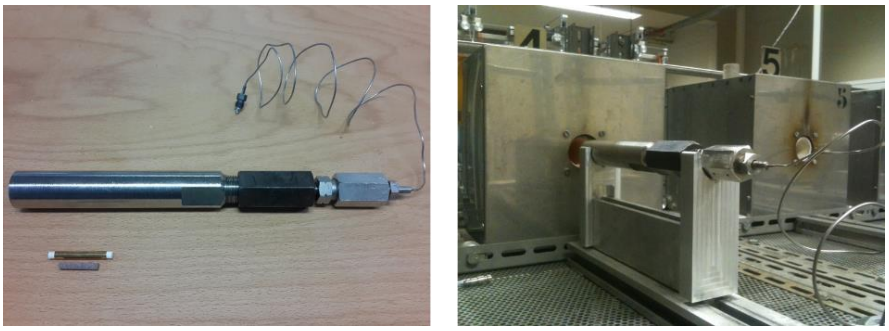

Figure 3-12 Left: hydrothermal autoclave and pressure capillary, Right: Furnace and autoclave before starting an experiment

3.3 Experimental results

Experimental conditions and results are summarized in Table 3-3. Durations ranged from 1.5 to 6 months. Five experiments were performed at 100°C and three at 200°C. Experiment no. 3 is the one which started from a wet core, instead of a dry one as in all the other experiments. The experiment with the mixed H_2O-H_2 fluid phase (no. 8, Table 3-3) was performed at a temperature of 100°C and a pressure of 100 bar, and the partial pressure of hydrogen in the H_2O-H_2 fluid mixture is estimated to be in the 10-50 bar range. The reference charge for the XRD data was synthesized in experiment no. 1.

Table 3-3 Experimental conditions and results for sandstone #1

No	Pressure (bar)	Temperature (°C)	Duration (month)	Hydrogen source	Water	Rock type	Water-Rock ratio	Analytical results			
								Quartz	K-Feldspar	Muscovite	Hematite
1	100	100	1,5	-	-	Core	0	T X	T X	T X	T X
2	100	100	1,5	Pure H_2	-	Powder	0	T X	T X	T <u>X</u>	T <u>X</u>
3	100	200	1,5	Pure H_2	-	Core[b]	0	T X S	T X S	T <u>X</u> <u>S</u>	T <u>X</u> S
4	100	200	3	Pure H_2	-	Powder	0	T X	T X	T <u>X</u>	T <u>X</u>
5	100	200	3	Pure H_2	-	Core	0	T X S	T X S	T <u>X</u> <u>S</u>	T <u>X</u> S
6	100	100	6	Pure H_2	-	Powder	0	T X	T X	T <u>X</u>	T <u>X</u>
7	100	100	6	Pure H_2	-	Core	0	T X S	T X S	T <u>X</u> <u>S</u>	T <u>X</u> S
8	10 to 50	100	1,5	H_2[a]	H_2O	Core	0,1	T X S	T X S	T <u>X</u> <u>S</u>	T <u>X</u> S

[a]Hydrogen generated from the reaction of water and iron
[b]The core was saturated with water before the experiment
T: texture analysis
X: XRD analysis
S: chemical analysis
Changes indicate by underlined text (i.e. <u>X</u> indicates a change in XRD data in comparison with the reference)

- **Textural evolution**

Textures of starting materials and representative experimental products are summarized in Figure 3-13. Observations by optical microscopy and SEM yielded similar results. SEM microphotographs of experimental charges for "dry" conditions as well as for the "wet" experiment are illustrated. Overall, no clear textural change appears between samples, whether coming from the starting materials or from experimentally reacted charges. Quartz and feldspar minerals form grains with sizes mostly in the 100-200 µm range and they show typical anhedral rounded morphologies. No difference can be noted between experimental samples, whether "dry" or "wet" (Figure 3-13a; d; g). Muscovite appears as sub-euhedral flakes, 50 to 200 µm in size, and no apparent textural modification emerges between the three different types of samples, starting material, experimental "dry" and experimental "wet" (Figure 3-13b; e; h). Fe oxides were found to occur under more variable habits in the sandstones, from small crystals included in quartz or feldspar minerals (Figure 3-13c; f) to interstitial grains, sometimes large (50 µm) in size (Figure 3-13i). However, they show no textural indication for a mineralogical transformation, even partial or local. Therefore, the optical and SEM examinations reveal no significant textural changes in experimental products in comparison with the starting sandstones. This is true both for experimental samples reacted with and without H_2O (Figure 3-13g; h; i) and at 100 and at 200°C (Figure 3-13f).

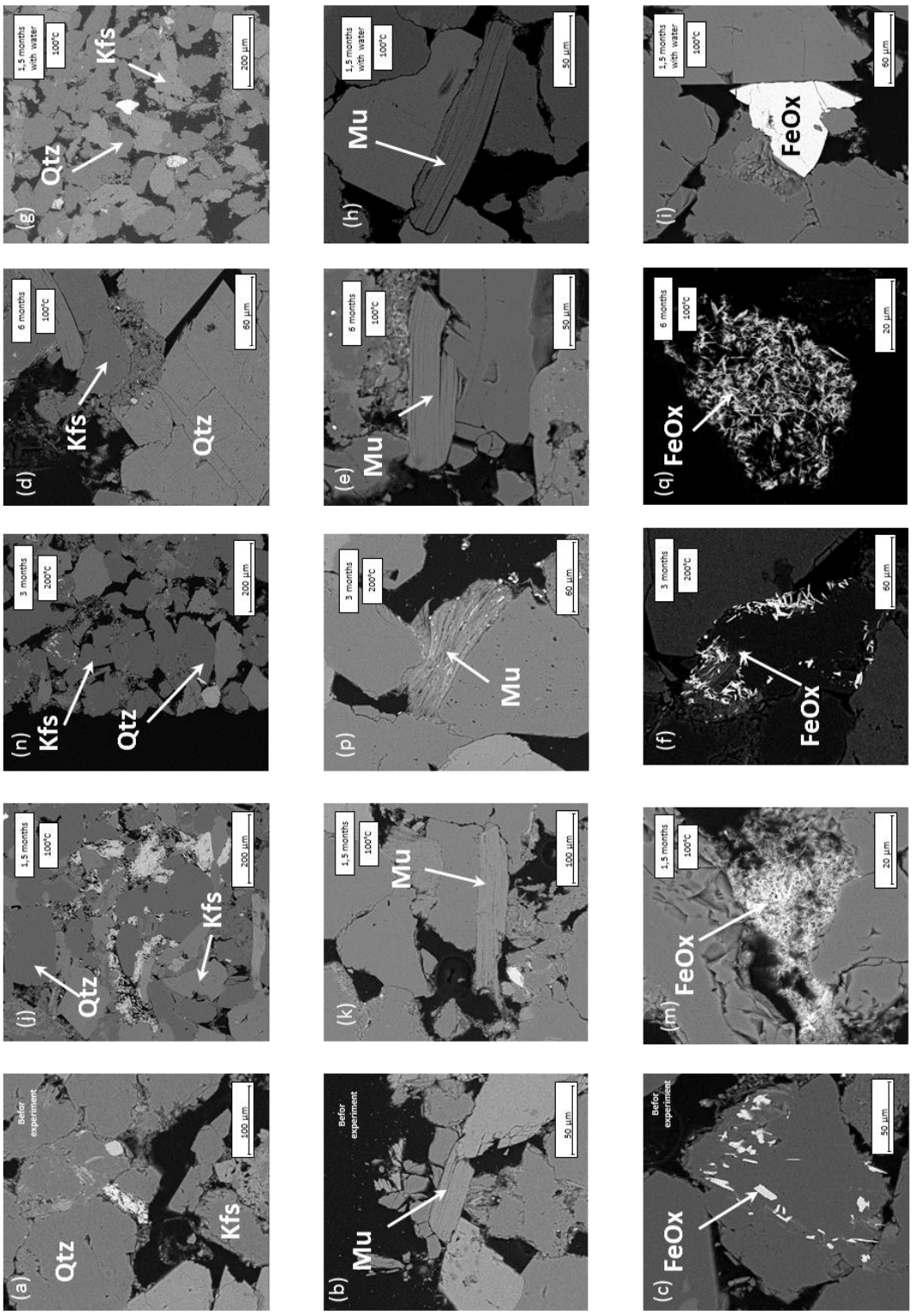

Figure 3-13 SEM photomicrographs of starting materials and experimental products. (a), (b), (c), photomicrographs of the main mineral phases in the starting sandstone, quartz (Qtz, a), K-feldspar (Kfs, a), muscovite (Mu, b) and hematite (FeOx, c). (d), (e), (f), photomicrographs of representative products from the "dry" experiments (performed with pure H2 gas) showing quartz and K-feldspar (d), muscovite (e) and hematite (f). Same abbreviations as in (a), (b) and (c). (g), (h), (i), photomicrographs of products from the "wet" experiment (performed with a H2O-H2 gas mixture) showing quartz and K-feldspar (g), muscovite (h) and hematite (i). Same abbreviations as in (a), (b) and (c). See text for explanations.

- **Phase assemblages and structural evolution**

The XRD results are summarized on Table 3-4. They show that the same phase assemblage (quartz, feldspar, muscovite, hematite) is present in the samples before and after the experiments. Magnetite was looked for but never positively identified. Clay minerals were not positively detected although a weak peak indicative of kaolinite might be present in some samples. Therefore, reacting the sandstone with hydrogen caused no first-order modification in the phase assemblage from the starting rock.

Table 3-4 XRD analysis of experimental charges

experiment number	Phases present					
	Quartz	K-feldspar	Muscovite	Hematite	Magnetite	Kaolinite
1	+	+	+	+	-	-
2	+	+	+	+	-	-
3	+	+	+	+	-	?
4	+	+	+	+	-	-
5	+	+	+	+	-	-
6	+	+	+	+	-	-
7	+	+	+	+	-	-
8	+	+	+	+	-	-

The XRD signatures of quartz and feldspars did not change before and after the experiments. However, differences were noted between the reference and the experimental samples concerning muscovite (Table 3-4). Most sandstones annealed under hydrogen showed an increase of muscovite XRD peak intensities compared to the reference, as illustrated in Figure 3-14. The most marked intensity increases were noted for charges no. 4, 5, 6 and 7, i.e., for two “dry” 200°C, 3 month (4, 5) and two “dry” 100°C, 6 month (6, 7) experiments. In comparison, the “wet” charge (no. 8, 1.5 month, Table 3-3) did not show much variation compared to the reference, and the two 1.5 month experiments (no. 2, 3) were relatively little modified (Figure 3-14). Although overall these changes are of minor importance, they are considered as significant since they occur in several charges. They indicate that some mineralogical transformations, such as muscovite recrystallization or growth, took place during the experiments.

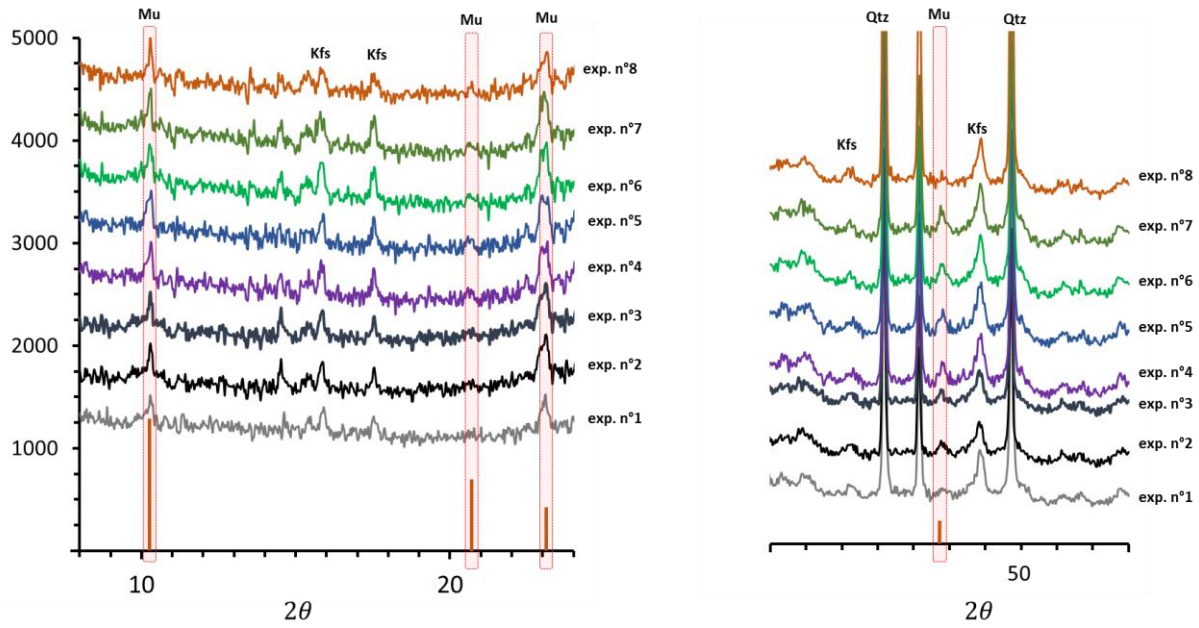

Figure 3-14 Evolution of XRD peaks of muscovite at 2Θ = 10.315°, 20.737°, 23.087°, 47.796° in experimental products (exp. n° 2, 4, 6, 8) and in the reference (exp. n°1). See Table 3-3 for experimental conditions and text for explanations.

Additional evidence for mineral reaction during the experiments is provided by the Fe oxides. In our experimental charges, the only Fe oxide identified by XRD is hematite and magnetite was never found. Contrary to an expected reduction of hematite under the influence of hydrogen, the XRD peaks diagnostic of hematite showed intensity increases in several charges, in particular in experiments 6 and 7 (Figure 3-15). Again, in the "wet" no. 8 charge, hematite peaks showed little intensity changes relative to the reference (Figure 3-15). Therefore, and although detailed information is lacking to interpret these changes, the XRD signature of Fe oxides further demonstrates that limited but detectable mineral reaction takes place in the experiments as a result of interaction with hydrogen.

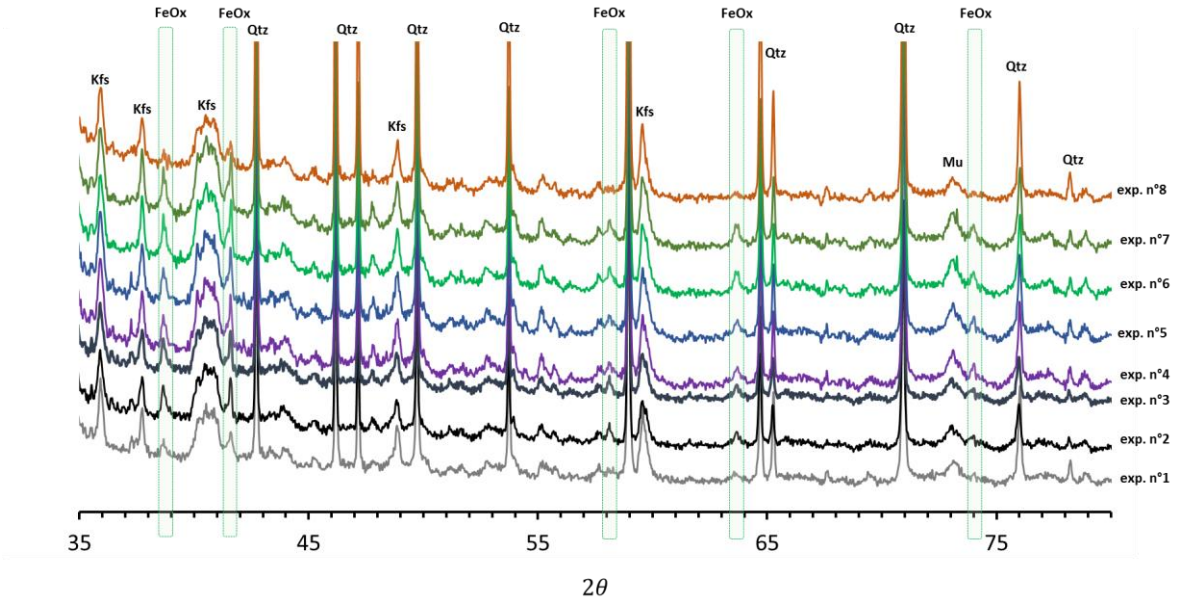

Figure 3-15 Evolution of XRD peaks of hematite at 2Θ = 38.694°, 41.599°, 58.153°, 63.741796°, 74.024° in experimental products (exp. n° 2, 3, 4, 5, 6, 7, 8) and in the reference (exp. n°1). See Table 3-3 for experimental conditions and text for explanations.

- **Compositional evolution**

Results of electron microprobe analyses of minerals before and after the annealing experiments under hydrogen are summarized on Table 3-5. Three phases in particular were investigated, K-feldspar, muscovite and hematite and, for each, electron microprobe data before and after the experiments are given. Average values and standard deviations are provided especially for muscovite whereas, for the other phases, only starting compositions have been averaged because of more limited data. The generally low standard deviations (e.g., < 0.5 wt% for SiO_2 in K-feldspar, FeO in muscovite and TiO_2 in hematite) indicate that mineral phases in the starting sandstone are sub-homogeneous. K-feldspar is nearly pure, containing very little Na_2O (on average 0.37 wt%) and very low (below detection) FeO_t. Muscovite contains significant amounts of FeO_t (on average 3.54 wt%), MgO (1.20 wt%), TiO_2 (0.78 wt%) and Na_2O (0.44 wt%). Hematite has low Al_2O_3 (on average 0.48 wt%), MnO (0.22 wt%) and MgO (0.02 wt%) but relatively high TiO_2 (9.12 wt%), which corresponds to a solid solution between ilmenite and hematite in a 0.18:0.82 proportion (mole fraction). Experimentally reacted K-feldspars and hematites are chemically homogeneous and they show little compositional differences with minerals in the starting sandstone. One K-feldspar analysis (no. 5) is exceptionally Na_2O-rich (1.38 wt%). The range of TiO_2 concentrations in experimental hematites (9.01 to 10.2) encloses the average in the starting sample. In contrast, experimental muscovites record a minor but detectable compositional change from the starting sandstone. FeO_t concentrations decrease from ~ 3.5 wt% before experiments to values ranging from 1.24 to 2.48 wt% in experimental samples. Charges no. 3 and 8 (respectively performed with a wet starting core and a H_2O-H_2 fluid, Table 3-3) show the maximum deviations, whereas muscovites in charges no. 5 and 7 (two "dry" charges at 200 and 100°C, Table 3-3) appear less chemically modified. Apart from FeO_t concentrations, the other oxides show no significant changes when compared with the starting composition and, so, the chemical modifications recorded by muscovite are relatively minor. However, they demonstrate that mineral phases can change their compositions during the experiments as a result of interaction with hydrogen.

Table 3-5. Representative electron microprobe analysis of minerals before and after the experiments

	K-feldspar					Muscovite					Hematite				
	Starting sandstone	Exp. n°3	Exp. n°5	Exp. n°7	Exp. n°8	Starting sandstone	Exp. n°3	Exp. n°5	Exp. n°7	Exp. n°8	Starting sandstone	Exp. n°3	Exp. n°5	Exp. n°7	Exp. n°8
SiO2	64.9 (3)	64.3	65.4	64.1	64.8	47.3 (9)	46.7 (10)	47.5 (98)	46.9 (7)	45.8 (9)	0.08 (2)	0.02	0.09	0.04	0.07
TiO2	0.07 (1)	0.00	0.00	0.00	0.10	0.78 (44)	0.61 (17)	0.67 (25)	0.84 (20)	1.06 (21)	9.12 (34)	10.2	10.0	9.70	9.01
Al2O3	18.1 (6)	18.1	18.0	18.3	17.9	31.4 (5)	34.3 (9)	31.9 (9)	31.3 (10)	32.8 (2)	0.48 (11)	0.00	0.00	0.52	0.30
FeOt	0.00 (0)	0.11	0.10	0.17	0.10	3.54 (44)	1.34 (58)	2.14 (45)	2.48 (38)	1.24 (14)	85.2 (5)	87.4	86.3	84.1	85.3
MnO	0.00 (1)	0.00	0.13	0.00	0.00	0.03 (5)	0.06 (6)	0.03 (4)	0.05 (6)	0.04 (3)	0.22 (27)	0.16	0.38	0.50	0.63
MgO	0.00 (0)	0.00	0.01	0.03	0.00	1.20 (1)	0.74 (19)	1.21 (31)	0.65 (48)	0.82 (10)	0.02 (5)	0.50	0,00	0,00	0.02
CaO	0.00 (0)	0.01	0.00	0.00	0.01	0.00 (0)	0.03 (2)	0.03 (4)	0.00 (0)	0.00 (1)	0.03 (1)	0.00	0.00	0.00	0.03
Na2O	0.37 (26)	0.21	1.38	0.62	0.15	0.44 (9)	0.41 (15)	0.33 (15)	0.39 (12)	0.59 (5)	0.01 (1)	0.00	0.00	0.00	0.00
K2O	16.1 (7)	16.5	14.5	15.6	16.2	10.2 (2)	10.5 (2)	10.2 (3)	9.86 (26)	9.12 (24)	0.03 (2)	0.05	0.03	0.01	0.00
Total	**99.6 (2)**	**99.2**	**99.6**	**98.9**	**99.3**	**94.8 (10)**	**94.3 (10)**	**94.1 (1)**	**95.5 (2)**	**91.5 (9)**	**95.2 (9)**	**98.3**	**96.9**	**94.9**	**95.4**

Results of electron microprobe analyses for muscovite are illustrated in Figure 3-16. The graphs show in particular the marked decrease in the FeO_t concentration of muscovite between the starting sample and the experimental charges.

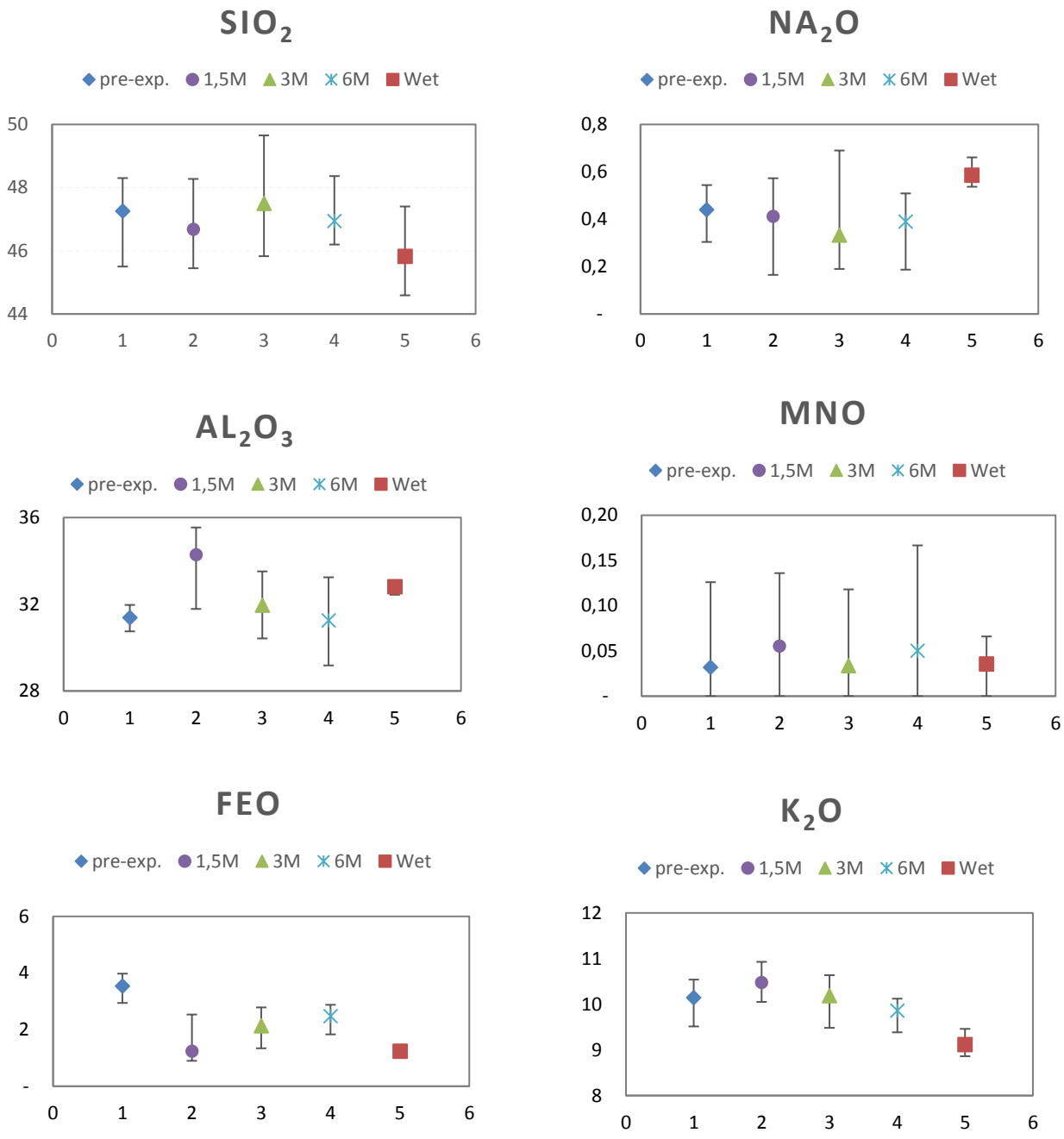

Figure 3-16 Variations in muscovite composition between the starting (pre-exp) and the experimental samples, as determined from EMP analyses

3.4 Discussion

Laboratory experiments from this study have provided direct observations on the reaction of sandstone minerals in presence of hydrogen. Experimental conditions were adjusted to those considered typical for underground hydrogen storage in Triassic geological formations in eastern France at about 1500 m depth (hydrogen pressure 100 bar, temperature 100°C, exceptionally 200°C). Some experiments lasted up to 6 months. It is worth emphasizing that most experiments were performed in the absence of water. Only one experiment has simulated the influence of hydrogen on sandstone in presence of water.

Overall, the experimental results indicate very limited modifications of sandstone minerals because of the presence of hydrogen. No significant textural changes were found in experimental products in comparison with the starting sandstones (Figure 3-13). The XRD data showed no major mineral transformation from the reference sample. However, limited but systematic mineralogical changes were noted on the XRD spectra for both muscovite and hematite. For muscovite, the most extensive modifications were found in the 3 and 6 month charges (Figure 3-14). No influence of the presence of water could be detected but the experiment performed in presence of water had a rather short duration (1.5 month). For hematite, the maximum changes were also found in the 6 month charges (Figure 3-15). Electron microprobe data revealed shifts in the composition of certain mineral phases as a result of interaction with hydrogen. Muscovite, with FeO_t concentrations decreasing in experimental samples, is clearly chemically modified. In comparison, neither hematite nor K-feldspar showed significant compositional variations (Table 3-5). Interestingly, the maximum chemical deviations in muscovite are associated with the "wet" samples, and not with the longest experimental charges. This suggests that the mineralogical transformations seen in the XRD data and those revealed by the mineral compositional data are decoupled.

Despite the limited mineralogical transformations identified in experimental products, the results undoubtly indicate that mineral reactions take place in sandstone during interaction with hydrogen. In this study, mechanisms of mineralogical transformations have not been clearly identified and this would probably require experiments of durations longer than 6 months (to promote the advancement of the reactions) as well as the implementation of analytical methods allowing mineral characterization at spatial resolutions < 1 µm. However, we emphasize that all traces of mineral reaction found in the experiments concern muscovite and hematite. In the same way, the new phases identified from the geochemical calculations (see Chapter 6) are Fe-bearing hydrous and anhydrous silicates and oxides. No changes have been found in experimental products for quartz and K-feldspar. Since quartz and K-feldspar are major mineral phases in sandstones, the sandstone microstructure is not expected to be significantly modified during interaction with hydrogen, even if minor phases such as muscovite or Fe oxide undergo mineral transformations. Therefore, the physical properties (porosity, permeability) that control the efficiency of sandstone as a reservoir will remain essentially unmodified. It is concluded that

quartz- and K-feldspar-rich lithologies such as sandstone are highly stable with respect to interaction with hydrogen.

Chapter 4

Experimental determination of relative permeability and capillary pressure in the hydrogen-water system

As for other types of large-scale underground storage (e.g., for carbon dioxide or natural gas), an important challenge for the development of a storage project is the good understanding of the fluid migration during and after the injection. Characterizing the parameters governing the fluid migration is therefore of critical importance. Rock intrinsic properties (porosity, absolute permeability) and the multi-phase flow properties (constitutive relationships between capillary pressure/relative permeability and the fluid saturation) are, in this view, essential flow characteristics to be characterized since they are usual inputs in classical large-scale flow simulations. However, multiphase flow properties are usually unknown as they are dependent on the fluid to be injected. Presently, capillary pressure and relative permeability data are lacking for the hydrogen-water system. The development of underground hydrogen storage emphasizes the need of a characterization effort regarding those properties. The experimental work presented in this study was performed toward this aim: capillary pressure and relative permeability characteristics of water-hydrogen flow in a Triassic sandstones sample have been measured for two different potential underground hydrogen storage conditions.

4.1 Experimental setup and apparatus

In this study, the laboratory core-flooding technique was performed to measure the intrinsic properties of the core sandstones (porosity and permeability) and the multiphase flow characteristics (relative permeability and capillary pressure) of the hydrogen-water system. The temperature, the pressure drop across the cell, the injection flow rates, the injection pressures and the volumes of each pump are all recorded by a data acquisition system. Figure 4-1 shows the experimental apparatus that was employed for the core flooding measurements. It consists of different components, detailed below:

- Metering pumps;
- Linkages and valves;
- Reaction cell;
- Core holder vessel;
- Furnace;
- Separator (for the saturation measurement).

Figure 4-1 General view of the core-flooding experimental set-up.

- **Metering pumps**

The fluid circulation system includes four metering pumps (PMHP 100-500, Top Industrie, pressures accurate to + 0.1 bar, volumes to + 0.5 cm^3) which were used to inject and collect water and gas through the core sample upstream and downstream the cell in the core-flooding experiments. Each metering pump has two options, *injection* and *suction*. In injection mode, fluids are injected into the system while, in suction mode, fluids are collected from the system. In addition, the pumps can work either at constant pressure or at constant flow rate during the experiments. At constant flow rate, fluids are injected (or

sucked up) into (from) the system at constant flow rate and, therefore, the pressure of injection (or suction) changes. Conversely, at constant pressure, the flow rate varies while pressure is kept constant. The volume of the pumps is 100.070 ml (33 mm in diameter and 117 mm in length), their maximum working pressure is 500 bar and the maximum working flow rate is 30.79 ml/min.

In this study, two metering pumps were positioned upstream the cell and two others downstream the cell. The two upstream pumps were used for fluid injection. The two downstream pumps (working in constant pressure mode) were positioned after the separator to collect water and gas separately at the outlet of the core, and measure the amount of gas and water (Figure 4-2). These two metering pumps also allowed the fluid pressure to be kept constant at the outlet of the cell. Furthermore, the fluid pressure (i.e., the pore pressure) was always kept ~30 bar below the confining pressure (imposed inside the vessel) to keep the core holder under negative pressure and avoid any fluid leakage around the core, through the core holder.

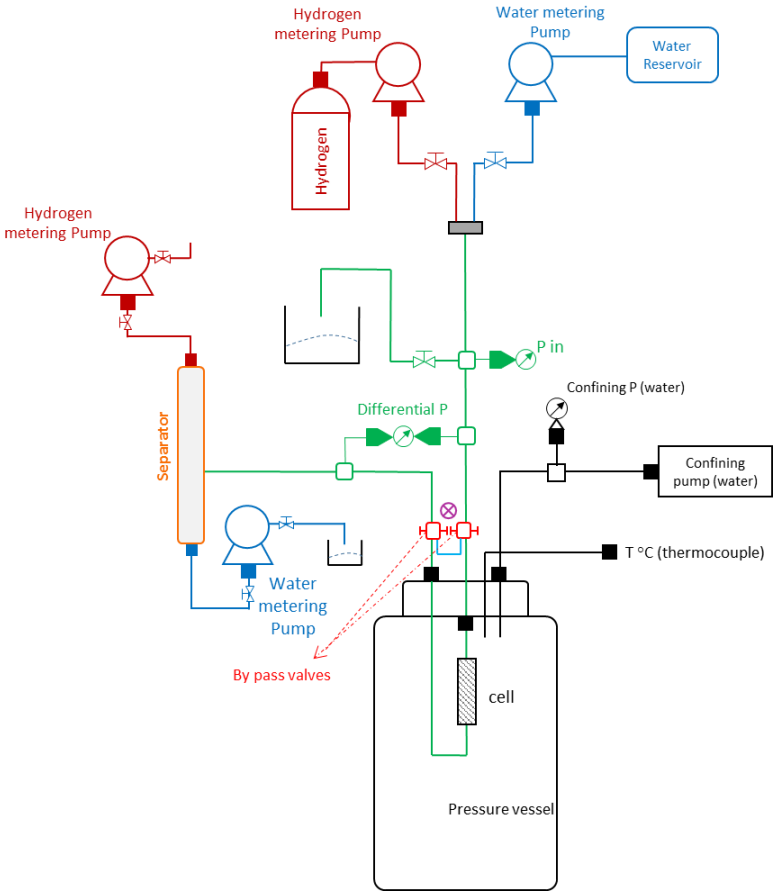

Figure 4-2 Schematic description of experiment setup for core-flooding measurements.

- **Linkages and valves**

Fluid is circulated from the pumps to the measuring cell through 1/16” steel capillary tubing. These linkages connect the metering pumps to the core, the core to the separator and the separator to the metering pumps to collect the separated fluids (water and gas). The pressure of the fluid system is measured before entering the core sample with the metering pumps while the differential pressure

between the inlet and the outlet of the core is measured with a differential pressure transducer (Honeywell Model HL-A-5 with a 0.50% scale accuracy).

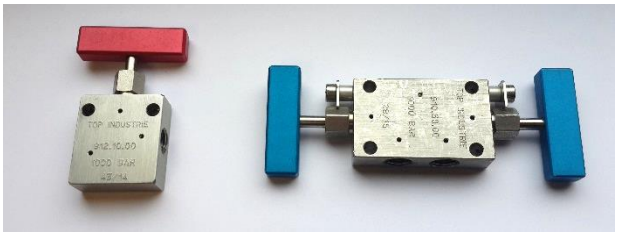

Figure 4-3 Close/open valve and by-pass valves were used in core flooding experiments

Two types of valves were used in the system, close/open valve and by-pass valves (Figure 4-3). Two by-pass valves are inserted in the fluid circulation system respectively before and after the cell, in order to measure the saturation of water in the cell after each experimental step, as detailed below.

- **Reaction cell**

One core sample from the Adamswiller quarry (61 mm long, 15 mm diameter) was used for all the core-flooding experiments. The two faces of the core were machined flat to ensure good contact with the fluids. The core sample was wrapped in the Teflon – PTFE tube as the impermeable sleeve. The confining pressure in the core holder vessel is transmitted to the core sample through the sleeve (Figure 4-4).

Teflon-PTFE is a high molecular weight polymer, one of the most versatile plastic materials known, useful for a large range of applications and thermally very stable (Figure 4-4). There are no appreciable decomposition at 260°C, so that PTFE, at this temperature, still possesses most of its properties. PTFE is highly resistant to chemical agents and solvents. Two highly permeable ceramic plugs were fitted at both ends of the core to ensure uniformity of the fluid circulations at the inlet as well as at the outlet.

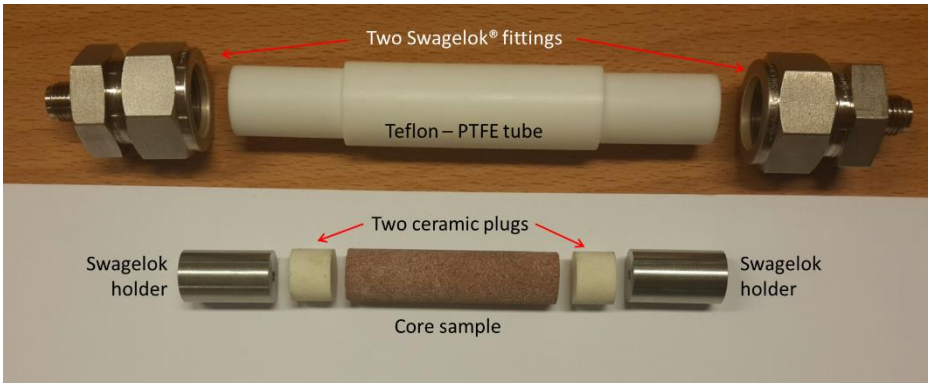

Figure 4-4 View of the reaction cell: core sample, Teflon-PTFE tube sleeve and Swagelok® fittings

In addition, two Swagelok® fittings were used to seal the sleeve tube and reaction cell to the fluid circulation system, both at the inlet and at the outlet. The rock core sample was loaded in the sleeve core holder together with the ceramic plugs.

- **Pressure vessel**

A cylindrical 316SS pressure vessel (Autoclave Engineers) was used to confine the reaction cell under desired confining pressure and temperature conditions (Figure 4-5). The vessel has a volume of 1 L and an inner diameter of 76 mm. The maximum operating pressure and temperature are 500 bar and 450°C. The seal and end plug design allow for hand tight operation of the vessel, enabling easy assembly and disassembly for cleaning and inspection. This pressure vessel can be used for various purposes including gas and liquid permeability measurements, fluid-rock interactions and other core flooding experiments.

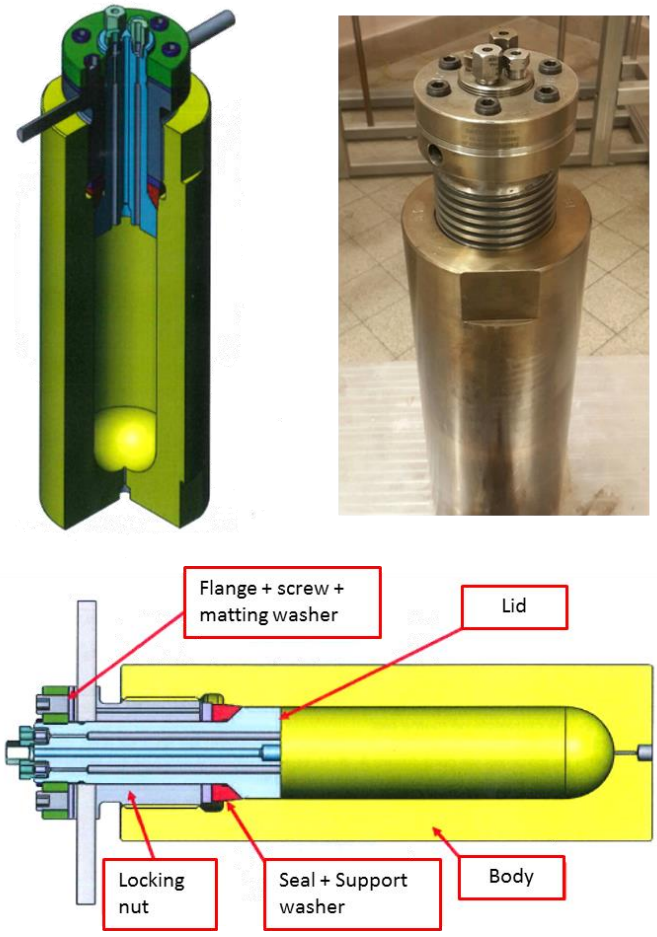

Figure 4-5 Description of the pressure vessel.

Inlet and outlet capillaries, connected to the head of the vessel, allow fluids and gases to be injected through the core sample (Figure 4-6). All capillary volumes inside the vessel (internal volumes) are kept to a minimum so that accurate flow data can be determined. After the sleeve and reaction cell are connected to the capillaries (Figure 4-6), the vessel is closed and brought to the desired confining pressure (to simulate the lithostatic pressure in the reservoir) and to the desired temperature (in case temperature must be different from the room temperature). The confining pressure is monitored by injection of water with an hydraulic (Maximator) pump. During the measurements, the confining/external pressure applied on the cell is kept constant to approximately 130 bar. This allows the external confining pressure to be always maintained at a minimum of ~30 bar above the fluid pressure inside the cell to avoid any fluid flow between the core and the Teflon tube. For the non-room

temperature measurements, the vessel is inserted in a cylindrical furnace monitored with an electronic regulator. Temperature inside the vessel is measured permanently by an internal thermocouple located immediately above the cell.

Figure 4-6 Connections between the reaction cell and the capillary tubings and between the capillary tubings and the vessel head.

- **Furnace**

A vertical movable furnace was used to heat up the system for experiments performed at a temperature different from the room temperature. The pressure vessel was placed in a fixed position and the furnace moved around the vessel. The maximum temperature of the furnace was 300°C.

- **Separator**

For the relative permeability measurements, two phases (water and gas) had to be injected into the core sample. These two fluids were injected from two metering pumps (one for gas and another for water). They were mixed in the system and injected together into the core sample. However, downstream the core sample, these fluids had to be separated and collected by the downstream metering pumps. To achieve this goal, a separator was inserted in the fluid circulation system between the cell and the metering pumps so that water and hydrogen would be collected separately, at the bottom and at the top, respectively.

The separator used in this study is a cylindrical tube, 2 m high and 8 mm in inner diameter working vertically. The mixture is injected at the middle of the tube. Because of gravity, water drops in the lower part of the tube while gas rises up, thus both fluids are separated. The two downstream metering pump at both ends of the separator collect the water and gas.

4.2 Experimental conditions and procedures

The capillary pressure (P_c) and relative permeability (k_r) experiments were performed under two different types of conditions simulating natural hydrogen storage. The first (20 °C, 55 bar) simulates “shallow” gas storage and the second (45 °C, 100 bar) a deeper situation. Conditions of the four definitive experiments and the associated hydrogen and water properties are listed in Table 4-1. Before each experiment, the absolute water permeability was measured to test the equipment and check the

physical integrity of the core, since the same sample was used in the four experiments. No major change of the absolute permeability was noticed during the course of the experiments (Table 4-1).

Table 4-1 Experimental conditions and core fluid parameters for both capillary pressure experiments (indicated by Pc) and relative permeability experiments (indicated by kr)

Experiment	Type	Non-wetting Fluid	Temp. (°C)	Pressure (bar)	Confining pressure (bar)	Absolute water permeability (mD)	$\mu_{hydrogen}$ (µPa s)	$\rho_{hydrogen}$ (Kg/m^3)	μ_{water} (µPa s)	ρ_{water} (Kg/m^3)
1	P_c	Hydrogen	20	55	130	46	8.94	5.6	999	1000.5
2	P_c	Hydrogen	45	100	130	48	9.54	7.2	597	994.5
3	k_r	Hydrogen	20	55	130	45	8.94	5.6	999	1000.5
4	k_r	Hydrogen	45	100	130	47	9.54	7.2	597	994.5

µ=viscosity

ρ=density

The core-flooding/characterization techniques used in this study have been derived from the extensive literature existing for the CO_2-water system built on the experience gained in the oil and gas fields (see for instance a review of the existing studies in *Manceau et al.*, 2015 or in *Reynolds and Krevor*, 2015). Intrinsic permeabilities of sandstones samples were measured by using Darcy's law equation. Capillary pressure was measured following a modified semi-dynamic technique initially proposed by Ramakrishnan and *Capiello (1991)* for the oil-water system, while relative permeability was measured following the classical steady-state technique.

Each experiment started with saturating the core by water. Then, fluids (either hydrogen alone or water and hydrogen together depending on the type of experiment) were injected at different flow rates and the experiment performed. After completion of the experiment, the saturation of the core sample was measured with mass balance (explained in 5.2.2).

4.2.1 Intrinsic permeability measurements

Intrinsic or absolute permeability specifies the ability of a fluid to penetrate through a rock. Intrinsic permeability is defined by Darcy's law (Equation (4-1)) in single-phase flow in porous media which is written after Equation (2-4) with one fluid (water or gas), which means $k_{r,i} = 1$ (gravity is not considered):

$$-\frac{\Delta P}{L} = \frac{\mu}{K}\frac{Q}{A} \qquad (4\text{-}1)$$

where Q is the flow rate of the fluid across a cylindrical core, A is the cross-section of the core, K is the intrinsic permeability of the core, μ is the viscosity of the fluid, L is the length of the core and ΔP is the pressure difference across the rock core.

In this study, intrinsic permeability measurements were performed by using single-phase flow of water, hydrogen and of argon gas. Fluid (water or gas) was injected in through the core at several flow rates

and after stability, the pressure drop at both ends of the core were recorded. The slope of differential pressure vs. flow rate gives the intrinsic or absolute permeability, taking into account the viscosity of fluid and the geometry of the core.

To measure the intrinsic permeability, just two metering pumps were used, one to inject water or gas into the core sample and the other to collect water or gas (Figure 4-7). In this measurement, the separator is not needed. The first metering pump was set in constant flow rate mode (in this case, the pressure of injection, which is unknown, becomes constant after a while). The second metering pump was set in constant pressure mode (defining the backpressure, ideally in the range of typical reservoir fluid pressures).

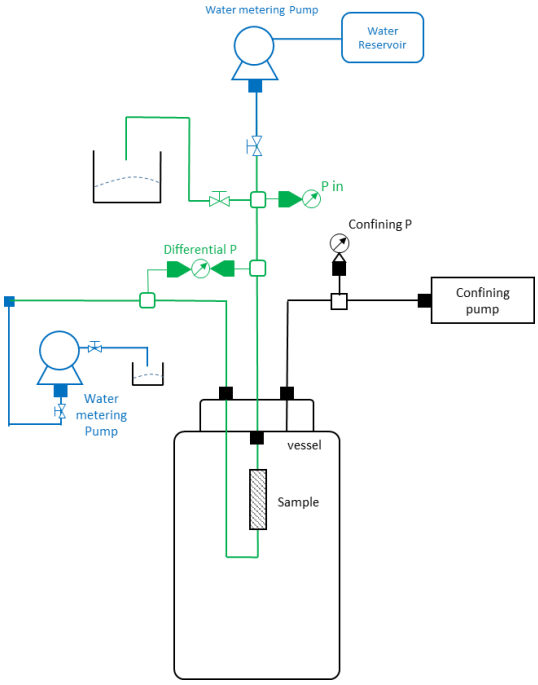

Figure 4-7 Experimental setup for absolute permeability measurements

In this study, absolute permeability of the rock samples were measured with water, argon and hydrogen. These measurements were performed in the range of reservoir temperatures and pressures. For the water absolute permeability, the core should be saturated with water completely before the measurements and, for the gas intrinsic permeability measurements, the core should be dried completely and saturated with the gas.

4.2.2 Protocol followed for saturation measurements

Contrary to the absolute permeability measurement, in the relative permeability and capillary pressure measurements, two-phase flow (gas and water) are injected together to the core sample. Therefore, the volume of water or gas in the pore volume of the core sample is not constant (100%) and it can vary for each total bulk flow rate. Hence, measuring the volume of the water in the core pore volume (*water saturation*) is critical and it needs to be determined for each flow rate. In this study, the water saturation measurements have been performed by mass balance. This was achieved by inserting, in the fluid

circulation system working in two-phase flow mode, two by-pass valves (Figure 4-3). In detail, the water saturation was measured as follows.

Each experiment started with an evacuation step. After saturating the core with water and setting the pressure inside the fluid circulation system at the desired value, the water in the system (except the core) was evacuated by closing both ends of the core with the bypass loop. Then, the water saturation was determined as follows. A known volume of water (v_i) was first injected under the desired experimental temperature and fluid pressure conditions. Second, fluids (either hydrogen alone or water and hydrogen together depending on the type of experiment, relative permeability or capillary pressure) were injected at different flow rates and the experiment performed (see below). Third, after completion of the experiment, the volume of water inside the system (v_f), except in the core, was measured with the bypass loop. Knowing v_i and v_f, the volume of water in the core (v_s) can be determined . Below, the water saturation is expressed as $S_w\% = v_s/v_p \times 100$, where v_p is the pore volume. This mass balance method involves a dead volume of 0.1 mL maximum (corresponding to the tubing between the by-pass valves and the core which contains a mixture of hydrogen and water). Therefore, since v_p is 2.05 mL in this study (and so the maximum v_s is 2.05 mL), the dead volume causes a maximum uncertainty on water saturation of $\leq \pm 2.5\%$.

Diagrams below summarize the different operations for the saturation measurements. This sequence needed to be performed for each step of the experiments.

---

1. Saturate the core sample with water at the pressure of experiment (Table 4-1);

Blue color: water

Red color: Gas

Green color: Mixture of water and gas

--➤ : The direction of flow

⊗ : Closed

: Valve

: Metering-pump

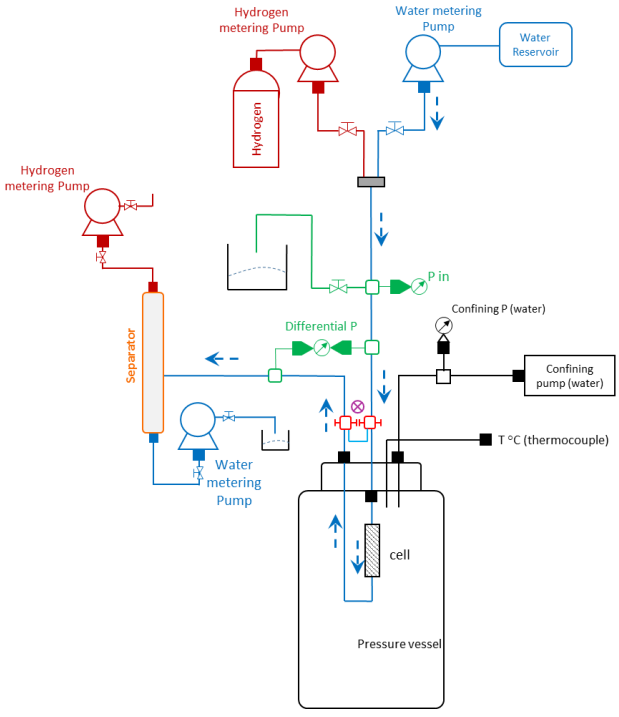

---

2. Close the valves at both ends of the core and open the by-pass valves. Remove all the water from the pressure capillaries and separator by injecting the gas. The volume of water that is removed is not important but it is essential that there is no water left in the system. Before opening the by-pass valves, a known amount of water (v_i) should be injected into the fluid circulation system;

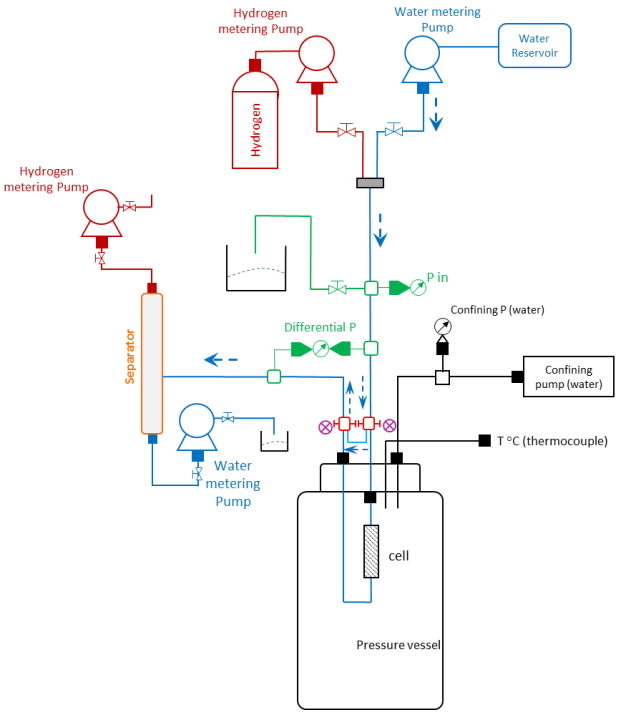

3. Close the by-pass valves and open the valves of both ends of the core and the system is ready to any core-flooding experiment. After each steps of experiment, the core water saturation should be measured. Therefore, the valves in the both ends of the core should be closed and by-pass valves should be opened. All the water in the system is removed (like step 2) and the amount of removed water is measured (v_f). By knowing this volume and the volume that was injected (v_i) before starting the experiment, the core saturation is calculated.

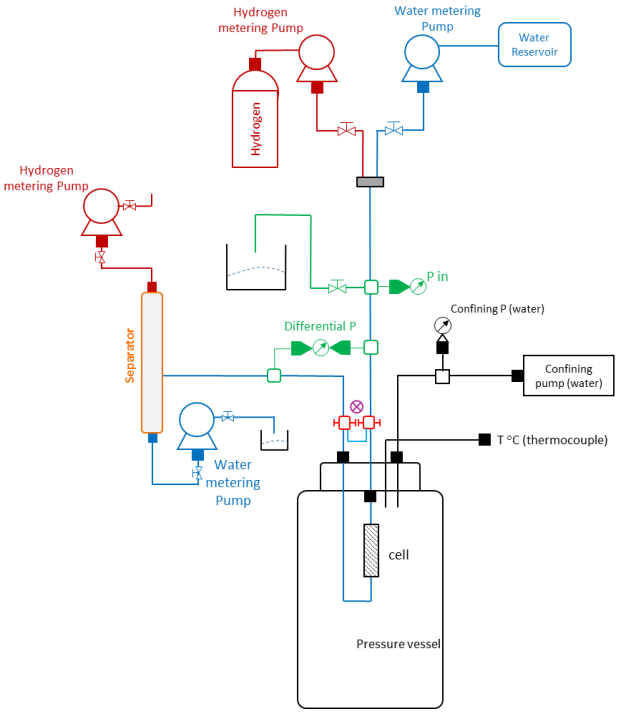

4.2.3 Capillary pressure measurement

A basic parameter of multiphase flow in porous media is the capillary pressure (Equation (2-5)). Capillary pressure is expressed as the pressure differential across an interface between two fluids, i.e.,

as the pressure differential between the non-wetting and the wetting phase. It is dependent on the interfacial tension, pore size and wetting angle as expressed by Equation (4-2):

$$P_c = P_n - P_w = \frac{2\sigma_{nw}cos\theta}{r} \qquad (4\text{-}2)$$

where P_c is the capillary pressure, P_w and P_n are the pressures of the wetting and non-wetting phases, respectively, and θ is the contact angle. The capillary pressure is a measure of the tendency of a porous medium to attract the wetting phase and repel the non-wetting phase (*Bear*, 1972). Capillary pressure is the most fundamental property for multiphase flow, just as porosity and permeability are for single-phase flow.

The relationship between the capillary pressure and fluid saturation is referred to as the capillary pressure-saturation function or capillary pressure curve. When a non-wetting phase (gas) invades a water saturated porous medium, the water saturation decreases and the capillary pressure increases. This process is termed as "drainage", as water is drained out of the porous medium.

A first approach to retrieve capillary pressure data for a gas-water system in a given porous medium is through mercury intrusion capillary pressure (*MICP*) analysis. With this method, the capillary pressure for the mercury/air system is measured and, using the Young-Laplace equation, the data can be converted to any gas-water system by knowing the interfacial tension and contact angle for the two respective systems. The validity of this method is questionable, especially regarding the assumptions used for the conversion and the different conditions of measurements (*Pini et al.,* 2012). Yet, this method was employed in this study to measure the capillary pressure curve for the hydrogen-water system.

One direct method to measure capillary pressure directly on reservoir fluids is the *semi permeable disk method*. It relies on a specific set-up that allows the flow of only the wetting phase (water) and prevents the non-wetting phase flow (gas) to be displaced. This is done through the addition at the end of the core of a porous disk or specific membrane with a very high capillary entry pressure (see *Brown*, 1951 or *Christoffersen*, 1995). In such a system, the non-wetting phase is injected at a given pressure; at steady state (static capillary equilibrium), the pressure difference between inlet and outlet corresponds to the capillary pressure at the saturation of the core. The implementation of this method is presented in *Pentland et al.* (2011) for the CO_2-water system. These measurements are however time-consuming since the permeability of the outlet-disk is low and steady state takes time to be attained.

Another direct measurement method has been recently proposed by *Pini et al.* (2012) and *Pini and Benson* (2013). The same protocol as above is followed: the non-wetting fluid (gas in our experiments) is injected through a core initially saturated with the wetting phase (water in our experiments) to displace the wetting phase. However, in this case, no porous disk is needed. The gas flow rate is progressively increased and for each gas flow rate, when steady state is established, the water pressure is the same wherever in the core ($P_{wi} = P_{wo} = P_w$), where subscript $\underline{i}$ refers to the inlet and $\underline{o}$ to the outlet). The gas pressure is highest at the inlet and decreases towards the outlet (Figure 4-8). The gas pressure (P_{gas}) is

known at the inlet of the core (P_{gi}). According to equation (4-2), the capillary pressure is the difference between the gas pressure and the water pressure ($P_c = P_g - P_w$). The capillary pressure goes to zero outside the core, where there are no capillary forces ($P_{go} = P_{wo}$). This is known as the capillary end effect which is discussed in section 5.4.3. The differential pressure measured in the experiment is $\Delta P = P_i - P_o$ where P_i is the pressure of the gas at inlet ($= P_{gi}$) and P_o is the pressure of the gas at outlet which is equal to the pressure of water ($P_o = P_{go} = P_{wo}$). Therefore, $\Delta P = P_{gi} - P_{wo}$ or $\Delta P = P_{gi} - P_{wi}$, which is the capillary pressure at the inlet ($P_{ci} = P_{gi} - P_{wi}$). Thus, measurement of the differential pressure between the inlet and the outlet of the core gives the capillary pressure at the core inlet (i.e., which corresponds to the water saturation at the core inlet). This technique has been used by *Manceau et al.*, (2015), *Al-Menhali and Krevor* (2015) to measure drainage capillary pressure curves for the CO_2-water system.

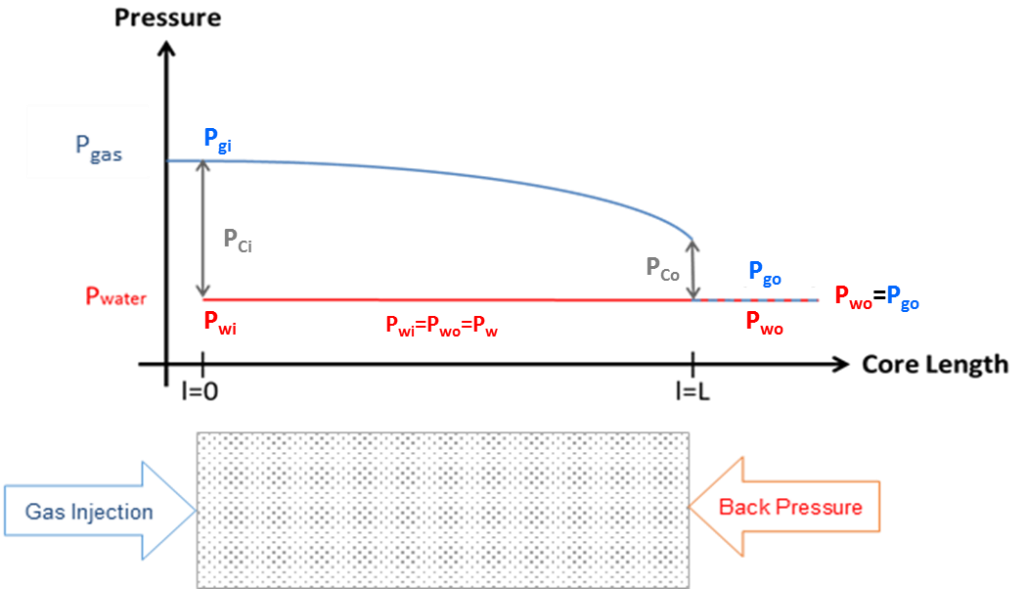

Figure 4-8 Principle of the capillary pressure measurements. Capillary pressure (P_c) is the difference of pressure between the water and the gas pressure measured experimentally both at inlet and outlet. See text.

In this study, a combination of two methods was implemented to obtain capillary pressures for the hydrogen-water system. *First*, a modified semi-dynamic capillary pressure measurement technique was set up, as described below. *Second*, the semi-dynamic capillary pressure data were combined with MICP measurements. This was done by converting the MICP capillary pressures for the mercury-air system to capillary pressures for the hydrogen-water system, using Young-Laplace scaling (Equation (4-13)). To achieve this goal, the interfacial tension and contact angle for the hydrogen-water system were adjusted from the semi-dynamic capillary pressure data. This combined approach enabled capillary pressures to be determined for a wide range of water saturation values.

- **Modified semi-dynamic capillary pressure measurements**

The experimental protocol described in this section allows for measuring capillary pressure drainage curves during a core-flooding experiment. Different variants of this method have been proposed by *Ramakrishnan* and *Capiello* (1991), *Lenormand et al.*, (1995) and *Pini et al.*, (2012). Once water saturation is achieved in the core (see above), the capillary pressure experiments involve injection of hydrogen gas. Constant hydrogen flow rates were successively imposed, from 2 to 10 mL/min (Figure 4-9).

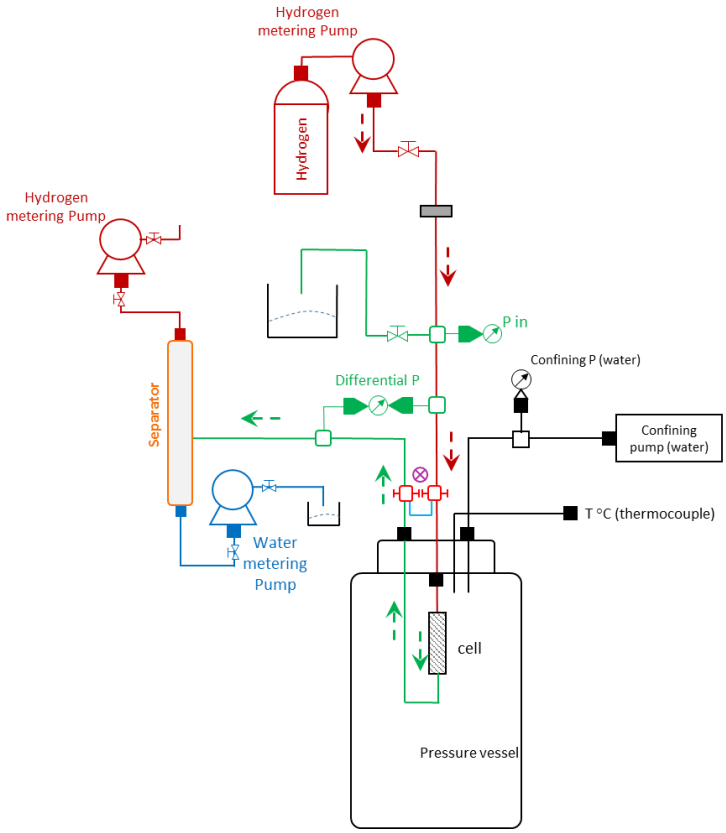

Figure 4-9 Schematic description of capillary pressure core-flooding measurements. Only gas (hydrogen) is injected into the water-saturated core at different flow rates. For each flow rate, when steady state is established, the differential pressure is measured and the water saturation is determined as detailed above.

For each flow rate, after steady state is reached, the differential pressure across the core was recorded and the water saturation measured with the procedure detailed above. For a given flow rate, the water pressure inside the core is constant and equal to the pressure at the outlet, and the inlet pressure is the pressure of the gas injection. Therefore, the differential pressure between the core inlet and outlet corresponds to the differential pressure of the gas and water phases (which is the capillary pressure) for the water saturation conditions of the inlet.

With the experimental set-up used for this study, the water saturation at the inlet cannot be measured directly, since only an average water saturation corresponding to the entire length of the core is measurable with our procedure. *Ramakrishnan and Cappiello* (1991) proposed a method for evaluating the water saturation at the inlet of the core as a function of the capillary pressure. However, this method

requires the knowledge of the gas injection flow rate and of the associated differential pressure between the core inlet and outlet. The computation procedure is detailed below.

As already explained, during capillary pressure measurement, just gas is injected to the water saturated core sample. Therefore, Darcy's law (Equation (2-4)) under steady state conditions can be written:

$$-\frac{dP_c}{dx} = \frac{\mu_g}{Kk_{r,g}(S)}\frac{Q_g}{A} \tag{4-3}$$

where x is the variable position along the core, $\frac{dP_c}{dx}$ is the variation of the capillary pressure along the core, $k_{r,g}$ the relative permeability of the gas phase which is a function of the water saturation, S, μ_g is the viscosity of the gas, Q_g the flow rate of the gas phase, K the absolute permeability and A the cross-sectional area of the core. Since saturation is varying along the core, the capillary pressure and relative permeability to gas are changing as well. However, since the differential pressure through the core is very small compared to the fluid pressure, the volumetric flow rate and the viscosity can be assumed constant along the core. Therefore, integrating Equation (4-3) along the length of the core gives:

$$Q_g L = -\frac{AK}{\mu_g}\int_{P_{c,x=0}}^{P_{c,x=L}} k_{r,g}\left(P_{c,x}\right)dP_{c,x}, \tag{4-4}$$

where $P_{c,x=0}$ corresponds to the capillary pressure measured during the measurements and $P_{c,x=L}$ to the capillary pressure at the outlet of the core, considered as the entry capillary pressure of the rock. By noting $\Delta P_{c,x} = P_{c,x} - P_{c,x=L}$ (the capillary pressure difference between one location along the core and the core outlet), Equation (4-4) becomes:

$$Q_g L = -\frac{AK}{\mu_g}\int_{\Delta P_{c,x=0}}^{0} k_{r,g}\left(\Delta P_{c,x}\right)d\Delta P_{c,x} \tag{4-5}$$

Assuming a homogeneous relative permeability law along the core, differentiation of equation (4-5) relatively to $\Delta P_{c,x=0}$ gives:

$$\frac{dQ}{d\Delta P_{c,x=0}} = \frac{AK}{\mu_g L}\cdot k_{r,g}(\Delta P_{c,x=0}) \tag{4-6}$$

This equation means that the relative permeability of the gas can be obtained if the relationship between the flow (or injection) rate and the differential pressure measured during the capillary pressure experiments is known.

In parallel, the average saturation in the core can be computed as:

$$\bar{S_w} = \frac{1}{L}\int_{x=0}^{x=L} S_w\, dx \tag{4-7}$$

Combined with equation (4-3), this leads to:

$$Q\bar{S}_w = \frac{AK}{L\mu_g}\int_{\Delta P_{c,x=0}}^{0} k_{r,g}\left(\Delta P_{c,x}\right)S_w(\Delta P_{c,x})d\Delta P_{c,x}. \quad (4\text{-}8)$$

The differentiation of this equation relatively to $\Delta P_{c,x=0}$ gives:

$$\frac{d(Q\bar{S}_w)}{d\Delta P_{c,x=0}} = \frac{AK}{\mu_g L}\cdot k_{r,g}\left(\Delta P_{c,x=0}\right)\cdot S_w(\Delta P_{c,x=0}) \quad (4\text{-}9)$$

Equations (4-9) and (4-6) can be changed into:

$$S_w\left(\Delta P_{c,x=0}\right) = \frac{\mu_g L}{Akk_{r,g}\left(\Delta P_{c,x=0}\right)}\cdot\frac{d(Q\bar{S}_w)}{d\Delta P_{c,x=0}} \;\; with \;\; \frac{AK}{\mu_g L}\cdot k_{r,g}\left(\Delta P_{c,x=0}\right) = \frac{dQ}{d\Delta P_{c,x=0}} \quad (4\text{-}10)$$

In other words (with v_{inj} being the Darcy velocity, equal to Q/A):

$$S_w(\Delta P_{c,x=0}) = \frac{L}{\Lambda\left(\Delta P_{c,x=0}\right)}\cdot\frac{d(v_{inj}\bar{S}_w)}{d\Delta P_{c,x=0}} \quad (4\text{-}11)$$

where

$$\Lambda\left(\Delta P_{c,x=0}\right) = \frac{k}{\mu_g}\cdot k_{r,g}\left(\Delta P_{c,x=0}\right) = \frac{dv_{inj}}{d\Delta P_{c,x=0}}\cdot L \quad (4\text{-}12)$$

and $S_w(\Delta P_{c,x=0})$ is the water saturation at the inlet. Therefore, with information on the injection rate, the differential pressure between the inlet and outlet of the core, and the average saturation in the core during the measurements, it is possible to retrieve the water saturation at the inlet.

- **Mercury injection capillary pressure (MICP)**

Using the same sample as for the semi-dynamic capillary pressure measurements, a 1 cm^3 rock plug was prepared for Mercury Intrusion Porosimetry (MIP) and MICP measurements. Both were performed using a Micromeritics Autopore IV 9500 covering the pressure range from vacuum to 2130 bar. The contact angle and the surface tension of mercury were taken from the literature at 141.3° and 0.48 N/m, respectively. Using the Young-Laplace scaling, the MICP Hg/air data can be converted to any fluid-pair system using the equation:

$$P_c = P_{c,Hg/Air}\frac{\tau\cos\theta}{\tau_{Hg/Air}\cos\theta_{Hg/Air}} \quad (4\text{-}13)$$

where P_c is the capillary pressure, τ is the interfacial tension and θ is the contact angle for the fluid-pair system of interest. This conversion requires the interfacial tension and contact angle values for both systems (i.e., for hydrogen-water and mercury-air) at experimental conditions. However, no such data exist for the hydrogen-water system. Therefore, we have fitted the capillary pressure data obtained with the core-flooding technique to derive values of the interfacial tension and contact angle in Equation (4-13) for hydrogen-water. Then, by using Equation (4-13), the capillary pressure data can be extended to almost the entire water saturation range.

4.2.4 Relative permeability measurement

Relative permeability describes how each phase is displaced in the porous space when other phases are present. It is a key property of multiphase flow in porous media. Relative permeability is one of the most important properties influencing gas transport at subsurface conditions.

Considering two-phase flow through porous media, the concept of relative permeability (permeability relatively to one phase), which comes from the generalization of the single-phase flow Darcy's law (*Bear* 1972), can be written from Equation (2-4)):

$$-\frac{\Delta P}{L} = \frac{\mu_i}{K k_{r,i}(S_w)} \frac{Q_i}{A}, \qquad i = hydrogen\ or\ water \tag{4-14}$$

where $\frac{\Delta P}{L}$ is the pressure drop per unit length, $k_{r,i}$ the relative permeability (a function of the water saturation inside the core, S_w), μ the phase viscosity, Q the phase flow rate, K the absolute permeability and A the cross-sectional area of the core.

There are several methods for measuring the relative permeability experimentally. Two basic approaches are steady state and unsteady state (*Muller et al.,* 2011). For the steady-state method, the two (non-wetting and wetting) fluids are injected simultaneously into the core at different fractional flows (f_{H2}). Once steady state conditions are established, both the water saturation and the differential pressure between the core inlet and outlet are measured for each fractional flow. This method allows relative permeabilities to be directly calculated with Darcy's law (Equation (4-14) although the attainment of a steady state situation usually requires a long time. For the unsteady-state method, only one phase (usually the non-wetting) is injected at a constant flow rate to displace the other phase (usually the wetting) already present in the core. The pressure drop and flow rates are then measured simultaneously (*Muller et al.,* 2011). As stability (in flow parameters and pressure) is not required, the measurements can be performed rapidly, but the derivation of the relative permeability is more challenging, generally requiring numerical modeling (*Toth et al.,* 2002).

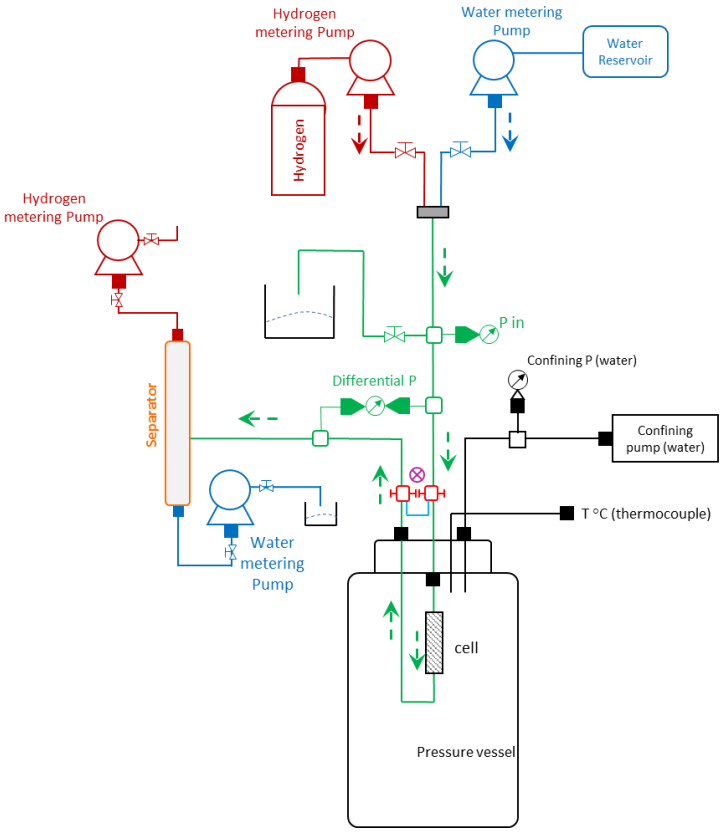

Figure 4-10 Schematic description of relative permeability core-flooding measurements. The two fluids (hydrogen and water) are both injected into the water-saturated core. A constant total volumetric flow rate ($Q_t = Q_{H_2} + Q_w$) is imposed and several gas fractional flows ($f_{H_2} = Q_{H_2}/(Q_{H_2} + Q_w)$) are studied. For each fractional flow, when steady state is established, the pressure drop between the core inlet and outlet is recorded and the core water saturation is measured as discussed above.

For the experimental work presented in this study, the steady state approach has been followed. (Figure 4-10) Water and hydrogen were both injected into the core under a constant total volumetric flow rate (Q_t = 1mL/min) and for several fractional flow parameters (Q_{H_2}= 0.05 to 0.99 mL/min; Q_w = 0.95 to 0.01 mL/min; $f_{H_2} = Q_{H_2}/(Q_{H_2} + Q_w)$, Table 2). For each fractional flow, the pressure drop between the core inlet and outlet was recorded once steady state was established. This usually needed a time corresponding to the injection of a volume of ~8 times the pore volume of the core. The water saturation was measured with the same protocol as detailed in section 5.2.2. Finally, knowing the hydrogen and water flow rates for each fractional flow, the relative permeability of hydrogen and water were computed using Equation (4-14). Relative permeability results with Equation (4-14) are known to be affected by capillary end effects (discussed below) and gravitational influence since the core is in vertical position. However, if Darcy's law (Equation (2-4)) is modified to take into account gravity ($Q_i = Kk_{r,i}(S_i)\ \frac{A}{\mu_i}\left(\frac{\Delta P}{L} - \rho_i g\right)$), the effects of gravity on relative permeabilities are < 0.003% for hydrogen and < 0.7% for water and, therefore, can be neglected.

4.3 Experimental results

4.3.1 Absolute permeability

Absolute permeability of water or gas (e.g. either hydrogen or argon) were performed using pressure differences measured across the core for a series of seven flow rates (Figure 4-11). At each flow rate, water or gas was injected until a stable pressure drop across the core was registered.

Table 4-2 Measured differential pressures across the core at different flow rates and for different fluids

Experiment	Q (mL/min)	ΔP (kPa)
Water absolute permeability measurement	4	4,1
	3,5	3,8
	3	3,5
	2,5	3,1
	2	2,7
	1	1,9
Hydrogen absolute permeability measurement	28	0,97
	22	0,9
	16	0,84
	10	0,75
	5	0,71
	1	0,65
Argon absolute permeability measurement	28	1,7
	22	1,5
	16	1,35
	10	1,2
	5	1,05
	1	0,91

A linear regression fit to this series of data provides an average ratio of pressure drops to flow rates used to calculate absolute permeability from Darcy's law (Equation (4-1)). The results of the core-flooding experiments for absolute permeability measurements are presented in Table 4-2.

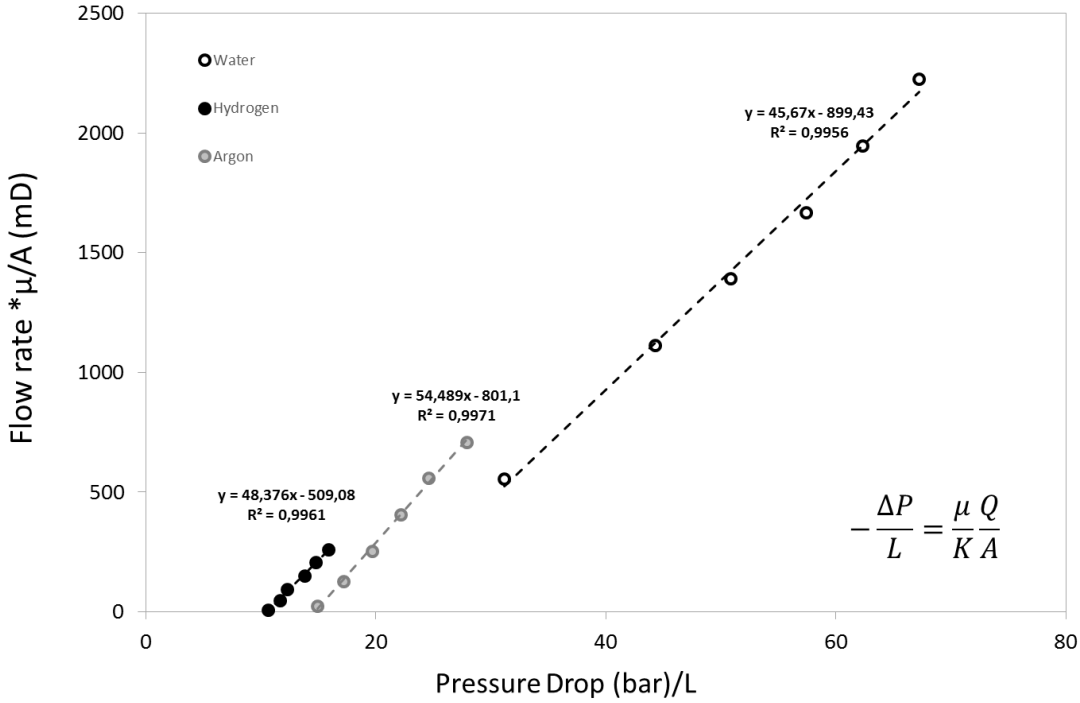

Figure 4-11 Results of absolute permeability measurements performed with water, hydrogen or argon.

4.3.2 Capillary pressure measurement

Representative responses of the experimental system following injection of hydrogen are illustrated in Figure 4-12. Variations in differential pressure are shown as a function of time in the two experiments (Table 2) and for a constant hydrogen flow rate (2 mL/min).

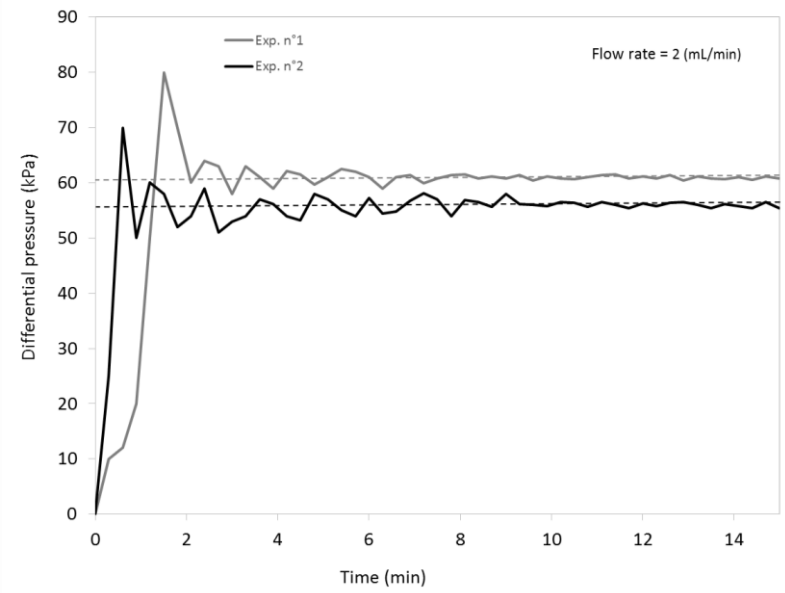

Figure 4-12 Variation of differential pressure with time for the two experimental conditions investigated (exp. n°1 and exp. n°2, see Table 5-3 for conditions) under constant hydrogen flow rate (2 mL/min).

Changing the flow rate does not change the general aspect of the curves. Both comprise a transition region, marked by an initial increase in differential pressure and large fluctuations. A steady state region, corresponding to stable ΔP values, is attained after ~ 8 min (Table 4-3).

Table 4-3 Measured and corrected capillary pressures of hydrogen and pure water

Experiment	Q_{H2} (mL/min)	ΔP (kPa)	$S_{w\ (average)}$ %	$S_{w\ (at\ inlet)}$ %
Experiment 1 Hydrogen-water 20°C, 55 bar	1.25	61	31	33
	1.5	67	28	17
	1.75	73	22	14
	2	77	20	13
	3	82	19	13
	5	84	19	12
	7	104	17	12
	9	110	17	11
Experiment 2 Hydrogen-water 45°C, 100 bar	1.5	56	41	22
	1.75	59	32	19
	2	67	27	15
	3	71	23	14
	5	77	21	13
	7	80	20	13
	9	81	19	13

For each flow rate, the corresponding water saturation values, both measured (average) and corrected (at the inlet, described in section 5.2.3) are given in Table 4-3 and plotted in Figure 4-13 .

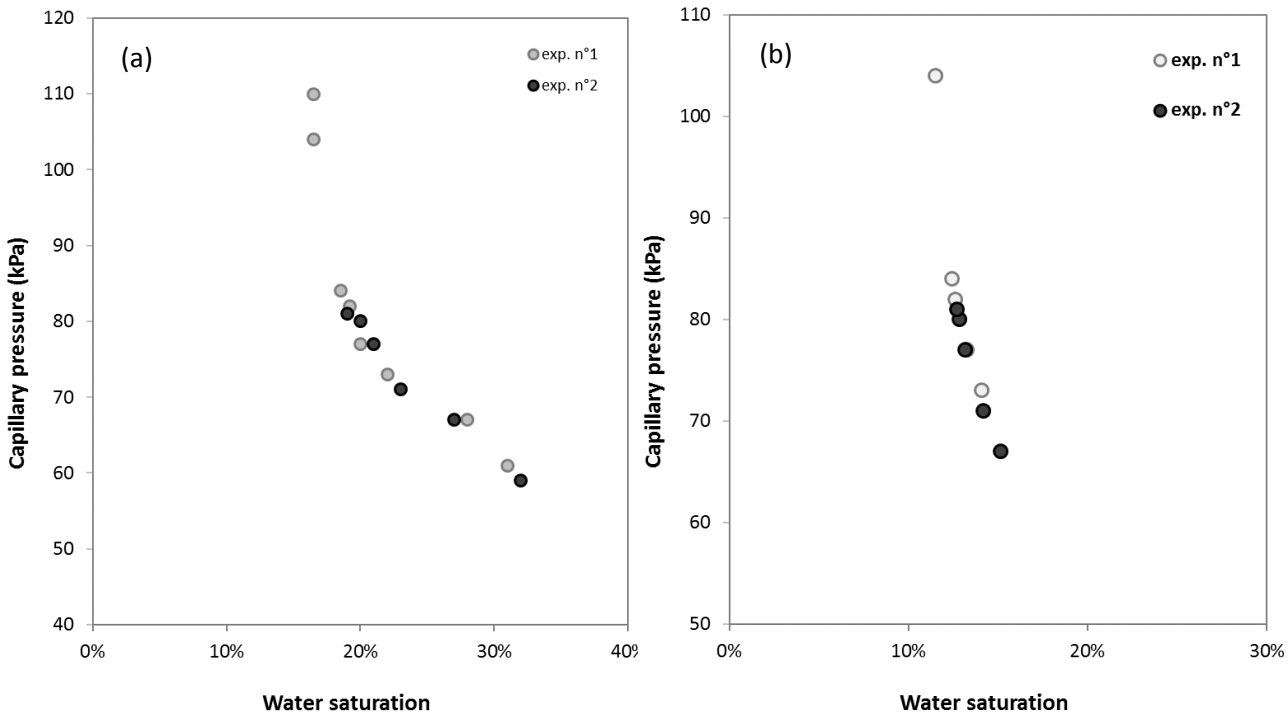

Figure 4-13 Capillary pressure vs (a) average water saturation and (b) corrected (inlet) water saturation.

However, in order to use Equation (4-11) , precise knowledge of the relationship between Darcy velocity (v_{inj}), average saturation ($\bar{S}_w$) and measured capillary pressure ($\Delta P_{c,x=0}$) is required. This relationship was obtained by fitting second-order polynomials of $v_{inj}\bar{S}_w$ as a function of $\Delta P_{c,x=0}$ for experiments n°1 and n°2 respectively (Table 4-3; Figure 4-14). This regression was performed using flow rates comprised between 2 mL/min to 7 mL/min. These polynomials were used to calculate the water saturation at the inlet for each experiment.

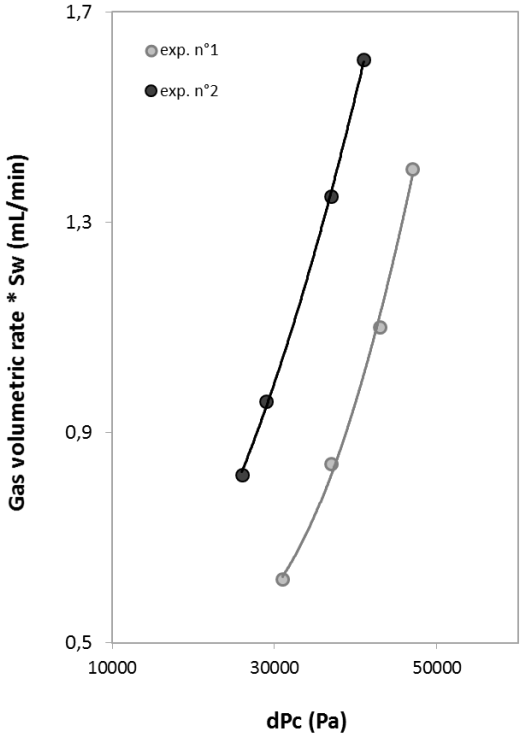

Figure 4-14 Relationships between hydrogen flow rate, average water saturation and differential pressure in experiments 1 and 2.

Capillary pressures (Figure 4-13) increase with decreasing water saturation until a maximum value of ΔP or Pc (110 kPa) is attained for a water saturation of 11%. Data for the two experiments overlap because the viscosity of hydrogen changes only a little between the two sets of P-T conditions. It is worth noting that the data are available only over a narrow water saturation range (Figure 4-13a, b). The measured capillary pressure curves as a function of the estimated water saturation at inlet (Table 4-3) are shown in Figure 4-13b. The results illustrate that, because of the relatively low absolute permeability of the rock sample, the capillary pressure measured for the smallest flow rate is relatively high, leading to an impossibility of reaching high water saturation values with our core flooding method. Only the low water saturation range is covered and the data highlight the sharp increase of capillary pressure in that range.

In order to extend the water saturation range, the core-flooding data have been combined with MICP Hg/air data (Table 4-4). *First*, raw MICP data have been obtained and corrected for the effects of surface roughness or irregularities at low pressures and the conformance volume removed (*Busch et al.,* 2013).

Table 4-4 Measured and corrected MICP capillary pressures

Experiment	ΔP (kPa)	$S_{w\ (raw)}$ %	$S_{w\ (corrected)}$ %
MICP measurement (Hg/air)	3	1	-
	5	2	-
	5	3	-
	6	4	-
	8	5	-
	10	6	-
	11	7	-
	13	8	-
	15	9	-
	17	10	0
	20	12	2
	23	16	7
	27	26	18
	31	47	42
	36	61	57
	42	69	65
	45	72	69
	48	74	71
	52	76	73
	56	77	74
	64	79	76
	75	80	78
	86	82	80
	100	83	81
	115	84	82
	135	84	83
	154	85	83
	180	86	84

The corrected MICP data (Table 4-4) are shown on Figure 4-15.

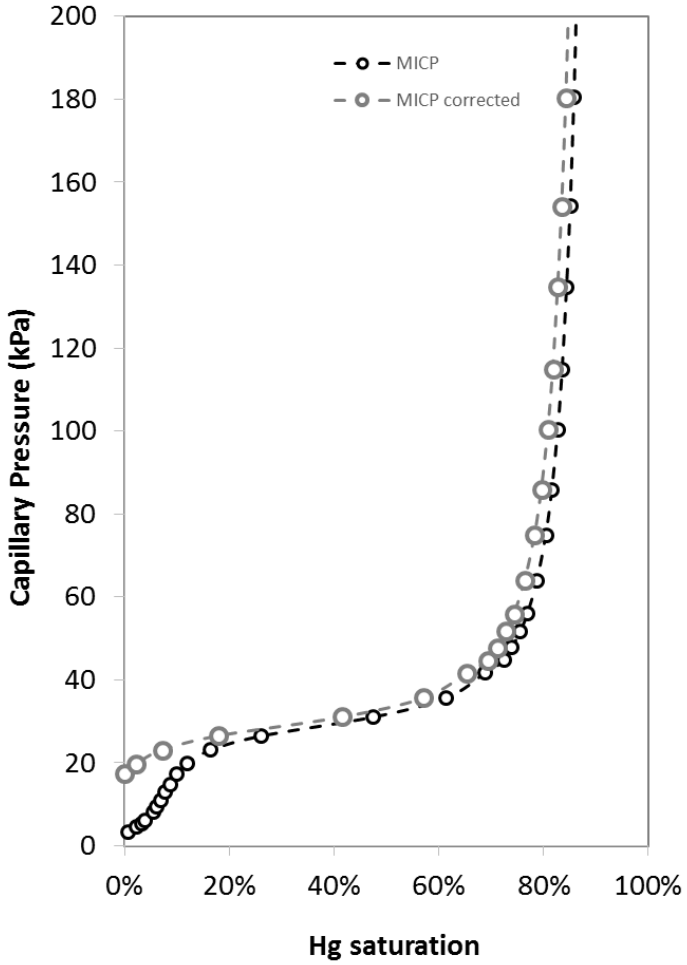

Figure 4-15 Mercury injection capillary pressure (MICP) curves measured and corrected for the effects of surface roughness or irregularities at low pressures.

Second, the dimensionless *J*-function was used to scale the capillary pressure data for hydrogen-water against those for Hg/air. It is defined as (*Al-Menhali et al.*, 2015; *Brown* 1951):

$$J(S_w) = \frac{P_c(S_w)\sqrt{K/\varphi}}{\tau} \qquad (4\text{-}15)$$

where P_c is the capillary pressure, S_w is saturation of the wetting phase, φ is the porosity of the core sample, τ is the surface tension and K is the absolute permeability. Therefore, equating the capillary pressure results obtained by the two methods (MICP and semi-dynamic capillary pressure measurement) enables the surface tension to be obtained. For experiment n°1, the surface tension is 0.051 N/m and 0.046 N/m for experiment n°2 (Figure 4-16).

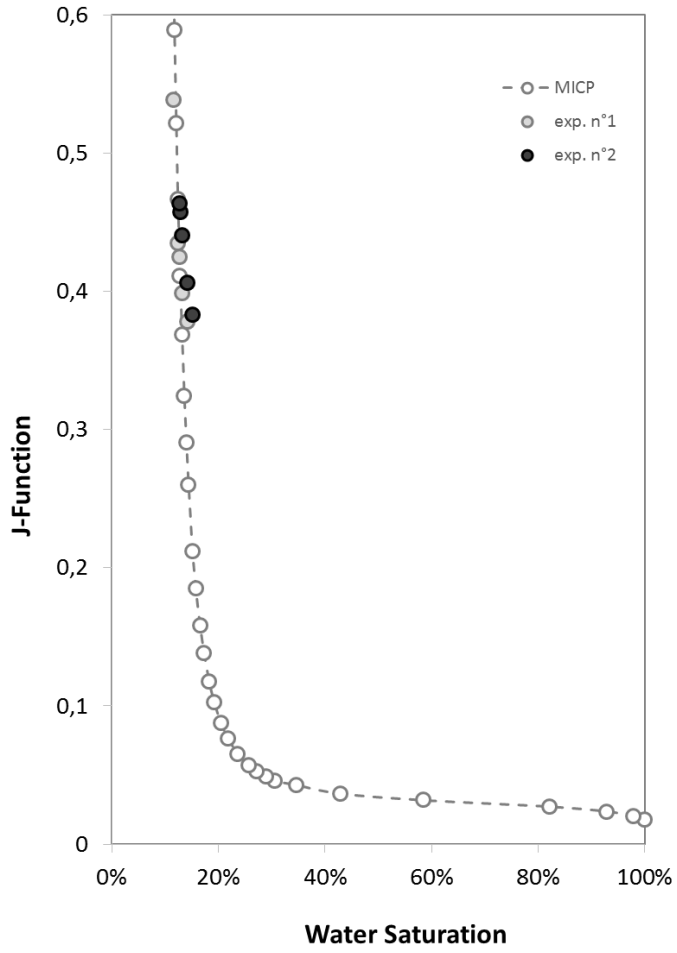

Figure 4-16 Capillary pressure measurements showing data for the MICP and the semi-dynamic experiments and extensions after scaling using the dimensionless J-function.

Third, the contact angle for the hydrogen-water system was calculated from Equation (4-13) using the surface tension as above and data (contact angle and surface tension) for mercury (141.3° and 0.48 N/m, respectively). A good fit between the core-flooding and MICP data was obtained for $cos\theta = 0.93$ and $cos\theta = 0.82$ for experiments n°1 and n°2 respectively (Figure 4-17). The processing of the two sets of capillary pressure data thus enables capillary pressure for the hydrogen-water system to be defined over a wide range of water saturation values.

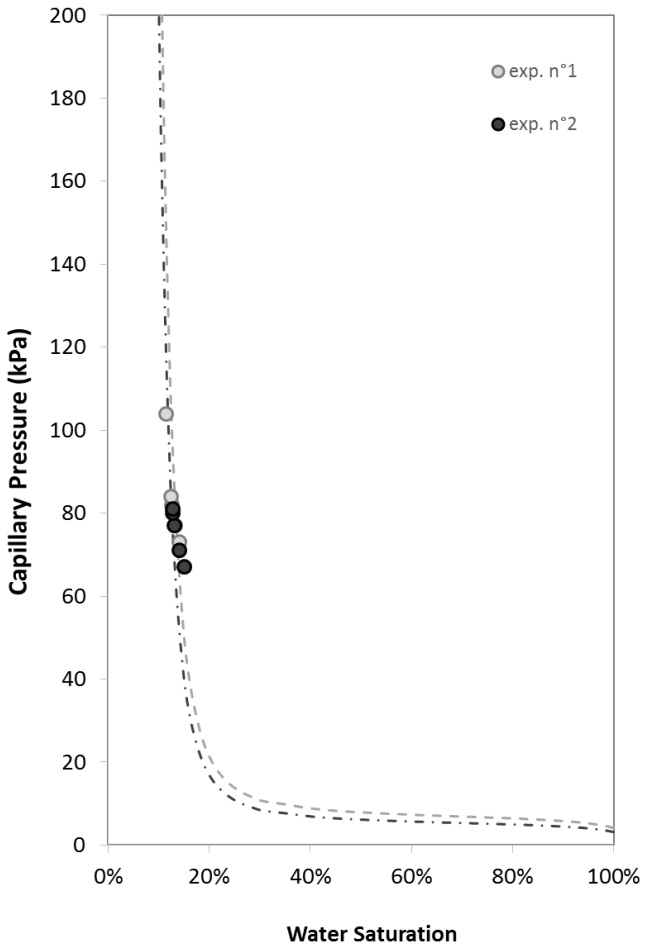

Figure 4-17 Hydrogen-water capillary pressure curves for the Vosges sandstone. The dotted lines are derived from the MICP measurements and the circles are capillary pressure data from the modified semi-dynamic measurements.

4.3.3 Steady state relative permeability measurements

Drainage relative permeability curves were measured with the steady state technique at a total flow rate of 1 mL/min, for both hydrogen gas and pure water. Experiments were performed under two different conditions (Table 4-1), but the same hydrogen fractional flows (f_{H2}) were considered. The recorded saturation and differential pressure data and the derived relative permeabilities for hydrogen and water are given in Table 4-5.

Table 4-5 Measured Relative Permeabilities in the hydrogen-water system

Experiment	f_{h2}	ΔP (bar)	$k_{r\text{-hydrogen}}$	k_{rw}	S_w (%)
Experiment 3	0.05	1.92	0.00029	0.62	90
Hydrogen-water	0.10	2.00	0.00056	0.56	87
20°C, 55 bar	0.30	1.67	0.00200	0.52	85
q_T=1 mL/min	0.50	1.44	0.00386	0.43	79
	0.70	1.10	0.00707	0.34	73
	0.90	0.88	0.01136	0.14	56
	0.99	1.16	0.04404	0.05	41
Experiment 4	0.05	0.92	0.00040	0.45	82
Hydrogen-water	0.10	0.91	0.00081	0.42	81
45°C, 100 bar	0.30	0.87	0.00273	0.37	77
q_T=1 mL/min	0.50	0.83	0.00542	0.32	73
	0.70	0.76	0.00922	0.23	66
	0.90	0.63	0.01489	0.10	53
	0.98	0.55	0.03492	0.04	40
Experiment 1			0.08		33
Hydrogen-water			0.27		17
20°C, 55 bar*			0.47		14
			0.60		13
			0.76		13
Experiment 2			0.21		22
Hydrogen-water			0.28		19
45°C, 100 bar*			0.47		15
			0.56		14
			0.71		13
			0.78		13

*Calculated values (Appendix B)

The steady state drainage relative permeability curves for hydrogen-water are shown in Figure 4-18 as a function of the water saturation. Notice that error bars on relative permeabilities incorporate errors and uncertainties on differential pressure and water saturation.

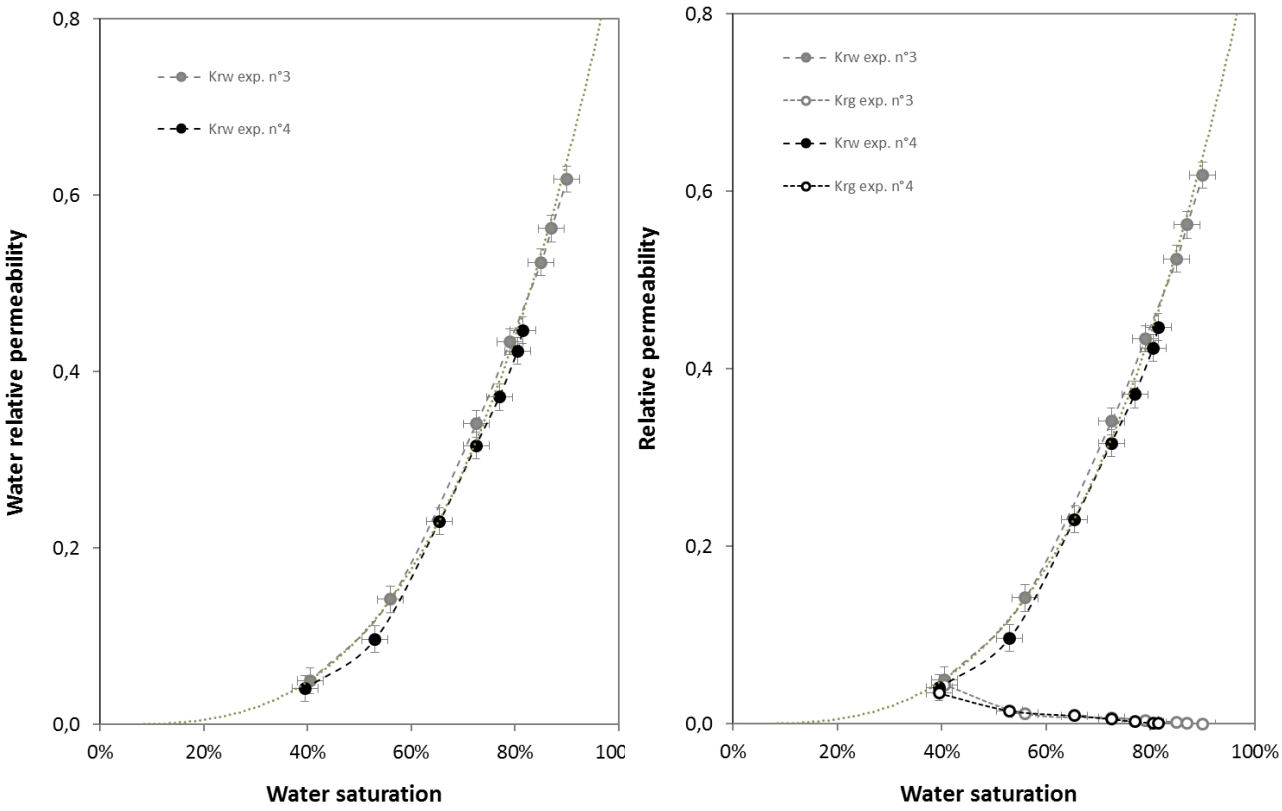

Figure 4-18 Steady state drainage relative permeability curves for the hydrogen-water system measured in Vosges sandstone for different conditions.

The relative permeability curves for hydrogen and water in the two experiments are very similar (Figure 4-18), despite gas fractional flows being different for a given saturation (Figure 4-19), higher in experiment n°3 (20 °C/55 bar) than in experiment n°4 (45 °C/100 bar). This implies that, upon increasing temperature and pressure, and for a constant gas fractional flow, hydrogen will become less efficient to remove residual water from the core. The relative permeability for hydrogen appears to be low (Figure 4-18), meaning that the hydrogen flow is significantly slowered by two-phase flow interactions.

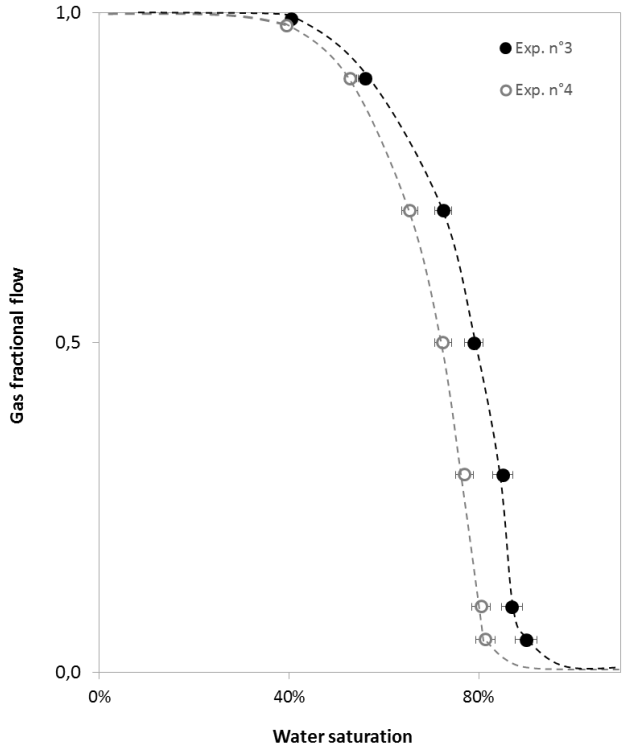

Figure 4-19 Plot of experimental gas fractional flows vs. water saturation in experiments n°3, 4 (Table 5-5).

As shown by Figure 4-18, it was not possible to decrease the water saturation below 40% during the measurements. This low apparent endpoint is likely to be due to a limitation from the experimental apparatus. *Krevor et al.* (2012), *Akbarabadi and Piri* (2013), *Pini and Benson* (2013), and *Manceau et al.*, (2015) observed a similar phenomenon: even at the highest hydrogen fractional flow, the average saturation in the core was limited by the capillary pressure reachable with the imposed flow rate (1 mL/min in our case). However, it is possible to extend the relative permeability data for the non-wetting phase toward low water saturations by using the capillary pressure data obtained from the core-flooding measurement. This method was suggested by *Pini and Benson* (2013) based on the work of *Ramakrishnan and Capiello* (1991). The relative permeability of the non-wetting phase can be calculated from the relationship between the Darcy velocity (v_{inj}) and the capillary pressure ($\Delta P_{c,x=0}$). Starting with Equation (4-12), we have:

$$\frac{K}{\mu_g} \cdot k_{r,g}\left(\Delta P_{c,x=0}\right) = \frac{dv_{inj}}{d\Delta P_{c,x=0}} \cdot L \tag{4-16}$$

which can be rewritten as:

$$k_{r,g}(s) = \frac{dv_{inj}}{d\Delta P_c} \cdot L \cdot \frac{\mu_g}{K} \tag{4-17}$$

Relative permeabilities were obtained by fitting second-order polynomials of v_{inj} as a function of ΔP_c for experiments n°1 and n°2 respectively (Table 4-3). These polynomials were used to extend the relative

permeability data for experiments n°3 and n°4 (Figure 4-20). Relative permeabilities calculated using the polynomials for experiments n°1 and n°2 are given in Table 4-5.

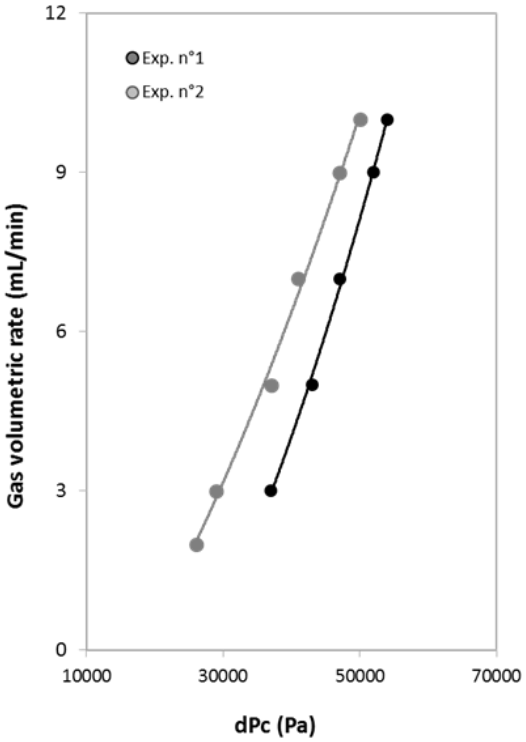

Figure 4-20 Relationship between gas volumetric rate and differential pressure in experiments n°1 and 2 (Table 4-5).

Results of the hydrogen relative permeabilities calculated with this procedure, together with those obtained with the steady state method (exp. n°3 and n°4), are shown on Figure 4-21. The calculated relative permeabilities fit well and extend the data for water saturations < 40% in experiments n°3 and n°4, down to values ~10%. This allows the evaluation of the relative permeability of hydrogen for almost the total range of water saturation.

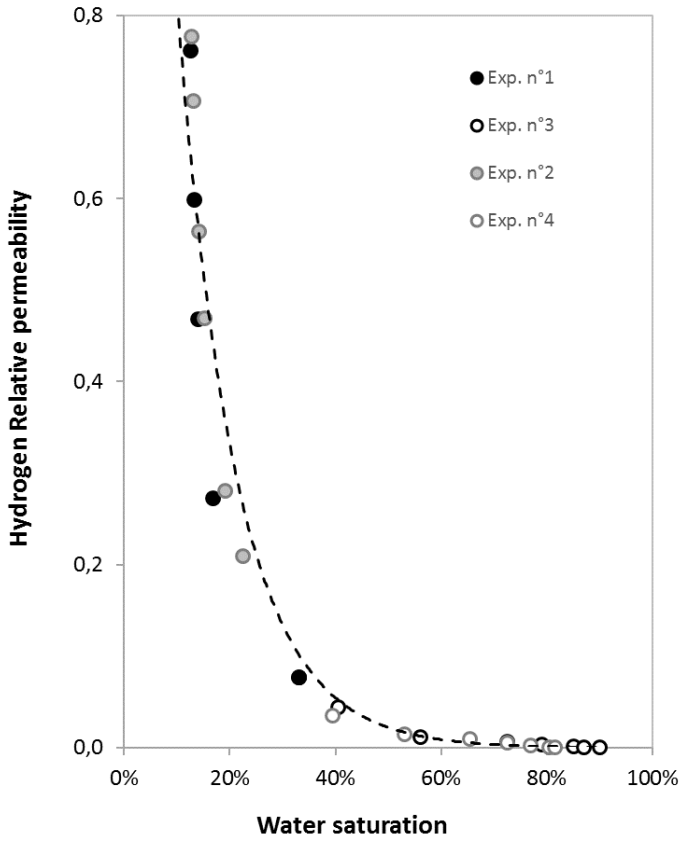

Figure 4-21 Hydrogen relative permeabilities calculated from capillary pressure experiments n°1 and 2 (i.e., at low water saturation) and comparison with relative permeabilities measured in experiments n°3 and 4 (Table 4-5).

4.4 Discussion

4.4.1 Discussion of the results

As discussed in section 4.3, the experimental conditions investigated were chosen to be representative of potential large-scale hydrogen injections. To further interpret our results and more fully characterize the type of flow that occurred in the experiments, it is convenient to introduce the capillary number. Different formulations exist for the capillary number (N_c). In this study, we will use the definition of *Yokoyama and Lake* (1981) and *Zhou et al.*, (1997):

$$N_c = \frac{D^2 \mu V_T}{LKP_{ec}} \tag{4-18}$$

where D and L (m) are the diameter and length of the core, μ (Pa s) is the gas viscosity, K is the core permeability (m^2), P_{ec} is the entry capillary pressure (i.e., the capillary pressure at the inlet) and V_T ($m\ s^{-1}$) is the total fluid velocity. Below, we use an entry capillary pressure of 5 kPa (Figure 4-17). The calculated capillary numbers (Equation (4-18)) for our experiments are shown on Table 4-6. For the

relative permeability experiments n°3 and n°4, the N_c are relatively low (< 0.5), meaning that these experiments have been performed with high capillary forces with regards to viscous forces.

Table 4-6 Capillary number[a] for both capillary pressure experiments (indicated by P_c) and relative permeability experiments (indicated by k_r)

Experiment	Type	Fluid injection	Total flow rate (cm^3/min)	N_c[a]
1	P_c	Hydrogen	2	0.67
1	P_c	Hydrogen	3	1.03
1	P_c	Hydrogen	5	1.68
1	P_c	Hydrogen	7	2.36
2	P_c	Hydrogen	2	0.71
2	P_c	Hydrogen	3	1.06
2	P_c	Hydrogen	5	1.77
2	P_c	Hydrogen	7	2.47
3	k_r	Hydrogen-water	1	0.34
4	k_r	Hydrogen-water	1	0.35

[a]Calculated from equation (4-18)

According to Reynolds et al., (2015), the transition between a capillary-dominated flow regime and a viscous dominated one generally occurs at capillary numbers comprised between 0.1 and 100. It is therefore likely that, under our experimental conditions (and by inference under injection conditions), a capillary-limited flow regime would prevail. *Reynolds et al.* (2015) have shown that, for such conditions, the relative permeability depends on the capillary number. Since the capillary number varies with the flow rate and the viscosity of the non-wetting phase and, therefore, with experimental conditions, changes in relative permeability would be expected in our experiments. However, for the two types of conditions investigated in this study (Table 4-1), no large difference in terms of relative permeability was observed, consistent with capillary numbers (Table 4-6) being almost constant in experiments n°3 and n°4.

This interpretation attributes to the capillary number and the viscosity of the non-wetting phase the essential role in controlling relative permeabilities for hydrogen (Figure 4-18). However, an alternative explanation of the data is possible. Under conditions of capillary-dominated regime, heterogeneities in capillary forces (for example arising from changes in the pore structure of the rock) are known to play a significant role in fluid migration. According to *Reynolds et al.* (2015), rock heterogeneities can exert an important influence on relative permeabilities. For example, the low relative permeabilities measured for hydrogen (Figure 4-18) could reflect such rock heterogeneities rather than the specific properties of hydrogen. Testing of this interpretation would require additional measurements on different rock samples and/or different gases.

Extension of the relative permeability data toward low water saturations involves significant increases in capillary number (experiments n°1 and n°2, Table 4-1). However, these changes remain relatively low (less than a 10 fold increase compared to values for experiments n°3 and 4) and, so, the type of flow should not be fundamentally affected. It is important to notice that, for potential hydrogen storage pressures (< 100 bar) and temperatures (< 100°C), the hydrogen viscosity does not largely vary (Table 4-1). This implies that the capillary number and, therefore, the relative permeability in the hydrogen-water system, will not be largely modified upon changing pressure and temperature in the ranges above. This is in contrast with other fluid pairs (e.g., the CO2-water system) where capillary numbers can strongly vary with pressure and temperature. This stresses that the relative permeability data from this study are likely to be valid for the entire range of pressures and temperatures appropriate for hydrogen storage. Similarly, despite the two differing sets of conditions investigated in this study, the two capillary pressure curves (Figure 4-17) are very close from each other indicating that wettability and contact angles between hydrogen gas and water do not largely change with pressure and temperature.

4.4.2 Validation of the core flooding experimental set-up

To validate and confirm the core-flooding set-up and the stability of the multiphase flow parameters obtained for the hydrogen-water system, core-flooding experiments for another fluid-pair, argon-water system were performed. Two experiments (Table 4-7) were carried out to measure capillary pressures and relative permeabilities for the argon-water system. These two experiments helped us to calibrate the core-flooding experimental set-up before the measurements in the hydrogen-water system.

Table 4-7 Conditions and parameters of capillary pressure and relative permeability experiments performed in the argon-water system

Experiment	Type	Non-wetting Fluid	Temperature/Pressure (°C)/(bar)	μ_{argon} (µPa s)	ρ_{argon} (Kg/m^3)	μ_{water} (µPa s)	ρ_{water} (Kg/m^3)
I	P_c	Ar	20/55	23.2	172.6	999	1000.5
II	k_r	Ar	20/55	23.2	172.6	999	1000.5

- **Capillary pressure results**

Figure 4-22 illustrates the measured argon-water capillary pressure curve as a function of the average saturation along the core using our core flooding method.

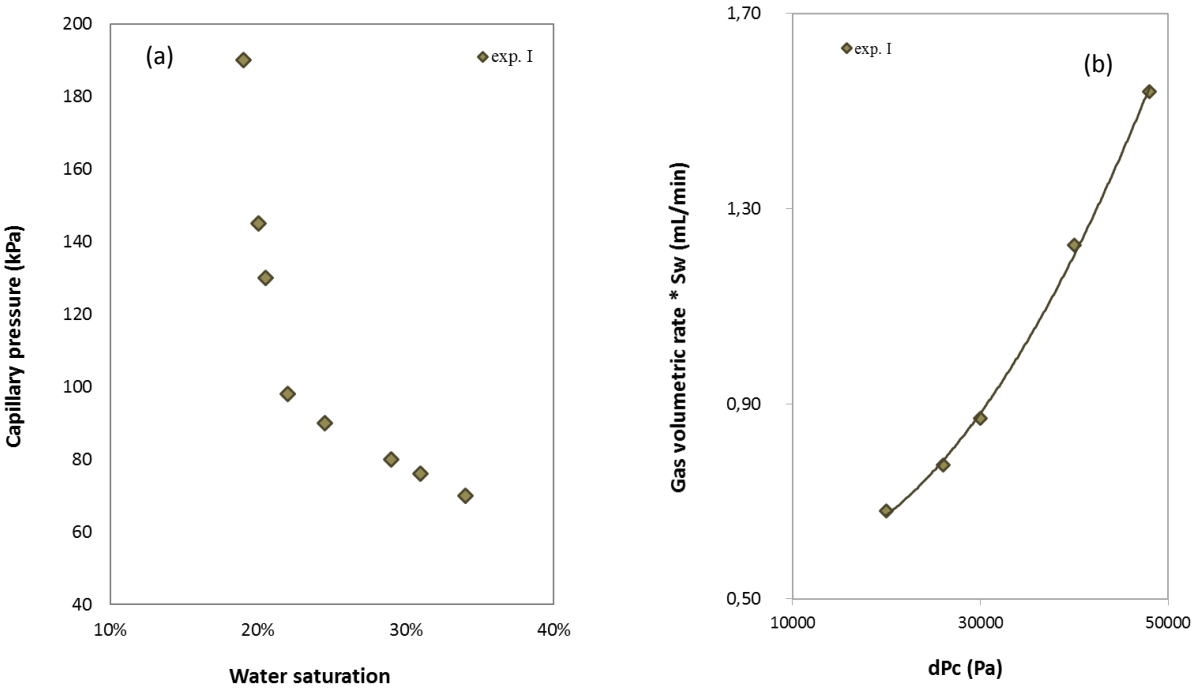

Figure 4-22 (a) Capillary pressure measurements for the argon-water system (Table 5-7). (b) Relationship between the argon flow rate, water saturation and the differential pressure in experiment I (Table 4-7).

The recorded average saturation and pressure data as well as the computed capillary pressures are given in Table 4-8. Argon has a higher viscosity and density than hydrogen; therefore, the capillary number for the argon-water system should be higher than for hydrogen-water system at the same flow rate (Table 4-8). Regarding to Table 4-8, the capillary number is the highest (1.58) for the maximum flow rate (9 mL/min) and the lowest (0.26) for the minimum flow rate (1.5 mL/min).

Table 4-8 Results of capillary pressures for the argon-water system

Experiment	Q_g (mL/min)	S_w	P_c (kPa)	N_c
Experiment I argon-water 20°C, 55 bar	1.5	0.34	70	0.26
	1.75	0.31	76	0.31
	2	0.29	80	0.35
	2.5	0.25	90	0.44
	3	0.22	98	0.53
	5	0.21	130	0.88
	7	0.20	145	1.23
	9	0.19	190	1.58

However, by converting average water saturations to inlet water saturations using argon volumetric flow rates Figure 4-22b one obtains the capillary pressure vs. water saturation for the argon-water system (Figure 4-23).

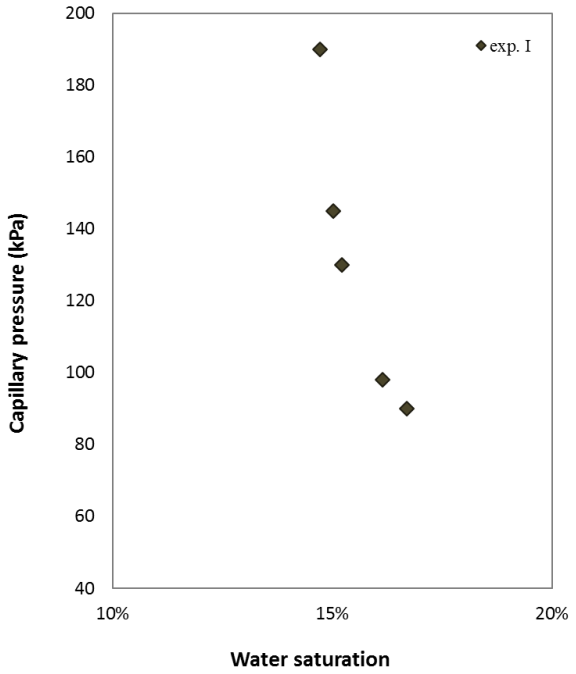

Figure 4-23 experimentally measured capillary pressures for the argon-water system.

In order to compare the capillary pressure results from the core flooding measurements with the MICP data, the surface tension of the argon-water system under our experiments conditions (see Table 4-7) is needed. Hence, a J-function analysis was performed to obtain the surface tension. After adjusting the J-function, the surface tension obtained is 0.074 N/m under conditions of experiment I (Table 4-8; Figure 4-24).

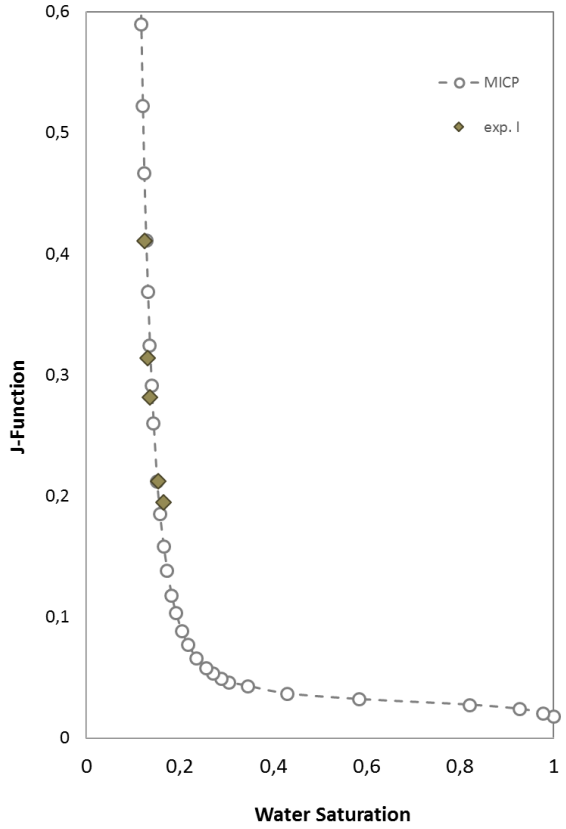

Figure 4-24 MICP and semi-dynamic capillary pressure measurements and extensions after scaling using the dimensionless J-function.

The MICP capillary pressure data were converted to capillary pressures for the argon-water system using Equation (4-13). A good fitting with the core-flooding technique was obtained for $cos\theta = 0.92$ for experiment I (Figure 4-25). The good match between results of the two capillary pressure measurement techniques enables to propose a capillary pressure curve for the argon-water system valid over a large range of water saturation values.

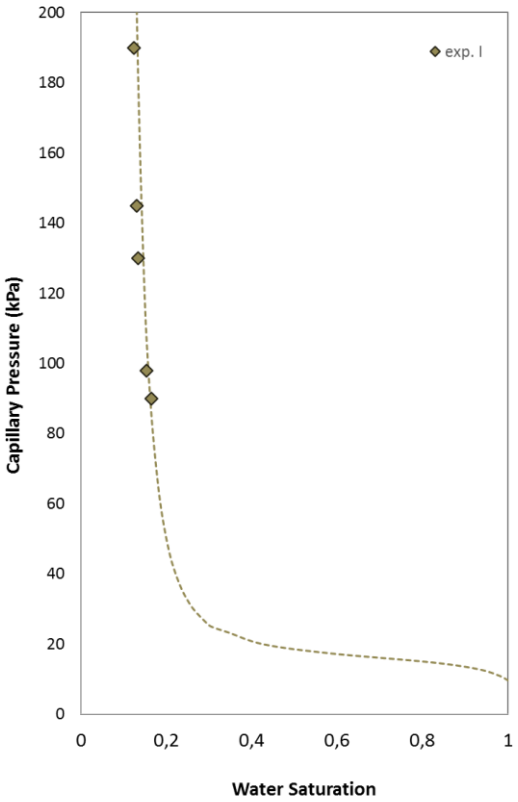

Figure 4-25 Capillary pressure curve for the argon-water system. The dotted line represents MICP-derived data converted to the gas-water system. See text for the scaling of the MICP data using the dimensionless J-function and for the fitting of the contact angle (cosθ).

- **Relative permeability results**

The steady state drainage relative permeability curves for argon-water are shown in Figure 4-26 as a function of water saturation.

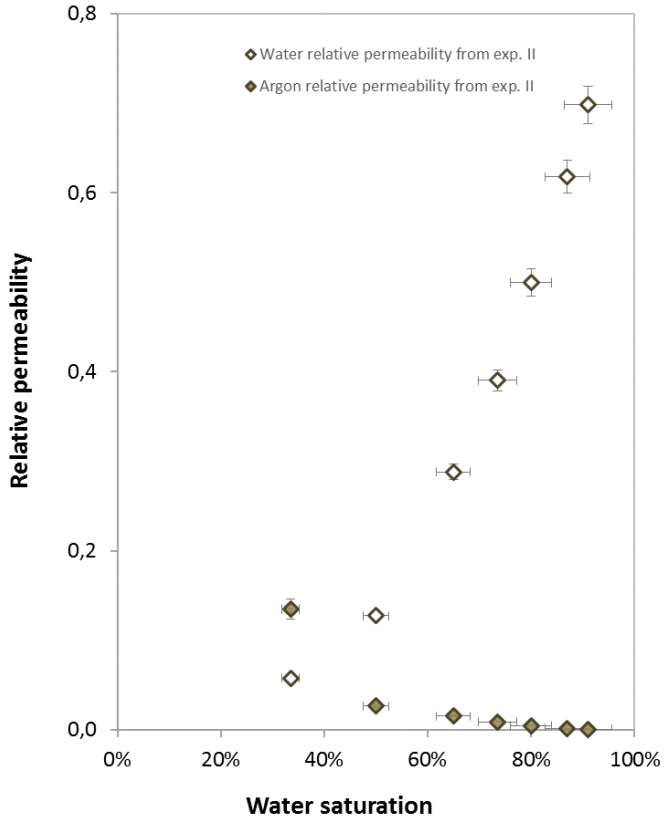

Figure 4-26 Steady state drainage relative permeabilities for the argon-water system.

The recorded saturation and pressure data as well as the computed relative permeability are given in Table 4-9.

Table 4-9 Measured relative permeabilities for the argon-water system

Experiment	f_{argon}	S_w	$k_{r\text{-}argon}$	k_{rw}	ΔP (bar)
Experiment II argon-water 20°C, 55 bar q_T=1 mL/min	0.05	0.91	0.00085	0.70	1.70
	0.10	0.87	0.00159	0.62	1.82
	0.30	0.80	0.00497	0.50	1.75
	0.50	0.74	0.00907	0.39	1.60
	0.70	0.65	0.01562	0.29	1.30
	0.90	0.50	0.02665	0.13	0.98
	0.99	0.34	0.13496	0.06	2.15

However, in order to evaluate relative permeabilities at lower water saturations, we have applied to the argon-water system the same method as described in section 5.3.3. Results of the argon-water relative permeabilities, either calculated with this method or directly measured, are illustrated in Figure 4-27.

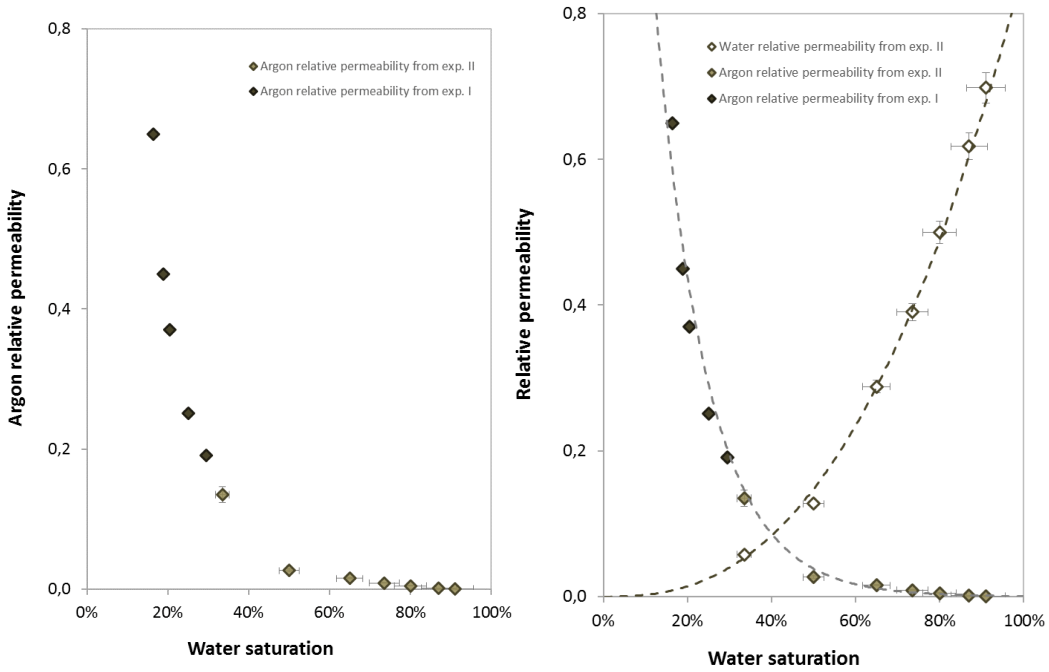

Figure 4-27 Left: argon relative permeabilities calculated from capillary pressure experiment I (Table 4-8) and measured in experiment II (Table 4-9). Right: fitted relative permeabilities for argon and water

- **Comparison between the hydrogen-water and argon-water systems**

As indicated, in this study, core-flooding experiments have been performed on two types of fluid-pair systems, hydrogen-water and argon-water. Comparison of results between these two system stresses the differences between hydrogen and argon in terms of viscosity and density.

The capillary pressure measurements showed a higher interfacial tension and therefore a higher capillary pressure for argon-water (74 mN/m) than for hydrogen-water (46-51 mN/m). The capillary pressures are compared in Figure 4-28.

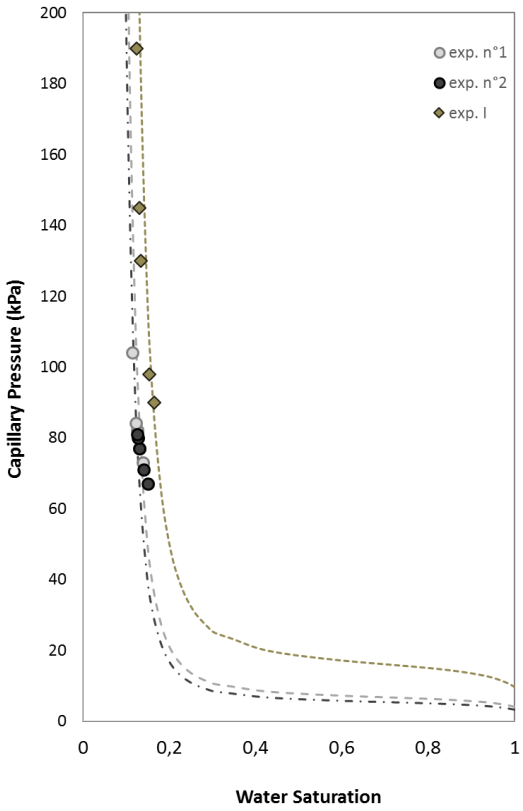

Figure 4-28 Comparison between capillary pressures for hydrogen-water (exp. n°1 and 2) and for argon-water (exp. I).

In terms of relative permeability, as explained, the steady state approach was performed for both the argon-water and hydrogen-water systems at a similar total flow rate of 1 mL/min (Figure 4-29).

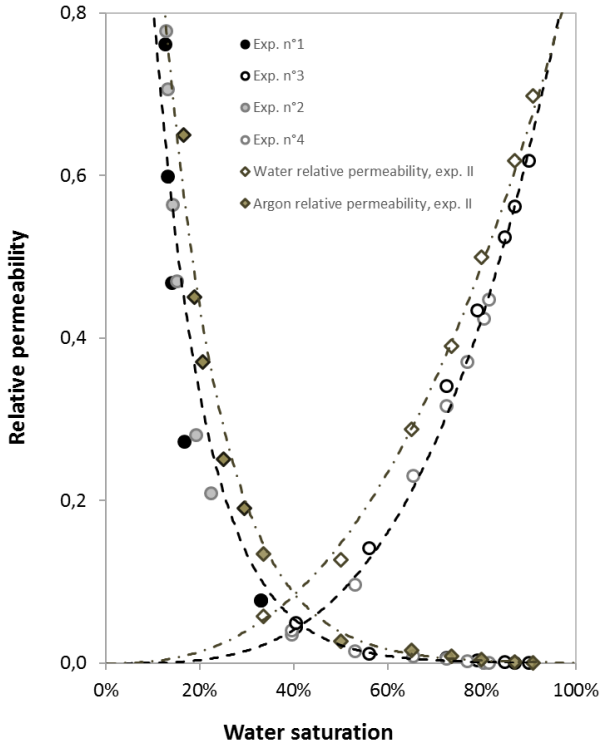

Figure 4-29 Comparison of relative permeability curves for the hydrogen-water and argon-water systems. The curves represent best fits to the data. The argon-water system has a higher capillary number than the hydrogen-water system and so the relative permeability is higher in the argon-water than in the hydrogen-water system.

As mentioned recently, in capillary-dominated flow regime (capillary number <100) the relative permeability depends on the capillary number (*Reynolds et al.*, 2015). In this study, the change of fluid pair led to an increase of the capillary number (see Table 4-10) and it has been shown that the relative permeability curves (hydrogen-water curve and argon water curve) were changed by varying the capillary number (Figure 4-29).

Table 4-10 Capillary number[a] for both relative permeability experiments hydrogen/water and argon/water system (indicated by k_r)

Experiment	Type	Fluid injection	Total flow rate (mL/min)	N_c [a]
3	k_r	Hydrogen/water	1	0.06
4	k_r	Hydrogen/water	1	0.07
II	k_r	argon/water	1	0.17

[a]Capillary number from equation (4-18)

4.4.3 Capillary end effect

In core-flooding experiments to measure relative permeabilities, capillary discontinuities in the wetting phase at the outlet of the core sample (capillary end effect) can happen. This can potentially affect the fluid flow and the measurements (Figure 4-30).

In fact, capillary end effect is an important issue in core-flooding experiments, because it can impact the calculation of the water saturation and the relative permeability measurements from the pressure drop method.

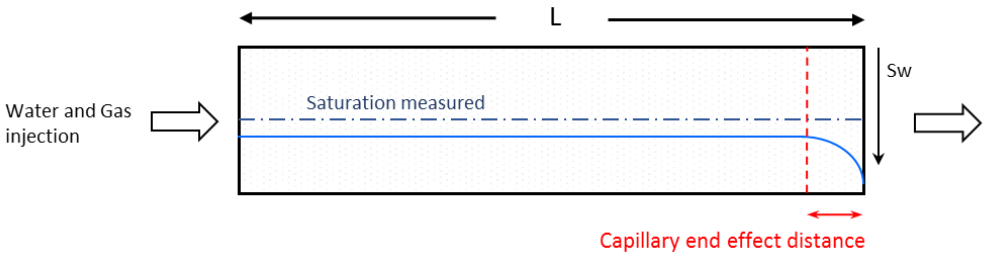

Figure 4-30 Water saturation across a core showing the region where capillary end effects are expected. The measured water saturation (Sw, dashed dotted line) is the average water saturation whereas the blue continuous curve is the real water saturation.

Capillary end effects refer to a water saturation anomaly which occurs close to the outlet face of the core sample subjected to the flooding procedure. For relative permeability measurements, under steady state, both water and gas are flowing through the water saturated core. It can be expected that both fluids, when they reach the outlet face of the core, leave the sample at the same pressure. Therefore, the capillary pressure inside the sample, which is defined by Equation (2-5), must be zero at the outlet since

at the outlet P_{gas}=P_{water}. However, since the capillary pressure is a direct function of the saturation, the wetting phase saturation at the outlet has to be equal to the saturation corresponding to zero capillary pressure. Capillary end effects depend on the gas-water relative permeability, capillary pressure, absolute permeability and the gas-water flow rate.

Therefore, to evaluate the magnitude of these effects, a numerical simulation of hydrogen-water two-phase flow in the core was performed with COMSOL by using the Darcy equation. The capillary pressure and relative permeability data from experiments n°2 and 4 respectively (both at 45°C and 100 bar) were used as input values. The highest f_{H2} (0.98, Table 4-5) was considered in the simulation so that capillary end effects would be maximum. The results of the simulation shows that the water saturation is constant over 95% of the length of the core and that the experimental water saturation value is well reproduced numerically. In the last 5% of the core length, the computed water saturation markedly increases, becoming twice as high as the measured value at the outlet (Figure 4-31). Therefore, the simulation demonstrates that capillary end effects are effectively restricted to the very end part of the core (i.e., to the last 3 mm of the 61 mm core).

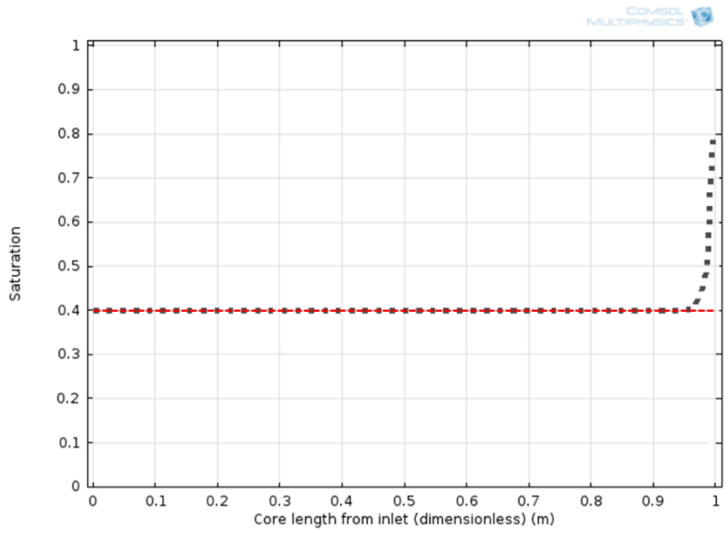

Figure 4-31 Computed vs. measured water saturation along the core during relative permeability measurements where both water and gas are flowing through the core. Black dots: results of numerical modeling, Red dashes: experimental measurement. Results are for a fractional flow of hydrogen (*f*H2) of 0.98 (Table 4-5). Notice the deviation between the simulation and the measurement near the very end part of the core.

Chapter 5

Numerical simulation

In this study, two approaches were followed to simulate the impact of hydrogen on underground storage. (1) A batch numerical simulation approach without any fluid migration was implemented to study the temporal evolution of sandstone in presence of hydrogen. This approach complemented the experiments presented in Chapter 4. It focused on changes in the mineralogical composition of sandstone following introduction of hydrogen gas. (2) An applied geochemical reactive transport model was tested to evaluate the hydrodynamic behavior of hydrogen under conditions representative of operation (injection, production) of a hydrogen reservoir. This numerical simulation served to investigate the response of an underground hydrogen storage site to seasonal fluctuations of the energy demand.

5.1 Hydrogen-water-rock interaction numerical simulation

Geochemical modeling of fluid-rock interactions was performed with the PHREEQC geochemical software V.3.1.5 (*Parkhurst and Appelo,* 2000). This code enables complex interactions between dissolved gases, aqueous solutions, and mineral assemblages to be simulated up to moderate temperatures and pressures (*Van Pham et al.,* 2012).

The calculations were performed without any transport, i.e., the fluid phase is static and every single chemical component is homogeneously distributed. The simulations were carried out to test the influence of hydrogen on sandstone assuming that an aqueous fluid phase is always present (compare with Chapter 4). They provide a theoretical reference frame to predict mineralogical reactions in sandstone, the appearance of mineral product phases and to constrain the timescales of the mineralogical transformations.

PHREEQC modeling was used in two different ways. *First*, it was used to check the stability of mineral phases initially present in sandstone and to identify mineral reaction products. This was based on the use of saturation indices (Equation (5-1)) which were calculated from PHREEQC:

$$SI = \log\left(\frac{Q}{K_e}\right) \leftrightarrow \begin{Bmatrix} < 0\ undersaturated: & dissolution \\ = 0\ saturated: & equilibrium \\ > 0\ oversaturated: & precipitation \end{Bmatrix} \quad (5\text{-}1)$$

where Q is the corresponding ion activity product and K_e is the equilibrium constant. These *SI* served to identify mineral phases either at equilibrium with the fluid, undergoing dissolution or appearing as reaction products. In this approach, PHREEQC is used in "equilibrium mode", i.e., thermodynamic equilibrium is assumed between fluids and sandstone minerals. These calculations in equilibrium mode are useful to assess the stability of sandstone phases. They provide informations applicable to the very long term (compare with Chapter 4) but rates of mineralogical transformations are left unexplored.

Mineralogical transformations are the expression of sandstone minerals such as quartz, feldspars, micas or other minor phases becoming unstable in presence of the coexisting hydrogen-bearing reservoir fluid. These usually take place through a sequence of complex, kinetically controlled, heterogeneous reactions. Therefore, temporal constraints need to be involved, especially at low temperatures. In the case of geological hydrogen storage, the time required for reservoir minerals to react and transform (following hydrogen injection and if unstable with the fluid) is an important issue because this would affect the stability of the reservoir site. Therefore, *second*, PHREEQC was used in "kinetic mode" to analyze rates of mineralogical transformations.

Rate law kinetic parameters in PHREEQC are derived from *Palandri and Kharaka* (2004). The reaction rate depends on how much of the mineral is available, how fast is the reaction and how far it is from equilibrium (*Gundogan et al.*, 2011). The kinetic rate of each reaction is calculated using the expression given by *Lasaga et al*. (1994):

$$r = kS_r\left(1 - \left(\frac{Q}{K_e}\right)^{\theta}\right)^{\eta} a_{H^+}^{n} \quad (5\text{-}2)$$

where r is the kinetic rate (positive values of r indicate dissolution, negative indicate precipitation); k is the rate constant (mol/m^2/s), which is temperature dependent, S_r is the specific reactive surface area (m^2/g), $a_{H^+}^{n}$ is the aqueous activity of H^+ ion and n is the order of the reaction. The parameters θ and η are two parameters that depend on the experimental data and they are usually set equal to one.

To calculate the kinetic rate constant k in Equation (5-2), acid-base mechanisms must be taken into account. Therefore, a general form of kinetic rate which includes the three k variables (*Palandri and Kharaka*, 2004) is:

$$r = S_r\left[k_{25}^{N} exp\left(\frac{-E_{a,N}}{RT_\alpha}\right) + k_{25}^{H} exp\left(\frac{-E_{a,H}}{RT_\alpha}\right) a_H^{n_H} + k_{25}^{OH} exp\left(\frac{-E_{a,OH}}{RT_\alpha}\right) a_H^{n_{OH}}\right](1 - SR) \quad (5\text{-}3)$$

$$\frac{1}{T_\alpha} = \frac{1}{T} - \frac{1}{298.15} \quad (5\text{-}4)$$

where k_{25} is the rate constant at 25°C, E_a is the apparent activation energy, R is the gas constant, T is the absolute temperature, a^H is the H^+ activity, n is the reaction order with respect to H^+ and OH^-, and SR is the saturation state given by:

$$SR = exp\left(\frac{\Delta G_r}{RT}\right) \quad (5\text{-}5)$$

where ΔG_r is the Gibbs free energy of the reaction.

The input data for the PHREEQC kinetic modeling are summarized in Table 5-1. Determining specific surface areas for multi-mineralic system is still being discussed (*Mitiku et al.,* 2013). Most often, surface areas are calculated based on geometrical considerations, e.g., assuming an assemblage of truncated spheres (*Sonnenthal and Spycher*, 2001). This, however, might overestimate the reactive surface area as one mineral can be coated by precipitates of other minerals. The calculations assume constant specific surfaces of 10 cm^2/g and 20 cm^2/g for quartz and feldspar, and muscovite and hematite, respectively, which are the dominant minerals in the studies sandstones (Table 5-1).

Table 5-1 List of kinetic rate parameters

Primary minerals	Volume fraction %	Specific surface area, A (cm^2/g)	Kinetic rate parameters							
			Neutral mechanism		Acid mechanism			Base mechanism		
			k_{25} (mol/m^2 s)	E_a (kJ/mol)	k_{25}	E_a	n(H^+)	k_{25}	E_a	n(H^+)
Quartz	74	10	$10.2x10^{-14}$	87.7						
K-feldspar	22	10	$3.89x10^{-13}$	38.0	$8.71x10^{-11}$	51.7	0.5	$6.31x10^{-22}$	94.1	-0.823
Muscovite	2	20	$1.00x10^{-13}$	22.0						
Hematite	1	20	$2.51x10^{-15}$	66.2	$4.07x10^{-10}$	66.2	1.0			

Kinetic rate constants of all the mechanisms are given at 25° C. These kinetic parameters were taken from the scientific literature, mostly from Palandri and Kharaka (2004).

5.1.1 Results of geochemical simulations

In order to simulate the temporal evolution of sandstone under the influence of hydrogen, 100 moles of sandstone rock from Adamswiller were reacted with pure water in presence of H_2 gas. The simulations were performed at 100°C, and for a H_2 pressure set at 100 bar in most cases, and more rarely at 10 bar. Three water-rock mass ratios (W/R) were tested, 0.1 (as in the experiments), 1 and 10, to reproduce long time-integrated fluid circulations. As an initial step, calculations in *equilibrium mode* guided the choice of mineral product phases to be considered since, in the experiments (Chapter 4), phase assemblages did not vary and no product phase was identified. Then, simulations in *kinetic mode* were performed in two cases, the first without mineral product phases (and so simulating the simple dissolution of sandstone

minerals in the fluid, the mineralogical composition being set constant as in Table 3-3) and the second with selected product mineral phases included (coupled mineral dissolution and precipitation).

Equilibrium calculations

When in equilibrium mode, a number of phases appeared as possible products of the interaction between sandstone and hydrogen in presence of water. These product phases did not change significantly when varying input parameters such as the H_2 pressure which was reduced from 100 to 10 bar in a few runs. They include: magnetite (Fe_3O_4), Fe-mica (annite), Fe-chlorite (chamosite), Fe-serpentine (cronstedtite), fayalite (Fe_2SiO_4), wustite (FeO), ferrosilite ($FeSiO_3$), greenalite, minnesotaïte and nontronite (Table 5-2).

Table 5-2 Stable and product minerals and saturation indices (SI) predicted to the be present at equilibrium from PHREEQC calculations

Stable minerals	Product minerals	Saturation indexes
Quartz	-	0.00
K-feldspar	-	0.00
	Magnetite	3.01
	Annite	9.43
	Chamosite	3.85
	Cronstedtite	5.63
	Fayalite	3.98
	Wustite	0.49
	Ferrosilite	2.03
	Greenalite	8.31
	Minesotaite	9.23
	Nontronite	0.37

The highest computed saturation indexes were found for annite, greenalite and minnesotaïte. These equilibrium calculations predict phase assemblages expected to be present at equilibrium upon transformation of sandstone by hydrogen. They stress the presence of various hydrous Fe silicates (annite, chamosite, cronstedtite, greenalite, minnesotaïte, nontronite) and the reduction of Fe from Fe^{3+} in mainly hematite to Fe^{2+} in magnetite, fayalite, wustite and ferrosilite. It is important to emphasize that quartz and K-feldspar remain stable during the interaction. Therefore, the mineral changes above concern phases such as muscovite, hematite and clay minerals which overall form a minor volumetric fraction in our sandstones.

Kinetic calculations

Results for simple dissolution are illustrated in Figure 5-1 and Figure 5-2. Changes in mass fractions of mineral phases from the sandstone are plotted as a function of time for the 3 W/R considered (Figure 5-2).

The influence of hydrogen can be appreciated from the curves calculated without hydrogen for W/R = 1. Results show that, with and without hydrogen, the dissolution curves for quartz, K-feldspar and muscovite are identical but the dissolution of hematite becomes strongly affected (Figure 5-1).

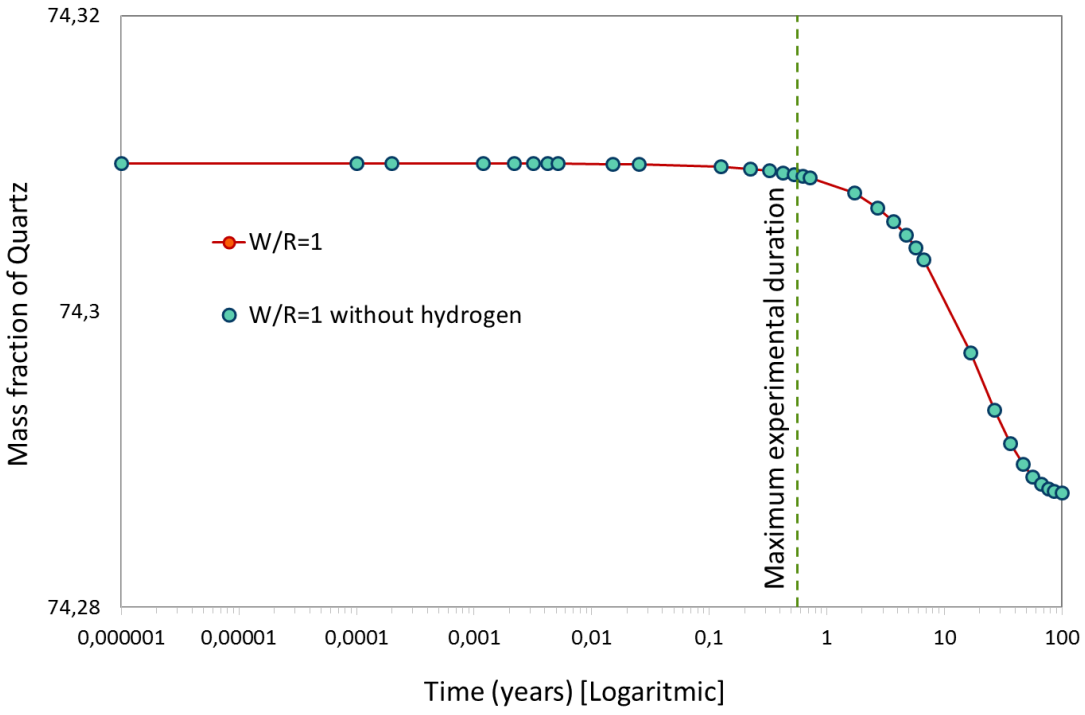

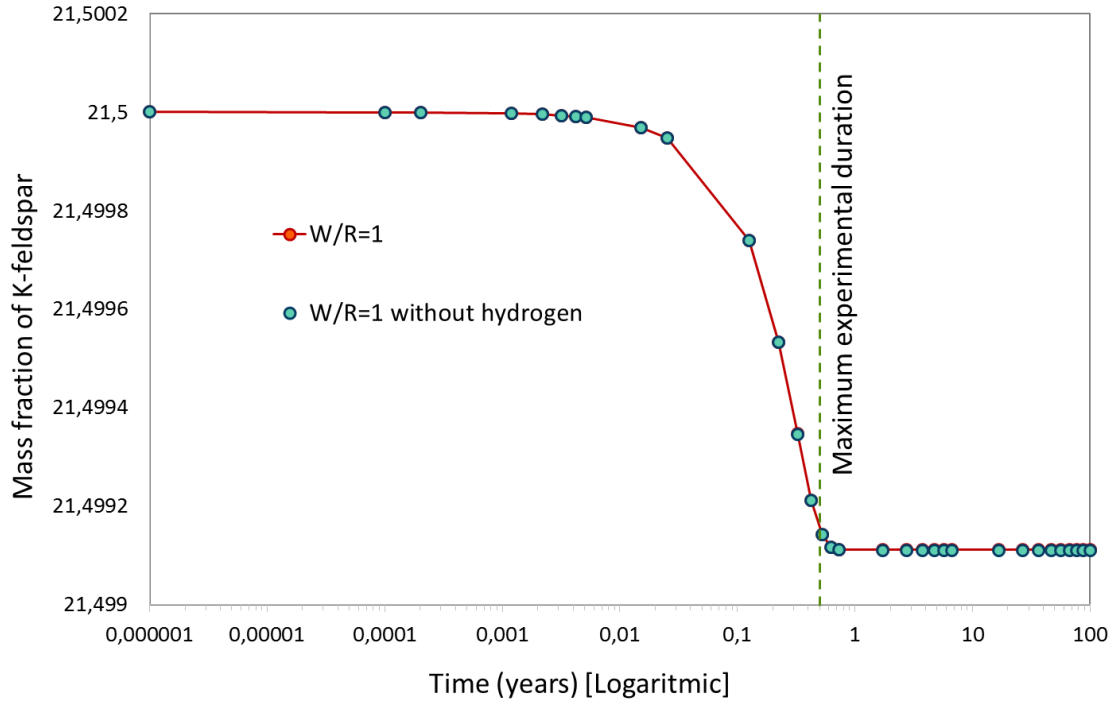
21,5002
21,5
21,4998
21,4996
21,4994
21,4992
21,499
Mass fraction of K-feldspar
W/R=1
W/R=1 without hydrogen
Maximum experimental duration
0,000001
0,00001
0,0001
0,001
0,01
0,1
1
10
100
Time (years) [Logaritmic]

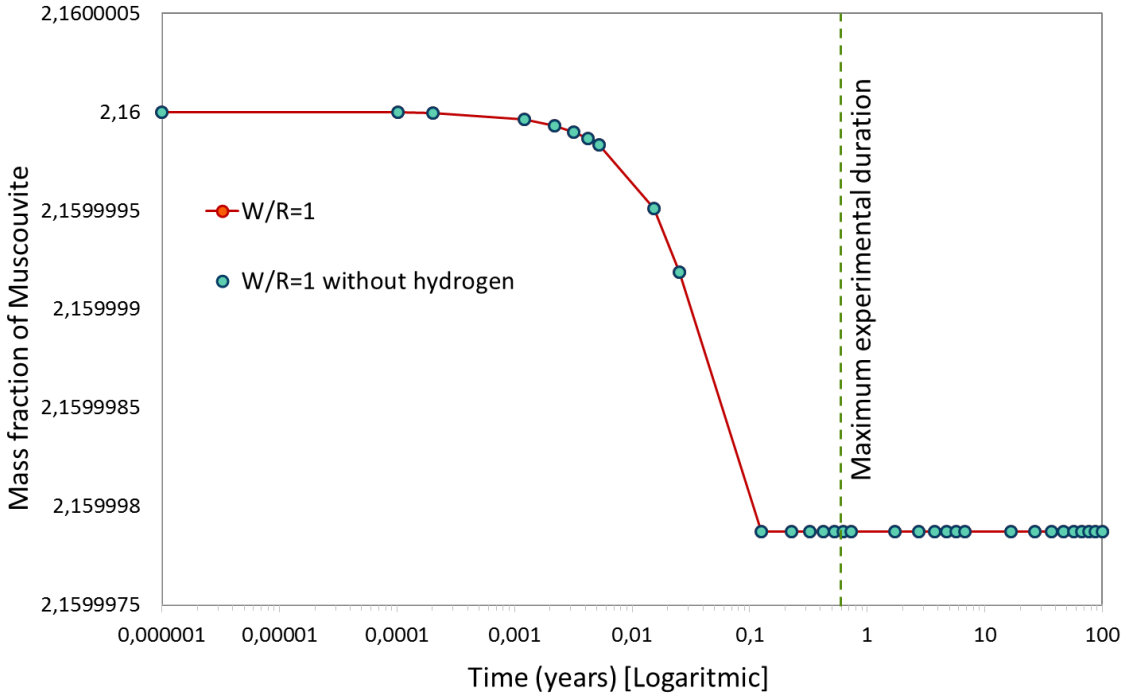
2,1600005
2,16
2,1599995
2,159999
2,1599985
2,159998
2,1599975
Mass fraction of Muscouvite
W/R=1
W/R=1 without hydrogen
Maximum experimental duration
0,000001
0,00001
0,0001
0,001
0,01
0,1
1
10
100
Time (years) [Logaritmic]

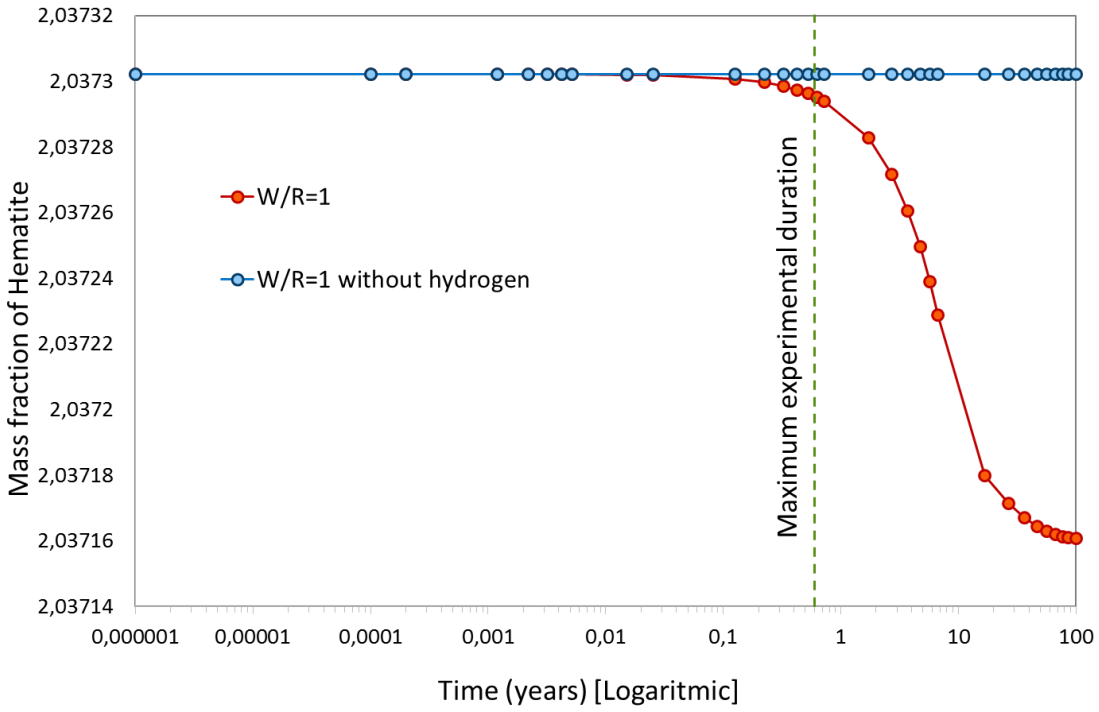

Figure 5-1 Geochemical modeling of simple sandstone minerals vs time with and without hydrogen

In presence of hydrogen, the 4 major minerals follow an initial decrease of their mass fraction, interpreted as mineral dissolution in the fluid (Figure 5-2). Then, plateau values are reached for each mineral phase, although these are attained after durations that depend on the mineral, and in particular on the W/R for a given mineral. These plateau values are interpreted to reflect saturation of the fluid with respect to the dissolving mineral phase. For quartz and hematite, plateau values are attained only for a W/R of 0.1, in both cases after 1-10 years. No saturation is observed after 10^2 years for a W/R of 1 and 10 (Figure 5-2). In contrast, aluminous phases (K-feldspar and muscovite) reach saturation for the 3 W/R considered. In both cases, saturation is attained after durations that increase monotonously with the W/R, from 0.1 to < 10 years for K-feldspar and from < 0.01 to < 1 years for muscovite.

Figure 5-2 illustrates geochemical modeling of simple sandstone mineral dissolution in a H_2O-H_2 fluid using PHREEQC. Mass fractions of mineral phases (normalized to 100 g of sandstone) are plotted as a function of time for timescales ranging from 10^{-6} to 10^2 years. For each panel, results are shown for the 3 water/rock ratios (W/R) considered. The vertical dashed line gives the maximum duration of the experiments (Table 3-3).

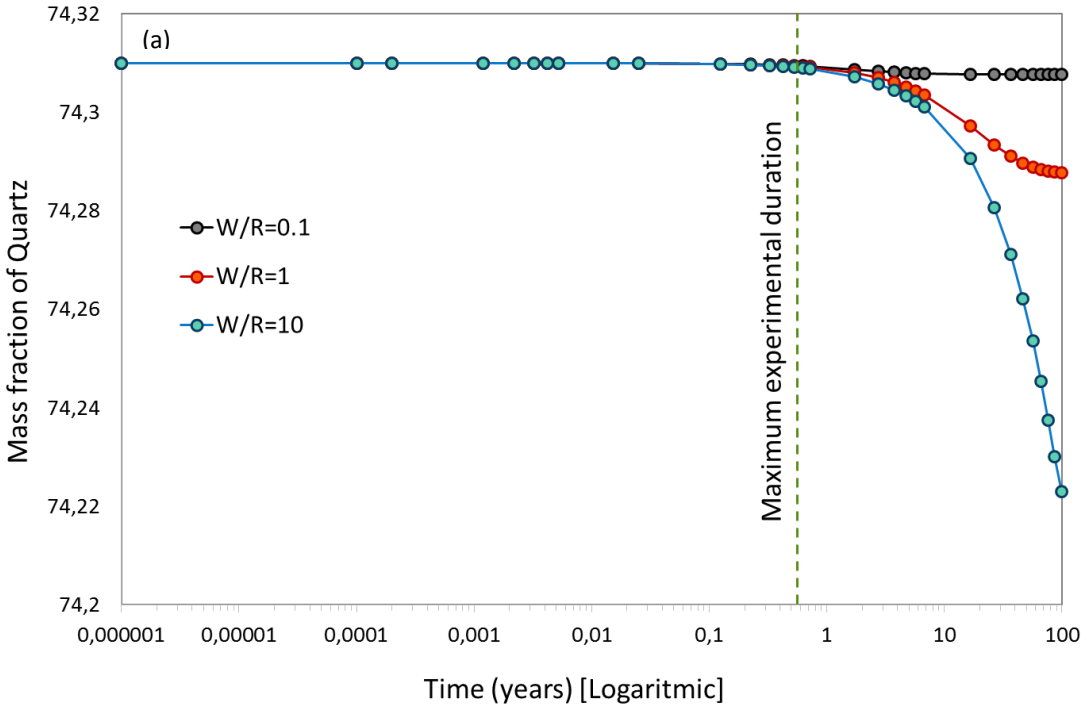
(a)
74,32
74,3
74,28
74,26
74,24
74,22
74,2
Mass fraction of Quartz
W/R=0.1
W/R=1
W/R=10
Maximum experimental duration
0,000001
0,00001
0,0001
0,001
0,01
0,1
1
10
100
Time (years) [Logaritmic]

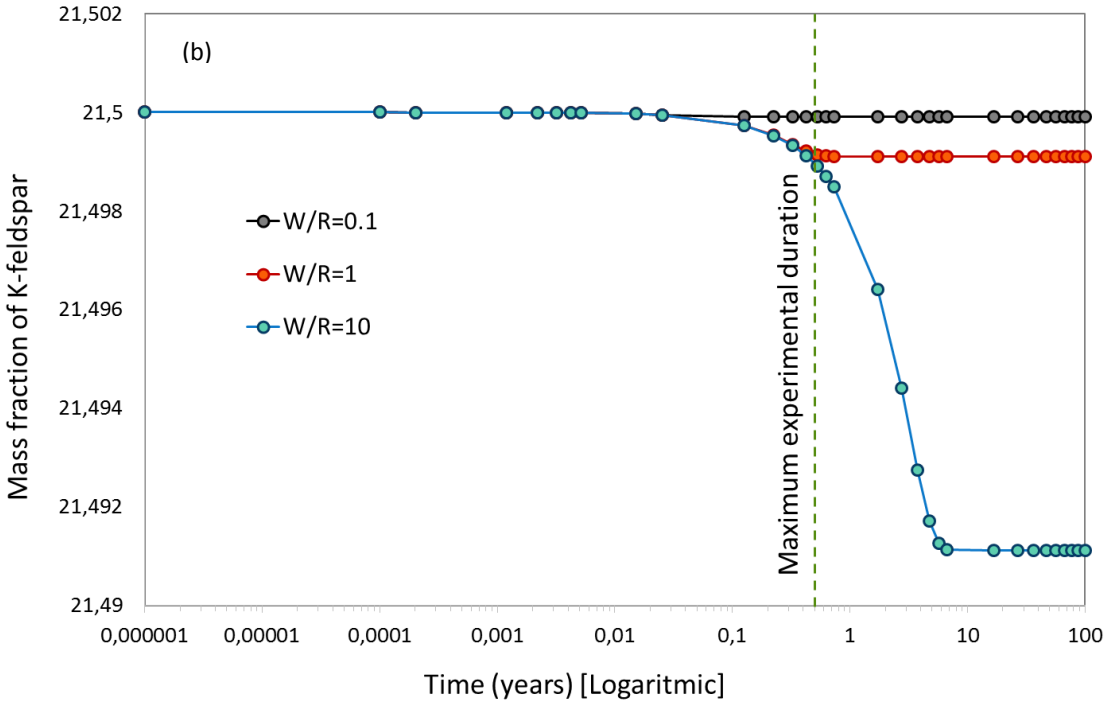
(b)
21,502
21,5
21,498
21,496
21,494
21,492
21,49
Mass fraction of K-feldspar
W/R=0.1
W/R=1
W/R=10
Maximum experimental duration
0,000001
0,00001
0,0001
0,001
0,01
0,1
1
10
100
Time (years) [Logaritmic]

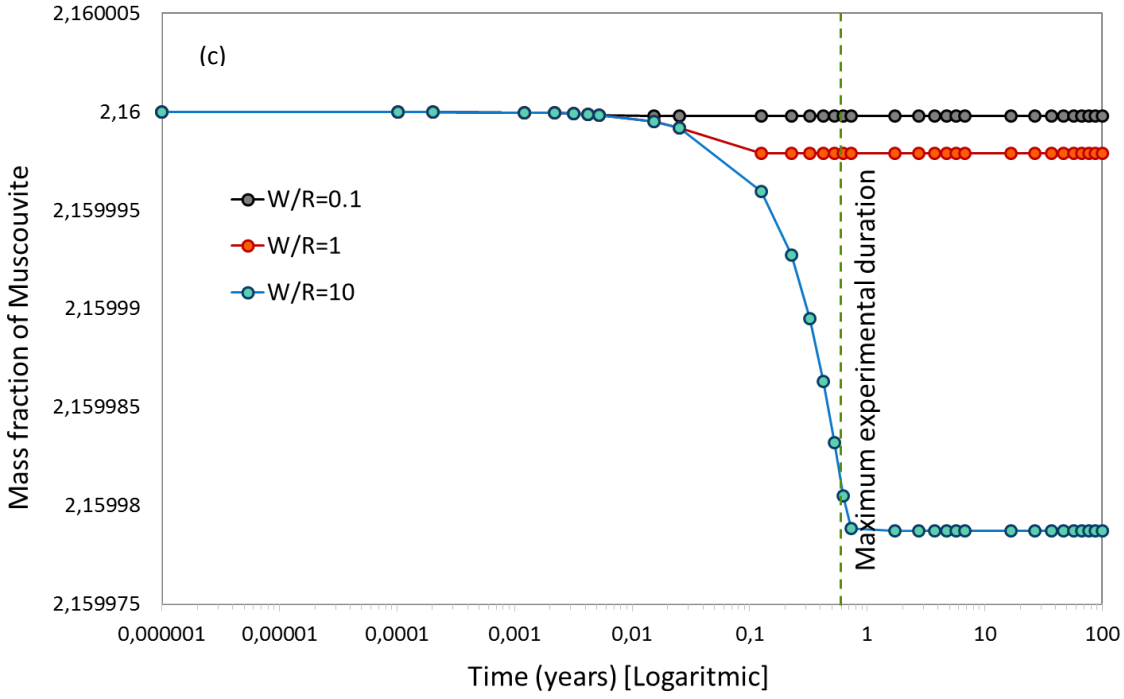

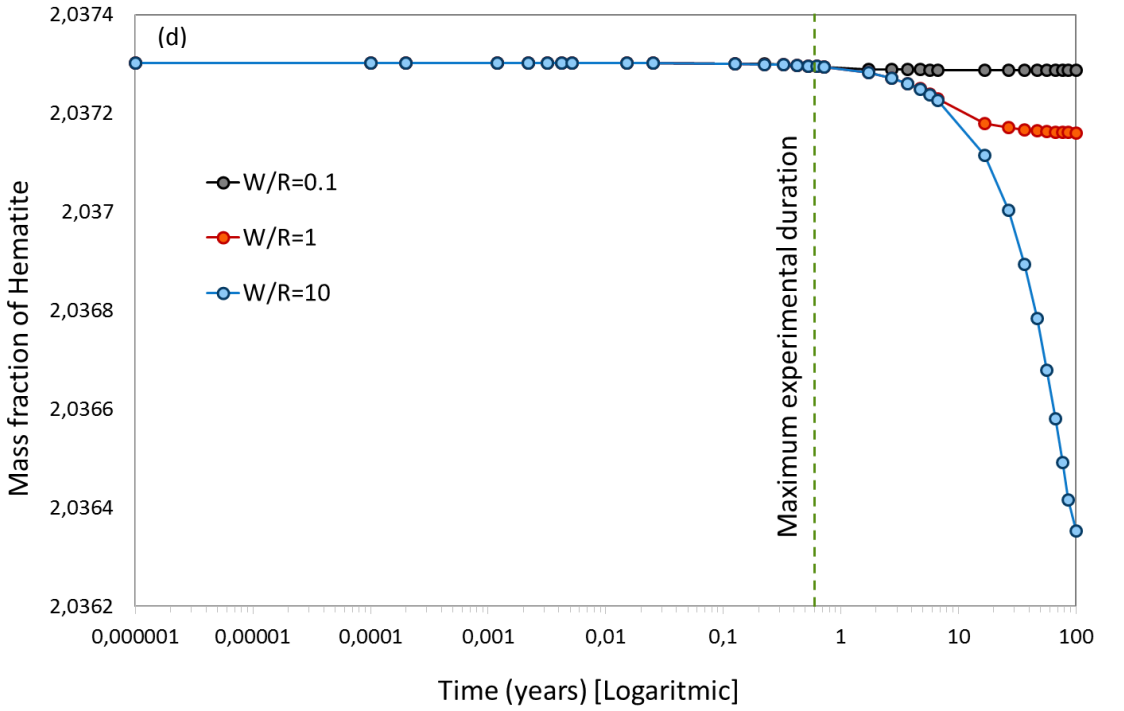

Figure 5-2 Geochemical modeling of simple sandstone mineral dissolution vs time in a H_2O-H_2 fluid using PHREEQC. (a) evolution of the quartz mass fraction; (b) evolution of the K-feldspar mass fraction; (c) evolution of the muscovite mass fraction; (d) evolution of the hematite mass fraction.

Results for combined mineral dissolution and precipitation are illustrated by considering *first* magnetite as the only product phase. The evolution of the mass fraction of minerals during dissolution in the fluid

(left axis, normalized to 100 g of reacted sandstone) is plotted as a function of time for timescales ranging from 10^{-6} to 10^{2} years and for the three W/R (Figure 5-3 ; 6-4). For each mineral, dissolution curves with and without magnetite precipitation (simple dissolution, as in Figure 5-2) are also plotted to demonstrate the influence of magnetite on minerals dissolution. The curve describing the mass of produced magnetite is shown with the scale on the right axis (normalized to 100 g of reacted sandstone).

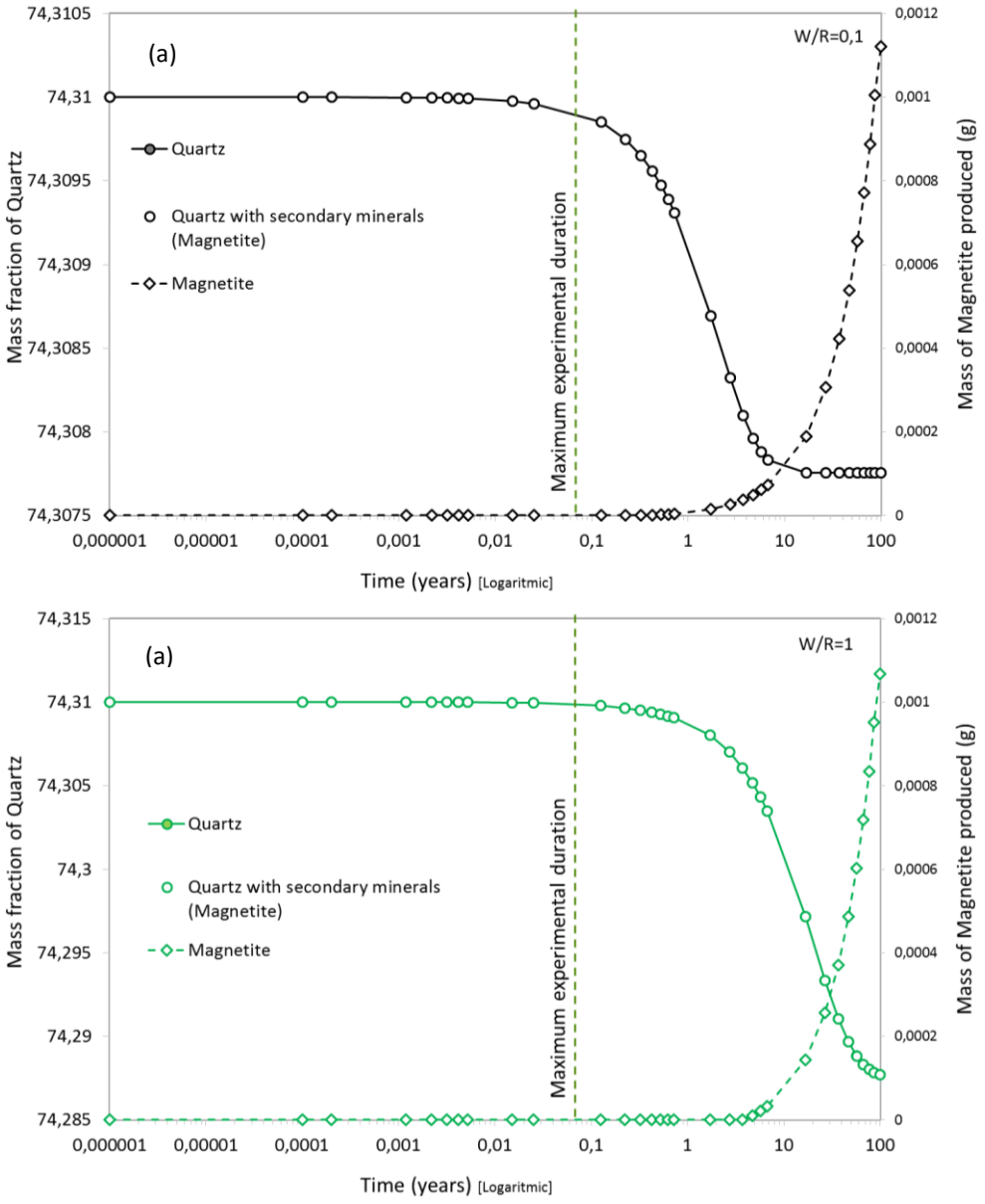

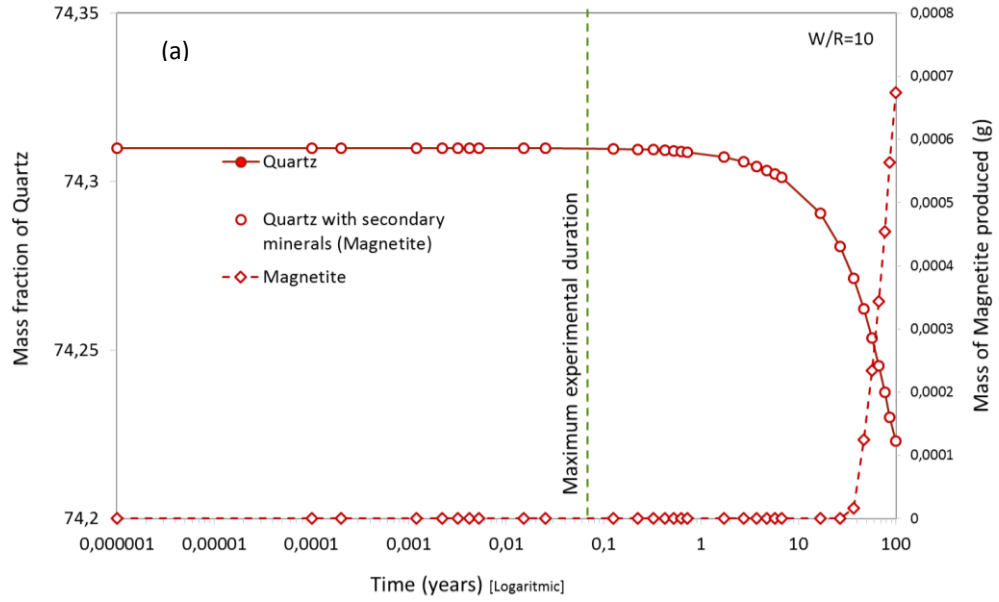
(a)
W/R=10
Quartz
Quartz with secondary minerals (Magnetite)
Magnetite
Maximum experimental duration
Mass fraction of Quartz
Mass of Magnetite produced (g)
Time (years) [Logaritmic]
74,35
74,3
74,25
74,2
0,0008
0,0007
0,0006
0,0005
0,0004
0,0003
0,0002
0,0001
0
0,000001
0,00001
0,0001
0,001
0,01
0,1
1
10
100

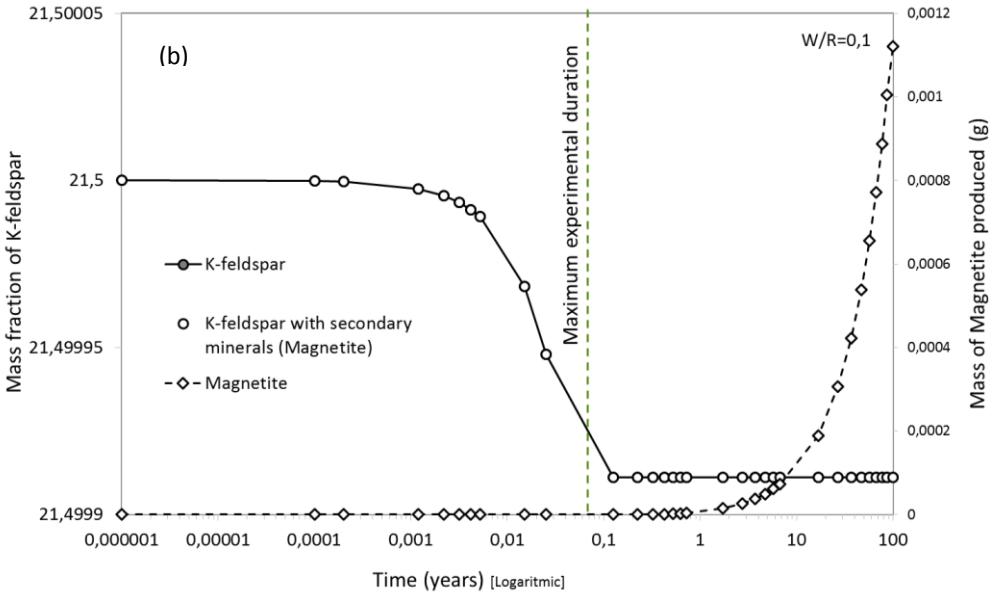
(b)
W/R=0,1
K-feldspar
K-feldspar with secondary minerals (Magnetite)
Magnetite
Maximum experimental duration
Mass fraction of K-feldspar
Mass of Magnetite produced (g)
Time (years) [Logaritmic]
21,50005
21,5
21,49995
21,4999
0,0012
0,001
0,0008
0,0006
0,0004
0,0002
0
0,000001
0,00001
0,0001
0,001
0,01
0,1
1
10
100

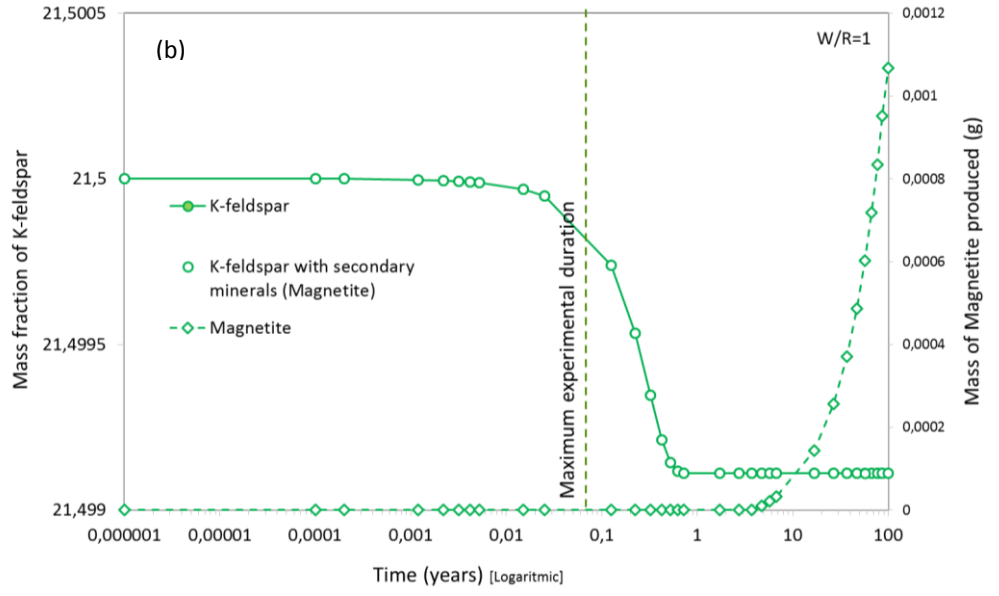
(b)
W/R=1
K-feldspar
K-feldspar with secondary minerals (Magnetite)
Magnetite
Maximum experimental duration
Mass fraction of K-feldspar
Mass of Magnetite produced (g)
Time (years) [Logaritmic]
21,5005
21,5
21,4995
21,499
0,0012
0,001
0,0008
0,0006
0,0004
0,0002
0
0,000001
0,00001
0,0001
0,001
0,01
0,1
1
10
100

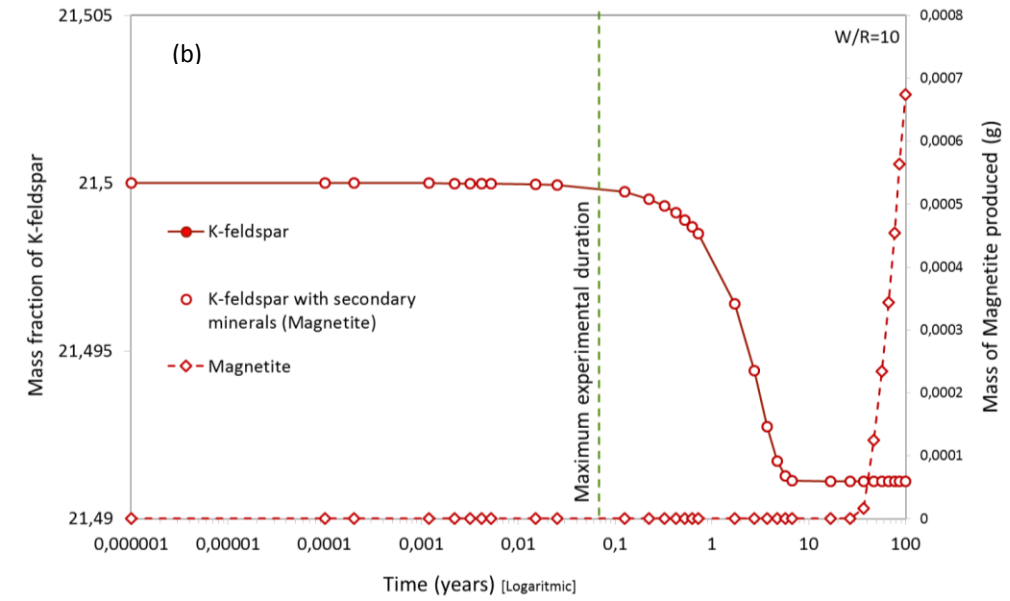
(b)
W/R=10
21,505
21,5
21,495
21,49
0,0008
0,0007
0,0006
0,0005
0,0004
0,0003
0,0002
0,0001
0
Mass fraction of K-feldspar
Mass of Magnetite produced (g)
K-feldspar
K-feldspar with secondary minerals (Magnetite)
Magnetite
Maximum experimental duration
0,000001
0,00001
0,0001
0,001
0,01
0,1
1
10
100
Time (years) [Logaritmic]

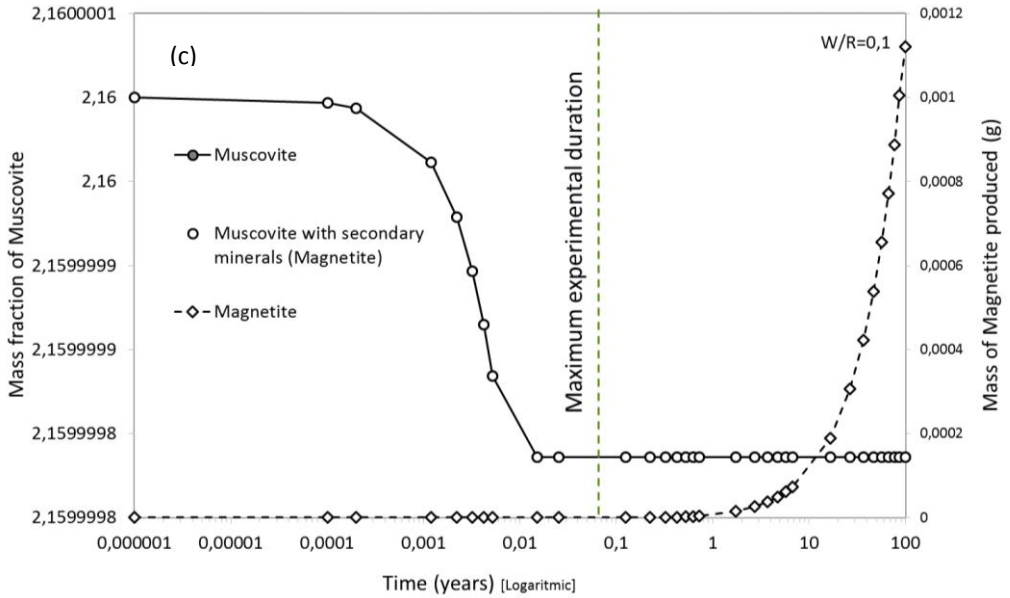
(c)
W/R=0,1
2,1600001
2,16
2,16
2,1599999
2,1599999
2,1599998
2,1599998
0,0012
0,001
0,0008
0,0006
0,0004
0,0002
0
Mass fraction of Muscovite
Mass of Magnetite produced (g)
Muscovite
Muscovite with secondary minerals (Magnetite)
Magnetite
Maximum experimental duration
0,000001
0,00001
0,0001
0,001
0,01
0,1
1
10
100
Time (years) [Logaritmic]

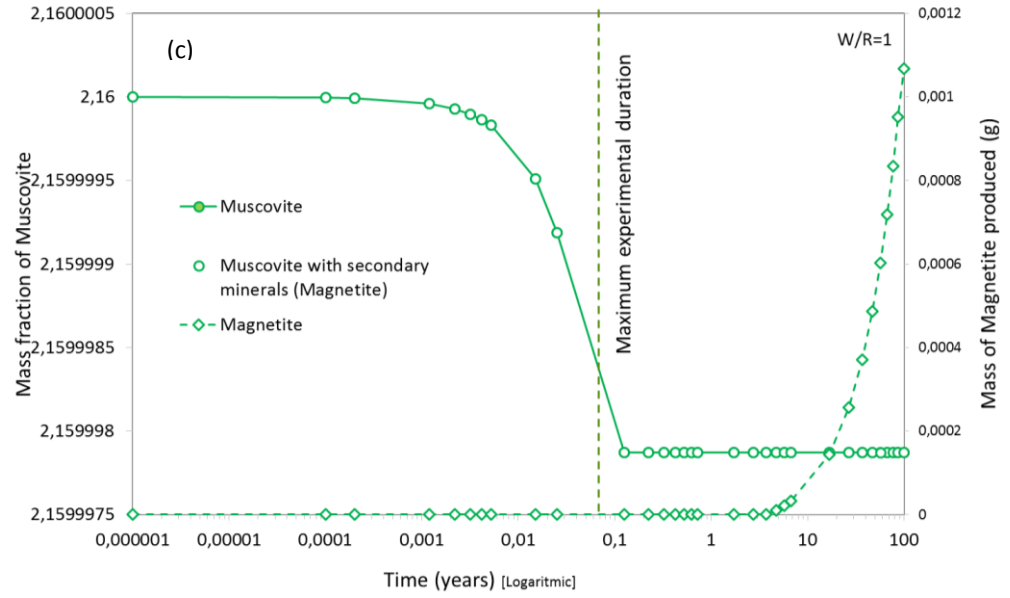
(c)
W/R=1
2,1600005
2,16
2,1599995
2,159999
2,1599985
2,159998
2,1599975
0,0012
0,001
0,0008
0,0006
0,0004
0,0002
0
Mass fraction of Muscovite
Mass of Magnetite produced (g)
Muscovite
Muscovite with secondary minerals (Magnetite)
Magnetite
Maximum experimental duration
0,000001
0,00001
0,0001
0,001
0,01
0,1
1
10
100
Time (years) [Logaritmic]

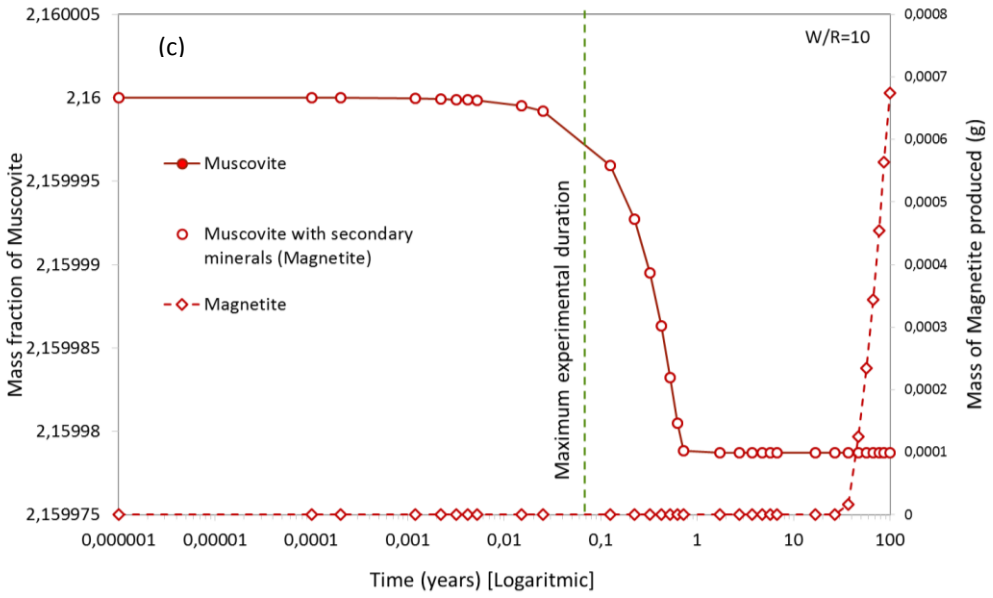

Figure 5-3 Geochemical modeling of coupled quartz (a), K-feldspar (b) and muscovite (c) dissolution and magnetite precipitation in a H_2O-H_2 fluid using PHREEQC. Each panel is for a given W/R ratio, from 0.1, 1 to 10.

When compared with simple mineral dissolution (Figure 5-2), mass fractions for quartz, K-feldspar and muscovite show no variations and dissolution curves for the "with" and "without magnetite" cases perfectly overlap, irrespective of the W/R (Figure 5-3). However, for hematite, the introduction of magnetite leads to a decrease of its mass fraction when compared (for the same duration) with the "without magnetite" case (Figure 5-4). Therefore, the mass fraction of hematite decreases more rapidly when magnetite precipitates as a reaction product. The mass of magnetite progressively increases with time and curves for the production of magnetite are progressively shifted to longer durations when the W/R is increased. For W/R = 0.1, i.e., for conditions approaching the experiments, the calculations suggest that 100 years are necessary to produce 0.001 g of magnetite (mass normalized to 100 g of reactant rock).

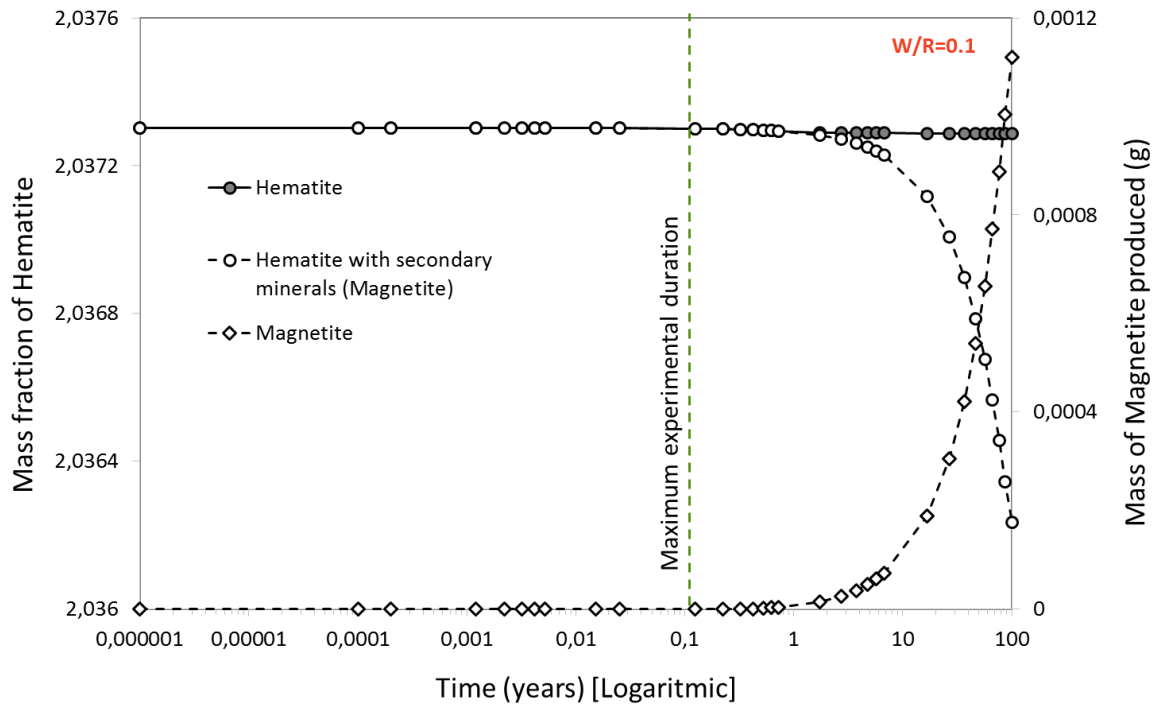
W/R=0.1
Hematite
Hematite with secondary minerals (Magnetite)
Magnetite
Maximum experimental duration
Mass fraction of Hematite
Mass of Magnetite produced (g)
Time (years) [Logaritmic]
2,0376
2,0372
2,0368
2,0364
2,036
0,0012
0,0008
0,0004
0
0,000001
0,00001
0,0001
0,001
0,01
0,1
1
10
100

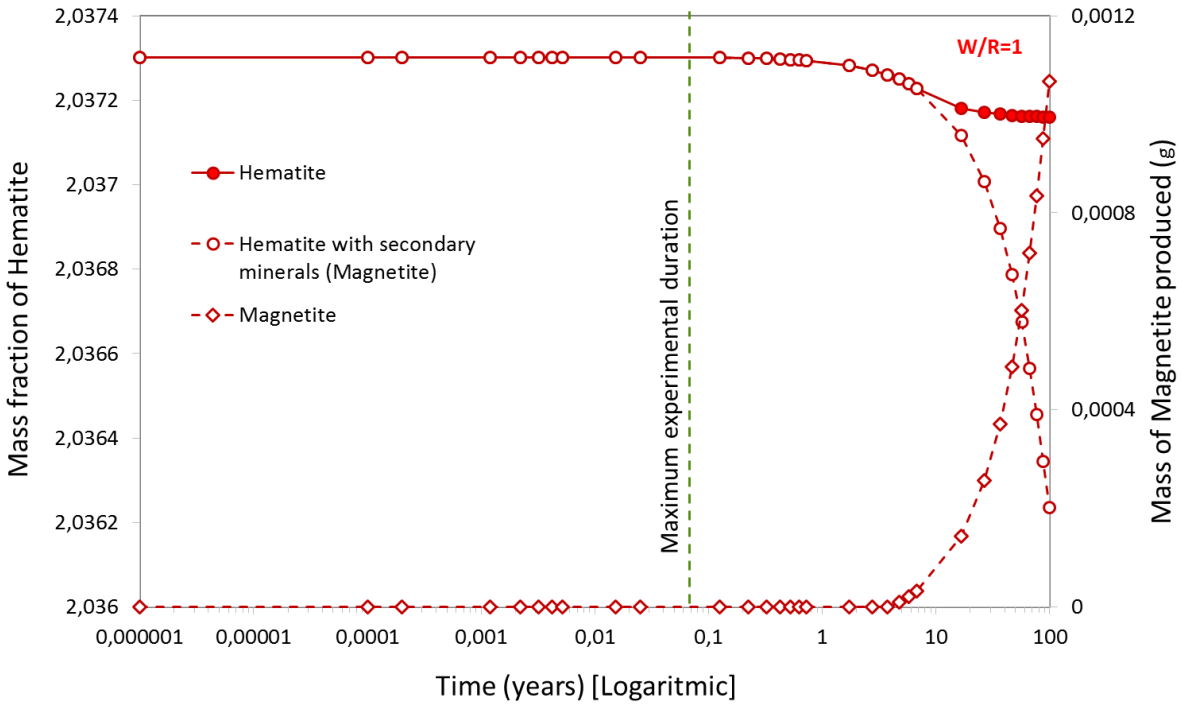
W/R=1
Hematite
Hematite with secondary minerals (Magnetite)
Magnetite
Maximum experimental duration
Mass fraction of Hematite
Mass of Magnetite produced (g)
Time (years) [Logaritmic]
2,0374
2,0372
2,037
2,0368
2,0366
2,0364
2,0362
2,036
0,0012
0,0008
0,0004
0
0,000001
0,00001
0,0001
0,001
0,01
0,1
1
10
100

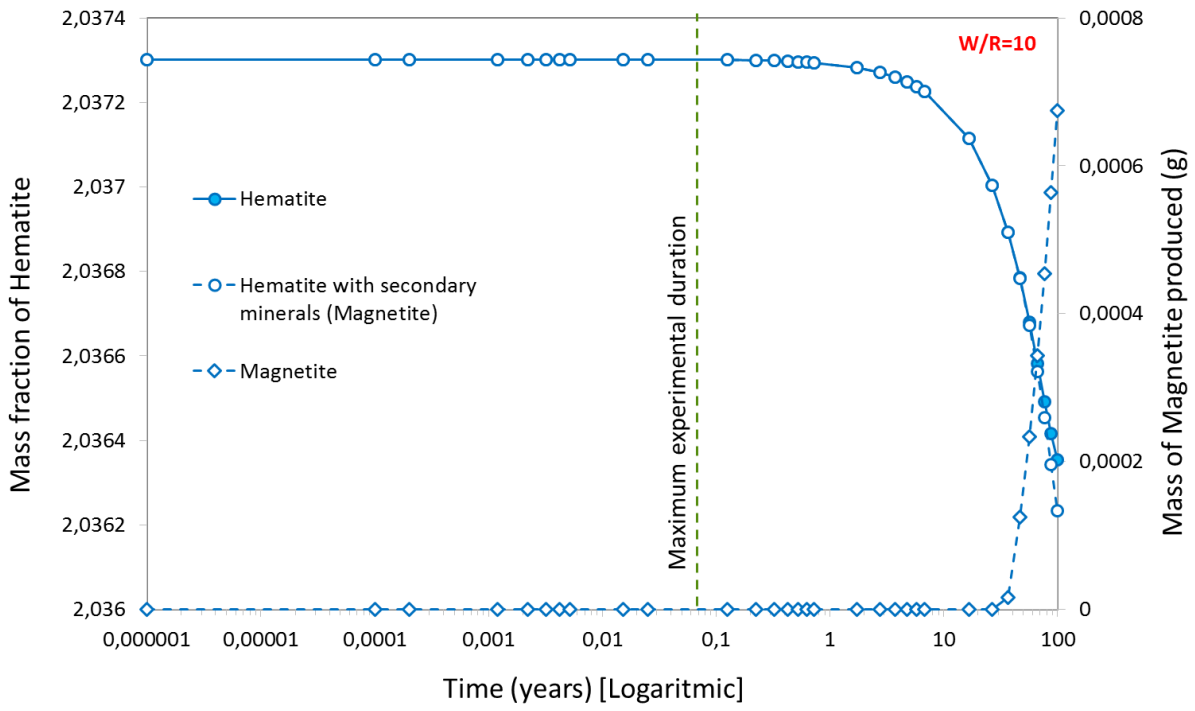

Figure 5-4 Geochemical modeling of coupled hematite dissolution and magnetite precipitation in a H_2O-H_2 fluid using PHREEQC. Each panel is for a given W/R ratio, from 0.1 (a), 1 (b) to 10 (c).

In a second case, a multiphase product assemblage, including magnetite, annite and chamosite (Table 5-2) was considered. This complex assemblage leads to modifications of rates of dissolution of quartz and K-feldspar. Focusing on results for a W/R of 1, the quartz and K-feldspar dissolution curves are both shifted from those obtained when no product mineral is considered (Figure 5-5a). For quartz, the effect of the multiphase product assemblage becomes apparent only after long durations, higher than 10 years. Quartz dissolution is slightly faster when product minerals are included. In contrast, the dissolution of K-feldspar proceeds slightly more slowly in presence of the product assemblage. The difference between the two dissolution curves appears very early, for durations < 0.1 year (Figure 5-5a). Muscovite dissolution (not shown) is not affected. Masses of annite and chamosite increase progressively with time to reach values > 0.001 g (normalized to 100 g of reactant rock). No magnetite appears in product assemblages most probably because it is allowed to react to form annite. The chamosite production curve shows a complex evolution with time with a maximum mass attained after ~50 years (Figure 5-5b).

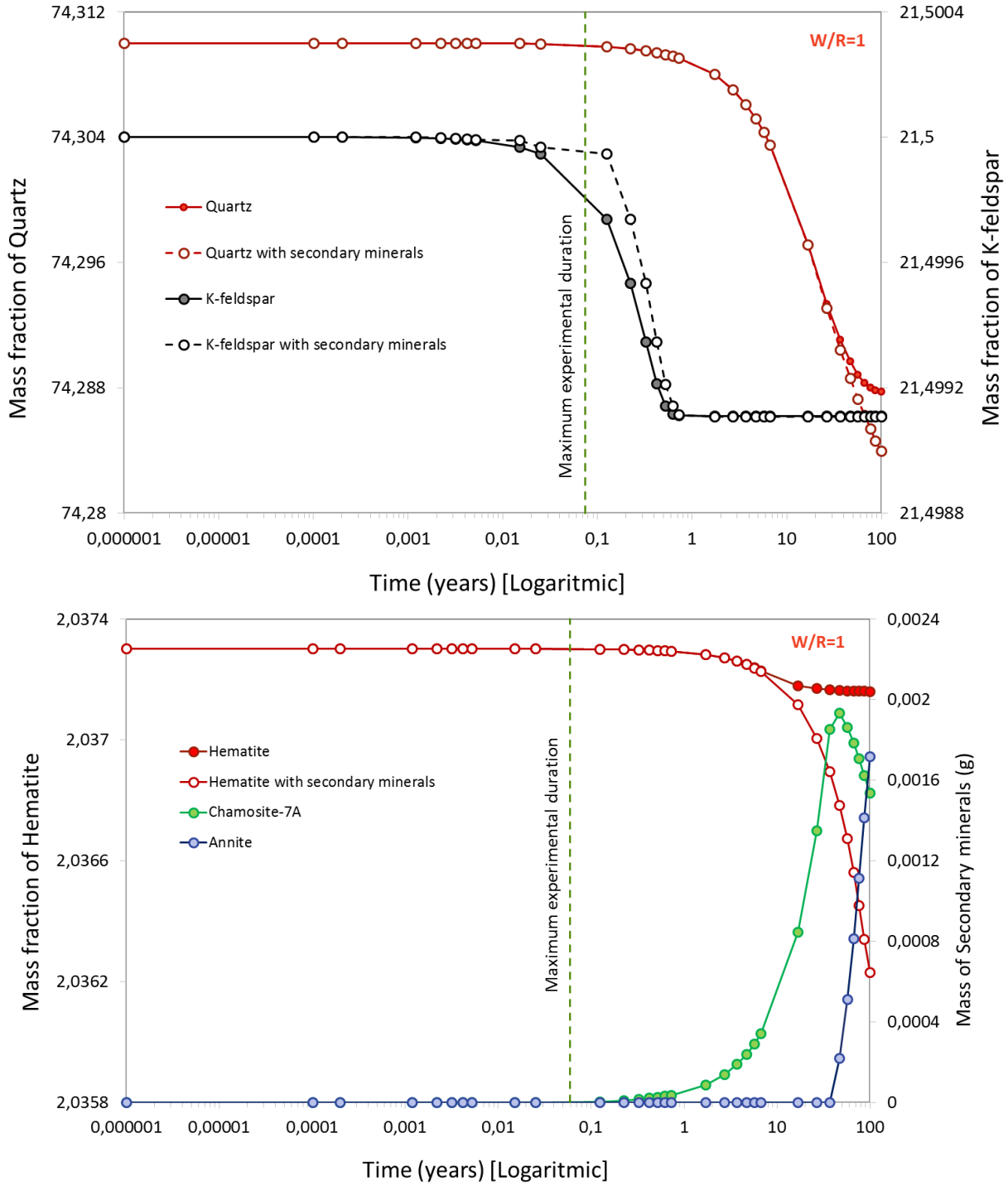

Figure 5-5 Geochemical modeling of coupled mineral dissolution and precipitation in a H_2O-H_2 fluid using PHREEQC. Product phases considered in the calculations include magnetite, annite and chamosite. W/R is fixed to 1 in both panels. (a) evolution of the mass fraction of quartz and K-feldspar during dissolution in the fluid with and without product phases included. Mass fractions of quartz and K-feldspar (left axis, normalized to 100 g of reacted sandstone) are plotted as a function of time for timescales ranging from 10^{-6} to 10^{2} years. (b) evolution of the mass fraction of hematite during dissolution in the fluid with and without product phases. The mass fraction of hematite (left axis, normalized to 100 g of reacted sandstone) is plotted as a function of time for timescales ranging from 10^{-6} to 10^{2} years. The curves describing the mass of product phases (only annite and chamosite, magnetite never appears as a product phase when annite is allowed to be present) are shown with the scale on the right axis (normalized to 100 g of reacted sandstone). The vertical dashed line gives the maximum duration of the experiments (Table 3-3). See text for details about the calculations.

5.1.2 Temporal evolution of sandstone reservoir in presence of hydrogen

As discussed previously, our experimental conditions have been chosen to be representative of large-scale hydrogen injection in Triassic sandstone formations in France. Yet, in the experiments (Chapter 4), no product phase was identified and mineral phase assemblages did not vary with time, despite experimental durations up to 6 months. The experiments thus bring no constraint on the temporal evolution at long timescales of the sandstone reservoir in presence of hydrogen. In comparison, results of the geochemical simulations allow the durability of the sandstone reservoir to be explored over timescales that largely exceed the experimental range. Conditions chosen for the calculations (temperature of 100°C, same mineralogical composition as the Adamswiller sandstone, presence of water, range of W/R values, hydrogen pressure in the 10-100 bar range) overlap with the conditions in the experiments, although the latter have been performed mostly water-free. Therefore, the main differences between the experiments and the simulations concern time and W/R, extended to 100 years and to 1 and 10 respectively in the simulations.

Underground gas storage operations are usually performed using a cushion (inert) gas like nitrogen to prevent any leak out of the reservoir or any contact between the injected gas and ground waters of the reservoir formation. Nevertheless, after injection, some residual water is still present inside the pore structure of the rock and therefore fluid rock geochemical interactions require to be considered. This statement highlights the importance of evaluating the potential reactivity of hydrogen with native fluid and rocks of the reservoir under both dry and wet conditions.

Results of the simulations constrain the timescales of fluid-mineral interaction processes that take place in the reservoir. Saturation of the fluid with respect to the main sandstone minerals is attained for durations that depend on the mineral and W/R, but range from < 1 to > 100 years. Hydrogen has little effect on the dissolution kinetics of quartz, K-feldspar and muscovite, but it strongly influences (accelerates) hematite dissolution (Figure 5-2). Hematite dissolution in the fluid is also faster when magnetite is introduced as a product mineral (Figure 5-5). Magnetite reaches 0.1 mg after durations of < 10 to ≈50 years depending on the W/R, i.e., for timescales well beyond the experimental range. It is also worth emphasizing that the proportion of magnetite produced (100 g normalized mass corresponding to ≈0.0011 g after 100 years for W/R = 0.1, Figure 5-5a) would make its detection by XRD difficult. In other words, the masses of magnetite expected to be produced as a result of interaction between sandstone and hydrogen are not inconsistent with the fact that magnetite was not detected in the experimental products. When more complex product assemblages are considered, the kinetics of quartz and K-feldspar dissolution become modified but saturation is attained in both cases after durations in the same range (from < 1 to > 10 years) as for simple mineral dissolution (Figure 5-5).

5.2 Numerical simulation of a hydrogen geological storage in the Trias Formation, France

5.2.1 Introduction to underground energy storage

The global energy production is at a turning point, from carbon-based fuels and nuclear power to renewables. Renewable energy technologies offer the promise of clean, abundant energy gathered from self-renewing resources such as the sun, wind, earth, and plants. According to the EU Roadmap, renewable energy is essential to cut greenhouse gases by at least 80% by 2050 (*EU Commission* 2011). However, the production of electrical energy from wind and solar power depends on unpredictable weather conditions. Efficiency in the use of electrical energy production from renewable energy sources strictly depends on the balance between the demand for energy and its production (*Reitenbach et al.*, 2015). These processes can only then be successful if large amounts of highly fluctuating renewable energy can be stored (Figure 5-6) while efficient energy storage allows shifting energy peak production from times of large production to times of big demand (*Després et al.*, 2016).

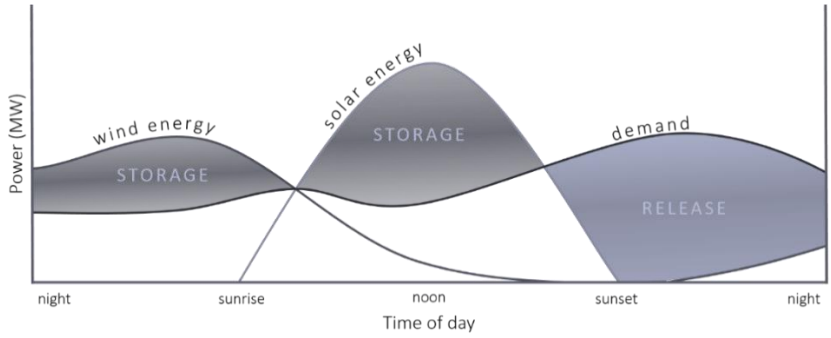

Figure 5-6 : Fluctuation of renewable energy in one day. Renewable energy are variable across several timescales: years, seasons, days, hours

5.2.2 Energy supply in France

In France, the energy needs are mainly the production of electricity and fuel for houses and transport. Before the 60's, the production of energy was mainly supplied by the coal industry before a decline of activity due to economic reasons (French coal became not competitive and reserves became limited). As France has no oil reserves, a policy of building nuclear power stations was started in the 1950s and accelerated over the next half century. Today 75% of Frances electricity production is provided by nuclear power (Figure 5-7). France is the world's biggest producer of electricity from nuclear power with 18% of the production exported to European countries (Belgium, the Netherlands and the UK).

Nuclear power is not the only source of electricity in France, hydroelectric, solar and wind energy production also contributes to the supply in a smaller amount. In 2011 electricity production was 561.96TWh with 79% coming from nuclear, 9% from hydro, 8.5% from thermal, 2.2% from wind generation and less than 1% from biomass. During the period 2011-2021, French overall power generation is expected to increase by an annual average of 1.01%, reaching 601.90TWh. Driving this

growth is an annual 1.56% gain in gas-fired generation, an increase of 1.21% in nuclear power and a 4.42% rise in renewables-based electricity supply and notably 25,000MW of wind capacity and 5000MW for solar by 2020 (following the roadmap of the Agence de l'Environnement et de la Maîtrise de l'Energie (ADEME, 2011)).

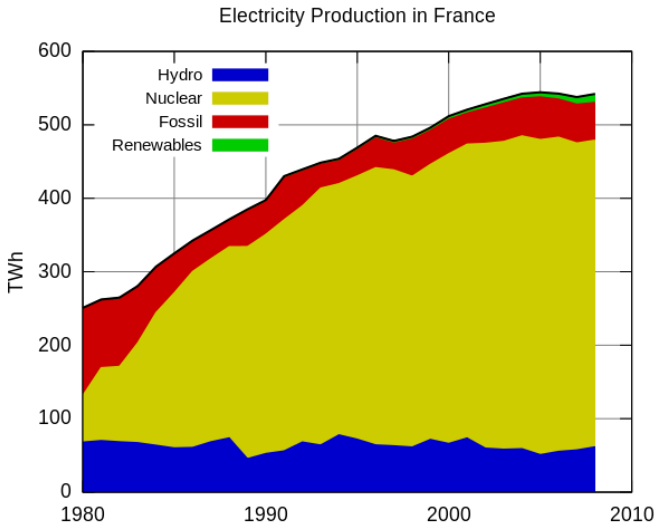

Figure 5-7 : Electricity production in France (Wikipedia)

5.2.3 Renewables energy in France

In France, the use of renewable energy has long been concentrated on the production of electricity through a growing number of wind and solar power plants; and such topic is already the major research focus in France (*Ya, A. Z.* 2016). The goal is to use pertinent resources to develop alternative to technologies based on fossil fuels. In 2015, renewable energy accounted for 18.7% of electricity consumption in France while it has held approximately 19% for past three years (Figure 5-8). The share percentage of renewable energy generation from the total electricity consumption for seven years shows the importance and growth of renewable energy. However, France is aiming to extend this sharing coverage to 23% in 2020 and 32% in 2030 (*RTE*[1] *report* 2015).

[1] Le réseau de l'intelligence électrique

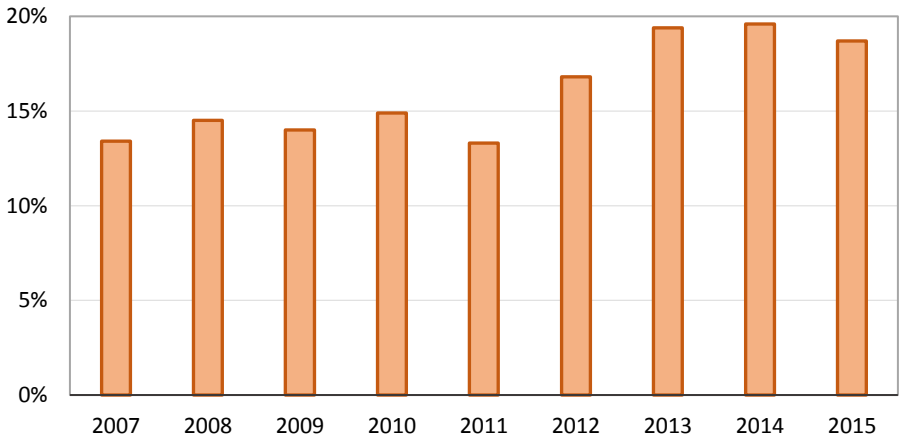

Figure 5-8 Share of renewable energy generation in total annual electricity consumption (RTE report 2015)

Looking at the monthly trend generation in 2015, one can notice that wind and solar power plants are the most important sources of renewable energy (excluding hydro) in France (Figure 5-9). The observed fluctuations are mainly due to the climate variations. These variations are extremely variable according to the timescales of observation (years, seasons, days, hours and even less). They are mainly unpredictable, and the system operator or a producer cannot control their output. Such events in the power production influence not only the availability of energy, but also the stability of the entire power grid. For instance, electricity generation from solar power (photovoltaic) is maximal in summer while wind power is higher in winter (Figure 5-9). Therefore the total in energy along a year remains variable and quite unpredictable: for 2015, the lowest of electricity generation from renewable energy is in October with 2 232 GWh and the highest is in November with 3 654 GWh while the average is 2 912 GWh. The other renewable energies like the bioenergy are much more stable and do not vary drastically during the year.

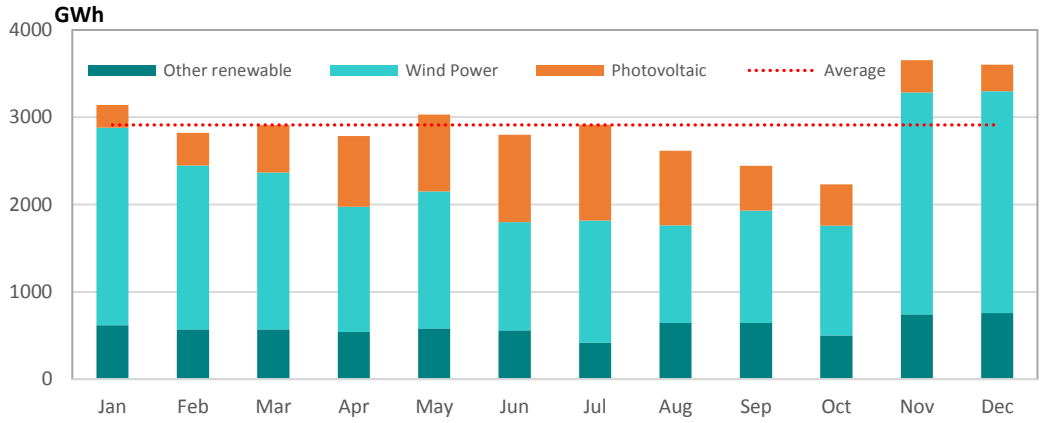

Figure 5-9 Monthly trend renewable energy generation (excluding hydro) in 2015

The fluctuations of renewable energy revealed by the power produced from renewable sources in one month are illustrated on Figure 5-10. Bioenergy production is very stable at 800 MW in contrast with

wind and solar power which vary drastically each day from about 1000 MW to 8000 MW. In total, the variations can range from 1000 MW to 10000 MW which is one order of magnitude.

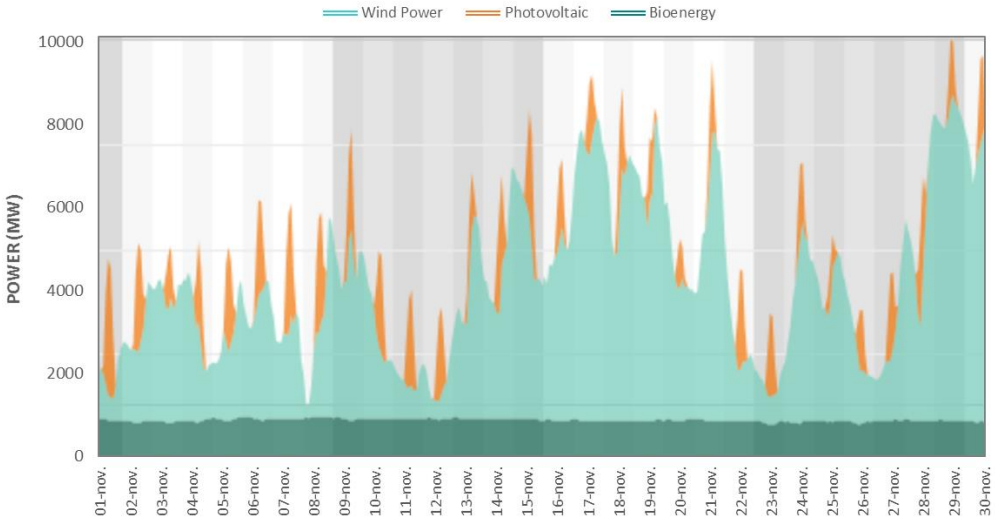

Figure 5-10 Fluctuations of renewable energy production in France in November 2015

Regarding to Figure 5-9, the net average of renewable energy generation is estimated at 2 912 GWh. The sum of the total energy deficit in Feb. (91GWh) Apr. (129GWh) Jun. (113GWh) Aug. (279GWh) Sep. (469GWh) and Oct. (680GWh) until the net average for one year is around 1779 GWh which should be redressed due to the fluctuations. Hence, approximately 1.8 TWh (or 6.5 x 10^{15} *J*) energy is needed to compensate the renewable energy fluctuation in one year as a discharge time. Thus, renewable energy needs a technology i.e., energy storage (with the capacity at least in the 1.8 TWh), which can balance out these fluctuations.

Energy storage technologies can be defined as technologies that are used to store energy in the form of thermal, electrical, chemical, kinetic or potential energy and discharge this energy whenever required (*Larsen et al.*, 2013). Energy storage technologies/systems are diverse yielding their services at power ratings from kW to GW and provide storage services at timescales from seconds to years (Figure 5-11). Energy storage systems can contribute to grid stability and reliability.

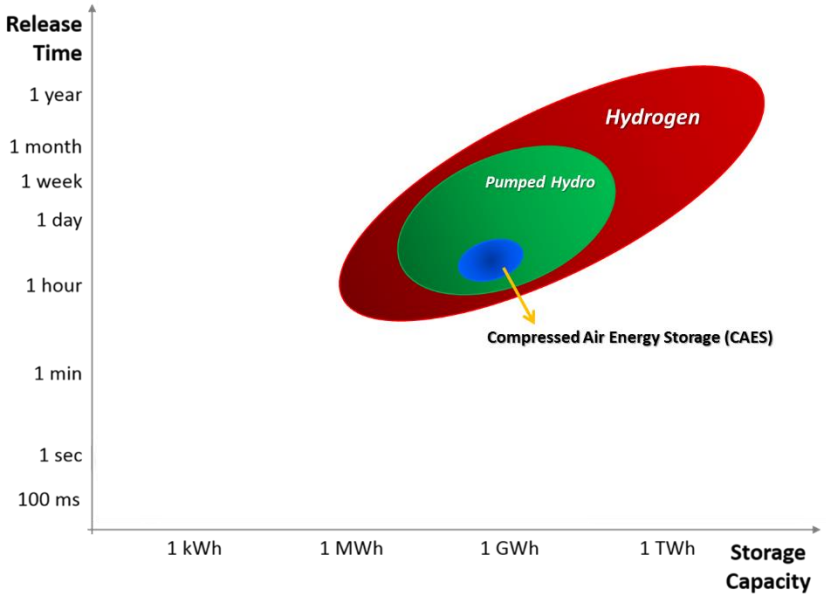

Figure 5-11: A comparison of large-scale storage options based on energy storage capacity (GWh) and discharge time scale (modified after Decourt et al., 2014)

There are three main options of energy storage technology with storage capacity in order of GWh and higher (bulk-storage): Pumped Hydro storage, compressed air energy storage (CAES) and hydrogen-based energy storage (see Figure 5-11). Pumped hydro storage (PHS) uses two water reservoirs, separated vertically, pumping water from the low one to the high one during charging and releasing it through a turbine back to the low reservoir during discharge (*Luo et al.,* 2015). Compressed air energy storage (CAES) uses electricity to compress air into a confined space and releases the pressurized air to drive the compressor of a gas turbine. Both of them use mechanical technology to store the energy (*Mahlia et al.,* 2014). Hydrogen energy storage solutions are based on the electro-chemical conversion of electricity into a hydrogen by means of water electrolysis. In other hands, at the concept of the renewable energy fluctuation, electrolyze are used to transform excessively produced electrical energy into chemical energy in the form of hydrogen (*Feldmann et al.,* 2016). This energy storage could be the best way of absorbing peaks in renewable energy and avoiding the waste of large quantities of renewable power, especially when natural sites for pumped hydro storage are not available or already occupied (*Decourt et al.,* 2014).

5.2.4 Geological potential in France for energy storage: sitology and needs

Today, in France, the potential for implementation of geological storage of energy remains relatively unknown. Underground is already intensively used for several purposes, and furthermore, urban area can be relatively dense in some region of the country. There is a need to conduct studies to complete data base gathering information on suitable underground geological formations coupled with (i) surface data on electrical energy supply and transmission, (ii) protected area like potable ground-waters area, and (iii) permanent industrial activities like natural gas storage and geothermal production.

The main geological targets identified are:

- Saline aquifers (storage in porous media)
- Depleted oil/gas field (storage in porous media)
- Saline rocks (storage in solution salt formations)
- Crystalline rocks (storage in mined caverns)
- Abandoned mines (storage in existing mined caverns)

5.2.4.1 Saline aquifers and depleted gas/oil field (Porous Formations)

France is mainly composed of two large basin sedimentary structures which could offer a large potential for massive storage of energy (Figure 5-12): (i) the Paris Basin which is the largest, the Aquitaine Basin. These two basins have a large area of several thousands of km² and several hundred meters thick, with a vast level of lithology structure appropriate for fluid and gas storage as demonstrated in the past. Still, depleted reservoirs are apparently much limited in France compared to aquifer storage (Table 5-4). The rest of the country also contains other sedimentary basin structures much smaller: Alsace, Bresse, Limagne and Provence basins. These targets have been largely investigated for CO_2 geological storage (Bonijoly et al., 2009) and estimation of capacity storage in volumes of several Gt of CO_2 storable have been provided but with a very large level of uncertainty due to the high degree of difficulty to estimate the connectivity within the porous structure at such large scale area.

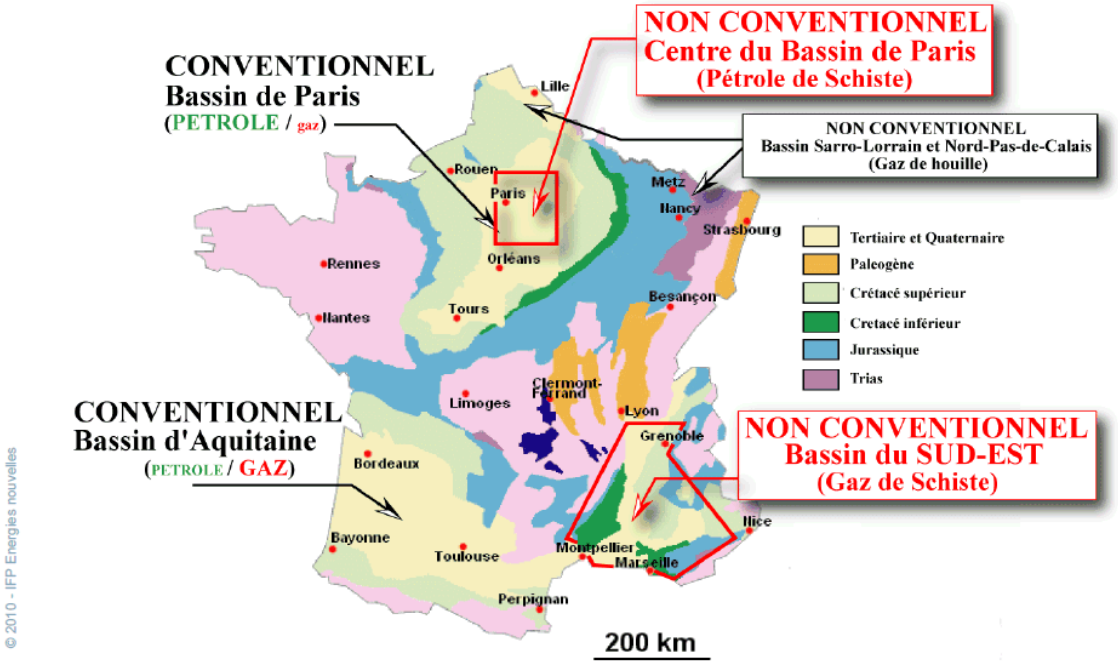

Figure 5-12 : Sedimentary basins in France used for oil and gas production (Copyright IFPEN)

5.2.4.2 Saline rocks

Saline caverns are built by dissolution of salt rock (solution mining technique) in evaporate formations. Volumes can range between 200 and 500 10^3 m^3. Elaborated 50 years ago for oil and gas storage purpose solution mining techniques allows for a perfect control of the shape and the size of cavities. Still, geological characteristics remain primordial: saline formations must be relatively homogeneous with a relatively low proportion of unsolvable (<30%) and a thickness about 300 m. Formations with a thickness lower than a 100 m are considered not suitable. To make a good screening of suitable formations it is therefore necessary to have a good knowledge of the lateral extension, the thickness and the percentage of unsolvable for the considered saline basins.

France geology is composed of six main saline basin areas appropriated for investigations: Alsacian basin in the North East, Aquitaine basin (onshore and offshore) in the South West, Bourg en Bresse and Jura in the Eastern part, Paris Basin, South East basin (onshore and offshore), and Valence basin in the South East as well (Figure 5-13).

Today, the situation in France concerning the use of saline formations for storage is mainly concentrated in Manosque (operated by GEOMETHANE) where 28 caverns are used for crude oil and refinery products storage. One cavern in Grand Serres (operated by NOVAPEX) is also used for propylene storage and one in Viriat (operated by TOTAL) for ethylene. Tersanne caverns are operated by Gaz de France and contain natural gas. Gaz de France have recently created new sites in Hauterives and Alsace (2011, Ministère de l'écologie, du développement durable et de l'énergie).

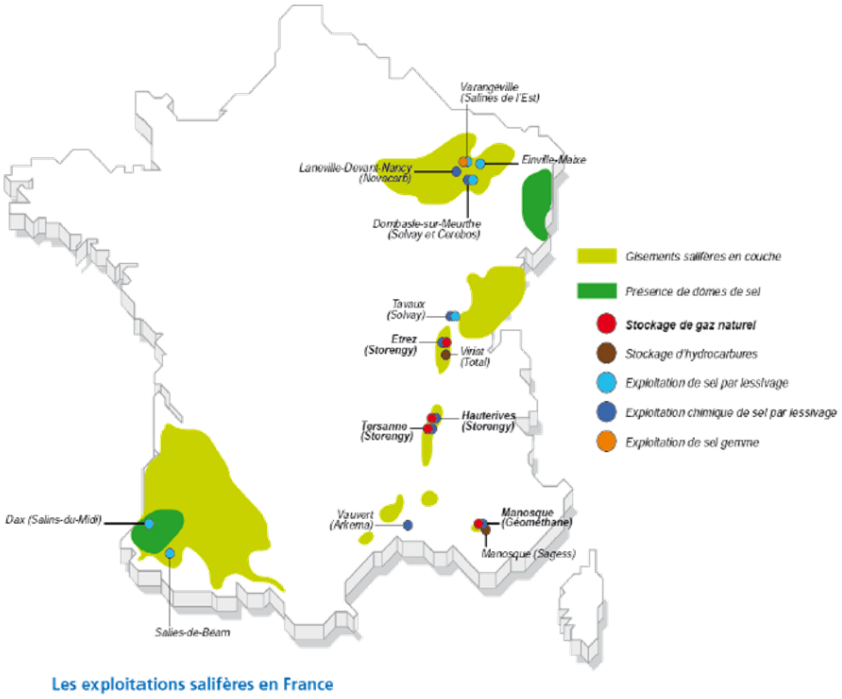

Figure 5-13: saline formations in France and associated storage experience, CH_4 liquid fuels and hydrocarbures

A recent study conducted to evaluate the potential of the different saline formations in France suitable for conducting CAES operations has been performed (Beccaletto, et al., 2010). For each saline basin, estimates of the ability and performance potential are provided in three categories: good, medium or poor. Based on the cross cutting of several characteristics of the formations, Alsacian, Bourg-en-Bresse, and Valence saline basins have been identified the most suitable saline formations for CAES application (Figure 5-13).

5.2.4.3 Crystalline rock (mined cavities)

An alternative for natural storage environment can also be found in crystalline rock formed in the crust of the earth's surface. Using conventional mining techniques, caverns are excavated and intersecting galleries are built for several types of storage applications (Liquid Hydrocarbons, Liquefied Hydrocarbons, Natural gas, Industrial Wastes, Chemicals). The selection of the sites must ensure high sealing properties, geomechanical stability and relative low surface subsidence. A cavern design must provide the optimal geometry and depth of the cavern along with a pertinent scenario of operational pressure of the cavern in order to compensate the ambient hydrostatic pressure of the rock. It may be necessary to create a water curtain above the cavern to improve the cavern storage pressure. Typical caverns depths range from 50 to 250 m. Rock caverns can also be lined to improve sealing properties. Though transmission lines may be costly, it allows for excavation at shallow depth compared with unlined caverns which in turns can reduce significantly the total cost of construction.

Storage of gas or liquefied hydrocarbons in lined or unlined caverns is today widely developed in the world. Lined Rock Caverns (LRC) concept has been more investigated in Scandinavian countries, especially in Sweden at Gränsgerberg and Skallen sites (Mansson et al., 2006). In France, several operations have been conducted by different operators: propane stored in Petite Courrone by SHELL, butane and propane in Martigues by GEOGAZ-LAVERA, liquefied hydrocarbons and oil in Manosque by GEOSEL, and propane in Senecey-le-grand by BUTAGAZ, in Martigues by PRIMAGAZ-LAVERA, in Donges by TOTAL, and in Gargenville by GEOVEXIN. All of these mined caverns are built in salt formations.

The potential in France of crystalline formations for lined or unlined rock caverns is granitoïdes rocks and certain metamorphic rocks non-altered by presence of faults or fracturation. To investigate such systems one need to (i) select favorable rock mass, (ii) to remove regions containing contacts (weak zones) and faults, (iii) and to keep regions with a sufficient surface area (several tens of km²) deemed large enough to ensure feasibility in a safe domain. Based on this approach and using 50 km² as a surface area, and without having a notion of the thickness of the formations, Beccaletto et al. (2010) investigate a first screening in France highlighting a large potential in the Massif Central and Brittany region of the country as well as in Corsica island.

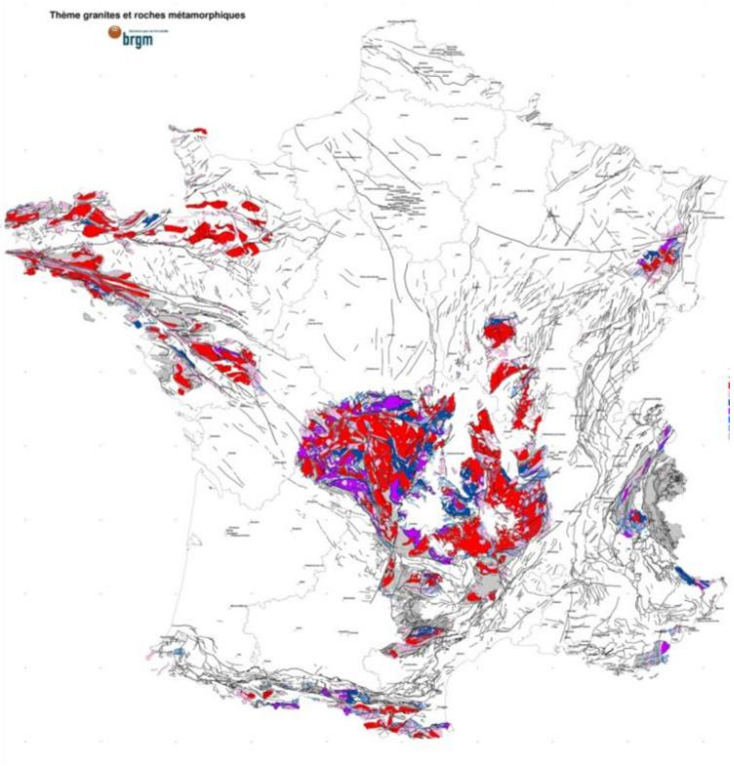

Figure 5-14 : Crystaline formations in France (copyright BRGM)

5.2.4.4 Abandoned mines

Mineral resources are and have been for many countries a key employer and economic driver promoting a large and fast deployment of such industry sometime accompanied with important environmental issues. France has a very large history in mining industry which is almost completely dormant today. The decline of mine industry initiate in the sixties for coal and iron, and at the beginning of the eighties for the other minerals. The last mine of iron and uranium closed in 1995 and 2001, respectively. The potash exploitation stopped in 2003 and the complete closure of coal production occurred in 2004. The only remaining mining industry in the Metropolitan France is the extraction of salt by underground or by solution mining. About 4,000 abandoned sites have been identified all over the country (Figure 5-15 and see also Didier et al., 2008).

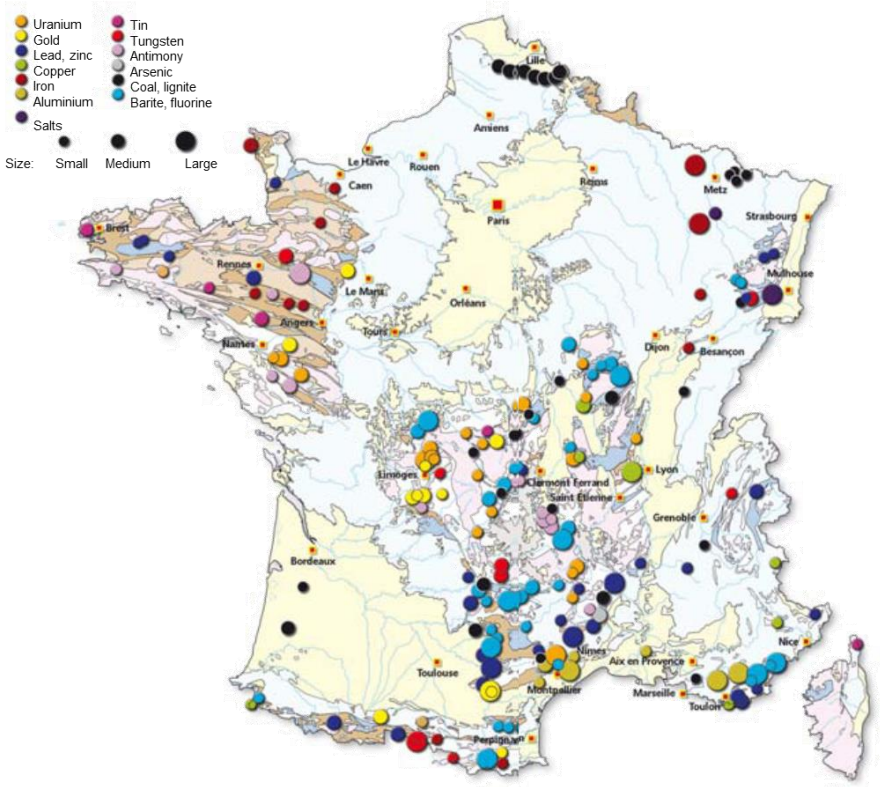

Figure 5-15: Major former mining fields in France (copyright BRGM)

5.2.4.5 Natural Gas Storage

The concept of gas underground storage in geological formations comes from the need to compensate for the seasonal fluctuations in consumption. Natural gas consists mainly in methane, ethane and propane. Gas is stored during periods of low demand and withdrawn during period of peak demand. Suitable geological formations can be found all around world and are currently used for to store natural gas underground since the 40's. Unlike surface gas tanks, storing into porous formations offers a larger volume for gas storage with higher pressures and a less risky environment. Originally considered as a secondary energy resources, natural gas was initially flared or vented involving negative environmental consequences: air pollution, greenhouse effect, economic loss (Atoyebi, 2010). Three main types of geological formations are in use today: depleted oil/gas reservoirs, aquifers, and salt caverns. Abandoned mines and lined rock caverns have also been investigated in a less extend on a world scale.

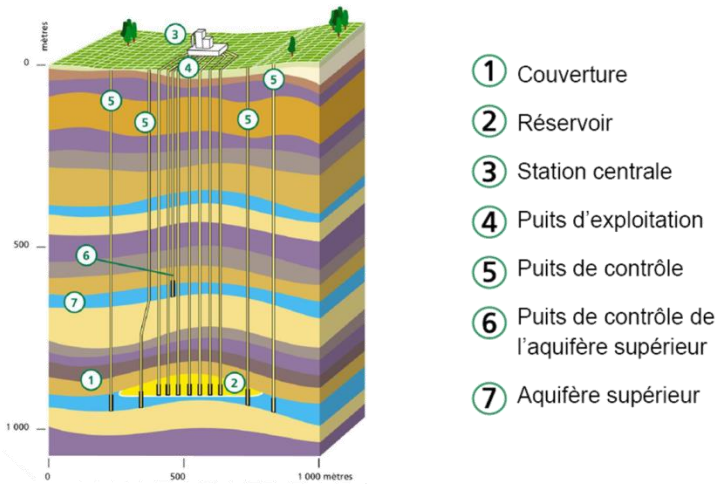

Figure 5-16: Concept of underground gas storage and monitoring (copyright Storengy)

The main characteristics of an underground gas storage facility are (i) its storage capacity and (ii) its deliverability rate. The presence of a "cushion" gas is needed to maintain an adequate minimum storage pressure. The "working" gas is defined as the volume of gas withdrawn or injected during operational periods. Table 5-3 summarizes the worldwide distribution of underground gas storage types and capacities (*Ozarslan*, 2012).

Table 5-3: Worldwide distribution of underground gas storage types and capacities (Ozarslan, 2012 and International Gas Union, 2009)

Storage type	Number of sites	Working gas volumes ($10^9 m^3$)	Cushion gas volumes ($10^9 m^3$)	Peak withdrawal capacity ($10^6 m^3/d$)
Gas field	428	274	291	5777
Oil Field	39	17	15	595
Aquifer	86	44	68	1214
Salt cavern	74	16	6.6	1434
Rock cavern	2	0.069	0.014	12
Abandoned mines	1	0.003	0.002	1.7
World total	**630**	**352**	**381**	**9034**

From this table, it can be noticed that the two third of the storage is conducted in gas field, then come aquifers and salt caverns and finally in a less amount, depleted oil field. Oil/gas reservoirs and aquifers offer the larger volume capacity but requiring a large cushion gas volume which can be equal or higher than the working gas volume. Salt caverns in comparison provide a large deliverability rate compared to their working gas capacity. Generally used to meet seasonal demand, reservoirs or aquifers are cycled

once a year while salt cavern can be used several times a year to meet peak load demand (*Ozarslan*, 2012; *International Gas Union*, 2009). In comparison, compressed air or hydrogen storage facilities should provide facilities able to be cycled several times a day (*Succar and Williams*, 2008; *Ozarslan*, 2012)

The underground gas storage in France is operated by two main operators: Storengy (subsidiary of ENGIE) and TIGF (Transport et Infrastructures Gaz France) formerly a subsidiary of TOTAL since 2013 and today belonging to a consortium composed of the Italian operator Snam, the Singaporian GIC state funds and EDF invest. Storengy operates thirteen sites (nine in aquifers located in the Paris Basin at depths varying between 400 and 1200 m; three in salt caverns situated at 900 and 1400 m depth in the southeast of France, and one depleted reservoir). TIGF operates two storage sites both in aquifers southwest France at Izaute and Lussagnet, respectively located at 500 and 600 m deep. Figure 5-17 is a map localizing sites and operations of underground gas storage conducted in France.

Figure 5-17: The natural gas grid in France (IEA, 2012)

Table 5-4 summarizes the storage capacity in France (IEA, 2012). The type of gas storage in France is mainly conducted in aquifers. Storengy's total storage capacity is 10.4 billion cubic meters (80% of French storage capacity) against 2.7 bcm for TIGF operations. In total, France capacity storage represents about 3.7% of the worldwide capacity storage. The maximum gas supply capacity of France's natural gas infrastructure (including pipelines imports, Liquefied Natural Gas regasification and peak

storage output) is 528 106 m^3/day (with a pick daily natural gas demand estimated at around 363 106 m^3/day) which leaves 31% (165 106 m3/day) spare capacity in the natural gas network (IEA, 2012).

Table 5-4 : Natural gas storage capacity in France (IEA, 2012)

Type of storage	Volumes (10^9m^3)	Withdrawal capacity (10^6m^3/d)
Aquifers	11.96	204.77
Salt caverns	1.07	75.34
Depleted reservoir	0.08	0.567
World total	**13.11**	**280.68**

5.2.5 Modeling of underground storage of hydrogen to compensate a week-long shortage of energy production in Ile de France

Regarding to Paris climate changes agreement (COP21 2016), increasing renewables energy (wind and solar power) to 36% of the global energy mix by 2030 would provide about half emissions reductions needed to hold warming to 2°C (IRENA 2016). In 2015, the final electricity consumption in Île-de-France reached 67,713 GWh (RTE report). It increased by 1.7% compared to 2014, due to cooler temperatures early in the year and warmer in the summer. In addition, renewable energies accounted nearly 19% of Île-de-France electricity consumption. Therefore, if we consider the same trend of electricity consumption in Île-de-France until 2030, the electricity that should be covered by renewable energy will be 34,150 GWh.

In this study, we estimate the need to compensate a week-long shortage period of renewable energy electricity which would result in a deficit of 467 GWh (that is about two days of electricity consumption in Île-de-France). However, the possibility to provide this volume of electricity consumption by underground hydrogen storage was examined by numerical simulation. The process of converting hydrogen into electricity has a poor level of energy efficiency and is estimated at a maximum about 60% (*Bai et al.*, 2014). Therefore, by assuming an energy density of hydrogen about 33.3 kWh/kg and the hydrogen density at surface conditions around 0.084 kg/m3 (*Mallard et al.*, 1998), the volume of hydrogen which has to be stored to cover the deficit would equate around 279 million Sm^3 of hydrogen gas. The scenario to implement the underground hydrogen storage includes 3.5 years for the development period to charge the reservoir with hydrogen, six month of no injection to stabilize the reservoir pressure and then withdrawal period. The average daily injection is approximately 255,000 Sm^3, which provides the necessary volume of hydrogen (279 million Sm^3) after 3.5 years.

5.2.6 Geological model

A typical aquifer from the eastern France at the Buntsandstein layer of the Paris Basin was selected as a reservoir target for investigation of hydrogen injection and storage (Figure 5-18). The Paris Basin is the largest on-shore French sedimentary basin and it has been extensively studied for evaluating its potential for CO_2 geological storage (*Bader et al.*, 2014) and for geothermal production (*Aquilina et al.*, 2010).

The Buntsandstein layer represents the lower group of the tripartite classic Triassic and it is subdivided by lithological criteria into three layers of sandstone: Voltzia sandstone, Couches intermediate sandstone, and the Vosges sandstone. Thickness, geometry and the petrophysical properties of layers are different and depend on the location of the injection. However, regarding to the reservoir parameters (permeability and porosity) the position of the well that was considered in this study is shown in Figure 5-18 and the petrophysical properties and thickness of the layers were shown in Table 5-5.

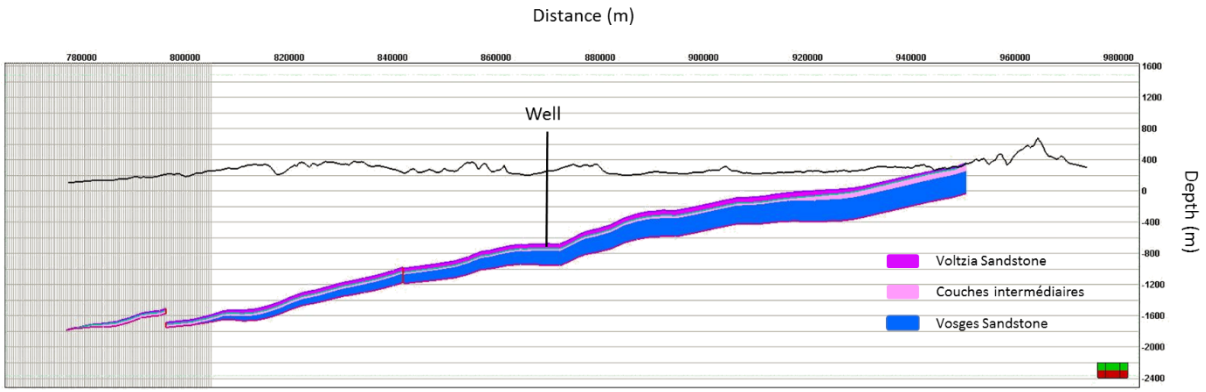

Figure 5-18 Three layers of Buntsandstein and the position of the well in this study

The depth of the considered storage ranges from around 200 m at the top of the structure to more than 20 km at the flanks. The western flank of the structure was chosen to accommodate the storage site with the average deep of 1 degree.

Table 5-5 Thickness and petrophysical properties of Buntsandstein layers sandstones

Layers	Thickness (m)	Permeability (mD)	Porosity (%)	Pressure (bar)	Temperature (°C)
Voltzia	44	1050	24	46	30
Couches intermediate	44	946	20	52	31.5
Vosges	303	1244	18	56	33

The thickness of the Vosges layer is one order of magnitude larger than the two others, however, the porosity and the permeability are similar for all the layers, around 20% for porosity and 1000 mD for permeability, making the reservoir a good candidate with large capacity and good characteristics for injection (Figure 5-19). In addition, the layers pressure and temperature range from 46 to 56 bar and from

30 to 33°C, respectively. We will consider relative permeability and capillary pressure of the hydrogen-water system of the Vosges sandstone measured in chapter 5.

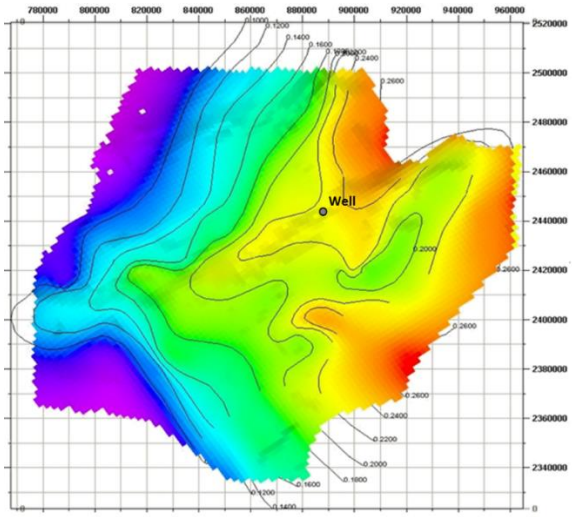

Figure 5-19 Top view plan of the Vosges layer permeability and porosity and the well position

5.2.7 Geochemical data

The Triassic sandstones formations are dominated with quartz and feldspar representing 95-97% of the overall mineral volume. The interstitial materials are composed of muscovite, hematite, anhydrite, calcite and clay minerals (Table 5-6). We considered the reservoir initially saturated with pore water with a pH of 6.055 and chemical elements with the initial concentrations measured by *Millot et al.*, (2011) and presented in (Table 5-6).

Table 5-6 The mineralogical composition of Triassic sandstone and the Initial total aqueous concentration

Minerals component mods and volume		Initial total aqueous concentration	
Minerals	Volume fraction (%)	Species	Concentration (mol/kgw)
Quartz	72.0	Br	1.01e-02
K-feldspar	22.9	C	1.07e-03
Muscovite	2.00	Ca	2.02e-01
Hematite	1.00	Cl	2.37e+00
Anhydrite	1.00	Fe	2.02e-12
Calcite	1.00	K	2.82e-02
Clay minerals	0.10	Mg	5.29e-02
		N	4.05e-03
		Na	1.85e+00
		S	7.84e-03
		Si	8.94e-04

5.2.8 Hydrogen storage reactive transport modeling

To simulate the hydrogen storage development and operations, a 2D open saline aquifer with the average one degree slope is considered (see Figure 5-18). The reservoir is composed of the three identified formations layers, i.e. Voltzia, Couche Intermediaires and Vosges layers with the corresponding petrophysical properties presented in Table 5-5 and with the initial value of the rock minerals compositions and the aqueous concentrations presented in Table 5-6.

Hydrogen is injected with a constant flow rate of 255,000 Sm^3/day through the well, placed at the top 10.5 m of the upper layer (Figure 5-18). Injection lasts for 3.5 years followed by a production period through the same well of 6 years after 6 month of idle to stabilize the reservoir. The gas density is calculated using the Peng-Robinson EOS (*D.B.Robinson and D.-Y.Peng*, 1978) (0-1% err). The liquid density is modeled by the McCain model (*McCain Jr*, 1991). Since the hydrogen is slightly soluble, its impact on viscosity is neglected, and the viscosity of both phases is supposed constant for simplicity. The rocks above the Voltzia layer are assumed to be tight against the stored hydrogen and are thus represented in the simulation as a no-flow boundary.

The reactive transport software HYTEC (*Van der Lee et al.,* 2003 and *Sin et al.,* 2016) is used in this study. HYTEC is a reactive transport code that integrates a wide variety of features and options that have evolved, after more than a decade of development, to a widely used and versatile simulation tool (*Steefel et al.,* 2015). The formulation model and reactive transport have been presented in section 3.2.

The rock mineral composition in Table 5-6 reveals that quartz and K-feldspar are the abundant mineral components of the sandstone of the storage. As mentioned in section 4 of this manuscript, experimental study revealed that hydrogen has no major impact on the quartz and the k-feldspar lithology of this sandstone under conditions of natural hydrogen storage. In addition, it has illustrated that the sandstone microstructure is not expected to be significantly modified during interaction with hydrogen and the physical properties (porosity, permeability) that control the efficiency of sandstone as a reservoir will remain essentially unmodified. Therefore, abiotic reaction seems unimportant and there is no need to consider this type fluid rock interaction in the models. On the opposite and as explained previously in section 2.4.2 several studies have revealed the importance of biotic reactions on the modification of the gas composition during underground storage (*Panfilov et al.,* 2016) and therefore such complex reactive process should be considered in the models. As mentioned in section 2.4.2, there are different redox reactions (hydrogen-trophic bacteria) that could occur (see Figure 2-11). These hydrogen perturbation effects are not initially observed in the reservoir. These reactions are progressive and kinetically controlled with the activity of bacteria that consume hydrogen to lead reduction reactions. To reproduce the sequence of reduction reactions, an integrative approach is implemented where a reduction reaction is considered kinetically controlled while other reactions are at thermodynamic equilibrium (partial equilibrium approach). This approach frees successively hydrogen in solution and the redox potential of

the solution gradually decreases with changes in concentrations of different redox couples (*Jin et al.*, 2005). However, the sulfate-reduction due to the bacterial metabolism in presence of hydrogen is:

$$SO_4^{2-} + 4H_2 + H^+ = HS^- + 4H_2O \quad (12)$$

Sulphate-reduction is modeled by a kinetic Monod law provided a thermodynamic term (Jin et al., 2005). This kinetic law introduces a dependency on donor concentrations of chemical species and electron acceptor and a thermodynamic limiting factor when the reaction is thermodynamically possible. The general rate expression for microbial sulfate reduction, the dual-Monod equation (*Widdel*, 1988)

$$\frac{d[SO_4]}{dt} = -rB\frac{[SO_4]}{[SO_4] + K'_A}\frac{[H_2]}{[H_2] + K'_D}\left(1 - exp\left(\frac{\Delta G}{RT}\right)\right) \quad (13)$$

where r is the rate of reaction, B is the bacteria concentrations, K'_A and K'_D are half-saturation constants, R is the universal gas constant, T is the absolute temperature and ΔG is the Gibbs free energy of the reaction. In this kinetic law, two parameters have a particularly high uncertainty: the constant sulfate-reduction rate k (*Van Houten et al.*, 1996) and the bacterial concentration B. This bacterial concentration may vary over about 3 orders of magnitude (*Coldwell et al.*, 1997) so that it could be estimated that the product $k * B$ is about 2.7x10^{-11} (mo/L/s). In terms of reactivity in this study, the minerals like hematite and anhydrite are sensitive to redox reactions potentially and they should react due to the hydrogen injection. These minerals contain species which may be reduced (SO_4 from anhydrite and Fe^{+3} from hematite). However, in this study, the kinetic constraint of biotic reaction was decoupled with the other formulation of reaction and the reactive transport equations systems were calculated together.

5.2.9 Results

As mentioned, hydrogen was injected in the upper layer of the storage with the conditions explained in section 2. Hydrogen (g) has the lower density than the formation water, therefore, the gas accumulates at the top of the structure (Figure 5-20) and spreads rapidly after the duration of implementation stage that is illustrated in Figure 5-20 after 3.5 years of simulation. It indicates that the maximum hydrogen saturation in the storage after the injection duration reaches to 86%.

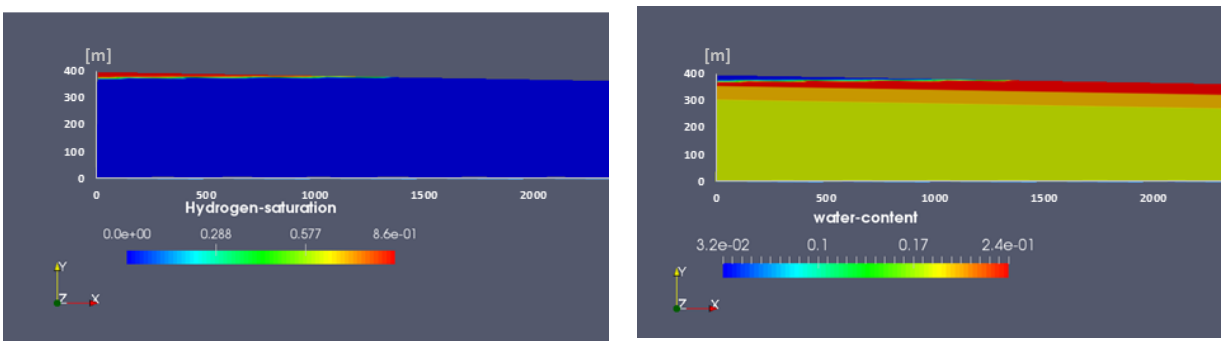

Figure 5-20 The results of the reservoir development after 3.5 years. Left: hydrogen saturation results, Right: water content results (3 layer of reservoir have been presented)

After three years, all the hydrogen reaches the top of the structure, and accumulates like a perfect circular up-side down "lake" thicker at the center and a radius of about 1500 m at the end of the storage development (Figure 5-20).

Figure 5-21 illustrates the hydrogen volume in the reservoir for three stages: 3.5 years of injection, 6 month of stability and 6 years of withdrawal with and without considering biotic chemical effects. By considering biotic reaction the volume of hydrogen in the storage is higher than in the other model and some hydrogen is consumed during the storage. Therefore the total volume of injected hydrogen is not completely recovered after 6 years of production as shown in Figure 5-21.

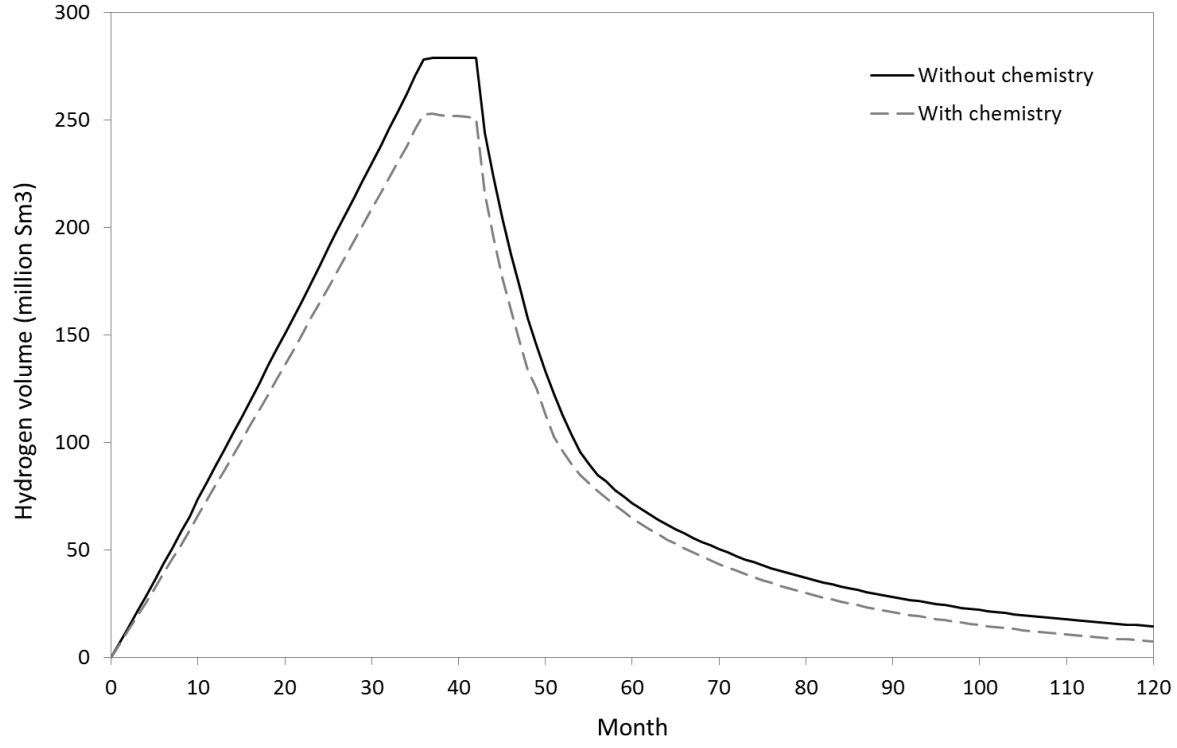

Figure 5-21 Evaluation of stored volume of hydrogen in the reservoir after 3.5 years of injection, 6 month of stability and 6 years of production

In both models, during the development stage, hydrogen is injected in the storage reservoir with a constant rate, therefore, the volume of hydrogen increases linearly for 42 month (3.5 years). During the idle period, the injection is stopped and thus for six-month hydrogen volume is constant (approximately for the model with chemistry). During the production stage hydrogen is produced from the reservoir for 6 years.

Figure 5-22 illustrate the percentage of hydrogen volume extracted from the produced fluid. This volume is not constant and it increases after each month.

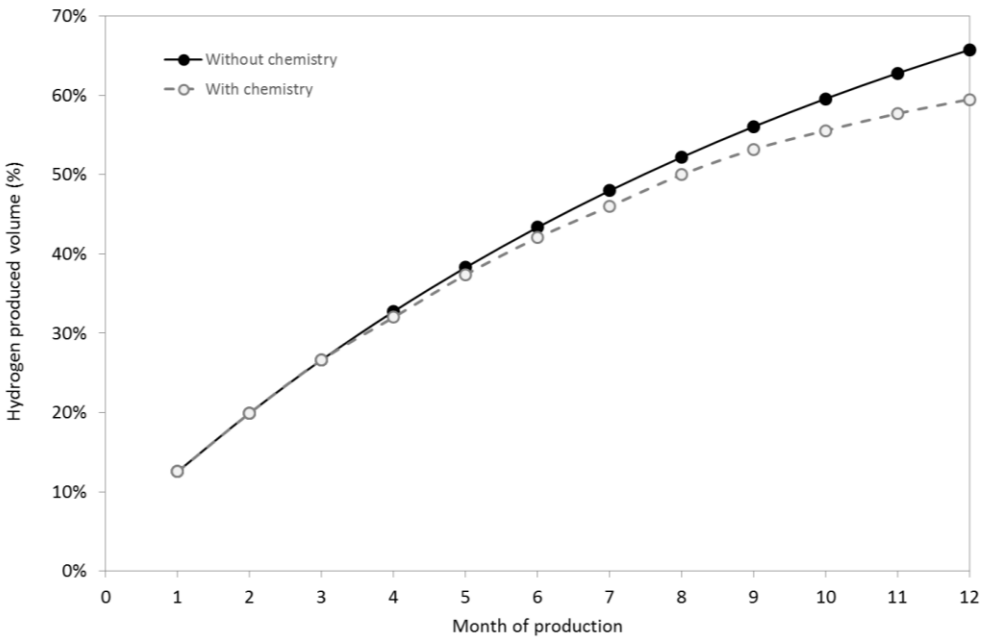

Figure 5-22 The volume of hydrogen produced and its percentage during one year

At the beginning of the production, the rate of the produced hydrogen extracted is high but after about 3 years it drops due to production of the gas surrounding the well and to water withdrawal. After one year approximately ~60% (63% for the without chemistry model) of the needed hydrogen is extracted from the reservoir (~ 140 million Sm^3). This volume of hydrogen after re-electrification could produce 235 GWh (235 million kWh) which equals the annual electricity consumption of roughly 83,185 France average households (ADEME[2] report 2012) or about one day of electricity consumption in Île-de-France.

However, the results of numerical simulation indicate that the volume of produced hydrogen in week-long shortage period is about 10 million Sm^3 and that is not sufficient to deficit the renewable energy consumption in Ile-de-France, therefore, other wells or other storage should be used to produce higher hydrogen in short time.

5.2.10 Discussion

The results of this numerical study illustrate that during of hydrogen storage into deep underground sandstone formation, the chemical impact due to abiotic reaction between hydrogen and minerals components of the rock is minor. On the other hand, the impact of biotic reaction are observed on the hydrogen production and seems not negligible (about 10% of the hydrogen production). The use of cushion gas is generally applied to reduce the risk of loss of hydrogen. However, after injection of the cushion gas, some residual water is still present inside the pore structure of the rock and therefore fluid rock geochemical interactions and also biotic reaction are still needed to be considered as they may have

[2] Agence de l'Environnement et de la Maitrise de l'Energie

an indirect impact on the composition of the involved fluids (gas composition, and native brine). However, this numerical modeling is a preliminary study of hydrogen reactive transport in underground storage and many further numerical simulations would be needed to investigate the influence of many parameters on the injection and production (like the influence of hydrogen reactivity on the seasonal injection and production (biotic or abiotic), the influence of more than one well on the hydrodynamic behavior of reservoir or influence of well positions on the productivity).

Chapter 6

General conclusion and applications

Underground hydrogen storage has been introduced as the energy storage in supply chain of renewable energy, while storing of hydrogen in underground and converting it into a reliable, affordable, flexible power source could help meet future energy demands. However, storage of hydrogen is not the same as storage of other gases (carbon dioxide, natural gas for instance), due to the hydrodynamic behaviors of hydrogen and geochemical reactions tendency's. Therefore, evaluating the underground hydrogen storage requires a precise knowledge of the hydrodynamic behavior of the fluids during and after the injection to the reservoir and its geochemical interactions with the fluids and the rock mineralogy and with the microbial activity which could possibly alter the gas composition and the pore structure of the rockHence, the objectives of this thesis were to evaluate the potential of underground hydrogen storage in terms of volume capacity and to estimate the integrity and sustainability of underground reservoir, including determining the chemical rock reactivity and hydrodynamic fluids behavior with the approach of experimental and numerical modeling. For this purpose, the Vosges sandstone formation (lower Triassic sandstones), as Buntsandstein presents interesting characteristics previously revealed for geothermal applications and also for CO_2 storage investigations in France, has been used for this study. The experiments observations and the numerical results were collected in two manuscripts that will be published. However, the parts of this study and the conclusions are:

1. ***Study Evaluation of geochemical reactivity of hydrogen in sandstone: application to geological storage;***

Hydrogen can be stored underground in several types of geological formation. Porous formations could potentially provide high storage capacity and impact of hydrogen on the rock formations should be considered, however, experiences with subsurface porous media hydrogen storage are relatively scarce. In this study, we have performed the experimental and numerical study to evaluate the geochemical reactivity of hydrogen on the mineral components of Vosges sandstone lithology at the underground hydrogen storage. The experimental results demonstrated that mineralogical changes of Vosges sandstone in contact with hydrogen in reservoir conditions are minor. In fact, compared with starting rocks (before experiments), there are no variation concerning quartz and K-feldspars. There are just minor mineralogical changes concerning muscovite and hematite proportions (XRD) and muscovite composition (Electron microprobe analysis). Therefore, these experimental results clearly show that hydrogen has a minor effect on the minerals present in the Vosges sandstone. In addition, 1D batch numerical simulation approach without any migration of phases (gas and water) and components was performed to simulate the laboratory experiments that were carried out in this study with the same conditions of temperature, hydrogen partial pressure and water-rock ratio. The geochemical modeling results illustrated that in the long term, hydrogen has no major effect on abundant minerals like quartz and K-feldspars and therefore on the formations of Vosges sandstone and only a minor reduction of hematite could be consider after at least one year.

Overall, this study illustrated that hydrogen has not major effect on Vosges sandstone and the impact of hydrogen could be limited on the reduction of hematite at the long duration and release of Iron from muscovite that are not influence on the rock properties (porosity and permeability) and therefore the reservoir properties. As the consequence, this study confirms that storing hydrogen in the porous geological formation of Vosges sandstone because of the minor influence of hydrogen on the rock formation is feasible. However, this experimental study shows that abiotic reactions between hydrogen and rocks can be excluded from the consideration as insignificant to hydrogen storage.

2. ***Study of the migration of hydrogen in the sandstone: experimental determination of relative permeability (kr) and capillary pressure (Pc) of hydrogen-water system;***

Core flooding experiments have been performed to measure drainage relative permeability and capillary pressure for the hydrogen-water system in a porous sandstone. Results provide

the first measurements of these properties essential for the development of underground hydrogen storage. Two capillary pressure and two relative permeability experiments were performed, enabling these properties to be determined for two sets of pressures and temperatures representative of conditions of underground hydrogen storage. Our main conclusions are as follows:

- Capillary pressure data have been obtained from semi-dynamic capillary pressure and Mercury injection capillary pressure measurements. Combining the two types of data allows the determination of the capillary pressure evolution for the hydrogen-water system over the entire water saturation range. The interfacial tension ($cos\theta = 0.93$ and $cos\theta = 0.82$) and contact angle (0.051 N/m and 0.046 N/m) of the hydrogen-water system have been determined for conditions of underground hydrogen storage.
- Steady state relative permeability measurements have been performed and the data extended to lower water saturations by using the capillary pressure measurements. Processing of the two sets of capillary pressure data allows the evaluation of the relative permeability of hydrogen in sandstone for almost the total range of water saturation.
- Capillary pressures little vary between the two different sets of experimental conditions. Therefore, our results suggest that capillary pressure is almost constant in the hydrogen-water system for the entire range of pressure and temperature conditions appropriate for hydrogen storage. In the same way, the surface tensions and contact angles determined under the two sets of experimental conditions are similar.
- Hydrogen properties (density, viscosity) and storage pressure and temperature conditions imply that the two-phase hydrogen-water flows under a capillary-dominated regime. Despite this capillary-dominated regime, no large difference in relative permeability was observed between the two types of experimental conditions. This can be explained by small variations in the capillary number when changing pressure and temperature. This suggests that our relative permeability results are applicable to a wide range of pressure and temperature conditions.

3. Numerical simulation of a geological hydrogen storage site at a commercial scale;

The experimental results that were obtained from laboratory experiments have been integrated in numerical simulations to simulate the biotic chemical interactions and the physical migration of hydrogen into sandstone at the reservoir scale. This numerical

simulation illustrated underground hydrogen storage as the energy storage for compensation of renewable energy fluctuation. The reactive transport modeling was performed to evaluate the hydrodynamic behavior and geochemical/microbial interaction of hydrogen in underground storage during development and production. A comprehensive hydrogen storage scenario was implemented inside an aquifer reservoir. During the development period, the reservoir was pressurized by injecting 280 million Sm^3 of hydrogen while the peak of hydrogen extraction was amount of 140 million Sm^3 in one annual gas withdrawal that equals the annual electricity consumption of roughly 83,185 France average households. The average hydrogen volume extracted was 63% in the first production cycle. However, the results indicated that the loss of hydrogen in the reservoir due to the reactions (with water components and biotic reactions) is ~15 million Sm^3. This amount of hydrogen consumption is about 10% of the hydrogen production and equals the annual electricity consumption of roughly 9000 France average households. This numerical exercise highlights the importance of considering inert cushion gas before injecting hydrogen in the reservoir to reduce the contact between hydrogen and the water of reservoir and therefore to reduce the potential loss during injection / production cycles.

Overall, the objectives of this study were to improve our knowledge on the understanding of the physic-chemical and the hydrogeological process which control the feasibility, the risk and the efficiency of the underground storage of hydrogen into porous deep saline aquifers. From the different results obtained in this work it can be noticed that the Triassic sandstones used in this study reveal minor modification of the rock mineralogy in contact with hydrogen. Nevertheless the investigation was not totally exhaustive and some other types of sandstones could be more reactive than the Triassic in presence of hydrogen due to redox processes not identified in this case. Standard measurements of Kr-Pc curves have been proposed apparently for the first time to our knowledge on Hydrogen-Water fluid systems percolating in sandstones. Though such results are not scientifically a novelty, the obtained results allow to the modeler community new set of data to implement the reservoir fluid flow simulators. Finally the simulation at a “commercial scale” of a hydrogen injection-production cycle has been estimated considering biotic reactivity. These preliminary results highlight the importance of using cushion gas to reduce the loss of Hydrogen during the production phase. In addition, the biotic reactivity seem to be an important parameter in underground hydrogen storage that influence the hydrogen production capacity. The French energy context was used for calibrating the amount to be stored and the timing of the cycle. Results show satisfying results in terms of feasibility and safety of the storage, but additional works would be needed to confirm theses concluding remarks.

Chapter 7

Perspective

In this study the geochemical reactivity of hydrogen in sandstone sedimentary formation and migration of hydrogen in porous sand stone saturated with water were investigated experimentally and the results of the experiments were used to simulate underground hydrogen storage. However these studies were performed in three parts and each parts have perspective to be completed:

1. Geochemical reactivity:
    - Additional experiments in presence of water;
2. Hydrodynamic behavior:
    - Measure the imbibition curve of hydrogen-water system;
    - Studding the gas (hydrogen) trapping by the drainage-imbibition effects;
3. Storage simulation :
    - Role of cushion gas to attenuate abiotic and biotic reactivity (residual water);
    - Extend the injection scenario (role of heterogeneity, dip angle, location of injection and production well) to optimize operational production;

Chapter 8

Results of papers

The outcomes of this thesis are present in the two manuscript that will be published. At the ***Paper I***, the interaction of hydrogen on the minerals of the sandstones that were used in this study, ware investigated experimentally and the results of the experiments were compared with the results of the numerical simulations. ***Paper II,*** presents the variation of fluid properties at the hydrogen storage. The relative permeability and the capillary pressure of the hydrogen-water system ware measured experimentally. These experiments allowed the derivation of the interfacial tension and contact angle of the hydrogen-water system at underground hydrogen conditions, which are not publicly available data.

8.1 Paper I

Determination of hydrogen-water relative permeability and capillary pressure in sandstone: application to underground hydrogen injection in sedimentary formations

E.Yekta, A. [(1)], Manceau, J.-C. [(2)], Gaboreau, S. [(2)], Pichavant, M. [(1)], Audigane, P. [(2)]

[(1)] ISTO : Institut des Sciences de la Terre d'Orléans, 1A Rue de la Ferollerie, 45100 Orléans, France

[(2)] BRGM Bureau de Recherches Géologiques et Minières, 3 Avenue Claude Guillemin, 45060 Orléans, France

Abstract

To provide quantitative data for the development of underground hydrogen storage in porous sedimentary rocks, capillary pressures and relative permeabilities have been measured for the hydrogen-water system. The tests have been performed on a Triassic sandstone. Two potential underground hydrogen storage conditions ('shallower': 55 bar, 20 °C and 'deeper': 100 bar, 45 °C) have been investigated. Capillary pressure curves have been measured following a modified semi-dynamic technique. The data have been combined with mercury injection capillary pressure measurements to derive a model for capillary pressure valid over almost the entire water saturation range. Interfacial tensions and contact angles for the hydrogen-water system have been also derived. Relative permeability curves measured with the steady-state technique yield low values for minimum water saturations of ~40%. When combined with the capillary pressure data, the relative permeability of hydrogen in sandstone can be evaluated for almost the total range of water saturation. Capillary numbers calculated for our relative permeability experiments indicate a capillary-limited flow regime for the hydrogen-water system. Despite the two differing sets of conditions investigated and this flow regime, the relative permeability curves stay very close from each other, an effect attributed to the almost constant viscosity of hydrogen under our pressure and temperature conditions. This is in contrast with other fluid pairs (e.g., CO2-water system) where capillary numbers can strongly vary with pressure and temperature. Similarly, capillary pressure data vary little between the experimental conditions. The interpretation of the results would suggest that the relative permeability and capillary pressure results from this study are applicable to a wide range of pressure and temperature conditions.

Keywords: Underground hydrogen storage; relative permeability; capillary pressure, Two-phase flow core flooding experiment

1. Introduction:

Because of environmental and safety concerns, the global energy production is rapidly changing, evolving towards a lower share of carbon-based fuels and nuclear power and a higher proportion of renewable energy within the energy supply mix. Wind and solar power are seen to play an important role in this energy transition. However, both of them have characteristics (geographical dispersion, annual fluctuation) that make challenging their integration in the power sector (e.g. *Schaber et al.*, 2012; *Després et al.*, 2016). Energy storage technologies, which consist in storing energy to make it available to meet demand when needed, allow the integration of intermittent energy sources (*Reitenbach et al.*, 2015). Among several options, hydrogen is now viewed as a candidate solution for large-scale energy storage (*Carden and Paterson*, 1979; *Li*, 2005; *Basniev et al.*, 2010; *Crotogino et al.*, 2010; *Ozarslan et*

al., 2012; *HyUnder* 2013; *Lord et al.,* 2014). Hydrogen offers a unique potential to store large amounts of energy. It can be stored underground in several types of geological formation, deep aquifers, depleted oil and gas reservoirs and rock (salt or crystalline) cavities (*Bai et al.,* 2014). However, so far, only salt caverns have been tested as potential storage sites (*Decourt et al.*, 2014; *Gupta et al.*, 2015). Since salt formations do not always occur in areas where energy storage is needed (*Bai et al.,* 2014), alternative storage sites must be sought for. Porous formations could potentially provide high storage capacities but mechanisms of hydrogen storage in subsurface porous media are still poorly known. This is the subject of current research, carried out in several projects such as H2STORE (*Ganzer et al.*, 2013), Underground Sun Storage (*Bauer et al.,* 2014) and Hychico (*Raballo et al.,* 2010) among others.

As for other types of large-scale underground storage (e.g., for carbon dioxide or natural gas), understanding the migration of the fluid during and after the injection represents a major challenge. Characterizing the parameters governing the fluid migration is therefore of critical importance. Physical properties (porosity, absolute permeability) of reservoir rocks must be known. Most importantly, the construction of large-scale models of gas storage (*Pfeiffer et al.,* 2015) requires constitutive relationships between capillary pressure, relative permeability and water saturation. Presently, capillary pressure and relative permeability data are lacking for the hydrogen-water system. Therefore, their determination is important for the development of underground hydrogen storage. This forms the subject of this paper which reports experimental measurements of capillary pressure and relative permeability systematics for hydrogen-water fluid mixtures in a Triassic sandstone. We find that capillary pressure and relative permeability data vary little between the experimental conditions. The interpretation of the results would suggest that the relative permeability and capillary pressure results from this study are applicable to a wide range of pressure and temperature conditions.

2. Properties of the reservoir rock

This study aims at the testing of sandstone lithologies for underground hydrogen storage. Therefore, lower Triassic sandstones (Buntsandstein formation) from the Vosges (France) were selected as test samples. These sandstones outcrop in a large geographical area and are now receiving increasing attention for geothermal applications (*Aquilina et al.*, 2010, *Haffen et al.*, 2015) as well as for CO2 storage (*Le Gallo et al.*, 2010; *Bader et al.*, 2014).

Sandstone samples from the Adamswiller quarry was used for all experiments from this study. Mineralogical characterization (*Yekta et al.,* 2017) shows that quartz and K-feldspar are the dominant minerals, accounting together for 98 vol% of the rock (quartz: 81 vol%; K-feldspar: 17 vol%). Accessory minerals include muscovite, hematite and clay minerals (illite). Absolute permeabilities, pore volumes, porosities and densities were measured on cores drilled in the sandstone samples (*Yekta et al.,* 2015). For the Adamswiller sample, the absolute permeability, obtained by the water core-flooding method using Darcy's law (see below) was measured at 44 mD. The pore volume (v_p) was determined by saturating the core with water and measuring the volume of water in the core (v_w). The total volume (v_t) was determined from the size of the core samples, yielding $v_p = v_t - v_w$. The porosity (v_p/v_t) is 19% corresponding to a volume of 2.05 mL. It was later confirmed by Mercury Intrusion Porosimetry, the data being corrected for the effects of surface roughness and irregularities (see below).

3. Experimental methods

The experimental set-up is derived from analoguous measurements previously performed for the CO_2-water system (*Manceau et al.,* 2015; *Reynolds and Krevor*, 2015). In this study, the capillary pressure was measured with a modified semi-dynamic technique initially proposed by *Ramakrishnan and Capiello* (1991) and *Lenormand et al.* (1995) for the oil-water system. Capillary pressure data were extended using independent measurements with the mercury injection capillary pressure (MICP)

method. The relative permeability has been measured with the classical steady-state technique (*Krevor et al.*, 2012). The mass balance method was used for the water saturation measurements.

3.1 Experimental setup and equipment

The experimental setup is illustrated in Figure 1. The rock core (length 61 mm, diameter 15 mm) is wrapped in a Teflon – PTFE tube. The measuring cell (core plus the Teflon container tube) is then positioned in a cylindrical 316SS 1 liter pressure vessel (Autoclave Engineers). The latter is pressurized by injection of water with an hydraulic (Maximator) pump. During the measurements, the external pressure applied on the cell is kept constant to approximately 130 bar. This allows the external confining pressure to be always maintained at minimum ~30 bar above the fluid pressure inside the cell to avoid any fluid flow between the core and the Teflon tube. The vessel is inserted in a cylindrical furnace monitored with an electronic regulator. Temperature inside the vessel is measured permanently by an internal thermocouple located immediately above the cell.

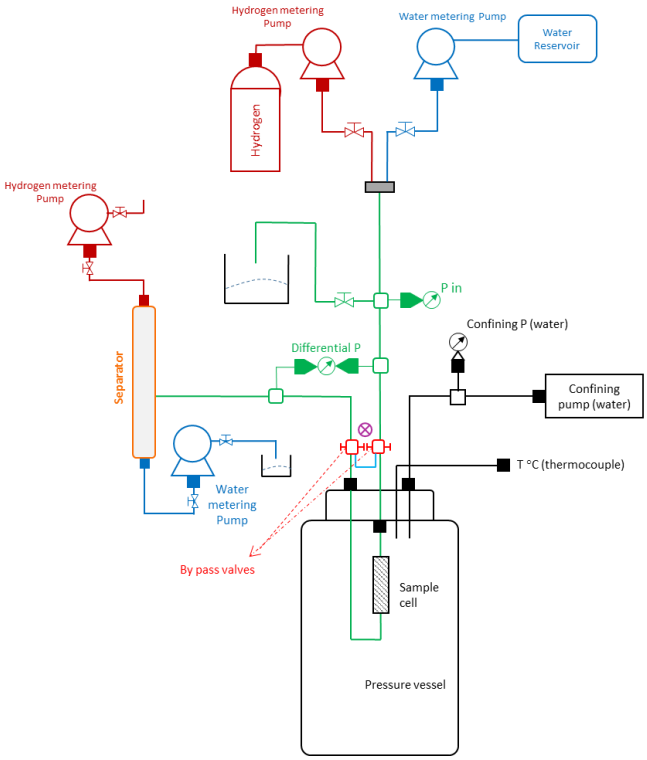

Figure 1. Experimental set-up.

The fluid circulation system includes two upstream metering pumps (PMHP 100-500, Top Industrie, pressures accurate to ± 0.1 bar, volumes to ± 0.5 cm^3), one for hydrogen gas and the other for water, both used for fluid injection. Fluid is circulated from the pumps to the measuring cell through a 1/16" steel capillary tubing. The differential pressure between inlet and outlet is measured with a differential pressure transducer (Honeywell HL-A-5, 0.50% scale accuracy). Two other metering pumps (PMHP 100-500, Top Industrie) measure the amount of hydrogen and water downstream the cell. A separator is inserted between the cell and the metering pumps to enable water and hydrogen to be collected separately. These two metering pumps also allow the fluid pressure to be kept constant at the outlet of the cell. Two by-pass valves are inserted in the fluid circulation system respectively before and after the cell, in order to measure the saturation of water in the cell after each experimental step, as detailed below. The temperature, the pressure drop across the cell, the injection flow rates, the injection pressures and the volumes of each pump are all recorded by a data acquisition system.

3.2 Experimental conditions and procedures

The capillary pressure (Pc) and relative permeability (kr) experiments were performed under two different types of conditions simulating hydrogen geological storage. The first (20 °C, 55 bar) simulates "shallow" gas storage and the second (45 °C, 100 bar) a deeper situation. Conditions of the four definitive experiments and the associated hydrogen and water properties are listed in Table 1. Before each experiment, the absolute water permeability was measured to test the equipment and check the physical integrity of the core, since the same sample was used in the four experiments. No major change of the absolute permeability was noticed during the course of the experiments (Table 1).

Table 1 Experimental conditions and core fluid parameters for both capillary pressure experiments (indicated by Pc) and relative permeability experiments (indicated by kr)

Experiment	Type	Non-wetting Fluid	Temp. (°C)	Pressure (bar)	Confining pressure (bar)	Absolute water permeability (mD)	$\mu_{hydrogen}$ (µPa s)	$\rho_{hydrogen}$ (Kg/m^3)	μ_{water} (µPa s)	ρ_{water} (Kg/m^3)
1	P_c	Hydrogen	20	55	130	46	8.94	5.6	999	1000.5
2	P_c	Hydrogen	45	100	130	48	9.54	7.2	597	994.5
3	k_r	Hydrogen	20	55	130	45	8.94	5.6	999	1000.5
4	k_r	Hydrogen	45	100	130	47	9.54	7.2	597	994.5

µ=viscosity

ρ=density

Each experiment started with an evacuation step. After saturating the core with water and setting the pressure inside the fluid circulation system at the desired experimental pressure, the water in the system (except the core) was evacuated by closing both ends of the core with the bypass loop. Then, the water saturation was determined as follows. A known volume of water (v_i) was first injected under the desired experimental temperature and fluid pressure conditions. Second, fluids (either hydrogen alone or water and hydrogen together depending on the type of experiment) were injected at different flow rates and the experiment performed. Third, after completion of the experiment, the volume of water inside the system, except in the core, was measured with the bypass loop (v_f). Knowing v_i and v_f, the volume of water in the core (v_s) could have been determined ($v_s = v_i - v_f$). Below, the water saturation is expressed as $S_w\% = v_s/v_p \times 100$. This mass balance method involves a dead volume of 0.1 mL maximum (corresponding to the tubing between the by-pass valves and the core which contains a mixture of hydrogen and water). Therefore, since v_p is 2.05 mL in this study (and so the maximum v_s is 2.05 mL), the dead volume causes a maximum uncertainty on water saturation of $\leq \pm 2.5\%$.

***Capillary pressure**:* Following water saturation of the core (see above), the *capillary pressure* experiments involved injection of hydrogen. Constant hydrogen flow rates were successively imposed, from 2 to 10 mL/min. For each flow rate, once a steady state was reached, the differential pressure across the core has been recorded and the water saturation measured using the procedure above. Under each steady state condition, the water pressure inside the core is constant and equal to the pressure at the outlet, and the inlet pressure is the pressure of the gas injection. Therefore, the differential pressure between the core inlet and outlet corresponds to the differential pressure of the gas and water phases (capillary pressure) at the inlet saturation conditions. With the experimental set-up used for this study, the inlet saturation cannot be measured directly, since only an average saturation over the core is measurable with our procedure. *Ramakrishnan and Cappiello* (1991) proposed a method for evaluating the saturation at the inlet of the core as a function of the capillary pressure. In addition to the average hydrogen saturation measured for each flow rate, this method requires the knowledge of the injection flow rate and of the associated differential pressure between the core inlet and outlet. The computation procedure is detailed in Appendix A.

Capillary pressure data derived as above were complemented by data obtained with the mercury/air system. A 1 cm^3 cubic plug of the same rock as for the core-flooding experiments was prepared for Mercury Intrusion Porosimetry (MIP) and Mercury Injection Capillary Pressure (MICP) measurements. These were performed using a Micromeritics Autopore IV 9500 covering the pressure range from vacuum to 2130 bar. Using the Young-Laplace scaling, Hg/air data can be converted to any fluid-pair system with the equation:

$$P_c = P_{c,Hg/Air} \frac{\tau \cos\theta}{\tau_{Hg/Air} \cos\theta_{Hg/Air}} \quad (1)$$

where P_c is the capillary pressure, τ is the interfacial tension and θ is the contact angle for the fluid-pair system of interest. This conversion requires the interfacial tension and contact angle values for both systems (i.e., for hydrogen-water and mercury-air) at experimental conditions. However, no such data exist for the hydrogen-water system. Therefore, we have fitted the capillary pressure data obtained with the core-flooding technique to derive values of the interfacial tension and contact angle in equation (1). This allows, by using equation (1), to extend the capillary pressure data over the entire water saturation range.

Relative permeability: There are several methods for measuring the relative permeability experimentally. Two basic approaches are steady state and unsteady state (Muller et al. 2011). For the steady-state method, the two (non-wetting and wetting) fluids are injected simultaneously into the core at different fractional flows. Once steady state conditions are established, both the water saturation and the differential pressure between the core inlet and outlet are measured for each fractional flow. This method allows relative permeabilities to be directly calculated with Darcy's law (see below) although the attainment of a steady state situation usually requires a long time. For the unsteady-state method, only one phase (usually the non-wetting) is injected at a constant flow rate to displace the other phase (usually the wetting) already present in the core. The pressure drop and flow rates are then measured simultaneously (Muller et al. 2011). As stability (in flow parameters and pressure) is not required, the measurements can be performed rapidly, but the derivation of the relative permeability is more challenging, generally requiring numerical modeling (*Toth et al.,* 2002).

For the experimental work presented in this study, the steady state approach has been followed. Water and hydrogen were both injected into the core under a constant total volumetric flow rate (Q_t = 1mL/min) and for several fractional flow parameters (Q_{H_2}= 0.05 to 0.99 mL/min; Q_w = 0.95 to 0.01 mL/min; $f_{H_2} = Q_{H_2}/(Q_{H_2} + Q_w)$, Table 2). For each fractional flow, the pressure drop between the core inlet and outlet was recorded once steady state was established. This corresponded to the injection of a volume of ~8 times the pore volume of the core. The water saturation was measured with the same protocol as above. The relative permeability of hydrogen and water were computed using Darcy's law written as:

$$-\frac{\Delta P}{L} = \frac{\mu_i}{K k_{r,i}(S_w)} \frac{Q_i}{A}, \qquad i = hydrogen\ or\ water \quad (2)$$

where $\frac{\Delta P}{L}$ is the pressure drop per unit length, $k_{r,i}$ the relative permeability (a function of the water saturation inside the core, S_w), μ the phase viscosity, Q the phase flow rate, K the absolute permeability and A the cross-sectional area of the core. Relative permeability results with this equation are known to be affected by capillary end effects (discussed below) and gravitational influence since the core is in vertical position. However, if Darcy's law (equation 2) is modified to take into account gravity ($Q_i = K k_{r,i}(S_i) \frac{A}{\mu_i}\left(\frac{\Delta P}{L} - \rho_i g\right)$), the effects of gravity on relative permeabilities are < 0.003% for hydrogen and < 0.7% for water.

4. Results

4.1. Capillary pressure measurements

Representative responses of the experimental system following injection of hydrogen are illustrated in Figure 2. Variations in differential pressure are shown as a function of time in the two experiments (Table 2) and for the same hydrogen flow rate (2 mL/min). Changing the flow rate does not change the general aspect of the curves. Both comprise a transition region (marked by an initial increase and large fluctuations in differential pressure) and a steady state region corresponding to stable ΔP values (Table 2).

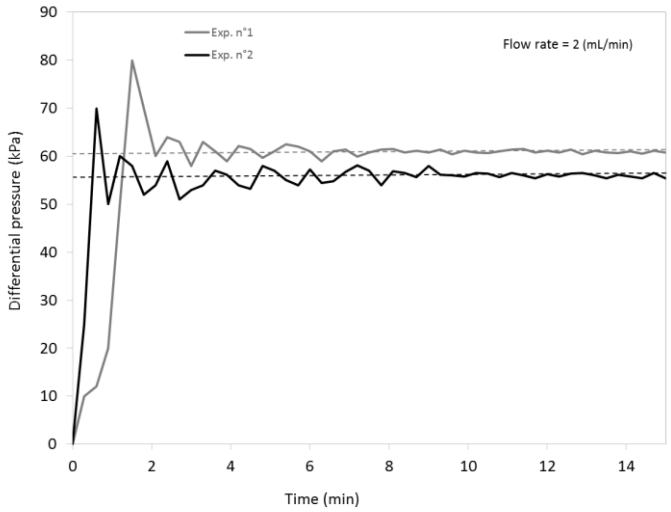

Figure 2. Measured differential pressure across the core at 2 mL/min flow rate and at different experimental conditions (exp. n°1 and exp. n°2).

For each flow rate, the corresponding water saturation values, both measured (average) and corrected (at the inlet, Appendix A) are given in Table 2 and plotted in Figure 3. Capillary pressures increase with decreasing water saturation until a maximum value of ΔP (or P_c) of 110 kPa is attained for a water saturation of 11%.

Table 2. Measured and corrected capillary pressure of hydrogen and pure water

Experiment	Q_{H2} (mL/min)	ΔP (kPa)	$S_{w\ (average)}$ %	$S_{w\ (at\ inlet)}$ %
Experiment 1 gHydrogen-water 20°C, 55 bar	1.25	61	31	33
	1.5	67	28	17
	1.75	73	22	14
	2	77	20	13
	3	82	19	13
	5	84	19	12
	7	104	17	12
	9	110	17	11
Experiment 2 gHydrogen-water 45°C, 100 bar	1.5	56	41	22
	1.75	59	32	19
	2	67	27	15
	3	71	23	14
	5	77	21	13
	7	80	20	13
	9	81	19	13

Data for the two experiments overlap because the viscosity of hydrogen changes only a little between the two sets of P-T conditions. It is worth noting that the data are available only over a narrow water saturation range (Figure 3a, b).

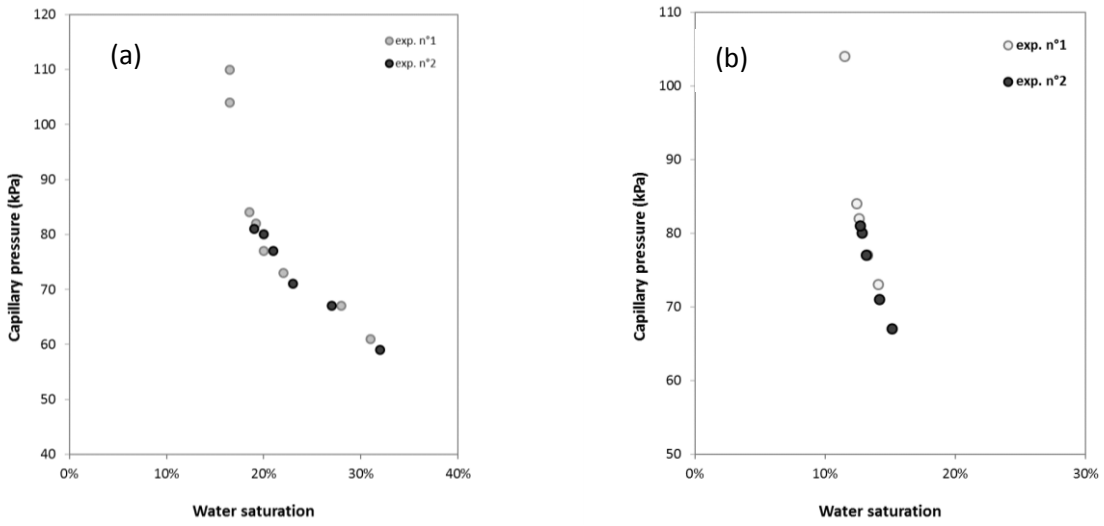

Figure 3. Capillary pressure vs (a) average saturation measured from laboratory experiment and (b) estimated inlet water saturation.

The measured capillary pressure curves as a function of the estimated inlet water saturation (Table 2) are shown in Figure 3b. The results illustrate that, because of the relatively low absolute permeability of the rock sample, the capillary pressure measured for the smallest flow rate is relatively high, leading to an impossibility of reaching high water saturation values with our core flooding method. Only the low water saturation range is covered and the data highlight the sharp increase of capillary pressure in that range.

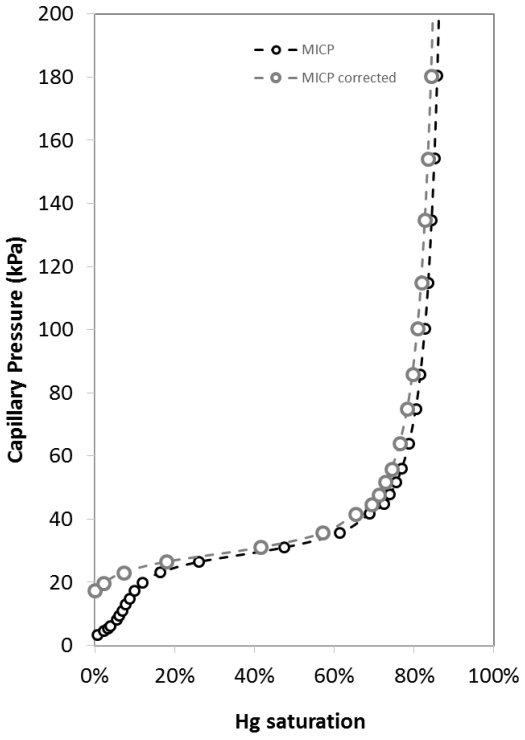

Figure 4. Mercury injection capillary pressure curves measured on a small-plug drilled from the main core and the corrected MICP curve.

In order to extend the water saturation range, the core-flooding data have been combined with MICP Hg/air data (Table 3). First, the raw MICP data have been corrected for the effects of surface roughness or irregularities at low pressures and the conformance volume removed (*Busch et al.,* 2013). The corrected MICP data (Table 3) are shown on Figure 4.

Table 3. Measured and corrected capillary pressure of Hg/air from MICP measurement

Experiment	ΔP (kPa)	$S_{w\ (raw)}$ %	$S_{w\ (corrected)}$ %
MICP measurement (Hg/air)	3	1	-
	5	2	-
	5	3	-
	6	4	-
	8	5	-
	10	6	-
	11	7	-
	13	8	-
	15	9	-
	17	10	0
	20	12	2
	23	16	7
	27	26	18
	31	47	42
	36	61	57
	42	69	65
	45	72	69
	48	74	71
	52	76	73
	56	77	74
	64	79	76
	75	80	78
	86	82	80
	100	83	81
	115	84	82
	135	84	83
	154	85	83
	180	86	84

Second, the dimensionless *J*-function was used to scale the capillary pressure data for hydrogen-water against those for Hg/air. It is defined as (*Al-Menhali et al.*, 2015):

$$J(S_w) = \frac{Pc(S_w)\sqrt{K/\varphi}}{\tau} \quad (3)$$

where P_c is the capillary pressure, S_w is saturation of the wetting phase, φ is the porosity of the core sample, τ is the surface tension and K is the absolute permeability. Since the experimental capillary pressure measurements and the MICP data have been performed on the same rock, both K and φ should be the same. Therefore, equating the capillary pressure results obtained by the two methods enables the surface tension to be obtained. For experiment n°1, the surface tension is 0.051 N/m and 0.046 N/m for experiment n°2 (Figure 5).

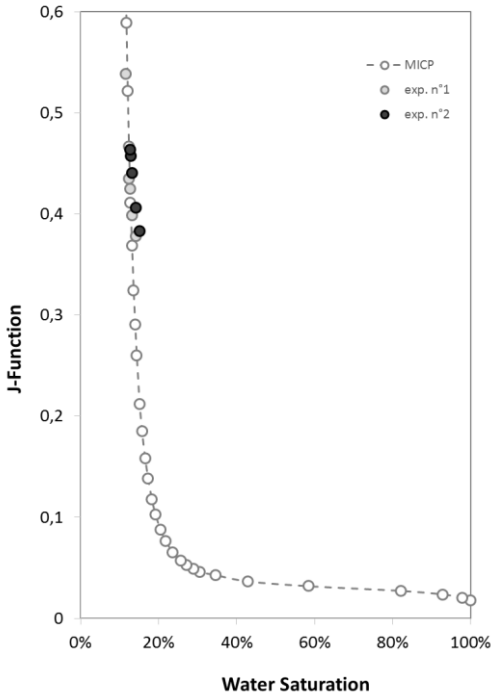

Figure 5. Data from the MICP measurement and adjusted capillary pressure measurements scaled by the dimensionless J-function. Experimental conditions were listed in Table 1.

Third, the contact angle for the hydrogen-water system was calculated from equation (1) using the surface tension as above and data (contact angle and surface tension) for mercury (141.3° and 0.48 N/m, respectively). A good fit between the core-flooding and MICP data was obtained for $cos\theta = 0.93$ and $cos\theta = 0.82$ for experiments n°1 and n°2 respectively (Figure 6). The processing of the two sets of capillary pressure data thus enables capillary pressure for the hydrogen-water system to be defined over a wide range of water saturation values.

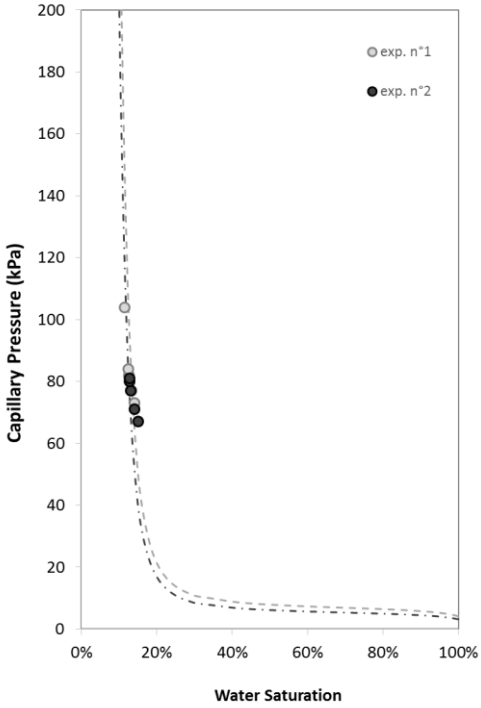

Figure 6. Hydrogen-water capillary pressure curves on Vosges sandstone core. The dotted lines represent the MICP curve converted to the hydrogen-water system and circles are results from capillary pressure experiments.

4.2. Steady state relative permeability measurements

Drainage relative permeability curves were measured with the steady state technique at a total flow rate of 1 mL/min, for both hydrogen gas and pure water. Experiments were performed under two different conditions (Table 1), but the same hydrogen fractional flows (f_{H2}) were considered. The recorded saturation and differential pressure data and the derived relative permeabilities for hydrogen and water are given in Table 4.

Table 4. Measured Relative Permeability to hydrogen and pure water

Experiment	f_{h2}	ΔP (bar)	$k_{r\text{-hydrogen}}$	k_{rw}	S_w (%)
Experiment 3	0.05	1.92	0.00029	0.62	90
gHydrogen-water	0.10	2.00	0.00056	0.56	87
20°C, 55 bar	0.30	1.67	0.00200	0.52	85
q_T=1 mL/min	0.50	1.44	0.00386	0.43	79
	0.70	1.10	0.00707	0.34	73
	0.90	0.88	0.01136	0.14	56
	0.99	1.16	0.04404	0.05	41
Experiment 4	0.05	0.92	0.00040	0.45	82
gHydrogen-water	0.10	0.91	0.00081	0.42	81
45°C, 100 bar	0.30	0.87	0.00273	0.37	77
q_T=1 mL/min	0.50	0.83	0.00542	0.32	73
	0.70	0.76	0.00922	0.23	66
	0.90	0.63	0.01489	0.10	53
	0.98	0.55	0.03492	0.04	40
Experiment 1			0,08		33
gHydrogen-water			0,27		17
20°C, 55 bar*			0,47		14
			0,60		13
			0,76		13
Experiment 2			0.21		22
gHydrogen-water			0.28		19
45°C, 100 bar*			0.47		15
			0.56		14
			0.71		13
			0.78		13

*Calculated values (Appendix B)

The steady state drainage relative permeability curves for hydrogen-water are shown in Figure 7 as a function of the water saturation. Notice that error bars on the relative permeabilities incorporate errors and uncertainties on differential pressure and water saturation.

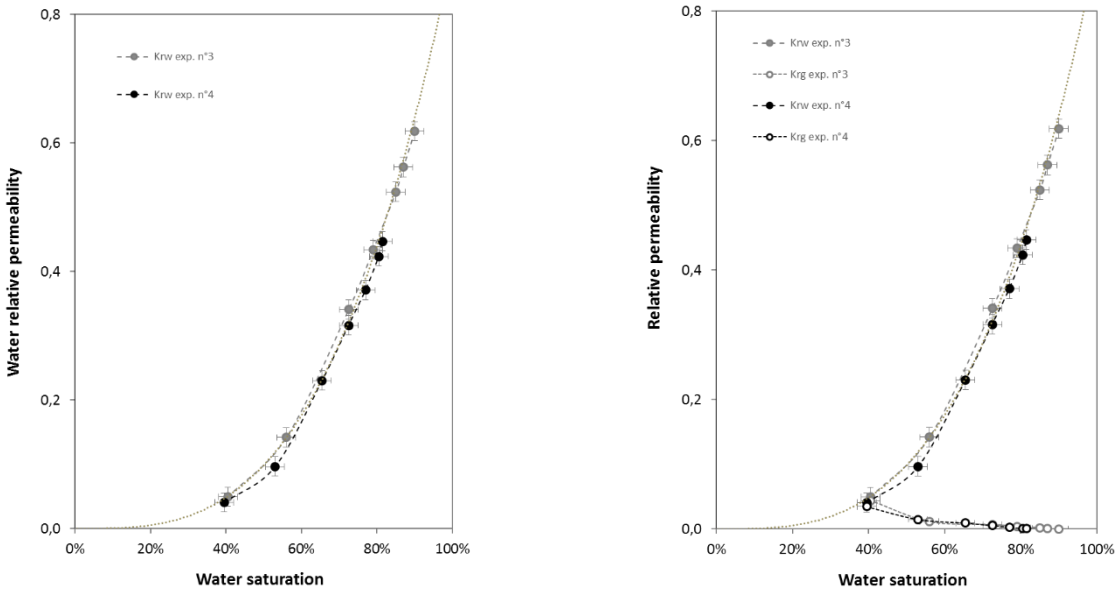

Figure 7. Steady state drainage relative permeabilities for Vosges sandstone core for hydrogen-water for different conditions

The relative permeability curves for hydrogen and water in the two experiments are very similar (Figure 7), despite gas fractional flows being different for a given saturation (Figure 8), higher in the 20 °C/55 bar experiment n°3 than in the 45 °C/100 bar experiment n°4. This implies that, upon increasing temperature and pressure, and for a constant gas fractional flow, hydrogen will become less efficient to remove the water from the core. The relative permeability for hydrogen appears to be low (Figure 7), meaning that the hydrogen flow is significantly slowered by two-phase flow interactions.

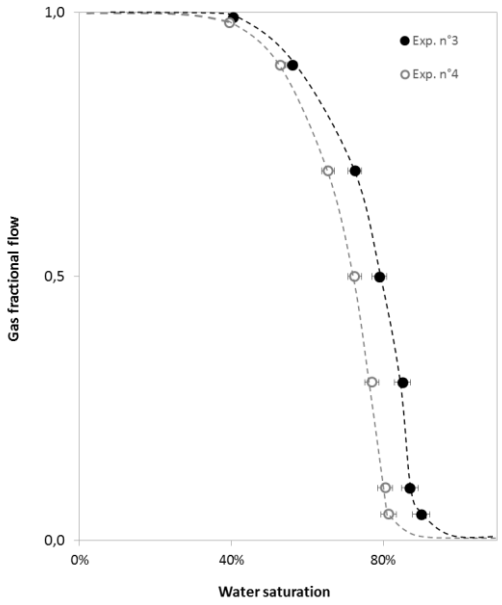

Figure 8. Comparison between the fractional flows as a function of the water saturations in experiments 3, 4.

As shown by Figure 7, it was not possible to decrease the water saturation below 40% during the measurements. This low apparent endpoint is likely to be due to a limitation from the experimental apparatus. *Krevor et al.* (2012), *Akbarabadi and Piri* (2013), *Pini and Benson* (2013), and *Manceau et al.*, (2015) observed a similar phenomenon: even at the highest hydrogen fractional flow, the average saturation in the core was limited by the capillary pressure reachable with the imposed flow rate (1 mL/min in our case). However, relative permeability data for the non-wetting phase could be extended toward low water saturations by using the capillary pressure data obtained from the core-flooding measurement. The procedure is

detailed in Appendix B. Results of the hydrogen relative permeabilities calculated with this procedure, together with those obtained with the steady state method (exp. n°3 and n°4), are shown on Figure 9. The calculated relative permeabilities fit well and extend the data for water saturations > 40% in experiments n°3 and n°4, down to values ~10%. This allows the evaluation of the relative permeability of hydrogen for almost the total range of water saturation.

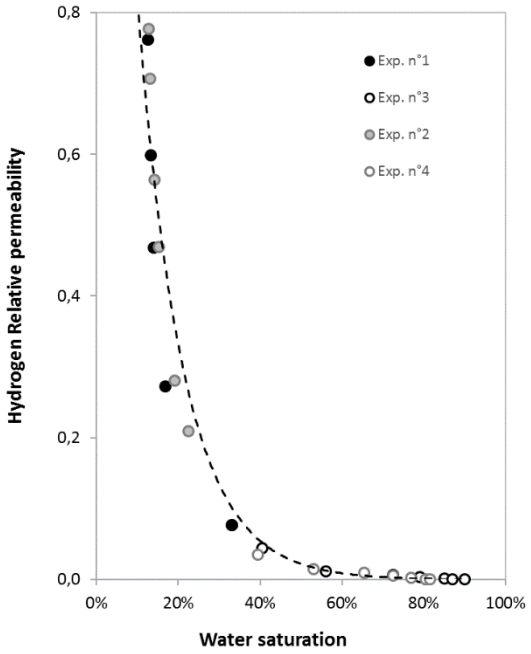

Figure 9. Calculation of hydrogen relative permeability from capillary pressure experiment 1 and 2 (for low saturation) and the relative permeability measurements experiment 3 and 4.

As mentioned before, the capillary end effects might have impacted the steady state relative permeability measurements. Therefore, to evaluate the magnitude of these effects, a numerical simulation of hydrogen-water two phase flow in the core was performed with COMSOL by using the Darcy equation (2). The capillary pressure and relative permeability data from experiments n°2 and 4 respectively (both at 45°C and 100 bar) were used as input values in the simulation. The highest fH2 (0.98, Table 4) was considered in the simulation so that capillary end effects would be maximum. The results of the simulation shows that the water saturation is constant over 95% of the length of the core and that the experimental water saturation value is well reproduced numerically (Figure 10). In the last 5% of the core length, the computed water saturation markedly increases, becoming twice as high as the measured value at the outlet. Therefore, the simulation demonstrates that capillary end effects are effectively restricted to the very end part of the core (i.e., to the last 3 mm of the 61 mm core).

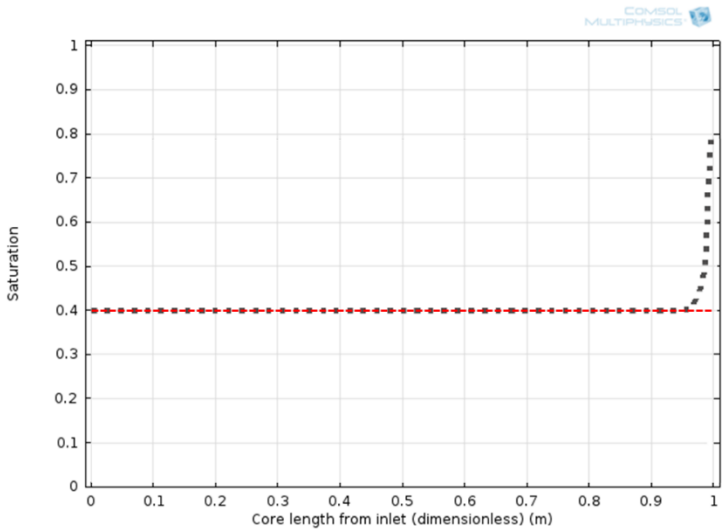

Figure 10. Computed vs. measured water saturation along the core during relative permeability measurements where both water and hydrogen are flowing through the core. Black dots: results of numerical modeling, Red dashes: experimental measurement. Notice the deviation between the simulation and the measurement near the very end part of the core.

5. Discussion of the results

As discussed in section 3.2, the experimental conditions investigated were chosen to be representative of potential large-scale hydrogen injection. To further interpret our results and more fully characterize the type of flow that occurred in the experiments, it is convenient to introduce the capillary number. Different formulations exist for the capillary number (N_c). In this study, we will use the definition of *Yokoyama and Lake* (1981) and *Zhou et al.*, (1997):

$$N_c = \frac{D^2 \mu V_T}{LKP_{ec}} \quad (4)$$

where D and L (m) are the diameter and length of the core, μ (Pa s) is the gas viscosity, K is the core permeability (m^2), P_{ec} is the entry capillary pressure (i.e., the capillary pressure at the inlet) and V_T ($m\ s^{-1}$) is the total fluid velocity. Below, we use an entry capillary pressure of 5 kPa (Figure 6). The calculated capillary numbers (equation 4) for our experiments are shown on Table 5. For the relative permeability experiments n°3 and n°4, the N_c are relatively low (< 0.5), meaning that these experiments have been performed with rather high capillary forces with regards to viscous forces.

Table 5. Capillary number[a] for both capillary pressure experiments (indicated by P_c) and relative permeability experiments (indicated by k_r)

Experiment	Type	Fluid injection	Total flow rate (cm^3/min)	N_c[a]
1	P_c	Hydrogen	2	0.67
1	P_c	Hydrogen	3	1.03
1	P_c	Hydrogen	5	1.68
1	P_c	Hydrogen	7	2.36
2	P_c	Hydrogen	2	0.71
2	P_c	Hydrogen	3	1.06
2	P_c	Hydrogen	5	1.77
2	P_c	Hydrogen	7	2.47
3	k_r	Hydrogen-water	1	0.34
4	k_r	Hydrogen-water	1	0.35

[a]Capillary number from equation (4)

According to *Reynolds et al.*, (2015), the transition between a capillary-dominated flow regime and a viscous dominated one generally occurs at capillary number comprised between 0.1 and 100. It is therefore likely that, under our experimental conditions (and by inference under injection conditions), a capillary-limited flow regime (or the beginning of the transition) would prevail. *Reynolds et al.*, (2015) have shown that, for such conditions, the relative permeability depends on the capillary number and, therefore, to the experimental conditions (in particular flow rate and viscosity of the non-wetting phase). The two types of conditions assessed in this study (shallow, and deeper) do did not lead to large difference in terms of capillary number (Table 5), and logically, we observed similar results in terms of relative permeability. The extension of the relative permeability data towards low water saturations involves significant increases in capillary number (experiments n°1 and n°2, Table 5). However, these changes remain relatively low (less than a 10 fold increase compared to values for experiments n°3 and 4) and, so, the type of flow should not be fundamentally affected. It is important to notice that, for potential hydrogen storage pressures (< 100 bar) and temperatures (< 100°C), the hydrogen viscosity does not largely vary (Table 1). This implies that the capillary number and, therefore, the relative permeability in the hydrogen-water system, will not be largely modified upon changing pressure and

temperature in the ranges above. This is in contrast with other fluid pairs (e.g., the CO2-water system) where capillary numbers can strongly vary with pressure and temperature. This stresses that the relative permeability data from this study are likely to be valid for the entire range of pressures and temperatures appropriate for hydrogen storage. Under conditions of capillary-dominated regime, heterogeneities in capillary forces (for example arising from changes in the pore structure of the rock) are known to play a significant role in fluid migration. According to *Reynolds et al.,* (2015), rock heterogeneities can exert an important influence on relative permeabilities, but the trend of relative permeability evolutions is a matter of rock specific heterogeneity. For example, in our situation, the low relative permeabilities measured for hydrogen (Figure 7) could reflect such rock heterogeneities rather than the specific properties of hydrogen. Testing of this interpretation would require additional measurements on different rock samples and/or different gases. Similarly than for the relative permeability, despite the two differing sets of conditions investigated in this study, the two capillary pressure curves (Figure 6) are very close from each other indicating that wettability and contact angles between hydrogen gas and water do not largely change with pressure and temperature.

6. Conclusion

Core flooding experiments have been performed to measure drainage relative permeability and capillary pressure for the hydrogen-water system in a porous sandstone. Results provide the first measurements of these properties essential for the development of underground hydrogen storage. Two capillary pressure and two relative permeability experiments were performed, enabling these properties to be determined for two sets of pressures and temperatures representative of conditions of underground hydrogen storage. Our main conclusions are as follows:

1. Capillary pressure data have been obtained from semi-dynamic capillary pressure and mercury injection capillary pressure measurements. Combining the two types of data allows the determination of the capillary pressure evolution for the hydrogen-water system over the entire water saturation range. The interfacial tension ($\cos\theta = 0.93$ and $\cos\theta = 0.82$) and contact angle (0.051 N/m and 0.046 N/m) of the hydrogen-water system have been determined for conditions of underground hydrogen storage.
2. Steady state relative permeability measurements have been performed and the data extended to lower water saturations by using the capillary pressure measurements. Processing of the two sets of capillary pressure data allows the evaluation of the relative permeability of hydrogen in sandstone for almost the total range of water saturation.
3. Capillary pressures little vary between the two different sets of experimental conditions. Therefore, our results suggest that capillary pressure is almost constant in the hydrogen-water system for the entire range of pressure and temperature conditions appropriate for hydrogen storage. In the same way, the surface tensions and contact angles determined under the two sets of experimental conditions are similar.
4. Hydrogen properties (in particular the viscosity) as well as the pressure, temperature and flow rate conditions imply that the two-phase hydrogen-water flows under a capillary-dominated regime. Despite this capillary-dominated regime, no large differences in relative permeability were observed between the two types of experimental conditions. This can be explained by small variations in the capillary number when changing pressure and temperature due to the low variation of hydrogen viscosity at those conditions. This suggests that our relative permeability results are applicable to a wide range of pressure and temperature conditions.

Appendix A: Protocol to compute the core inlet saturation from core-flooding capillary pressure data

This protocol has been proposed by *Ramakrishnan and Cappiello* (1991) for evaluating the non-wetting phase saturation at the core inlet with core-flooding capillary pressure measurements. As explained before, during capillary pressure measurement just gas is injected to the saturated core sample. Therefore, Darcy's law (equation 2) at steady state conditions will be:

$$-\frac{dP_c}{dx} = \frac{\mu_g}{K k_{r,g}(S)} \frac{Q_g}{A} \tag{A1}$$

where x is the position variable along the core, $\frac{dP_c}{dx}$ is the variation of the capillary pressure along the core, $k_{r,g}$ the relative permeability of the gas phase which is a function of the water saturation, s, μ_g the viscosity of the gas, Q_g the flow rate of the gas phase, K the absolute permeability and A the cross-sectional area of the core. Since saturation is varying along the core, the capillary pressure and relative permeability to gas are changing as well. However, since the pressure drop through the core is very small compared to the fluid pressure, the volumetric flow rate and the viscosity can be assumed constant along the core. Therefore, integrating equation (A1) along the length of the core gives:

$$QL = -\frac{AK}{\mu_g} \int_{P_{c,x=0}}^{P_{c,x=L}} k_{r,g}\left(P_{c,x}\right) dP_{c,x} \tag{A2}$$

where $P_{c,x=0}$ corresponds to the capillary pressure measured during the measurements and $P_{c,x=L}$ to the capillary pressure at the outlet of the core, considered as the entry capillary pressure of the rock. By noting $\Delta P_{c,x} = P_{c,x} - P_{c,x=L}$ (the capillary pressure difference between one location along the core and the core outlet), equation (A2) becomes:

$$QL = -\frac{AK}{\mu_g} \int_{\Delta P_{c,x=0}}^{0} k_{r,g}\left(\Delta P_{c,x}\right) d\Delta P_{c,x} \tag{A3}$$

Assuming a homogeneous relative permeability law along the core, differentiation of equation (A3) relatively to $\Delta P_{c,x=0}$ gives:

$$\frac{dQ}{d\Delta P_{c,x=0}} = \frac{AK}{\mu_g L} \cdot k_{r,g}(\Delta P_{c,x=0}) \tag{A4}$$

This equation means that the relative permeability of gas can be obtained if the relationship between the flow (or injection) rate and the differential pressure measured during the capillary pressure experiments is known.

In parallel, the average saturation in the core can be computed as:

$$\bar{S}_w = \frac{1}{L} \int_{x=0}^{x=L} S_w \, dx, \tag{A5}$$

Combined with equation (A1), this leads to:

$$Q\bar{S}_w = \frac{AK}{L\mu_g} \int_{\Delta P_{c,x=0}}^{0} k_{r,g}\left(\Delta P_{c,x}\right) S_w(\Delta P_{c,x}) d\Delta P_{c,x} \tag{A6}$$

The differentiation of this equation relatively to $\Delta P_{c,x=0}$ gives:

$$\frac{d(Q\bar{S}_w)}{d\Delta P_{c,x=0}} = \frac{AK}{\mu_g L} \cdot k_{r,g}\left(\Delta P_{c,x=0}\right) \cdot S_w(\Delta P_{c,x=0}) \tag{A7}$$

Equations (A7) and (A4) can be changed into:

$$S_w\left(\Delta P_{c,x=0}\right) = \frac{\mu_g L}{Akk_{r,g}\left(\Delta P_{c,x=0}\right)} \cdot \frac{d(Q\bar{S}_w)}{d\Delta P_{c,x=0}} \;\; with \;\; \frac{AK}{\mu_g L} \cdot k_{r,g}\left(\Delta P_{c,x=0}\right) = \frac{dQ}{d\Delta P_{c,x=0}} \tag{A8}$$

In other words (with v_{inj} being the Darcy velocity, equal to Q/A):

$$S_w(\Delta P_{c,x=0}) = \frac{L}{\Lambda\left(\Delta P_{c,x=0}\right)} \cdot \frac{d(v_{inj}\bar{S}_w)}{d\Delta P_{c,x=0}} \tag{A9}$$

where:

$$\Lambda\left(\Delta P_{c,x=0}\right) = \frac{K}{\mu_g} \cdot k_{r,g}\left(\Delta P_{c,x=0}\right) = \frac{dv_{inj}}{d\Delta P_{c,x=0}} \cdot L \tag{A10}$$

and $S_w(\Delta P_{c,x=0})$ is the water saturation at the inlet. Therefore, with information on the injection rate, the differential pressure between the inlet and outlet of the core, and the average saturation in the core during the measurements, it is possible to retrieve the water saturation at the inlet.

However, in order to use equation (A9), precise knowledge of the relationship between Darcy velocity (v_{inj}), average saturation ($\bar{S}_w$) and measured capillary pressure ($\Delta P_{c,x=0}$) is required. This relationship was obtained by fitting second-order polynomials of $v_{inj}\bar{S}_w$ as a function of $\Delta P_{c,x=0}$ for experiments n°1 and n°2 respectively (Table 2; Figure A1). These polynomials were used to calculate the water saturation at the inlet for each experiment.

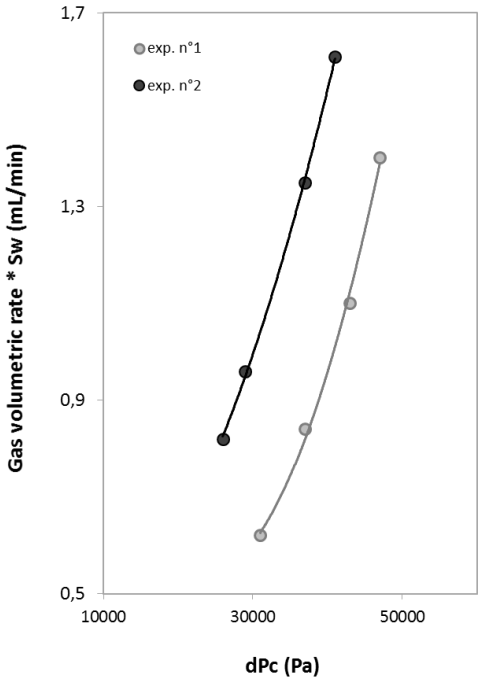

Figure A1. Relationship between hydrogen volumetric rate, saturation and the differential pressure in experiments 1 and 2.

Appendix B: Calculation of relative permeability of the non-wetting phase from core-flooding capillary pressure data

Relative permeability data for the non-wetting phase were extended toward low water saturations by using the capillary pressure data obtained from the core-flooding measurement. This method was suggested by *Pini and Benson* (2013) based on the work of *Ramakrishnan and Capiello* (1991). The relative permeability of the non-wetting phase can be calculated from the relationship between the Darcy velocity (v_{inj}) and the capillary pressure ($\Delta P_{c,x=0}$). Starting with equation (A10), we have:

$$\frac{K}{\mu_g} \cdot k_{r,g}\left(\Delta P_{c,x=0}\right) = \frac{dv_{inj}}{d\Delta P_{c,x=0}} \cdot L \tag{B1}$$

which can be rewritten as:

$$k_{r,g}(s) = \frac{dv_{inj}}{d\Delta P_c} \cdot L \cdot \frac{\mu_g}{K} \tag{B2}$$

Relative permeabilities were obtained by fitting second-order polynomials of v_{inj} as a function of ΔP_c for experiments n°1 and n°2 respectively (Table 2). These polynomials were used to extend the relative permeability data for experiments n°3 and n°4 (Figure B1). Relative permeabilities calculated using the polynomials for experiments n°1 and n°2 are given in Table 4.

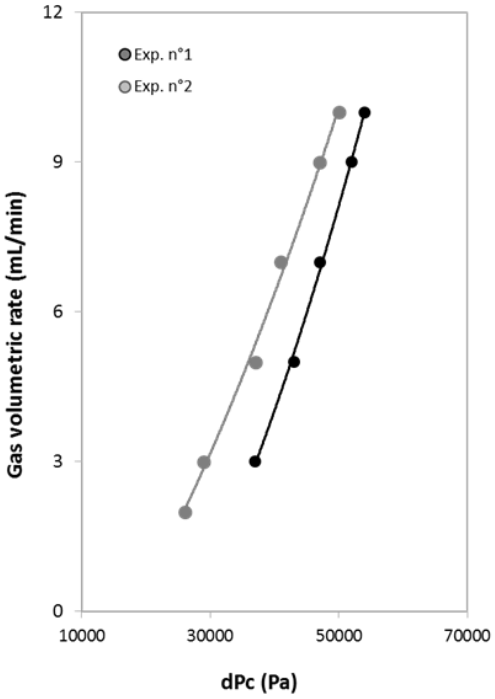

Figure B1. Relationship between gas volumetric rate and the differential pressure in experiments 1 and 2

Acknowledgments

This research has been supported by *ISTO* (Institut des Sciences de la Terre d'Orléans), *BRGM* (Bureau de Recherches Géologiques et Minières) and university of Orleans. We would like to thank Catherine Lerouge from *BRGM* for helping in the collection of the samples at the quarries in the Vosges area and Remi Champallier from *ISTO* for helping to prepare the experiments instruments.

References

Akbarabadi, M., & Piri, M. (2013). Relative permeability hysteresis and capillary trapping characteristics of supercritical CO 2/brine systems: An experimental study at reservoir conditions. Advances in Water Resources, 52, 190-206.

Akbarabadi, M., & Piri, M. (2015). Co-sequestration of SO 2 with supercritical CO 2 in carbonates: an experimental study of capillary trapping, relative permeability, and capillary pressure. Advances in Water Resources, 77, 44-56.

Al-Menhali, A., Niu, B., & Krevor, S. (2015). Capillarity and wetting of carbon dioxide and brine during drainage in Berea sandstone at reservoir conditions. Water Resources Research, 51(10), 7895-7914.

Aquilina, L., Pauwels, H., Genter, A., & Fouillac, C. (1997). Water-rock interaction processes in the Triassic sandstone and the granitic basement of the Rhine Graben: Geochemical investigation of a geothermal reservoir. Geochimica et cosmochimica acta, 61(20), 4281-4295.

Bai, M., Song, K., Sun, Y., He, M., Li, Y., & Sun, J. (2014). An overview of hydrogen underground storage technology and prospects in China. Journal of Petroleum Science and Engineering, 124, 132-136.

Basniev, K. S., Omelchenko, R. J., & Adzynova, F. A. (2010). Underground hydrogen storage problems in Russia. Essen, proceeding WHEC (May 2010).

Bauer, S., Head of Power to Gas Innovation and Development, RAG Rohöl-Aufsuchungs Aktiengesellschaft, Austria.

Bader, A. G., Thibeau, S., Vincké, O., Jannaud, F. D., Saysset, S., Joffre, G. H., ... & Copin, D. (2014). CO 2 Storage Capacity Evaluation in Deep Saline Aquifers for an Industrial Pilot Selection. Methodology and Results of the France Nord Project. Energy Procedia, 63, 2779-2788.

Bear, J. (2013). Dynamics of fluids in porous media. Courier Corporation.

Busch, A., & Amann-Hildenbrand, A. (2013). Predicting capillarity of mudrocks. Marine and petroleum geology, 45, 208-223.

Carden, P. O., & Paterson, L. (1979). Physical, chemical and energy aspects of underground hydrogen storage. International Journal of Hydrogen Energy, 4(6), 559-569.

Castillo, C., Kervévan, C., & Thiéry, D. (2015). Geochemical and reactive transport modeling of the injection of cooled Triassic brines into the Dogger aquifer (Paris basin, France). Geothermics, 53, 446-463.

Crotogino, F., Donadei, S., Bünger, U., & Landinger, H. (2010, May). Large-scale hydrogen underground storage for securing future energy supplies. In 18th World hydrogen energy conference (pp. 16-21).

Decourt, B., Lajoie, B., Debarre, R., & Soupa, O. (2014). Leading the energy transition: hydrogen-based energy conversion. Paris, France: Schlumberger Business Consulting (SBC) Energy Institute.

Després, J., Mima, S., Kitous, A., Criqui, P., Hadjsaid, N., & Noirot, I. (2016). Storage as a flexibility option in power systems with high shares of variable renewable energy sources: a POLES-based analysis. Energy Economics.

Ganzer, L., Reitenbach, V., Pudlo, D., Panfilov, M., Albrecht, D., & Gaupp, R. (2013, June). The H2STORE project-experimental and numerical simulation approach to investigate processes in underground hydrogen reservoir storage. In EAGE Annual Conference & Exhibition incorporating SPE Europec. Society of Petroleum Engineers.

Gupta, R., Basile, A., & Veziroglu, T. N. (Eds.). (2015). Compendium of Hydrogen Energy: Hydrogen Storage, Distribution and Infrastructure. Woodhead Publishing.

Haffen, S., Géraud, Y., & Diraison, M. (2015, April). Geothermal, structural and petrophysical characteristics of Buntsandstein sandstone reservoir (Upper Rhine Graben, France). In Proceedings World Geothermal Congress, Melbourne, Australia (pp. 1-11).

HyUnder, (2013) D(4)– "Overview on all Known. Underground Storage Technologies for Hydrogen". Grant agreement no. 2/93. 14.08.2013. 303417

Krevor, S., Pini, R., Zuo, L., & Benson, S. M. (2012). Relative permeability and trapping of CO2 and water in sandstone rocks at reservoir conditions. Water Resources Research, 48(2).

Le Gallo Y., Fillacier, S., Lecomte A., Munier G., Hanot F., Quisel N., Rampnoux N., Thomas S., (2010), Technical challenges in characterization of future CO2 storage site in a deep saline aquifer in the Paris basin. Lessons learned from practical application of site selection methodology, Energy Procedia 4 (2011) 4599–4606.

Li, J., 2005. Underground gas storage in the Beijing-Tianjin region balanced the role of natural gas supply and demand .Int.Pet.Econ.13(6), 37–38.

Lord, A. S., Kobos, P. H., & Borns, D. J. (2014). Geologic storage of hydrogen: Scaling up to meet city transportation demands. international journal of hydrogen energy, 39(28), 15570-15582.

Manceau, J. C., J. Ma, R. Li, P. Audigane, P. X. Jiang, R. N. Xu, J. Tremosa, and C. Lerouge (2015), Two-phase flow properties of a sandstone rock for the CO2/water system: Core-flooding experiments, and focus on impacts of mineralogical changes, Water Resour. Res., 51, doi:10.1002/2014WR015725.

Ozarslan, A. (2012). Large-scale hydrogen energy storage in salt caverns. International Journal of Hydrogen Energy, 37(19), 14265-14277.

Paterson, L. (1983). The implications of fingering in underground hydrogen storage. International journal of hydrogen energy, 8(1), 53-59.

Pfeiffer, W. T., & Bauer, S. (2015). Subsurface Porous Media Hydrogen Storage–Scenario Development and Simulation. Energy Procedia, 76, 565-572.

Pini R, Krevor SCM, Benson SM. Capillary pressure and heterogeneity for the CO2/water system in sandstone rocks at reservoir conditions. Adv Water Resour 2012;38:48–59

Pini, R., & Benson, S. M. (2013). Simultaneous determination of capillary pressure and relative permeability curves from core-flooding experiments with various fluid pairs. Water Resources Research, 49(6), 3516-3530.

Raballo, S., Llera, J., Pérez, A., Bolcich, J. C., Stolten, D., & Grube, T. (2010). Clean hydrogen production in patagonia argentina. Report Nr.: Schriften des Forschungszentrums Jülich/Energy & Environment.

Ramakrishnan T, Capiello A. A new technique to measure static and dynamic properties of a partially saturated porous medium. Chem Eng Sci 1991;16(4):1157–63.

Reitenbach, V., Ganzer, L., Albrecht, D., & Hagemann, B. (2015). Influence of added hydrogen on underground gas storage: a review of key issues. Environmental Earth Sciences, 73(11), 6927-6937.

Reynolds, C. A., & Krevor, S. (2015). Characterizing flow behavior for gas injection: Relative permeability of CO2-brine and N2-water in heterogeneous rocks. Water Resources Research, 51(12), 9464-9489.

Schaber, K., Steinke, F., Mühlich, P., & Hamacher, T. (2012). Parametric study of variable renewable energy integration in Europe: Advantages and costs of transmission grid extensions. Energy Policy, 42, 498-508.

Toth, J., Bodi, T., Szucs, P., & Civan, F. (2002). Convenient formulae for determination of relative permeability from unsteady-state fluid displacements in core plugs. Journal of Petroleum Science and Engineering, 36(1), 33-44.

Yekta, A., Audigane, P., & Pichavant, M., (2015). Geochemical reactivity and migration of pure hydrogen through sandstone: application to geological storage. 24e Réunion des Sciences de la Terre PAU, France.

Yokoyama, Y., and L. W. Lake (1981), The effects of capillary pressure on immiscible displacements in stratified porous media, paper presented at SPE 10109 SPE Annual Technical Conference and Exhibition, Soc. of Pet. Eng., San Antonio, Tex., 5–7 Oct.

Zhou, D., Fayers, F. J., & Orr Jr, F. M. (1997). Scaling of multiphase flow in simple heterogeneous porous media. SPE Reservoir Engineering, 12(03), 173-178.

8.2 Paper II

Evaluation of geochemical reactivity of hydrogen in sandstone: application to geological storage

E.Yekta, A. [(1)], Pichavant, M. [(1)], Audigane, P. [(2)]

[(1)] ISTO : Institut des Sciences de la Terre d'Orléans, 1A Rue de la Ferollerie, 45100 Orléans, France
[(2)] BRGM Bureau de Recherches Géologiques et Minières, 3 Avenue Claude Guillemin, 45060 Orléans, France

Abstract

The use of hydrogen as an alternative for electric energy storage has emerged recently. Being composed of small molecules, hydrogen has a strong ability to migrate in porous medium and can also be highly reactive with rock-forming minerals. In the case of storage in sedimentary rocks such as sandstone, mineralogical transformations due to the presence of hydrogen may modify the porous structure of the rock and affect the storage properties. In this study, the geochemical reactivity of hydrogen with sandstone was assessed both experimentally and numerically. Experiments were performed to test the possibility of mineral transformations due to hydrogen, either pure or in presence of water. The experiments were carried out mostly at 100 and more rarely at 200 °C. Maximum hydrogen pressures of 100 bar were imposed and experimental durations ranged from 1.5 to 6 months. The experimental products bear the mark of only very limited reaction between minerals in sandstone and hydrogen. Taken together with the numerical results, this study demonstrates that hydrogen, once injected, can be considered as relatively inert. Overall, our results support the feasibility of hydrogen confinement in geological reservoirs such as sandstones.

Keywords: Geochemical reaction, Abiotic reaction, Underground hydrogen storage, experimental study;

1. Introduction

The world's population will grow by 2 billion people by 2040 and we will need a lot more energy to meet demand. However, the most important energy source for the future is not fossil fuel so we have to move from fossil energy to renewable energy. Solar energy, wind power and moving water are all traditional sources of alternative energy that are making progress but these renewable energies have a weakness: their production is highly dependent on unpredictable climate conditions which may not fit in with population needs (*Schaber et al.*, 2012).

The objective to integrate renewable energy in the global market induces the need to develop storage technologies to obtain alternative availability for later use when electricity demand is surpassing electricity generation. Therefore, renewable energy requires storage to maintain the energy balance between production and consumption.

Hydrogen, having a high availability and being clean, has long been discussed as a candidate for large-scale energy storage for renewable energy systems (*Foh et al.*, 1979; *Carden and Paterson*, 1979; *Li*, 2005; *Crotogino et al.*, 2010; *Ozarslan et al.*, 2012; *HyUnder* 2013; *Lord et al.*, 2014). By way of electrolysis, it becomes one of the major actors in the possible conversion of wind power or solar energy. Favorable arguments include the high storage densities and the low environmental costs. Therefore, hydrogen can be an energy carrier for large scale use. However, this would require large volumes since hydrogen is gaseous. One solution would be to store hydrogen in subsurface geological formations, and in a way that would make it available depending on the customer's needs.

The current technology for underground storage of hydrogen uses the same types of reservoirs as for natural gas. Depleted gas fields, aquifers or salt caverns are considered as possible storage sites (*Bai et al.,* 2014). Although gas storage is a key step in the hydrogen economy (*Crotogino et al.,* 2010), the loss of hydrogen through chemical reactions with confining rocks is one of the major geochemical and operational challenges (*Bourgeois et al.,* 1979; *Carden and Paterson,* 1979; *Foh et al.,* 1979; *Lord,* 2009). Because it is composed of small and light molecules, gaseous hydrogen has a strong ability to migrate in porous media and could be highly reactive with rock forming minerals. In fact, redox reactions induced by hydrogen can change the rock mineral assemblage and modify mineral dissolution and precipitation (*Ganzer et al.,* 2013; *Truche et al.,* 2013). The physical properties of the confining rocks, notably porosity and permeability, would be affected by these mineralogical transformations. In the case of hydrogen storage in sedimentary rocks, changes of the porous structure of the rock are expected and these might influence the capacity for underground gas storage.

Mechanisms and kinetics of redox reactions induced by hydrogen in sedimentary rocks are yet poorly documented. Nevertheless, this is a topic of growing interest for underground hydrogen geological storage but also for nuclear waste storage assessment. The feasibility of hydrogen storage in porous geological formations has been discussed notably by *Ganzer et al.,* (2013), *Decourt et al.,* (2014) and *Panfilov* (2016). Temperatures of underground hydrogen storage are expected to range between 50°C and 100°C and the maximum hydrogen pressure is expected to be in the 100 bar range.

In the context of deep geological disposal of nuclear waste in a clay-rich host rock, *Truche et al.* (2010) presented an experimental kinetic study of mineralogical reactions induced by elevated hydrogen partial pressures ranging from 3 to 30 bar at low to medium temperatures (90-180°C). He showed that, under the influence of hydrogen and for slightly alkaline conditions, pyrite is partially reduced to pyrrhotite, releasing sulfide anions in the solution. Hydrogen had a major impact on sulphur chemistry, but no significant effect was found on the other minerals present in the natural rock (clay minerals, quartz, calcite, dolomite and feldspars), even for a PH_2 of 30 bar and a temperature of 150°C *(Truche et al.,* 2013). The pH of the fluid medium was identified as a critical parameter controlling the extent of the reaction as alkaline conditions promoted pyrrhotite precipitation at lower temperatures and hydrogen pressures.

The experimental study presented in this paper aims at evaluating the mineralogical impact of hydrogen on a sandstone lithology under conditions of natural hydrogen storage. To test the reactivity of the hydrogen/sandstone system, two distinct temperature ranges were chosen. A majority of experiments was performed at 100 °C, which is close to the maximum temperature range expected for underground hydrogen storage. Additional experiments were performed at a higher temperature (200°C) in order to: i) enhance reaction rates and ii) facilitate the identification of mineralogical transformations. The mineralogical changes were monitored by the analysis of experimental products with scanning electron microscopy (SEM), X-ray diffraction (XRD) and electron microprobe (EMP). In addition, numerical runs were performed with the PHREEQC (*Parkhurst and Appelo,* 1999) reactive transport code, mainly to extend the experimental observations to longer timescales. Results from this study emphasize the very limited reactivity of sandstones with respect to hydrogen gas. They document that hydrogen, once injected, can be considered as relatively inert and establish the feasibility of hydrogen confinement in geological reservoirs such as sandstones.

2. Materials and methods

2.1. Geological context

This study is directed at the testing of sandstone lithologies for underground hydrogen storage. To do so, lower Triassic sandstones (Buntsandstein formation) from the Vosges (France) were selected as test

samples. These sandstones are representative of western European sandstone lithologies. They outcrop in a large geographical area and are now receiving increasing attention for geothermal applications (*Aquilina et al.* 2010, *Blaise et al.* 2016) as well as for CO_2 storage (*Le Gallo et al.*, 2010; *Bader et al.*, 2014). Three sandstone samples were collected respectively from the Rotbach, Adamswiller and Cleebourg quarries.

2.2. Samples and analytical methods

Parts of each sample were crushed and sieved to grain sizes between 30 and 50 µm. The powders were analyzed by XRD and used as starting materials for the experiments. Sandstone thin sections were prepared and, in parallel, cores (5 mm diameter and 40 mm length) were drilled. These were used for the determination of rock physical properties and as starting materials for the experiments. Thin sections were also made from the cores recovered after the experiments.

Physical properties. Absolute permeabilities, pore volumes, porosities and densities were measured on cores drilled in the starting samples. The absolute permeability was obtained by the water core-flooding method using Darcy's law, as detailed in Yekta (2017). Pore volumes were determined by mercury intrusion porosimetry using a Micromeritics Autopore IV 9500 instrument working from vacuum to 200 MPa. The intrusion and extrusion curves were obtained with an equilibration time of 60 s from low to high pressure. The porosity was obtained from the total volume (determined from the size of the core samples) and using the pore volume from above. The density was measured by weighing the samples in air and in water.

Optical *microscopy*. The thin sections (sandstones and experimental cores) were examined with a Zeiss petrographic microscope. Modal proportions of mineral phases in starting samples were determined with an automated Peltron point counter coupled with a petrographic microscope.

X-ray diffraction (XRD). The X-ray diffraction (XRD) data were obtained with an INEL diffractometer equiped with a curved position-sensitive detector. Sample powders were loaded in a glass capillary (Hilgenberg GmbH n°50). A Cu anode was used and the Co Kα1 X-ray line was selected using a bent quartz crystal monochromator. The scan parameters used were 0–90° 2θ, with a step size of 0.02° 2θ. Both starting and experimentally reacted samples were analyzed, the latter including powders and cores which were analyzed after gentle crushing. To facilitate the detection of mineralogical transformations, XRD results on experimental samples were compared against a reference.

Scanning electron microscopy *(SEM).* The thin sections (sandstones and experimental cores) were carbon-coated and mineral textures examined with a TESCAN MIRA 3 XMU instrument from the ISTO-BRGM analytical platform at Orléans. Energy-dispersive spectroscopy (EDS) analyses of specific grains were also performed for mineral identification and element distribution maps acquired to assist mineral identification.

Electron microprobe (EMPA). Mineral phases in thin sections (sandstones and experimental cores) were analyzed with the Cameca SX Five instrument of the ISTO-BRGM analytical platform at Orléans. The microprobe was operated at 15 kV acceleration voltage and 6 nA sample current. Natural mineral standards were used. Counting times were 10 s on peak and 5 s on background, and a focused beam was used.

Numerical modeling. In parallel with the experiments, geochemical modeling of fluid-rock interactions was performed with the PHREEQC geochemical software V.3.1.5 (Parkhurst and Appelo, 1999). The simulations were carried out to test the influence of hydrogen on sandstone in presence of water only. They provide a theoretical reference frame to predict the appearance of mineral product phases and enable timescales to be extended beyond the experimental range. The calculations were performed both in equilibrium and kinetic modes (e.g., *Pudlo et al.*, 2013).

2.3. Experimental methods

Static batch reactor experiments were conducted to evaluate the effect of gaseous hydrogen on sandstone at pressures and temperatures representative of reservoir conditions. In these experiments, duration was taken as the main experimental parameter.

Experimental charges. Both cores and powders were experimentally tested and results with these two rock types are combined below. The starting materials (1.5 g for each charge) were dried in an oven at 120°C for 20 min and then loaded in Au capsules of 50 mm length. In one experiment, the core was saturated with water before being loaded in the capsule. In most cases, capsules were fitted with a porous ceramic plug at both ends (Figure 1a). This procedure enabled gas from the pressure medium (either H_2 or Ar) to access freely to the sandstone during the experiment while preserving the charge from being in contact with the autoclave walls. It also ensured the confinement of the charge for experiments performed with powders.

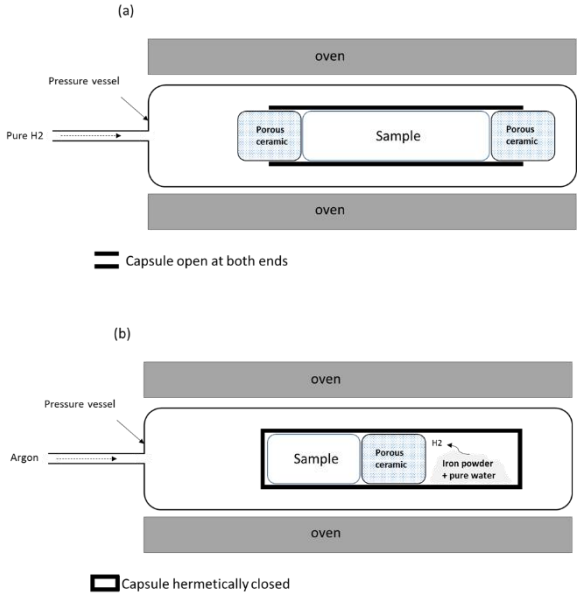

Figure 1. Configurations of experimental charges used in this study. (a) experiments performed under pure H_2 gas. The sandstone sample (either core or powder) is loaded in a Au capsule fitted with porous ceramic plugs at both ends, allowing H_2 to freely access to the sample. (b) experiment performed with a H_2O-H_2 gas mixture. The sample is loaded together with Fe powder and H_2O in a Au capsule that is hermetically closed by welding. Experimental charges such as in (a) or (b) are then placed in an horizontal pressure vessel. See text for additional details.

In one experiment designed to test the effect of hydrogen on sandstone in presence of water, a different charge assembly was used (Figure 1b). The charge (1.4 g of sandstone plus 150 mg of H_2O, water/rock ratio of ~0.1) was loaded in the Au capsule together with pure Fe powder, and the capsule was hermetically closed at both ends by welding. Hydrogen was generated from inside the capsule by allowing the water present to react with the Fe powder. The sandstone inside the capsule was thus allowed to react with a H_2O-H_2 fluid mixture. To prevent contamination with Fe, the sandstone was physically separated from the Fe powder by a porous ceramic plug.

Experimental equipment and procedures. Capsules with experimental charges were placed inside a rapid-quench hydrothermal pressure vessel made of a Ni-rich alloy and working horizontally (Pichavant, 1987). After being closed, the vessel was pressurized to a total pressure of 100 bar and then inserted into the furnace. In most cases, the pressurizing gas was pure hydrogen. In two cases (synthesis of the XRD reference and H_2O-H_2 fluid mixture experiment), Ar was used instead of hydrogen. During the experiment, temperature was monitored with an Eurotherm regulator and permanently recorded with a

thermocouple inserted in the autoclave wall. Pressure was measured with a manometer (pressure range: 0–500 bar; measurement error < 1 % of full scale value) and adjusted during the course of the experiment, if necessary. Uncertainties on temperature and pressure are +/-10°C and +/-20 bar respectively. Once the experiment was completed, the pressure vessel was removed from the furnace, allowed to cool at room temperature (< 1 hour) and opened. The capsules were recovered and the samples prepared for analysis.

3. Results

3.1. Mineralogical and physical parameters of sandstones

The mineral modes of the three studied sandstones are detailed in Table 1. Point counting results, plus XRD data, enable the mineralogical composition of the samples to be determined. Quartz and feldspar are the dominant minerals in the three rocks and, together, they account for 95-97 % of the total mineral proportion. With a modal amount of 74-80 %, quartz is the most abundant phase, followed by K-feldspar (17-26 %). Mica (muscovite according to the XRD results) is the main accessory mineral (0.6-2.3 %). An oxide phase (hematite according to the XRD results) and clay minerals (only distinguished from muscovite by microscopic examination) occur as minor phases (modal proportions 0.3-0.9 and 0.6-1.0 %, respectively). Although phase proportions can vary (Table 1), there is no change in mineral assemblage between the three studied samples. Because mica and oxide proportions are the highest in sample 1# (Adamswiller quarry), this sandstone was selected for the experimental study.

Table 1 Mineral modes of the studied sandstones

Sandstone sample #	Mineral types and content (Vol %)[a]				
	Quartz	K-feldspar	Mica	Oxide	Clay minerals
1 (Adamswiller)	73.8	22.4	2.3	0.9	0.6
2 (Cleebourg)	71.6	25.7	1.4	0.3	1.0
3 (Rotbach)	80.9	17.2	0.6	0.5	0.8

[a]Point counting of 500 points per thin section.

The physical data for the three sandstones are reported in Table 2. Although some dispersion is apparent, permeabilities do not vary by more than a factor of 2 between samples. Porosities are in the 15-20 % range and tightly grouped. The Rotbach sandstone has a high density compared to the two other samples.

Table 2 Physical parameters of the studied sandstones

Parameters	Sandstone #1	Sandstone #2	Sandstone #3
Permeability (mD)	46	85	98
Porosity (%)	19.8	16.4	18.8
Density ($g.cm^{-3}$)	1.96	1.85	2.31

3.2. Experimental results

General. Experimental conditions and results are summarized in Table 3. Durations ranged from 1.5 to 6 months. Five experiments were performed at 100°C and three at 200°C. Experiment no. 3 is the one which started from a wet core, instead of a dry one as in all the other experiments. The experiment with

the mixed H_2O-H_2 fluid phase (no. 8, Table 3) was performed at a temperature of 100°C and a pressure of 100 bar, and the partial pressure of hydrogen in the H_2O-H_2 fluid mixture is estimated to be in the 10-50 bar range. The reference charge for the XRD data was synthesized in experiment no. 1.

Table 3 Experimental conditions and results for sandstone #1

No	Pressure (bar)	Temperature (°C)	Duration (month)	Hydrogen source	Water	Rock type	Water-Rock ratio	Analytical results			
								Quartz	K-Feldspar	Muscovite	Hematite
1	100	100	1,5	-	-	Powder	0	T X	T X	T X	T X
2	100	100	1,5	Pure H_2	-	Powder	0	T X	T X	T X	T X
3	100	200	1,5	Pure H_2	-	Core[b]	0	T X S	T X S	T X S	T X S
4	100	200	3	Pure H_2	-	Powder	0	T X	T X	T X	T X
5	100	200	3	Pure H_2	-	Core	0	T X S	T X S	T X S	T X S
6	100	100	6	Pure H_2	-	Powder	0	T X	T X	T X	T X
7	100	100	6	Pure H_2	-	Core	0	T X S	T X S	T X S	T X S
8	10 to 50	100	1,5	H_2[a]	H_2O	Core	0,1	T X S	T X S	T X S	T X S

[a]Hydrogen generated from the reaction of water and iron
[b]The core was saturated with water before the experiment
T: texture analysis
X: XRD analysis
S: chemical analysis
Changes indicate by underlined text (i.e. X indicates a change in XRD data in comparison with the reference)

Textural evolution. Textures of starting materials and representative experimental products are summarized in Figure 2. Observations by optical microscopy and SEM yielded similar results. SEM microphotographs of experimental charges for "dry" conditions as well as for the "wet" experiment are illustrated. Overall, no clear textural change appears between samples, whether coming from the starting materials or from experimentally reacted charges. Quartz and feldspar minerals form grains with sizes mostly in the 100-200 µm range and they show typical anhedral rounded morphologies. No difference can be noted between experimental samples, whether "dry" or "wet" (Figure 2a; d; g). Muscovite appears as sub-euhedral flakes, 50 to 200 µm in size, and no apparent textural modification emerges between the three different types of samples, starting material, experimental "dry" and experimental "wet" (Figure 2b; e; h). Fe oxides were found to occur under more variable habits in the sandstones, from small crystals included in quartz or feldspar minerals (Figure 2c; f) to interstitial grains, sometimes large (50 µm) in size (Figure 2i). However, they show no textural indication for a mineralogical transformation, even partial or local. Therefore, the optical and SEM examinations reveal no significant textural changes in experimental products in comparison with the starting sandstones. This is true both for experimental samples reacted with and without H_2O (Figure 2g; h; i) and at 100 and at 200°C (Figure 2f).

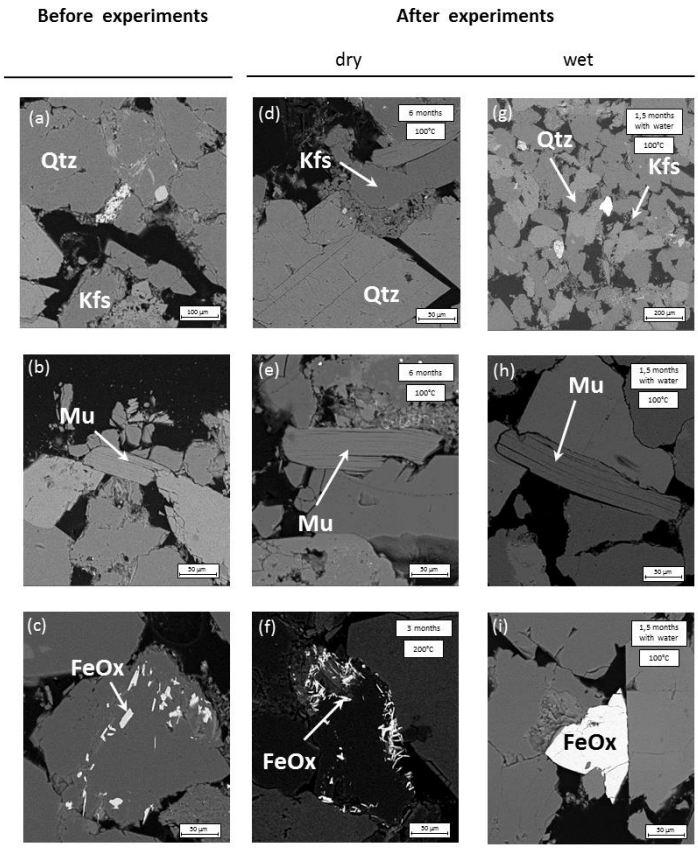

Figure 2. SEM photomicrographs of starting materials and experimental products. (a), (b), (c), photomicrographs of the main mineral phases in the starting sandstone, quartz (Qtz, a), K-feldspar (Kfs, a), muscovite (Mu, b) and hematite (FeOx, c). (d), (e), (f), photomicrographs of representative products from the "dry" experiments (performed with pure H_2 gas) showing quartz and K-feldspar (d), muscovite (e) and hematite (f). Same abbreviations as in (a), (b) and (c). (g), (h), (i), photomicrographs of products from the "wet" experiment (performed with a H_2O-H_2 gas mixture) showing quartz and K-feldspar (g), muscovite (h) and hematite (i). Same abbreviations as in (a), (b) and (c). See text for explanations.

Phase assemblages and structural evolution. The XRD results are summarized on Table 4. They show that the same phase assemblage (quartz, feldspar, muscovite, hematite) is present in the samples before and after the experiments. Magnetite was looked for but never positively identified. Clay minerals were not positively detected although a weak peak indicative of kaolinite might be present in some samples. Therefore, reacting the sandstone with hydrogen caused no first-order modification in the phase assemblage from the starting rock.

Table 4 Phases present in XRD analysis

experiment number	Phases present					
	Quartz	K-feldspar	Muscovite	Hematite	Magnetite	Kaolinite
1	+	+	+	+	-	-
2	+	+	+	+	-	-
3	+	+	+	+	-	?
4	+	+	+	+	-	-
5	+	+	+	+	-	-
6	+	+	+	+	-	-
7	+	+	+	+	-	-
8	+	+	+	+	-	-

The XRD signatures of quartz and feldspars did not change before and after the experiments. However, differences were noted between the reference and the experimental samples concerning muscovite (Table 3). Most sandstones annealed under hydrogen showed an increase of muscovite XRD peak

intensities compared to the reference, as illustrated in Figure 3. The most marked intensity increases were noted for charges no. 4, 5, 6 and 7, i.e., for two "dry" 200°C, 3 month (4, 5) and two "dry" 100°C, 6 month (6, 7) experiments. In comparison, the "wet" charge (no. 8, 1.5 month, Table 3) did not show much variation compared to the reference, and the two 1.5 month experiments (no. 2, 3) were relatively little modified (Figure 3). Although overall these changes are of minor importance, they are considered as significant since they occur in several charges. They indicate that some mineralogical transformations, such as muscovite recrystallization or growth, took place during the experiments.

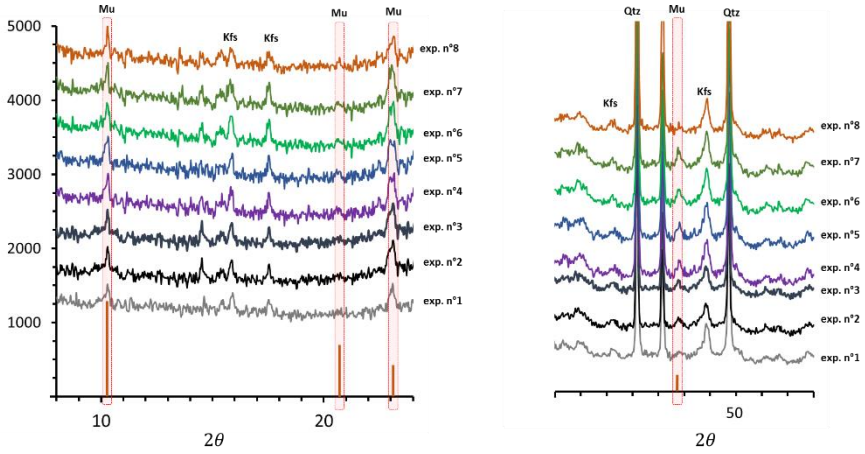

Figure 3. Evolution of XRD peaks of muscovite at 2Θ = 10.315°, 20.737°, 23.087°, 47.796° in experimental products (exp. n° 2, 4, 6, 8) and in the reference (exp. n°1). See Table 3 for experimental conditions and text for explanations.

Additional evidence for mineral reaction during the experiments is provided by the Fe oxides. In our experimental charges, the only Fe oxide identified by XRD is hematite and magnetite was never found. Contrary to an expected reduction of hematite under the influence of hydrogen, the XRD peaks diagnostic hematite showed intensity increases in several charges, in particular in experiments 6 and 7 (Figure 4). Again, in the "wet" no. 8 charge, hematite peaks showed little intensity changes relative to the reference (Figure 4). Therefore, and although detailed information is lacking to interpret these changes, the XRD signature of Fe oxides further demonstrates that limited but detectable mineral reaction takes place in the experiments as a result of hydrogen.

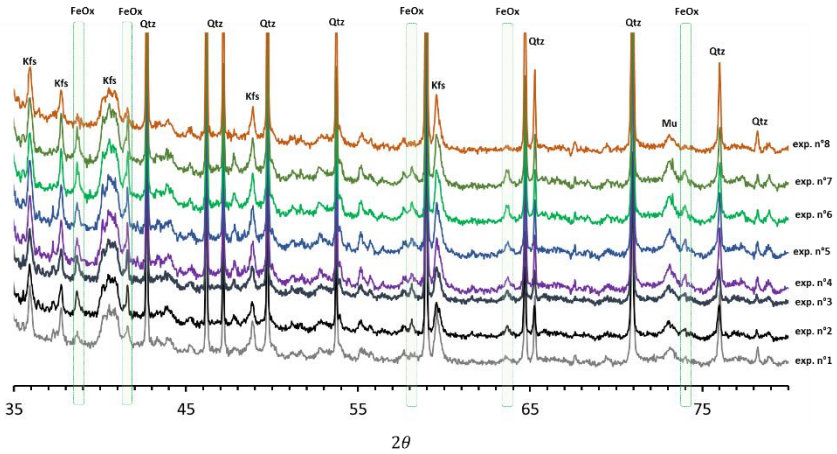

Figure 4. Evolution of XRD peaks of hematite at 2Θ = 38.694°, 41.599°, 58.153°, 63.741796°, 74.024° in experimental products (exp. n° 2, 3, 4, 5, 6, 7, 8) and in the reference (exp. n°1). See Table 3 for experimental conditions and text for explanations.

Compositional evolution. Results of electron microprobe analyses of minerals before and after the annealing experiments under hydrogen are summarized on Table 5. Three phases in particular were

investigated, K-feldspar, muscovite and hematite and, for each, electron microprobe data before and after the experiments are given. Average values and standard deviations are provided especially for muscovite whereas, for the other phases, only starting compositions have been averaged because of more limited data. The generally low standard deviations (e.g., < 0.5 wt% for SiO_2 in K-feldspar, FeO in muscovite and TiO_2 in hematite) indicate that mineral phases in the starting sandstone are sub-homogeneous. K-feldspar is nearly pure, containing very little Na_2O (on average 0.37 wt%) and very low (below detection) FeO_t. Muscovite contains significant amounts of FeO_t (on average 3.54 wt%), MgO (1.20 wt%), TiO_2 (0.78 wt%) and Na_2O (0.44 wt%). Hematite has low Al_2O_3 (on average 0.48 wt%), MnO (0.22 wt%) and MgO (0.02 wt%) but relatively high TiO_2 (9.12 wt%), which corresponds to a solid solution between ilmenite and hematite in a 0.18:0.82 proportion (mole fraction). Experimentally reacted K-feldspars and hematites are chemically homogeneous and they show little compositional differences with minerals in the starting sandstone. One K-feldspar analysis (no. 5) is exceptionally Na_2O-rich (1.38 wt%). The range of TiO_2 concentrations in experimental hematites (9.01 to 10.2) encloses the average in the starting sample. In contrast, experimental muscovites record a minor but detectable compositional change from the starting sandstone. FeO_t concentrations decrease from ~ 3.5 wt% before experiments to values ranging from 1.24 to 2.48 wt% in experimental samples. Charges no. 3 and 8 (respectively performed with a wet starting core and a H_2O-H_2 fluid, Table 3) show the maximum deviations, whereas muscovites in charges no. 5 and 7 (two "dry" charges at 200 and 100°C, Table 3) appear less chemically modified. Apart from FeO_t concentrations, the other oxides show no significant changes when compared with the starting composition and, so, the chemical modifications recorded by muscovite are relatively minor. However, they demonstrate that mineral phases can change their compositions during the experiments as a result of interaction with hydrogen.

Table 5 Representative electron microprobe analysis of minerals before and after the experiments

	K-feldspar					Muscovite					Hematite				
	Starting sandstone	Exp. n°3	Exp. n°5	Exp. n°7	Exp. n°8	Starting sandstone	Exp. n°3	Exp. n°5	Exp. n°7	Exp. n°8	Starting sandstone	Exp. n°3	Exp. n°5	Exp. n°7	Exp. n°8
SiO2	64.9 (3)	64.3	65.4	64.1	64.8	47.3 (9)	46.7 (10)	47.5 (98)	46.9 (7)	45.8 (9)	0.08 (2)	0.02	0.09	0.04	0.07
TiO2	0.07 (1)	0.00	0.00	0.00	0.10	0.78 (44)	0.61 (17)	0.67 (25)	0.84 (20)	1.06 (21)	9.12 (34)	10.2	10.0	9.70	9.01
Al2O3	18.1 (6)	18.1	18.0	18.3	17.9	31.4 (5)	34.3 (9)	31.9 (9)	31.3 (10)	32.8 (2)	0.48 (11)	0.00	0.00	0.52	0.30
FeO_t	0.00 (0)	0.11	0.10	0.17	0.10	3.54 (44)	1.34 (58)	2.14 (45)	2.48 (38)	1.24 (14)	85.2 (5)	87.4	86.3	84.1	85.3
MnO	0.00 (1)	0.00	0.13	0.00	0.00	0.03 (5)	0.06 (6)	0.03 (4)	0.05 (6)	0.04 (3)	0.22 (27)	0.16	0.38	0.50	0.63
MgO	0.00 (0)	0.00	0.01	0.03	0.00	1.20 (1)	0.74 (19)	1.21 (31)	0.65 (48)	0.82 (10)	0.02 (5)	0.50	0,00	0,00	0.02
CaO	0.00 (0)	0.01	0.00	0.00	0.01	0.00 (0)	0.03 (2)	0.03 (4)	0.00 (0)	0.00 (1)	0.03 (1)	0.00	0.00	0.00	0.03
Na2O	0.37 (26)	0.21	1.38	0.62	0.15	0.44 (9)	0.41 (15)	0.33 (15)	0.39 (12)	0.59 (5)	0.01 (1)	0.00	0.00	0.00	0.00
K2O	16.1 (7)	16.5	14.5	15.6	16.2	10.2 (2)	10.5 (2)	10.2 (3)	9.86 (26)	9.12 (24)	0.03 (2)	0.05	0.03	0.01	0.00
Total	**99.6 (2)**	**99.2**	**99.6**	**98.9**	**99.3**	**94.8 (10)**	**94.3 (10)**	**94.1 (1)**	**95.5 (2)**	**91.5 (9)**	**95.2 (9)**	**98.3**	**96.9**	**94.9**	**95.4**

3.3. Geochemical simulations

Parametrization. 100 moles of sandstone rock from Adamswiller were reacted with pure water in presence of H_2 gas. The simulations were performed at 100°C, and for a H_2 pressure set at 100 bar in most cases, and more rarely at 10 bar. Three water/rock mass ratios (W/R) were tested, 0.1 (as in the experiments), 1 and 10, to reproduce long time-integrated fluid circulations. As an initial step, calculations in equilibrium mode guided the choice of mineral product phases to be considered since, in the experiments, phase assemblages did not vary and no product phase was identified. Then, simulations in kinetic mode were performed in two cases, the first without mineral product phases (and so simulating the simple dissolution of sandstone minerals in the fluid, the mineralogical composition being set constant as in Table 1) and the second with selected product mineral phases included (coupled mineral dissolution and precipitation).

Equilibrium results. When in equilibrium mode, a number of phases appeared as possible products of the interaction between sandstone and hydrogen in presence of water. These product phases did not

change significantly with varying input parameters such as the H_2 pressure which was reduced from 100 to 10 bar in a few runs. They include: magnetite (Fe_3O_4), Fe-mica (annite), Fe-chlorite (chamosite), Fe-serpentine (cronstedtite), fayalite (Fe_2SiO_4), wustite (FeO), ferrosilite ($FeSiO_3$), greenalite, minnesotaïte and nontronite (Table 6). The highest computed saturation indexes were found for annite, chamosite and minnesotaïte. These equilibrium calculations predict phase assemblages expected to be present at equilibrium upon transformation of sandstone by hydrogen. They stress the presence of various hydrous Fe silicates (annite, chamosite, cronstedtite, greenalite, minnesotaïte, nontronite) and the reduction of Fe from Fe^{3+} in mainly hematite to Fe^{2+} in magnetite, fayalite, wustite and ferrosilite. It is important to emphasize that quartz and K-feldspar remain stable during the interaction. Therefore, the mineral changes above concern phases such as muscovite, hematite and clay minerals which overall form a minor volumetric fraction in our sandstone.

Table 6 Stable and product minerals and saturation indices (SI) predicted to the be present at equilibrium from PHREEQC calculations

Stable minerals	Product minerals	Saturation indexes
Quartz	-	0.00
K-feldspar	-	0.00
	Magnetite	3.01
	Annite	9.43
	Chamosite	3.85
	Cronstedtite	5.63
	Fayalite	3.98
	Wustite	0.49
	Ferrosilite	2.03
	Greenalite	8.31
	Minesotaite	9.23
	Nontronite	0.37

Kinetic results. Results for simple dissolution are illustrated in Figure 5. Changes in mass fractions of mineral phases from the sandstone are plotted as a function of time for the 3 W/R considered. The calculations assume constant specific surfaces of 10 cm^2/g and 20 cm^2/g for quartz and feldspar, and muscovite and hematite, respectively (Yekta 2017). The influence of hydrogen on mineral dissolution can be appreciated from the curves calculated without hydrogen for W/R = 1. Results show that, with and without hydrogen, the dissolution curves for quartz, K-feldspar and muscovite are identical but the dissolution of hematite becomes strongly affected. In presence of hydrogen, the 4 major minerals follow an initial decrease of their mass fraction, interpreted as mineral dissolution in the fluid. Then, plateau values are reached for each mineral phase, although these are attained after durations that depend on the mineral, and in particular on the W/R for a given mineral. These plateau values are interpreted to reflect saturation of the fluid with respect to the dissolving mineral phase. For quartz and hematite, plateau values are attained only for a W/R of 0.1, in both cases after 1-10 years. No saturation is observed after 10^2 years for a W/R of 1 and 10 (Figure 5). In contrast, aluminous phases (K-feldspar and muscovite) reach saturation for the 3 W/R considered. In both cases, saturation is attained after durations that increase monotonously with the W/R, from 0.1 to < 10 years for K-feldspar and from < 0.01 to < 1 years for muscovite.

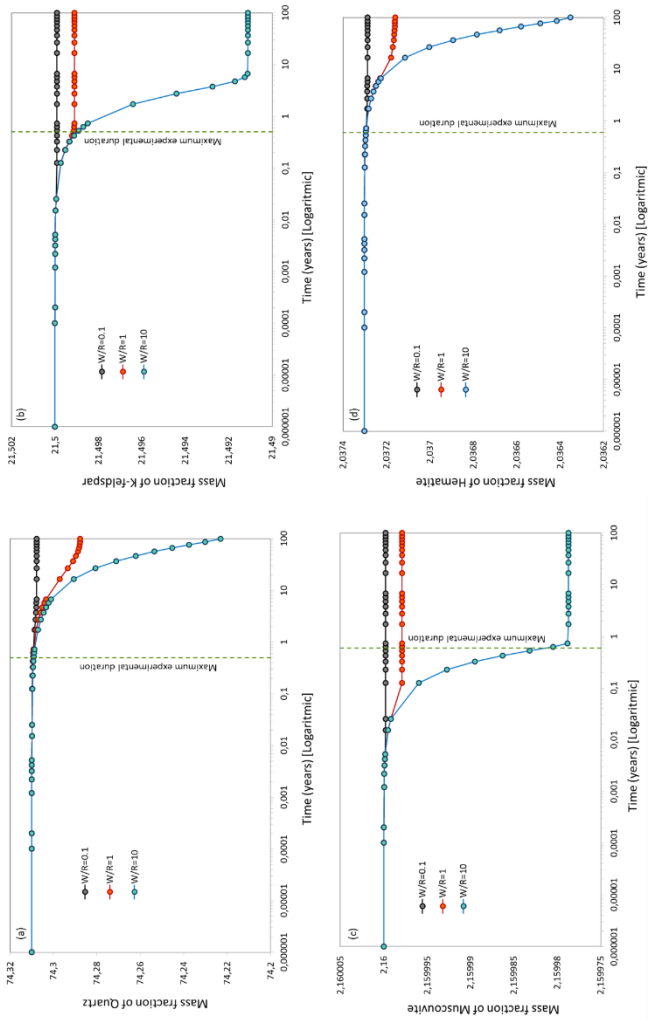

Figure 5. Geochemical modeling of simple sandstone mineral dissolution in a H_2O-H_2 fluid using PHREEQC. Mass fractions of mineral phases (normalized to 100 g of sandstone) are plotted as a function of time for timescales ranging from 10^{-6} to 10^{2} years. (a) evolution of the quartz mass fraction; (b) evolution of the K-feldspar mass fraction; (c) evolution of the muscovite mass fraction; (d) evolution of the hematite mass fraction. For each panel, results are shown for the 3 water/rock ratios (W/R) considered. The vertical dashed line gives the maximum duration of the experiments (Table 3). See text for details about the calculations.

Results for combined mineral dissolution and precipitation are illustrated by considering first magnetite as the only product phase. When compared with simple mineral dissolution (Figure 5), mass fractions for quartz, K-feldspar and muscovite show no variations and dissolution curves for the "with" and "without magnetite" cases perfectly overlap, irrespective of the W/R. For hematite, the introduction of magnetite leads to a decrease of its mass fraction when compared (for the same duration) with the "without magnetite" case (Figure 6). Therefore, the mass fraction of hematite decreases more rapidly when magnetite precipitates as a reaction product. The mass of magnetite progressively increases with time and curves for the production of magnetite are progressively shifted to longer durations when the W/R is increased. For W/R = 0.1, i.e., for conditions approaching the experiments, the calculations suggest that 100 years are necessary to produce 0.001 g of magnetite (mass normalized to 100 g of reactant rock).

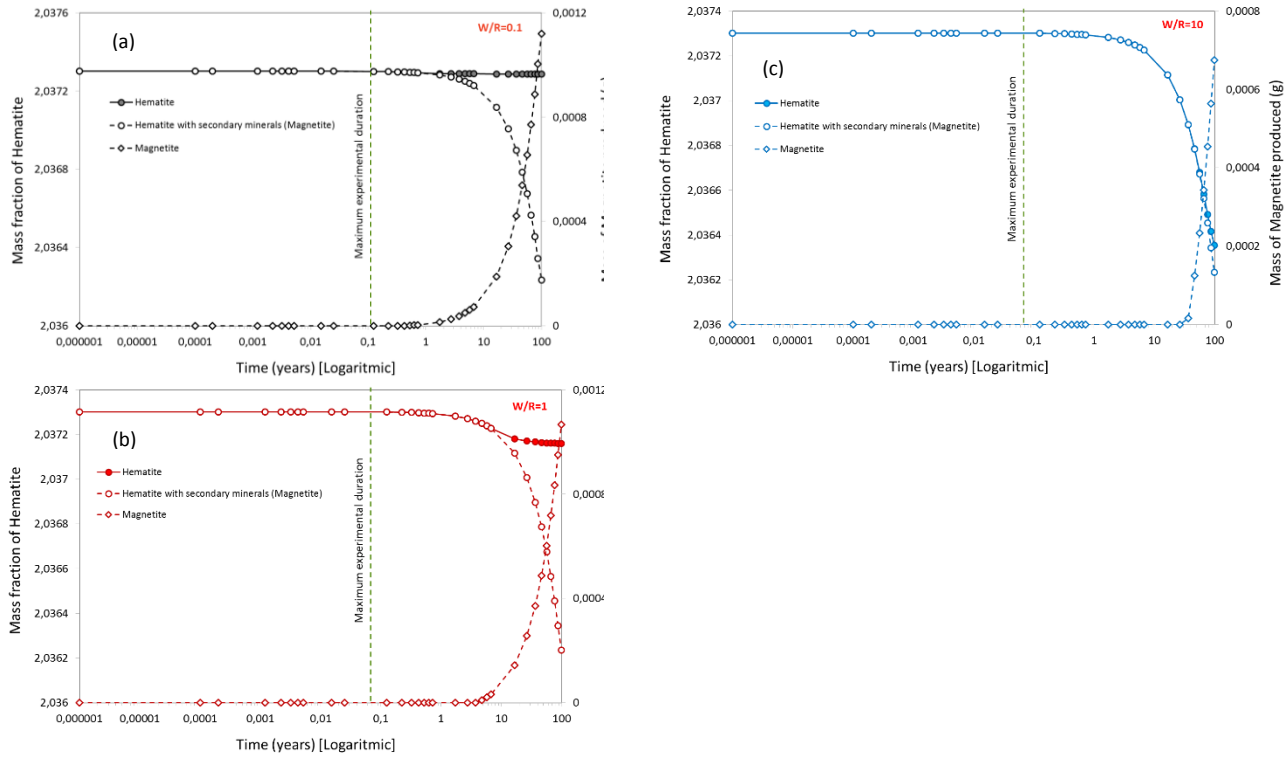

Figure 6. Geochemical modeling of coupled hematite dissolution and magnetite precipitation in a H_2O-H_2 fluid using PHREEQC. Each panel is for a given W/R ratio, from 0.1 (a), 1 (b) to 10 (c). On each panel, the evolution of the mass fraction of hematite during dissolution in the fluid (left axis, normalized to 100 g of reacted sandstone) is plotted as a function of time for timescales ranging from 10^{-6} to 10^{2} years. Dissolution curves for hematite with and without magnetite precipitation (simple dissolution, as in Figure 5) are compared to demonstrate the influence of magnetite on hematite dissolution. The curve describing the mass of produced magnetite is shown with the scale on the right axis (normalized to 100 g of reacted sandstone). The vertical dashed line gives the maximum duration of the experiments (Table 3). See text for details about the calculations.

In a second case, a multiphase product assemblage, including magnetite, annite and chamosite (Table 6) was considered. This complex assemblage leads to modifications of rates of dissolution of quartz and K-feldspar. Focusing on results for a W/R of 1, the quartz and K-feldspar dissolution curves are both shifted from those obtained when no product mineral is considered (Figure 7a). For quartz, the effect of the multiphase product assemblage becomes apparent only after long durations, higher than 10 years. Quartz dissolution is slightly faster when product minerals are included. In contrast, the dissolution of K-feldspar proceeds slightly more slowly in presence of the product assemblage. The difference between the two dissolution curves appears very early, for durations < 0.1 year (Figure 7a). Muscovite dissolution (not shown) is not affected. Masses of annite and chamosite increase progressively with time to reach values > 0.001 g (normalized to 100 g of reactant rock). No magnetite appears in product assemblages most probably because it is allowed to react to form annite. The chamosite production curve shows a complex evolution with time with a maximum mass attained after ~50 years (Figure 7b).

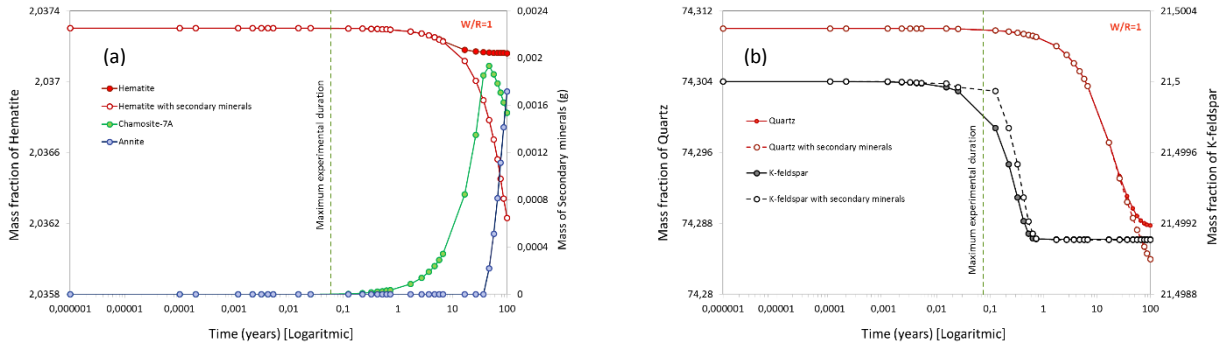

Figure 7. Geochemical modeling of coupled mineral dissolution and precipitation in a H_2O-H_2 fluid using PHREEQC. Product phases considered in the calculations include magnetite, annite and chamosite. W/R is fixed to 1 in both panels. (a) evolution of the mass fraction of quartz and K-feldspar during dissolution in the fluid with and without product phases included. Mass fractions of quartz and K-feldspar (left axis, normalized to 100 g of reacted sandstone) are plotted as a function of time for timescales ranging from 10^{-6} to 10^{2} years. (b) evolution of the mass fraction of hematite during dissolution in the fluid with and without product phases. The mass fraction of hematite (left axis, normalized to 100 g of reacted sandstone) is plotted as a function of time for timescales ranging from 10^{-6} to 10^{2} years. The curves describing the mass of product phases (only annite and chamosite, magnetite never appears as a product phase when annite is allowed to be present) are shown with the scale on the right axis (normalized to 100 g of reacted sandstone). The vertical dashed line gives the maximum duration of the experiments (Table 3). See text for details about the calculations.

4. Discussion

4.1. Mineralogical transformations of sandstone under the influence of hydrogen

Laboratory experiments from this study have provided direct observations on the reaction of sandstone minerals in presence of hydrogen. Experimental conditions were adjusted to those considered typical for underground hydrogen storage, considering the Trias geological context in France at about 1500m depth (hydrogen pressure 100 bar, temperature 100°C, sometimes 200°C). Some experiments lasted up to 6 months. It is worth emphasizing that most experiments were performed in the absence of water. Only one experiment has simulated the influence of hydrogen on sandstone in presence of water.

Overall, the experimental results indicate very limited modifications of sandstone minerals because of the presence of hydrogen. No significant textural changes were found in experimental products in comparison with the starting sandstones (Figure 2). The XRD data showed no major mineral transformation from the reference sample. However, limited but systematic mineralogical changes were noted on the XRD spectra for both muscovite and hematite. For muscovite, the most extensive modifications were found in the 3 and 6 month charges (Figure 3). No influence of the presence of water could be detected but the experiment performed in presence of water had a rather short duration (1.5 month). For hematite, the maximum changes were also found in the 6 month charges (Figure 4). Electron microprobe data revealed shifts in the composition of certain mineral phases as a result of interaction with hydrogen. Muscovite, with FeO_t concentrations decreasing in experimental samples, is clearly chemically modified. In comparison, neither hematite nor K-feldspar showed significant compositional variations (Table 5). Interestingly, the maximum chemical deviations in muscovite are associated with the "wet" samples, and not with the longest experimental charges. This suggests that the mineralogical transformations seen in the XRD data and those revealed by the mineral compositional data are decoupled.

Despite the limited mineralogical transformations identified in experimental products, the results undoubtly indicate that mineral reactions take place in sandstone during interaction with hydrogen. In this study, mechanisms of mineralogical transformations have not been clearly identified and this would probably require experiments of durations longer than 6 months (to promote the advancement of the reactions) as well as the implementation of analytical methods allowing mineral characterization at

spatial resolutions < 1 µm. The geochemical modeling results confirm that mineralogical changes are expected in sandstones upon interaction with hydrogen. They demonstrate that the attainment of equilibrium in the sandstone-hydrogen system is accompanied by the appearance of new stable mineral phases (Table 6). Therefore, and despite the geochemical calculations being performed in presence of water only, both the experimental and theoretical approaches indicate that mineralogical changes should occur in the sandstone reservoir. However, we emphasize that all traces of mineral reaction found in the experiments concern muscovite and hematite. In the same way, the new phases identified from the geochemical calculations are Fe-bearing hydrous and anhydrous silicates and oxides. No changes have been found in experimental products for quartz and K-feldspar, and the equilibrium geochemical calculations show that both phases remain stable during the interaction (Table 6). Since quartz and K-feldspar are major mineral phases in sandstones, the sandstone microstructure is not expected to be significantly modified during interaction with hydrogen, even if minor phases such as muscovite or Fe oxide undergo mineral transformations. Therefore, the physical properties (porosity, permeability) that control the efficiency of sandstone as a reservoir will remain essentially unmodified. It is concluded that quartz- and K-feldspar-rich lithologies such as sandstone are highly stable with respect to interaction with hydrogen.

4.2. Temporal evolution of sandstone reservoir in presence of hydrogen

As discussed in section 4.1, our experimental conditions have been chosen to be representative of large-scale hydrogen injection regarding the Trias geology in France. Yet, in the experiments, no product phase was identified and mineral phase assemblages did not vary with time, despite rather long experimental durations, up to 6 months. The experiments thus bring no constraint on the temporal evolution of the sandstone reservoir in presence of hydrogen. In comparison, results of the geochemical simulations allow the durability of the sandstone reservoir to be explored over timescales that largely exceed the experimental range. Conditions chosen for the calculations (temperature of 100°C, same mineralogical composition as the Adamswiller sandstone, presence of water, W/R, hydrogen pressure in the 10-100 bar range) overlap with the conditions in the experiments, although the latter have been mostly performed water-free. Therefore, the main differences between the experiments and the simulations concern time and W/R, extended to 100 years and to 1 and 10 respectively in the simulations.

Underground gas storage operations are usually performed using a cushion (inert) gas like nitrogen to prevent any leak out of the reservoir or any contact between the injected gas and ground waters of the reservoir formation. Nevertheless, after injection, some residual water is still present inside the pore structure of the rock and therefore fluid rock geochemical interactions require to be considered. This statement highlights the importance of evaluating the potential reactivity of hydrogen with native fluid and rocks of the reservoir at both dry and wet conditions.

Results of the simulations constrain the timescales of fluid-mineral interaction processes that take place in the reservoir. Saturation of the fluid with respect to the main sandstone minerals is attained for durations that depend on the mineral and W/R, but range from < 1 to > 100 years. Hydrogen has little effect on the dissolution kinetics of quartz, K-feldspar and muscovite, but it strongly influences (accelerates) hematite dissolution (Figure 5). Hematite dissolution in the fluid is also faster when magnetite is introduced as a product mineral (Figure 6). Magnetite reaches 0.1 mg after durations of < 10 to ≈50 years depending on the W/R, i.e., for timescales well beyond the experimental range. It is also worth emphasizing that the proportion of magnetite produced (100 g normalized mass ≈0.0011 g after 100 years for W/R = 0.1, Figure 6a) would make its detection by XRD difficult. In other words, the masses of magnetite expected to be produced as a result of interaction between sandstone and hydrogen are not inconsistent with the fact that magnetite was not detected in the experimental products. When more complex product assemblages are considered, the kinetics of quartz and K-feldspar dissolution

become modified but saturation is attained in both cases after durations in the same range (from < 1 to > 10 years) as for simple mineral dissolution (Figure 7).

5. Conclusions

Hydrogen can be stored underground in several types of geological formation. Porous formations could potentially provide high storage capacity and impact of hydrogen on the rock formations should be considered, however, experiences with subsurface porous media hydrogen storage are relatively scarce. In this study, we have performed the experimental and numerical study to evaluate the geochemical reactivity of hydrogen on the mineral components of Vosges sandstone lithology at the underground hydrogen storage.

The experimental results demonstrated that mineralogical changes of Vosges sandstone in contact with hydrogen in reservoir conditions is minor. In fact, compared with starting rocks (before experiments), there are no variation concerning quartz and K-feldspars. There are just minor mineralogical changes concerning muscovite and hematite proportions (XRD) and muscovite composition (Electron microprobe analysis). Therefore, these experimental results clearly show that hydrogen has a minor effect on the minerals present in the Vosges sandstone.

In addition, 1D batch numerical simulation approach without any migration of phases (gas and water) and components was performed to simulate the laboratory experiments that were carried out in this study with the same conditions of temperature, hydrogen partial pressure and water-rock ratio. The geochemical modeling results illustrated that in the long term, hydrogen has no major effect on abundant minerals like quartz and K-feldspars and therefore on the formations of Vosges sandstone and only a minor reduction of hematite could be consider after at least one year.

Overall, this study illustrated that hydrogen has not major effect on Vosges sandstone and the impact of hydrogen could be limited on the reduction of hematite at the long duration and release of Iron from muscovite that are not influence on the rock properties (porosity and permeability) and therefore the reservoir properties. As the consequence, this study confirm that storing hydrogen in the porous geological formation of Vosges sandstone because of the minor influence of hydrogen on the rock formation is feasible. However, this experimental study shows that abiotic reactions between hydrogen and rocks can be excluded from the consideration as insignificant to hydrogen storage.

6. Acknowledgements

This research has been supported by ISTO (Institut des Sciences de la Terre d'Orléans), BRGM (Bureau de Recherches Géologiques et Minières) and university of Orleans. We would like to thank Catherine Lerouge and Joachim Trémosa from BRGM for helping in the collection of the samples at the quarries in the Vosges area and geochemical modeling and Remi Champallier from ISTO for helping to prepare the experiments instruments.

7. REFERENCES

Aquilina, L., Pauwels, H., Genter, A., & Fouillac, C. (1997). Water-rock interaction processes in the Triassic sandstone and the granitic basement of the Rhine Graben: Geochemical investigation of a geothermal reservoir. Geochimica et cosmochimica acta, 61(20), 4281-4295.

Bader, A. G., Thibeau, S., Vincké, O., Jannaud, F. D., Saysset, S., Joffre, G. H., ... & Copin, D. (2014). CO 2 Storage Capacity Evaluation in Deep Saline Aquifers for an Industrial Pilot Selection. Methodology and Results of the France Nord Project. Energy Procedia, 63, 2779-2788.

Bai, M., Song, K., Song, K., Sun, Y., He, M., Li, Y., Sun, J., 2014. An overview of hydrogen underground storage technology and prospects in china. Journal of Petroleum Science and Engineering 124(2014)132–136.

Blaise, T., Clauer, N., Cathelineau, M., Boiron, M. C., Techer, I., & Boulvais, P. (2016). Reconstructing fluid-flow events in Lower-Triassic sandstones of the eastern Paris Basin by elemental tracing and isotopic dating of nanometric illite crystals. Geochimica et Cosmochimica Acta, 176, 157-184.

Bourgeois, J.P., Aupaix, N., Bloise, R., Millet, J.L., 1979. Proposition d'explication de la formation d'hydrogène sulfuré dans les stockages souterrains de gas naturel par reduction des sulfures minéraux de la roche magasin. Revue de l'Institut Français du Pétrole 34, 371–386.

Carden, P.O., Paterson, L., 1979. Physical, chemical and energy aspects of underground hydrogen storage. International Journal of Hydrogen Energy 4, 559–569.

Crotogino, F., Donadei, S., Bünger, U., Landinger, H., Large-scale hydrogen underground storage for securing future energy supplies, Detlef Stotlen, Thomas Grube (Eds.): 18th World Hydrogen Energy Conference 2010 – WHEC 2010, Proceedings, May 16-21 2010, Essen. ISBN: 978-3-89336-654-5.

Decourt, B., Lajoie, B., Debarre, R., & Soupa, O. (2014). The hydrogen-based energy conversion FactBook. The SBC Energy Institute.

Foh, S., Novil, M., Rockar, P., 1979. Underground Hydrogen Storage Final Report. Brookhaven National Laboratories, Upton, NY (268 pp.).

Ganzer L. V. Reitenbach, D. Pudlo, M. Panfilov, D. Albrecht, ,R. Gaupp, The H2STORE Project - Experimental and Numerical Simulation Approach to Investigate Processes in Underground Hydrogen Reservoir Storage Society of Petroleum Engineers, EAGE Annual Conference & Exhibition incorporating SPE Europec, 10-13 June, London, UK Publication, 2013.

HyUnder, (2013) D(4)– "Overview on all Known. Underground Storage Technologies for Hydrogen". Grant agreement no. 2/93. 14.08.2013. 303417

Le Gallo Y., Fillacier, S., Lecomte A., Munier G., Hanot F., Quisel N., Rampnoux N., Thomas S., (2010), Technical challenges in characterization of future CO2 storage site in a deep saline aquifer in the Paris basin. Lessons learned from practical application of site selection methodology, Energy Procedia 4 (2011) 4599–4606.

Li, J., 2005. Underground gas storage in the Beijing-Tianjin region balanced the role of natural gas supply and demand .Int.Pet.Econ.13(6), 37–38.

Lord, A.S., 2009. Overview of Geologic Storage of Natural Gas with an Emphasis on Assessing the Feasibility of Storing Hydrogen. Sandia National Laboratories, Albuquerque, NM (SAND2009-5878, 28 pp.).

Ozarslan, A. (2012). Large-scale hydrogen energy storage in salt caverns. International Journal of Hydrogen Energy, 37(19), 14265-14277.

Parkhurst, D. L., & Appelo, C. A. J. (1999). User's guide to PHREEQC (Version 2): A computer program for speciation, batch-reaction, one-dimensional transport, and inverse geochemical calculations.

Panfilov, M. (2016). 4.1 Underground hydrogen storage as an element of energy cycle. Compendium of Hydrogen Energy: Hydrogen Storage, Distribution and Infrastructure, 91.

Pichavant, M. (1987). Effects of B and H2O on liquidus phase relations in the haplogranite system at 1 kbar. American Mineralogist, 72, 1056-1070.

Pudlo, D., Ganzer, L., Henkel, S., Liebscher, A., Khn, M., Lucia, M., Panfilov, M., Pilz, P., Reitenbach, V., Albrecht, D., Wrdemann, H., Gaupp, R., 2013. Hydrogen underground storage in siliciclastic reservoirs—intention and topics of the H2STORE project. In: EGU General Assembly Conference Abstracts, Geophysical Research Abstracts, v.15, EGU2013-4179-3.

Schaber, K., Steinke, F., Mühlich, P., & Hamacher, T. (2012). Parametric study of variable renewable energy integration in Europe: Advantages and costs of transmission grid extensions. Energy Policy, 42, 498-508.

Truche, L., Berger, G., Destrigneville, C., Guillaume, D., Giffaut, E., 2010. Kinetics of pyrite to pyrrhotite reduction by hydrogen in calcite buffered solutions between 90 and 180 °C: implications for nuclear waste disposal. Geochimica et Cosmochimica Acta 74, 2894–2914.

Truche, L., Jodin-Caumon, M. C., Lerouge, C., Berger, G., Mosser-Ruck, R., Giffaut, E., & Michau, N. (2013). Sulphide mineral reactions in clay-rich rock induced by high hydrogen pressure. Application to disturbed or natural settings up to 250° C and 30bar. Chemical Geology, 351, 217-228.

YEKTA, A. E. (2017). Characterization of geochemical interactions and migration of hydrogen in sedimentary formations: application to geological storage (Doctoral dissertation, Université d'Orléans).

References

ADEME, 2011, Les systèmes de stockage d'énergie - Feuille de Route stratégique. http://www2.ademe.fr/servlet/getDoc?cid=96&m=3&id=77924&p1=30&ref=12441

Akbarabadi, M., & Piri, M. (2013). Relative permeability hysteresis and capillary trapping characteristics of supercritical CO 2/brine systems: An experimental study at reservoir conditions. Advances in Water Resources, 52, 190-206.

Albes, D., Ball, M., Becker, A., Bünger, U., Capito, S., Correas, L., ... & Landinger, H. (2014, June). HyUnder–Hydrogen Underground Storage at large scale, Part I: General project results (European Level)". In The 20th World Hydrogen Energy Conference (WHEC 2014), Gwangju, South Korea (pp. 15-20).

Al-Menhali, A., Niu, B., & Krevor, S. (2015). Capillarity and wetting of carbon dioxide and brine during drainage in Berea sandstone at reservoir conditions. Water Resources Research, 51(10), 7895-7914.

Aquilina, L., Pauwels, H., Genter, A., & Fouillac, C. (1997). Water-rock interaction processes in the Triassic sandstone and the granitic basement of the Rhine Graben: Geochemical investigation of a geothermal reservoir. Geochimica et cosmochimica acta, 61(20), 4281-4295.

Atoyebi, T. M., The preferred natural gas conservation option: underground storage of natural gas, SPE136984, Paper presented at the 34th Annual SPE Conference and Exhibition held in Tinapa – Calabar, Nigeria, 31 July-7 August 2010.

Bader, A. G., Thibeau, S., Vincké, O., Jannaud, F. D., Saysset, S., Joffre, G. H., ... & Copin, D. (2014). CO 2 Storage Capacity Evaluation in Deep Saline Aquifers for an Industrial Pilot Selection. Methodology and Results of the France Nord Project. Energy Procedia, 63, 2779-2788.

Bai, M., Song, K., Song, K., Sun, Y., He, M., Li, Y., Sun, J., 2014. An overview of hydrogen underground storage technology and prospects in china. Journal ofPetroleumScienceandEngineering124(2014)132–136.

Bauer, S., Head of Power to Gas Innovation and Development, RAG Rohöl-Aufsuchungs Aktiengesellschaft, Austria.

Bear, J., & Bachmat, Y. (1967, March). A generalized theory on hydrodynamic dispersion in porous media. In IASH Symposium on Artificial Recharge and Management of Aquifers (Vol. 72, pp. 7-16).

Bear, J.: Dynamics of fluids in porous media, p. 764. Dover Publications (1972)

Blaise, T., Clauer, N., Cathelineau, M., Boiron, M. C., Techer, I., & Boulvais, P. (2016). Reconstructing fluid-flow events in Lower-Triassic sandstones of the eastern Paris Basin by elemental tracing and isotopic dating of nanometric illite crystals. Geochimica et Cosmochimica Acta, 176, 157-184.

Bonijoly, D., Ha-Duong, M., Leynet, A., Bonneville, A., Broseta, D., Fradet, A., Le Gallo, Y., Munier, G., Lagny, G. and Lagneau, V., 2009, METSTOR: a GIS to look for potential CO2 storage zones in France, Energy Procedia, (1), 2809-2816.

Boulin, P. F., ngulo-Jaramillo, R., Daian, J. F., Talandier, J., and Berne, P. (2008) Experiments to estimate gas intrusion in Callovo-oxfordian argillites. Physics and Chemistry of the Earth, 33, S225-S230.

Bourgeat, A., Jurak, M., and Smai, F. (2009) Two-phase, partially miscible flow and transport modeling in porous media; application to gas migration in a nuclear waste repository. Computational Geosciences, 13, 29-42.

BARD, A.J. & FAULKNER, L.R. (1980): Electrochemical methods; fundamentals and applica-tions. John Wiley & Sons, New York.

Brown, H. W. (1951). Capillary pressure investigations. Journal of Petroleum Technology, 3(03), 67-74.

Bruninx, K., Madzharov, D., Delarue, E., & D'haeseleer, W. (2013). Impact of the German nuclear phase-out on Europe's electricity generation—A comprehensive study. Energy Policy, 60, 251-261.

Bulatov, G.G., 1979. Underground storage of hydrogen (Ph.D. thesis). Moscow Gubkin Oil and Gas University.

Burkhardt, M., & Busch, G. (2013). Methanation of hydrogen and carbon dioxide. Applied energy, 111, 74-79.

Busch, A., & Amann-Hildenbrand, A. (2013). Predicting capillarity of mudrocks. Marine and petroleum geology, 45, 208-223.

Buzek, F., Onderka, V., Vancura, P., Wolf, I., 1994. Carbon isotope study of methane production in a town gas storage reservoir. Fuel 73 (5), 747–752.

Carden P, Paterson L (1979) Physical, chemical and energy aspects of underground hydrogen storage. Int J Hydrogen Energy 4(6):559–569

Carriere, J. F., Fasanino, G., & Tek, M. R. (1985, January). Mixing in underground storage reservoirs. In SPE Annual Technical Conference and Exhibition. Society of Petroleum Engineers.

Christoffersen, K. R., & Whitson, C. H. (1995). Gas/oil capillary pressure of chalk at elevated pressures. SPE Formation Evaluation, 10(03), 153-159.

Coldwell et al., 1997. Microorganisms from deep, high temperature sandstones: constraints on microbial colonization. FEMS Microbiology reviews, 20, 425-435.

Crotogino F, Donadei S, Bu¨nger U, Landinger H (2010) Large-scale hydrogen underground storage for securing future energy supplies. 18th World Hydrogen Energy Conference 2010, Essen/Germany, 16–21/05/2010

Crotogino, F., Donadei, S., Bünger, U., Landinger, H., Large-scale hydrogen underground storage for securing future energy supplies, Detlef Stotlen, Thomas Grube (Eds.): 18th World Hydrogen Energy Conference 2010 – WHEC 2010, Proceedings, May 16-21 2010, Essen. ISBN: 978-3-89336-654-5.

Crozier T. E., Yamamoto S.," Solubility of Hydrogen in Water, Seawater and NaCl Solutions", Journal of Chemical and Engineering Data, Chemical Oceanographic Branch, Naval Undersea Center, San Diego, California, 1974

Cussler E.L.," Diffusion: Mass Transfer in Fluid Systems", Third Edition, University of Minesota, ISBN-13 978-0-511-47892-5 eBook (EBL), Cambridge University Press, (2009)

D. B. Robinson and D.-Y. Peng. The characterization of the heptanes and heavier fractions for the GPA Peng-Robinson programs. Technical report, 1978.

De Lucia, M., Pilz, P., Liebscher, A., & Kühn, M. (2015). Measurements of H 2 Solubility in Saline Solutions under Reservoir Conditions: Preliminary Results from Project H2STORE. Energy Procedia, 76, 487-494.

Decourt, B., Lajoie, B., Debarre, R., & Soupa, O. (2014). The hydrogen-based energy conversion FactBook. The SBC Energy Institute.

Denholm, P., Ela, E., Kirby, B., & Milligan, M. (2010). The role of energy storage with renewable electricity generation.

Després, J., Mima, S., Kitous, A., Criqui, P., Hadjsaid, N., & Noirot, I. (2016). Storage as a flexibility option in power systems with high shares of variable renewable energy sources: a POLES-based analysis. Energy Economics.

Didier, M., Talandier, J., Berne, P., & Charlet, L. (2012, January). Hydrogen Gas Transfer Experiments within Callovo-Oxfordian Clayrock. In 3rd EAGE Shale Workshop-Shale Physics and Shale Chemistry.

Didier, Ch., van der Merwe, N., Betournay, M., Mainz, M., Kotyrba, A., Aydan, Ö., Josien, J-P., Song, W-K., Mine closure and post-mining management, International Commission on mine closure, International Society for Rock Mechanics, Report, June 2008, 139 p.

Ebigbo, A., Golfier, F., & Quintard, M. (2013). A coupled, pore-scale model for methanogenic microbial activity in underground hydrogen storage. Advances in Water Resources, 61, 74-85.

EU Commission. (2011). Energy Roadmap 2050. Brussels, XXX COM (2011), 885(2).

Feldmann, F., Hagemann, B., Ganzer, L., & Panfilov, M. (2016). Numerical simulation of hydrodynamic and gas mixing processes in underground hydrogen storages. Environmental Earth Sciences, 75(16), 1165.

Foh, S., Novil, M., Rockar, P., Randolph, P., 1979. Underground hydrogen storage. Final report, Institute of Gas Technology, Chicago, 268 pp.

Ganzer L. V. Reitenbach, D. Pudlo, M. Panfilov, D. Albrecht, ,R. Gaupp, The H2STORE Project - Experimental and Numerical Simulation Approach to Investigate Processes in Underground Hydrogen Reservoir Storage Society of Petroleum Engineers, EAGE Annual Conference & Exhibition incorporating SPE Europec, 10-13 June, London, UK Publication, 2013.

Gniese, C., Bombach, P., Rakoczy, J., Hoth, N., Schlömann, M., Richnow, H. H., & Krüger, M. (2013). Relevance of deep-subsurface microbiology for underground gas storage and geothermal energy production. In Geobiotechnology II (pp. 95-121). Springer Berlin Heidelberg.

Goldman A, Leigh J, Samudrala R. Comprehensive computational analysis of hmd enzymes and paralogs in methanogenic archaea. BMC Evol Biol 2009;9:199.

Gundogan, O., Mackay, E., & Todd, A. (2011). Comparison of numerical codes for geochemical modelling of CO 2 storage in target sandstone reservoirs. Chemical Engineering Research and Design, 89(9), 1805-1816.

Haffen, S., Géraud, Y., & Diraison, M. (2015, April). Geothermal, structural and petrophysical characteristics of Buntsandstein sandstone reservoir (Upper Rhine Graben, France). In Proceedings World Geothermal Congress, Melbourne, Australia (pp. 1-11).

Hagemann, B., Rasoulzadeh, M., Panfilov, M., Ganzer, L., & Reitenbach, V. (2015). Mathematical modeling of unstable transport in underground hydrogen storage. Environmental Earth Sciences, 73(11), 6891-6898.

Hychico, 2014, http://www.hychico.com.ar/

Horseman, S.T., Harrington, J.F. et Sellin, P., 1999, Gas migration in clay barriers. Engineering Geology, v. 54, p. 139-149.

HyUnder, (2013) D(4)– "Overview on all Known. Underground Storage Technologies for Hydrogen". Grant agreement no. 2/93. 14.08.2013. 303417

IEA (International Energy Agency) (2013) World Energy Outlook Special Report 2013: Redrawing the Energy Climate Map. OECD/IEA, Paris.

IEA, Oil & Gas Security emergency response of IEA Countries, Chapter France, p 24. https://www.iea.org/publications/freepublications/publication/France_Oil_Security_Chapter_2012.pdf , 2012.

International Gas Union. 2006-2009 Triennium Work Report. Study Group 2.1: UGS Database, http://www.igu.org/html/wgc2009/committee/WOC2/Reports/2009-WOC 2 Study Group 2-1 Basic UGS Activities-Report 2009.pdf; 2009.

Jauregui-Haza, Pardillo-Fontdevila, E.J., Wilhelm, A.M. et Delmas, H., 2004, Solubility of hydrogen and carbon monoxide in water and some organic solvents. Latin American Applied Research v. 34, p. 71-74.

Jin, Q., & Bethke, C. M. (2005). Predicting the rate of microbial respiration in geochemical environments. Geochimica et Cosmochimica Acta, 69(5), 1133-1143.

Kireeva, T.A., Berestovskaya, Y.Y., 2012. Microbiological transformations of hydrogenized gases stored in underground reservoirs. Gas Ind. Spec. Issue 684, 51–55.

Krevor, S., Blunt, M. J., Benson, S. M., Pentland, C. H., Reynolds, C., Al-Menhali, A., & Niu, B. (2015). Capillary trapping for geologic carbon dioxide storage–From pore scale physics to field scale implications. International Journal of Greenhouse Gas Control, 40, 221-237.

Krevor, S., Pini, R., Zuo, L., & Benson, S. M. (2012). Relative permeability and trapping of CO2 and water in sandstone rocks at reservoir conditions. Water Resources Research, 48(2).

Krooss, B., 2008. Evaluation of database on gas migration through clayey host rocks. Belgian National Agency for Radioactive Waste and Enriched Fissile Material (ONDRAFNIRAS). RWTH, Aachen.

Lanz, A., Heffel, J., & Messer, C. (2001). Hydrogen fuel cell engines and related technologies. College of the Desert, Energy Technology Training Center.

Larsen, H. H., & Petersen, L. S. (2013). DTU International Energy Report 2013.

Lasaga, A.C., Soler, J.M., Ganor, J., Burch, T.E., Nagy, K.L., 1994. Chemical weathering rate laws and global geochemical cycles. Geochim. Cosmochim. Acta 58, 2361– 2386.

Lassin A., Dymitrowska M., Azaroual M.," Hydrogen solubility in pore water of partially saturated argillites: Application to Callovo-Oxfordian clayrock in the context of a nuclear waste geological disposal", doi:10.1016/j.pce.2011.07.092, Elesvier Ltd .(2011)

Lenormand, R., Eisenzimmer, A., & Delaplace, P. (1995, September). Improvements of the Semi-Dynamic method for capillary pressure measurements. In SCA-9531 in Proceedings of the 1995 International Symposium of the SCA, San Francisco, CA (pp. 12-14).

Li, J., 2005. Underground gas storage in the Beijing-Tianjin region balanced the role of natural gas supply and demand .Int.Pet.Econ.13(6), 37–38.

Liebscher, A., Wackerl, J., & Streibel, M. (2016). Geologic Storage of Hydrogen–Fundamentals, Processing, and Projects. Hydrogen Science and Engineering: Materials, Processes, Systems and Technology, 629-658.

Lindblom, U.E., 1985. A conceptual design for compressed hydrogen storage in mined caverns. Int. J. Hydrog. Energy 10 (10), 667–675.

Lord, A. S. (2009). Overview of geologic storage of natural gas with an emphasis on assessing the feasibility of storing hydrogen. SAND2009-5878, Sandia National Laboratory, Albuquerque, NM.

Luo, X., Wang, J., Dooner, M., & Clarke, J. (2015). Overview of current development in electrical energy storage technologies and the application potential in power system operation. Applied Energy, 137, 511-536.

Mahlia, T. M. I., Saktisahdan, T. J., Jannifar, A., Hasan, M. H., & Matseelar, H. S. C. (2014). A review of available methods and development on energy storage; technology update. Renewable and Sustainable Energy Reviews, 33, 532-545.

Mallard, W. G., & Linstrom, P. J. NIST Chemistry Webbook, NIST Standard Reference Database No. 69; National Institute of Standards and Technology: Gaithersburg, MD, March 1998. http. webbook. nist. gov/chemistry.

Manceau, J. C., J. Ma, R. Li, P. Audigane, P. X. Jiang, R. N. Xu, J. Tremosa, and C. Lerouge (2015), Two-phase flow properties of a sandstone rock for the CO2/water system: Core-flooding experiments, and focus on impacts of mineralogical changes, Water Resour. Res., 51, doi:10.1002/2014WR015725.

Mansson, L., Marion, P., Johansson, J., Demonstration of the LRC gas storage concept in Sweden. In: Proceedings of the world gas conference. Paper n° 2.2CS.03. Amsterdam; 5-9 June 2006.

Marbán, G., & Valdés-Solís, T. (2007). Towards the hydrogen economy?. International Journal of Hydrogen Energy, 32(12), 1625-1637.

McCain Jr. Reservoir-fluid property correlations-state of the art. SPE Reservoir Engineering, 6(02):266–272, 1991.

McCarty, R. D., Hord, J., & Roder, H. M. (1981). Selected properties of hydrogen (engineering design data) (No. NBS-Mono-168). National Engineering Lab.(NBS), Boulder, CO (USA).

ME. Ministère de l'écologie, du développement durable et de l'énergie, 2011, Prévention des risques, http://www.developpement-durable.gouv.fr/Stockages-souterrains,10937.html

Metz, B., Davidson, O., De Coninck, H., Loos, M., & Meyer, L. (2005). Carbon dioxide capture and storage.

Millot R, Guerrot C, Innocent C, Négrel P, Sanjuan B (2011) Chemical, multi-isotopic (Li–B–Sr–U–H–O) and thermal characterization of Triassic formation waters from the Paris Basin. Chemical Geology 283(3–4):226-241.

Monod, J. (1949). The growth of bacterial cultures. Annual Reviews in Microbiology, 3(1), 371-394.

Montel, F., Caillet, G., Pucheu, A., and Caltagirone, J. P. (1993) Diffusion-Model for Predicting Reservoir Gas Losses. Marine and Petroleum Geology, 10, 51-57.

Moser, A.: Bioprocess technology: kinetics and reactors. Springer (1988).

Muller, N. (2011), Supercritical CO2-brine relative permeability experiments in reservoir rocks: Literature review and recommendations,

Muskat, M., Wyckoff, R. D., Botset, H. G., & Meres, M. W. (1937). Flow of gas-liquid mixtures through sands. Transactions of the AIME, 123(01), 69-96. Transp. Porous Media, 87(2), 367–383.

Oldenburg, C.M., and Pan, L., Porous Media Compressed-Air Energy Storage (PM-CAES): Theory and simulation of the coupled wellbore-reservoir system, Transport in Porous Media, DOI 10.1007/s11242-012-0118-6, 2013.

Oldenburg CM (2003) Carbon dioxide as cushion gas for natural gas storage. Energy Fuels 17(1):240–246

Ortiz, L., Volckaert, G. et Mallants, D., 2002, Gas generation and migration in Boom Clay, a potential host rock formation for nuclear waste storage. Engineering Geology, v. 64, p.287-296.

Ozarslan, A. (2012). Large-scale hydrogen energy storage in salt caverns. International Journal of Hydrogen Energy, 37(19), 14265-14277.

Palandri, J.L., Kharaka, Y.K., 2004. A compilation of rate parameters of water-mineral interaction kinetics for application to geochemical modeling. U.S.Geol. Surv. Open File Report 2004-1068.

Panfilov M (2010) Underground storage of hydrogen: in situ self-organization and methane generation. Transp. Porous Media 85 (3), 841–865.

Panfilov M., Gravier G., and Fillacier S.," Underground Storage of H2 and H2-CO2-CH4 mixtures", Netherlands, 10th European Conference on the Mathematics of Oil Recovery, September 4-6, 2006

Panfilov, M. (2016). 4.1 Underground hydrogen storage as an element of energy cycle. Compendium of Hydrogen Energy: Hydrogen Storage, Distribution and Infrastructure, 91.

Panfilov, M., Reitenbach, V., & Ganzer, L. (2016). Self-organization and shock waves in underground methanation reactors and hydrogen storages. Environmental Earth Sciences, 75(4), 1-12.

Parkhurst, D. L., & Appelo, C. A. J. (1999). User's guide to PHREEQC (Version 2): A computer program for speciation, batch-reaction, one-dimensional transport, and inverse geochemical calculations.

Paterson, L. (1983). The implications of fingering in underground hydrogen storage. International journal of hydrogen energy, 8(1), 53-59.

Pentland, C. H., El-Maghraby, R., Iglauer, S., & Blunt, M. J. (2011). Measurements of the capillary trapping of super-critical carbon dioxide in Berea sandstone. Geophysical Research Letters, 38(6).

PEPS, 2013, Étude sur le potential du stockage d'énergies, http://atee.fr/sites/default/files/peps_-_rapport_public1.pdf

Perez, A., Pérez, E., Dupraz, S., & Bolcich, J. (2016, June). Patagonia Wind-Hydrogen Project: Underground Storage and Methanation. In 21st World Hydrogen Energy Conference 2016.

Pfeiffer, W. T., & Bauer, S. (2015). Subsurface Porous Media Hydrogen Storage–Scenario Development and Simulation. Energy Procedia, 76, 565-572.

Pichavant, M. (1987). Effects of B and H2O on liquidus phase relations in the haplogranite system at 1 kbar. American Mineralogist, 72, 1056-1070.

Pini R, Krevor SCM, Benson SM. Capillary pressure and heterogeneity for the CO2/water system in sandstone rocks at reservoir conditions. Adv Water Resour 2012;38:48–59

Pini, R., & Benson, S. M. (2013). Simultaneous determination of capillary pressure and relative permeability curves from core-flooding experiments with various fluid pairs. Water Resources Research, 49(6), 3516-3530.

Poling BE, Prausnitz JM, John Paul O, Reid RC (2001) The properties of gases and liquids, vol 5. McGraw-Hill, New York

Pudlo, D., Ganzer, L., Henkel, S., Liebscher, A., Khn, M., Lucia, M., Panfilov, M., Pilz, P., Reitenbach, V., Albrecht, D., Wrdemann, H., Gaupp, R., 2013. Hydrogen underground storage in siliciclastic reservoirs—intention and topics of the H2STORE project. In: EGU General Assembly Conference Abstracts, Geophysical Research Abstracts, v. 15, EGU2013-4179-3.

Pudukudy, M., Yaakob, Z., Mohammad, M., Narayanan, B., & Sopian, K. (2014). Renewable hydrogen economy in Asia–Opportunities and challenges: An overview. Renewable and Sustainable Energy Reviews, 30, 743-757.

Purwanto, Deshpande, R.M., Chaudhari, R.V. et Delmas, H., 1996, Solubility of Hydrogen, Carbon Monoxide, and 1-Octene in Various Solvents and Solvent Mixtures. Journal of Chemical & Engineering Data, v. 41, p. 1414-1417.

Ramakrishnan T, Capiello A. A new technique to measure static and dynamic properties of a partially saturated porous medium. Chem Eng Sci 1991;16(4):1157–63.

Reitenbach, V., Ganzer, L., Albrecht, D., & Hagemann, B. (2015). Influence of added hydrogen on underground gas storage: a review of key issues. Environmental Earth Sciences, 73(11), 6927-6937.

Reynolds, C. A., & Krevor, S. (2015). Characterizing flow behavior for gas injection: Relative permeability of CO2-brine and N2-water in heterogeneous rocks. Water Resources Research, 51(12), 9464-9489.

Roads2HyCom (2008) Large Hydrogen Underground Storage. www.roads2hy.com

Robinson, D.B. , Peng, D.-Y. , 1978. The Characterization of the Heptanes and Heavier Fractions for the GPA Peng-Robinson Programs. Technical Report .

Sahimi, M., Rasaei, M. R., & Haghighi, M. (2006). Gas injection and fingering in porous media. In Gas Transport in Porous Media (pp. 133-168). Springer Netherlands.

Sakoda N, Shindo K, Motomura K, Shinzato K, Kohno M, Takata Y, Fujii M. Burnett PVT Measurements of Hydrogen and the Development of a Virial Equation of State at Pressures up to 100 MPa. Int J Thermophys 2012;33:381–395, doi:10.1007/s10765-012-1168-2.

Schaber, K., Steinke, F., Mühlich, P., & Hamacher, T. (2012). Parametric study of variable renewable energy integration in Europe: Advantages and costs of transmission grid extensions. Energy Policy, 42, 498-508.

Scheidegger AE (1958) The physics of flow through porous media. Soil Sci 86(6):355

Schiebahn, S., Grube, T., Robinius, M., Tietze, V., Kumar, B., & Stolten, D. (2015). Power to gas: Technological overview, systems analysis and economic assessment for a case study in Germany. International journal of hydrogen energy, 40(12), 4285-4294.

Sigg, L., Redox : Fundamentals, Processes and Applications. Springer: 1999; p 248

Sin, I., Lagneau, V., & Corvisier, J. (2017). Integrating a compressible multicomponent two-phase flow into an existing reactive transport simulator. Advances in Water Resources, 100, 62-77.

Smigai P. Greksak M., Kosankova J., Buzek F., Onderka V., and Wolf I. (1990) Methanogenic bacteria as a key factor involved in changes of town gas in an underground reservoir. FEMS Microbiol. Ecol., 73: 221 – 224.

Sonnenthal, E., Spycher, N., 2001. Drift-scale Coupled Processes Model: Analysis and Model Report (AMR) N0120/U0110. Yucca Mountain Nuclear Waste Disposal Project. Lawrence Berkeley National Laboratory, Berkeley, CA.

Steefel, C. I., Appelo, C. A. J., Arora, B., Jacques, D., Kalbacher, T., Kolditz, O., ... & Molins, S. (2015). Reactive transport codes for subsurface environmental simulation. Computational Geosciences, 19(3), 445-478.

Stefánsson, A. et Seward, T.M., 2003, Stability of chloridogold(I) complexes in aqueous solutions from 300 to 600°C and from 500 to 1800 bar. Geochimica et Cosmochimica Acta, v. 67, p. 4559-4576.

Stolten, D. (2016). Hydrogen Science and Engineering: Materials, Processes, Systems and Technology, 2 Volume Set. John Wiley & Sons.

Stone, H. B., Veldhuis, I., & Richardson, R. N. (2009). Underground hydrogen storage in the UK. Geological Society, London, Special Publications, 313(1), 217-226.

Succar, S., Williams, R.H., Compressed air energy storage (CAES): theory, resources, and applications for wind power, p81. Princeton University, Energy analysis group, Princeton, 2008.

Taylor, J.B., Alderson, J.E.A., Kalyanam, K.M., Lyle, A.B., Phillips, L.A., 1986. Technical and economic assessment of methods for the storage of large quantities of hydrogen. Int. J. Hydrog. Energy 11 (1), 5–22.

Tek MR (1989) Underground storage of natural gas: theory and practice, vol 171. Springer, Berlin

Toleukhanov,A.,Panfilova, I., Panfilov, M., Kaltayev, A., 2012. Bioreactive two-phase transport and population dynamics in underground storage of hydrogen: natural self-organisation, Procs. ECMOR XIII—13th Europ. Conf. Mathematics of Oil Recovery. September 10–13, 2012, Biaritz. Paper B09.

Toth, J., Bodi, T., Szucs, P., & Civan, F. (2002). Convenient formulae for determination of relative permeability from unsteady-state fluid displacements in core plugs. Journal of Petroleum Science and Engineering, 36(1), 33-44.

Tremosa, J., Castillo, C., Vong, C. Q., Kervévan, C., Lassin, A., & Audigane, P. (2014). Long-term assessment of geochemical reactivity of CO 2 storage in highly saline aquifers: Application to Ketzin, In Salah and Snøhvit storage sites. international journal of Greenhouse Gas Control, 20, 2-26.

Truche, L., Jodin-Caumon, M. C., Lerouge, C., Berger, G., Mosser-Ruck, R., Giffaut, E., & Michau, N. (2013). Sulphide mineral reactions in clay-rich rock induced by high hydrogen pressure. Application to disturbed or natural settings up to 250° C and 30bar. Chemical Geology, 351, 217-228.

Uddin, N., Preliminary design of an underground reservoir for pumped storage, Geotechnical and Geological Engineering 21: 331–355, 2003.

Vacquand, C. (2011). Genèse et mobilité de l'hydrogène naturel: source d'énergie ou vecteur énegétique stockable? (Doctoral dissertation, Institut de Physique du Globe (Paris)).

Van der Lee, J., de Windt, L., Lagneau, V., Goblet, P. 2003. Module-oriented modeling of reactive transport with HYTEC. Computers & Geosciences, 29(3):265–275.

Van Houten, R.T., Van der Spoel, H., van Aelst, A.C., Hulshoff Pol, L. and Lettinga, G. (1996) Biological sulfates reduction using synthesis gas as energy and carbon source. Biotechnology and Bioengineering: 50, 136-144.

Walters, A.B., 1976, Technical and Environmental Aspects of Underground Hydrogen Storage in 1st World hydrogen energy conference proceedings, vol. 2, 15p, held in Miami Beach, Florida, March 1-3.

Widdel F. (1988) Microbiology and ecology of sulfate- and sulfurreducing bacteria. In Biology of Anaerobic Microorganisms (ed. A. J. B. Zehnder), pp. 469–585. Wiley.

Winkler-Goldstein, R., & Rastetter, A. (2013). Power to gas: the final breakthrough for the hydrogen economy?. Green, 3(1), 69-78.

Ya, A. Z. (2016). French Green Growth Paradigm In-line with EU Targets Towards Sustainable Development Goals. European Journal of Sustainable Development, 5(2), 143-170.

Yokoyama, Y., and L. W. Lake (1981), The effects of capillary pressure on immiscible displacements in stratified porous media, paper presented at SPE 10109 SPE Annual Technical Conference and Exhibition, Soc. of Pet. Eng., San Antonio, Tex., 5–7 Oct.

Zhou, D., Fayers, F. J., & Orr Jr, F. M. (1997). Scaling of multiphase flow in simple heterogeneous porous media. SPE Reservoir Engineering, 12(03), 173-178.

Zittel, W., Wurster, R., & Bolkow, L. (1996). Advantages and Disadvantages of Hydrogen. Hydrogen in the Energy Sector. Systemtechnik Gmbitt.

Züttel, A. (2004). Hydrogen storage methods. Naturwissenschaften, 91(4), 157-172.

Alireza EBRAHIMIYEKTA

Caractérisation des interactions géochimiques et migration de l'hydrogène dans des formations sédimentaires gréseuses : application au stockage géologique

Résumé : Parmi les options en cours d'investigation, le stockage souterrain de l'hydrogène dans les formations sédimentaires comme les grès pourrait offrir un potentiel unique pour stocker de grandes quantités d'énergie. L'évaluation des modalités de stockage souterrain de l'hydrogène nécessite donc à la fois une connaissance précise des transformations minéralogiques dues à la présence de l'hydrogène et l'acquisition de données sur le comportement hydrodynamique des fluides. Par conséquent, cette étude se composera de trois parties : 1- *Etude des interactions géochimiques de l'hydrogène dans des formations sédimentaires gréseuses :* Les produits expérimentaux portent la marque d'une réaction très limitée entre les minéraux du grès et l'hydrogène. Si les résultats expérimentaux sont combinés aux résultats numériques, l'étude démontre que l'hydrogène, une fois injecté, peut être considéré comme relativement inerte. De façon globale, nos résultats renforcent la faisabilité du confinement de l'hydrogène dans des réservoirs géologiques comme les grès. 2- *Etude de la migration de l'hydrogène dans les grès : détermination de la perméabilité relative et de la pression capillaire du système hydrogène-eau :* Afin de fournir des données quantitatives pour le développement du stockage souterrain de l'hydrogène, la pression capillaire et la perméabilité relative ont été mesurées pour le système hydrogène-eau en deux conditions potentielles. Les résultats indiquent que les données obtenues sont applicables à l'ensemble des conditions de stockage de l'hydrogène. 3- *Modélisation numérique d'un site de stockage géologique d'hydrogène :* La simulation numérique a été effectuée pour caractériser l'évolution dynamique d'un site de stockage d'hydrogène pur. Une fluctuation saisonnière du fonctionnement du réservoir et l'effet des fuites d'hydrogène dus aux réactions ont été pris en compte.

Mots clés : le stockage souterrain d'hydrogène, l'interaction géochimique, les transformations minéralogiques, la perméabilité relative, la pression capillaire, la simulation numérique de transport réactif

Characterization of geochemical interactions and migration of hydrogen in sandstone sedimentary formations: Application to geological storage

Abstract: Underground hydrogen storage has been introduced as storage solution for renewable energy systems as it offers a unique potential to store large amounts of energy, especially in sedimentary formations such as sandstones. However, evaluating the underground hydrogen storage requires a precise knowledge of the hydrodynamic behavior of the fluids and of mineralogical transformations due to the presence of hydrogen that may affect the storage properties. Therefore, this study is consists in three parts: 1- *Study of geochemical reactivity of hydrogen in sandstone sedimentary formations:* The experimental products bear the mark of only very limited reaction between sandstone minerals and hydrogen. Taken together with the numerical results, this study demonstrates that hydrogen, once injected, can be considered as relatively inert. Overall, our results support the feasibility of hydrogen confinement in geological reservoirs such as sandstones. 2- *Study of the migration of hydrogen in sandstone: determination of relative permeability and capillary pressure of hydrogen-water system:* To provide quantitative data for the development of underground hydrogen storage, capillary pressures and relative permeabilities of hydrogen-water system have been measured at two potential conditions. The interpretation of the results would suggest that the obtained data are applicable for the entire range of hydrogen storage conditions. Interfacial tensions and contact angles for the hydrogen-water system have been also derived. 3- *Numerical simulation of a geological hydrogen storage site:* The numerical simulation was performed to characterize the evolution of pure hydrogen storage, by considering the seasonal fluctuation of renewable energy and the effect of hydrogen loses due to the biotic reactions.

Keywords : Underground hydrogen storage, geochemical interaction, mineralogical transformations, two-phase flow, relative permeability, capillary pressure, reactive transport numerical simulation

Institut des Sciences de la Terre d'Orléans
UMR 7327 – CNRS/Université d'Orléans
1A, Rue de la Ferollerie
45071 Orléans Cedex 2 France